University of Cagliari

Department of Biomedical Science
Section of Microbiology and Virology

Research Doctorate in

"Development and Evaluation of Anti-infective Drugs"

XXVII cycle

Title of thesis

Biochemical, computer, and spectroscopic techniques applied to the study of prions and of combinations of antineoplastic drugs

Scientific Area BIO/19 – General Microbiology

Doctorate Coordinator
Prof. Alessandra Pani

Supervisor
Prof. Alessandra Pani

Abroad supervisor
Dr. *Byron Caughey*

Candidate
Dr.ssa Daniela Perra

Academic year
2013-2014

Acknowledgements

Daniela Perra gratefully acknowledges Sardinia Regional Government for the financial support of her PhD scholarship (P.O.R. Sardegna F.S.E. Operational Programme of the Autonomous Region of Sardinia, European Social Fund 2007-2013 - Axis IV Human Resources, Objective l.3, Line of Activity l.3.1.).

La presente tesi è stata prodotta durante la frequenza del corso di dottorato in Sviluppo e Sperimentazione dei Farmaci anti'infettivi dell'Università degli Studi di Cagliari, a.a. 2013/2014 - XXVII ciclo, con il supporto di una borsa di studio finanziata con le risorse del P.O.R. SARDEGNA F.S.E. 2007-2013 - Obiettivo competitività regionale e occupazione, Asse IV Capitale umano, Linea di Attività l.3.1 "Finanziamento di corsi di dottorato finalizzati alla formazione di capitale umano altamente specializzato, in particolare per i settori dell'ICT, delle nanotecnologie e delle biotecnologie, dell'energia e dello sviluppo sostenibile, dell'agroalimentare e dei materiali tradizionali"

I would like to thanks everyone who have helped me in realizing this thesis.

First of all, Professor Alessandra Pani, my supervisor, for having been professional, personal and valuable guide
in these three years of doctorate.

Dr. Byron Caughey, for allowing me in his laboratories.

Dr. Bradley Groverman, for teaching me patiently several laboratory techniques and for his many tips in my research activity.

Dr. Giuseppina Sanna, for always believing in me and making me feel more protected in all circumstances.

Dr. Elisabetta Pinna, Dr. Sara Vascellari and Dr. Silvia Madeddu, for being my friends as well as collegues.

Finally, I thanks my parents for always being presents in all my experiences.

Abstract

This thesis collects the work I have done during the three-year PhD Course. The results obtained are divided according to the research topics addressed:

- Drug discovery of anticancer agents and development of synergistic associations (Part I);
- Studies on the prion structure and the pathogenesis of prion diseases (Part II).

Studies referring to the Part I have been carried out at the University of Cagliari and were focalized on the evaluation and experimental validation of the method known as Artificial Neural Network (ANN), which allows to determine, and also to predict, types and degree of interaction of two or more drugs in combination with one another(s). I have successfully applied the ANN approach to combinations of two cytotoxic compounds, i.e. cis-platinum (CDDP), a potent antineoplastic used in the therapy of some types of carcinoma, with Cu(II) complexes that were previously shown to be endowed with potent cytotoxic activity *in vitro* (Pivetta et al., J Inorg Biochem. 2011 and 2012). Binary combinations comprising CDDP and Cu(II) complexes revealed (Part I, Chapter I) a strong synergistic cytotoxic effect against leukemia cell lines (Pivetta et al., Talanta 2013). The synergistic effect was confirmed in CDDP-resistant leukemia and ovarian cancer cell lines (Part I, Chapter II). Investigations on molecular bases of the CDDP – Cu(II) complexes synergism are in progress.

As for the Part II of my research, I firstly investigated the mechanisms underlying the process of generation of pathogenic prion protein (PrPSc). These studies were carried out in part at the University of Cagliari, and in part at the Rocky Mountains Laboratories (RML) of the NIAID/NIH in USA (Hamilton, Montana), during my 14-month research internship as supplemental visiting fellow in a graduate partnership program. The studies carried out in Cagliari have investigated 1H NMR modifications of brain metabolite profiles in sheep from a Sardinian farm hit by natural Scrapie with the aim to discriminate infected vs. Uninfected, and early vs. late phases of the prion infection (Part II, Chapter I). The overall results, obtained by different chemometric tools, were able to describe a metabolite profile of scrapie-infected sheep brain, with and without clinical sign, different to that of healthy ones, and to suggest Ala as a biomarker of PrPSc deposition (Scano et al., J Molecular Biosystem, 2015)

Studies conducted at the RML of NIAID/NIH have addressed the structural features of PrPSc in order to identify regions of the protein involved in the process of misfolding (Part II, Chapter II). So far, data suggest that i) the N-terminal portion of the prion protein may have a role in the modulation of the protein aggregation process, typical of prion diseases, while ii) the central portion seems capable to undergo aggregation into fibrils even in the absence of other regions of the protein. However, further studies are needed to confirm the proposed role in promoting/hindering the misfolding and subsequent aggregation process of the various protein regions.

Table of contents

Part I - Drug discovery of anticancer agents and development of synergistic associations

Chapter I - Artificial Neural Networks and Experimental Design to assess the synergism of drugs

The first part of my researchs has focused on the study of combinations of cytotoxic drugs by using a new method named Artificial Neural Networks (ANN).

The association of multiple drugs in the treatment of cancer allows: a) the administration of each drug at doses significantly lower than the maximum tolerated, by reducing the overall systemic toxicity for the patient, b) the reduction of drug-resistant cell mutants, c) to simultaneously inhibit several cellular processes and thus determining the cell death in various cellular stages.
Platinum derivatives, such as CDDP (cis-diammineplatinum (II) dichloride), are widely used in clinical practice for the treatment of several types of cancer, such as breast, ovarian, prostate, testes, and non-small cell lung carcinomas (Eckstein et al., J Exp Clin Cancer Res. 2011; Dhar et al., Proc Natl Acad Sci U S A. 2008; Rixe et al., Biochem Pharmacol. 1996; Michels et al., Cancer Res. 2013). However, continuous administration of this drug, as of any other antitumor agent, is limited by the onset of drug resistance, which may emerge in the neoplastic cells in response to various mechanisms (reduction/increase of the influx/efflux in the cells, enhanced drug inactivation by biomolecules, a greater capacity to repair or tolerate DNA damage, etc.), that reduce the drug's effectiveness. Previous findings from my lab have shown an interesting antiproliferative activity *in vitro* against human prostate and lung caricinoma cell lines, as well as against T and B leukemia derived cells of a class of complexes of copper (II) with phenantroline (Pivetta et al., J Inorg Biochem. 2011 and 2012).
Although the mechanism of action of the latter compounds has not yet been fully clarified, it seems to be different than that of CDDP. It was therefore decided to evaluate the effect of combinations of CDDP with the three most potent Cu(II)-phen complexes. The purpose of this combination was to verify if it was possible to obtain a synergistic effect of the two compounds that would allow to reduce the effective dose of CDDP and the frequency of the onset of resistant mutants. The cytotoxic effect of the compounds, alone and in combination, was first evaluated against cells of the human lymphoblastic leukemia T, CCRF-CEM, which were shown to be the most sensitive to the cytotoxic activity of Cu(II)complexes.

Since we have set this goal, we stumbled early in the definition of synergy between the two compounds. The synergistic effect is currently assessed using the Combination Index (CI) and Isobologram (IB) methods. The CI method is used to measure the degree of interaction between the two drugs; if the value of CI is less than 1 the combination of the two drugs has an antagonistic effect, if it is equal to 1 an additive effect and if it is greater than 1 an additive effect. The isobologram indicates the possible toxicological responses to a binary mixture of chemical compounds through a graphical representation in a Cartesian system. The isobolgramma has the same function of CI, but the type of interaction between the two compounds is defined by the resulting curve in the cartesian system, wherein the additive effect is represented by a straight line, while the curves above and below this straight line define the synergistic effect and antagonist, respectively. The CI method assumes that the compounds have a direct effect on enzymes, inhibiting their enzyme kinetics (Chou et al., Eur J Biochem. 1981). However, it is known that the compounds can carry out their function also through other mechanisms and therefore this assumption can not be considered valid for all compounds. Also, both CI and IB methods do

not have a predictive effect, establishing only the efficacy of the drug combinations experimentally tested.
However, both CDDP and Cu(II)complexes are examples of cytotoxic drugs that do not have a direct effect on enzymes; therefore, the IC and IB methods are not totally reliable for the evaluation of the potential drug interactions. Due to these limits of current methods, we have proposed a new approach that would allow not only to quantify the degree of synergism of a mixture of drugs, but also to predict the effect of all possible combinations of the drug, leading to the identification of optimal combinations with the most synergistic effect: these are the known methods such as Artificial Neural Network (ANN) and Experimental Design (ED). The results of this study, that have been already published (http://www.ncbi.nlm.nih.gov/pubmed/24054565) in Talanta in 2013 are fully described below.

Artificial Neural Networks and Experimental Design to assess the synergism of drugs: the case of copper(II) complexes with cisplatin

Tiziana PIVETTA[a)], Francesco ISAIA[a)], Federica TRUDU[a)], Alessandra PANI[b)], Matteo MANCA[b)], Daniela PERRA[b)], Filippo AMATO[c)], Josef HAVEL[c),d),e)]*

a) Dipartimento di Scienze Chimiche e Geologiche; b) Dipartimento di Scienze Biomediche, Università degli Studi di Cagliari, 09042 Monserrato (CA)-ITALY; c) Department of Chemistry, Faculty of Science, Masaryk University, Kampus Bohunice, Kamenice 5/A14, 62500 Brno, Czech Republic; d) Department of Physical Electronics, Faculty of Science, Masaryk University; e) R&D center for low-cost plasma and nanotechnology surface modifications, Masaryk University, Kotlářská 2, 611 37 Brno, Czech Republic.

The platinum compounds such as cisplatin (CDDP), carboplatin and oxaliplatin, are believed to kill cancer cells by binding to the nuclear DNA [1, 2], distorting its structure and thereby triggering cellularprocesses that result in apoptosis [3]. Only a tiny fraction of the cellular platinum binds to the nuclear DNA, being mainly engaged and inactivated by the plethora of sulphur-containing ligands present in the cytoplasm. CDDP is highly effective in treating a variety of cancers [4] but both inherited and acquired cell resistance seriously limits its applications [5]. Different mechanisms have been proposed to explain the cellular resistance to CDDP, such as a decreased accumulation of the drug, a higher deactivation due to the more efficient extracellular detoxification system, a decreased action on DNA or an increased capacity of DNA repair [6, 7]. In recent years, the treatment of the tumours was significantly improved through the use of appropriate combinations of chemotherapeutic agents. The combination of chemotherapeutic drugs gives the possibility to administer each drug in a dose significantly lower than the maximum tolerated one, reducing the overall systemic toxicity for the patient [8]. Moreover, because the cancer cells might be in different stages of their metabolism (proliferating, differentiating or resting), the combination of drugs that acts on different stages of the cell cycle, lead to an increase in the overall mortality of cancer cells.

Also, the complexes of copper(II) with 1,10-ortho-phenanthroline (phen) show antitumoral effects [9], both in vitro and in vivo. In this context the complexes $Cu(phen)(OH_2)_2(OClO_3)_2$ (**1**), $[Cu(phen)_2(OH_2)](ClO_4)_2$ (**2**) and $[Cu(phen)_2(imidazolidine\text{-}2\text{-}thione)](ClO_4)_2$ (**C1**) showed a high cytotoxic activity against mouse neuroblastoma, human hematologic and solid tumor-derived cell lines [10, 11]. Therefore we decided to investigate the cytotoxic activity of a series of mixtures containing CDDP and **1**, **2** and **C1** in different molar ratios (the studied compounds are reported in Table 1) against the human acute T lymphoblastic leukemia (CCRF-CEM).

In this work we also propose a new method, based on Artificial Neural Networks (ANNs) and Experimental Design (ED), to study the toxicity of the drug combinations and choose the best one in terms of toxicity and drug levels.

Three different sets of experiments were carried out, each one repeated at least three times, for the systems **1**-CDDP, **2**–CDDP and **C1**-CDDP. For each system, solutions containing one drug alone at the time and combinations of the two drugs were prepared following an experimental design (Supporting Information (S. I.), Fig. S2). Concentrations of **1** was in the range 0 – 5 μM while concentration of **2**, **C1** and CDDP were in the range 0 – 2 μM. The percentage of vitality was measured for each solutions with respect to the controls, and converted in mortality (as 100 % minus vitality). The concentrations and the cytotoxic activity of all the combinations are reported in S. I., Tables S1,S2, S3.

Table 1. *Formula and acronyms of the studied compounds*

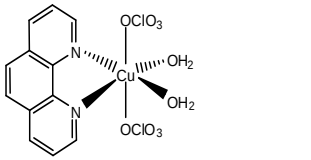

1
$Cu(phen)(OH_2)_2(OClO_3)_2$

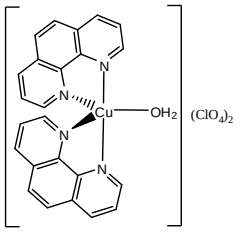

2
$[Cu(phen)_2(OH_2)](ClO_4)_2$

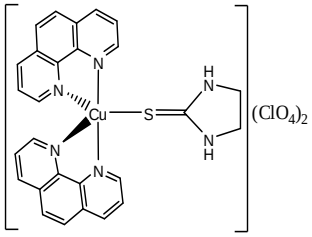

C1
$[Cu(phen)_2(imidazolidine\text{-}2\text{-}thione)](ClO_4)_2$

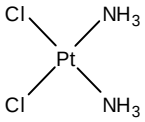

CDDP
$Pt(NH_3)_2Cl_2$

The data matrix (concentration of copper complex, concentration of CDDP and cytotoxicity) was evaluated with the programs EasyNN-plus [12] and Trajan [13]. It was found that both the programs gave comparable results. The neural network architecture was optimised and it was found that either 4 or 5 hidden neurons were needed. Standard back-propagation algorithm was used to train the network (for more details see S. I., sect.s 2.1-2.2).

The agreement between estimated and experimental values confirms the goodness of the training of the network (S. I., Fig. S3). The dose-response curves for **1**, **2**, **C1** and CDDP were calculated (S. I., Fig. S4); for **1**, **2** and **C1** a sigmoidal curve is obtained. The threshold doses for **1**, **2**, **C1** and CDDP are 1 μM, ≈ 0.5 μM, 0.25 μM and 0.375 μM, respectively.

The CC50 (the dose of the drug which inhibits the proliferation of 50 % of the cells) is in the order: **C1** (0.989 μM) > CDDP (0.922 μM) > **2** (1.26 μM) >> **1** (3.01 μM). **2** is more cytotoxic than **1** due to the presence of two phen units, **C1** is more toxic than **2** for the presence of the imidazolidine-2-thione auxiliary ligand. The predictive ability of the network was used to calculate the % of mortality on the whole concentration space (according to a 40x40 grid). In this way, a surface is obtained from the non-linear fit of experimental data obtained by the trained neural network. The response surface and its contour plot for **1**-CDDP system are shown in Fig. 1a and 1b, respectively. The calculated and experimental values are in good agreement (S.I., Fig. S4).

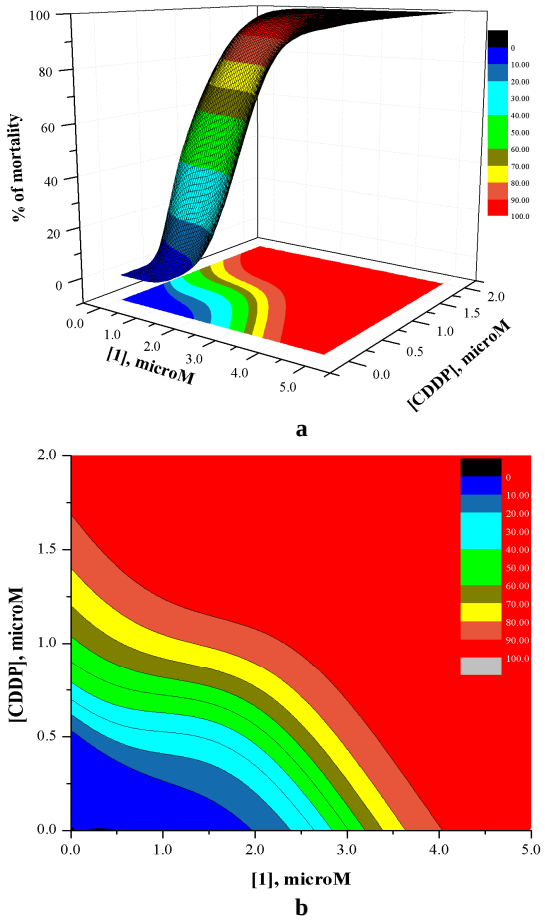

Fig. 1. Response surface (a) and contour plot of iso-values of cytotoxicity (b) as a function of the concentrations of **1** and CDDP

As can be seen in the Fig. 1a the mortality increases with the concentrations of the two drugs with a trend similar to a dose-response curve. The two drugs alone show a mortality > 90% for a concentration higher than 4 μM and 1.7 μM for **1** and CDDP, respectively. In the contour plot the areas of cytotoxicity isovalues for the various mixtures can be explored in order to choose the most suitable mixture that has a desired cytotoxicity value, with the lowest dose of both the drugs. For example, for a toxicity of 70%, instead of choosing **1** alone at a concentration of about 3.5 μM or CDDP alone at a concentration of about 1.25 μM, a combination of the two drugs at concentrations of 2 μM and 0.78 μM, for **1** and CDDP respectively, can be selected, minimizing the side effects related to the doses. Results for **2**-CDDP and **C1**-CDDP systems are shown in the S. I., Fig.s S6 and S7 respectively. In Table 2, some selected combinations of the three copper(II) complexes and CDDP that produce a 50% of antiproliferative effect are shown. As can be seen, it is possible to choose the proper combination depending on the desired doses of a drug, for example for a particular tolerability of the treated patients.

Table 2. *Selected combinations of Cu(II) complexes and CDDP producing an antiproliferative effect of 50 % against CCRF-CEM cell lines.*

System	[CDDP] μM	[Cu(II)] μM
1-CDDP	0.10	2.88
	0.40	2.38
	0.75	0.75
	0.70	1.38
	0.80	0.38
2-CDDP	0.05	1.25
	0.30	1.15
	0.40	1.10
	0.55	1.00
	0.90	0.60
C1-CDDP	0.15	0.85
	0.20	0.80
	0.25	0.75
	0.30	0.70
	0.55	0.35

Associations of two or more drugs exhibit synergistic, antagonistic or additive effect [14, 15] when the cytotoxicity of the combination is respectively greater, lower, or equal to the additive effect of the individual drugs. Thus the concept of synergism and / or antagonism strongly depends on the definition of purely additive contribution of two or more drugs. This definition has been proposed and interpreted very differently by various authors [16-21] but in our opinion, the traditional approaches used to assess whether a multidrug mixture shows synergistic, antagonistic or purely additive effect are limited because they do not consider the whole complexity of the system and force the application of a certain defined model, in particular the enzymatic kinetic one. Nowadays the drug action is known to occur not only by enzymatic reaction but also by drug-receptor interactions (drugs act on the cell membrane by physical and/or chemical interactions, through specific drug receptor sites known to be located on the membrane) and by non specific interaction (drugs act exclusively by physical means outside the cells, external surfaces of skin and gastrointestinal tract, or outside the cell membranes by chemical interactions). With these considerations, we decided to start from the simple concept proposed by Webb and Bliss in 1963 [22, 23], and to extend and express it in a rigorous mathematical form that allows to evaluate the effects of a virtually infinite number of drugs. This approach leads to a new operational definition of additive contribution. Summarising, our method allows to determine which combinations give a certain percentage of cytotoxic activity and seem optimal in terms of concentration (to reduce the cost and the possible side effects) and, among these suitable combinations, which present the greatest synergistic effect. This method has the advantage that no assumptions about the mechanism of action of the drugs is made (more detailed comments on the choice of the method are reported in the S.I. sect. 2.3). In brief, given n drugs with individual percentage of mortality values a_1, a_2, …, a_n, the additive contribution is calculated as in (1) for each mixture.

$$Effect = \sum_{i=1}^{n} a_i + \sum_{k=2}^{n} (-1)^{k-1} \frac{C_{n,k}\{a_1, a_2, \ldots, a_n\}}{100^{k-1}} \quad (1)$$

Where $C_{n,k}\{a_1, a_2, \ldots, a_n\}$ are the simple combinations without repetition of the cytotoxicities of the n drugs taken k at a time (with $k \geq 2$). The values given by equation 1 are bounded because no mixture of drugs can have an effect greater than 100% and/or lower than 0%. The terms of Equation 1 provided by the simple combinations, are formed

by linear combinations of products of *k* elements (with k ϵ R^+). The number of terms is given by Eq. (2):

$$Effect = \sum_{i=1}^{n} a_i - \frac{1}{100}\left[\sum_{i\neq j} a_i a_j\right] + \frac{1}{100^2}\left[\sum_{i\neq j\neq l} a_i a_j a_l\right] - \cdots + (-1)^{k-1}\frac{1}{100^{n-1}}\left[a_i a_j \ldots a_n\right] \quad (2)$$

The first term counts n elements, the second one [n!/(2!(n-2)!)] elements, the third one [n!/(3!(n-3)!)] elements and so on, the last term counts only 1 element. Then for two drugs, the additive effect is expressed according to eq. 3, while for 3 drugs according to eq. 4 and so on.

$$Effect = a_1 + a_2 - \frac{a_1 a_2}{100} \quad (3)$$

$$Effect = a_1 + a_2 + a_3 - \frac{a_1 a_2 + a_1 a_3 + a_2 a_3}{100} + \frac{a_1 a_2 a_3}{100^2} \quad (4)$$

Following this definition of additive effect and the corresponding mathematical description given above, the effect of the combined drugs might be calculated as difference between the mortality value of the combination and the calculated additive effect. In fact, from the response surface we subtract what we defined as the non-algebric additive effect of the drugs in the mixture. The resultant surface may show either positive or negative peaks respect to a "zero level". The positive and negative peaks so revealed correspond to combinations of the drugs that give synergic or antagonistic effect, respectively. The non-algebric additive effect is calculated as due to the sequential action of the drugs. Our definition of non-algebric additive effect does not need to be justified on biochemical basis. In fact, the ED-ANNs approach here described does not take into account the molecular basis of the mechanism of action of the multidrug mixture. Each phenomenon that occurs at the molecular level is projected on the shape of the response surface. Selected mixtures of the drugs (training and verification sets), are used to model the response surface by ANN and then the % of mortality is estimated on the whole space.

The response surface for the **1**-CDDP system, is shown in Fig. 2a and in Fig. 2b the contour plot is given. As can be seen, no antagonistic zones are present, while a synergistic area is evident, with a maximum at [**1**] = 2.63 μM and [CDDP] = 0.55 μM. This combination produces a 73.6 % of mortality, while **1** and CDDP alone, show at the same concentrations, a mortality of 29.3 and 11.8 %, respectively. In oder to confirm the predicted maximum of synergism and to check the overall predictive ability of the network, a set of 11 new combinations were prepared (test set) and the corresponding cytotoxic activities were measured. The test data values were corrected for the pure additive effect and compared with the calculated values confirming all the predicted data and in particular the maximum of synergistic effect (35.0 % and 34.5 % as predicted and measured synergism, respectively).

The same method was applied to the data of the systems **2**-CDDP and **C1**-CDDP. For **2**-CDDP a maximum of synergistic effect is observed at [**2**] = 1.05 μM e [CDDP] = 0.85 μM with a mortality equal to 81.6 %, for **C1**-CDDP a maximum is observed at [**C1**] = 0.87 μM e [CDDP] = 0.45 μM with a mortality equal to 82.8 %. The calculated surfaces with all the experimental values and the contour plot of synergism isovalues are reported for all the systems in the S.I., Fig.s S8-S10.

In all the cases, the mortality of the combinations is higher than the effect of the drugs alone. Slight differences among the cytotoxicity values of CDDP obtained in the three experiments are due to the variability of the cell reactivity, correlated to the growing time and the final density of the suspension cultures.

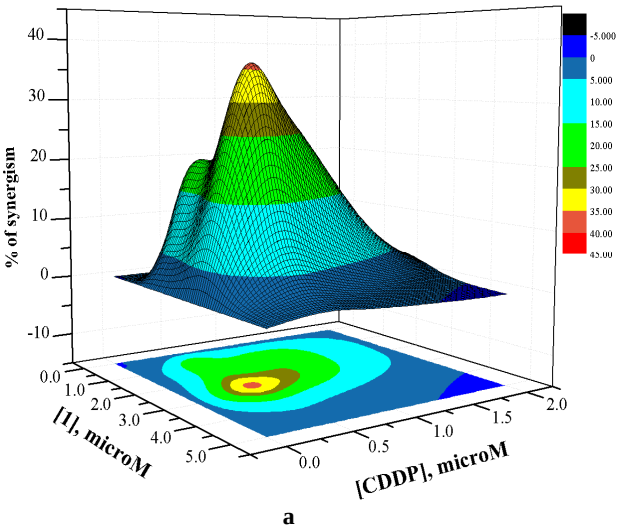

a

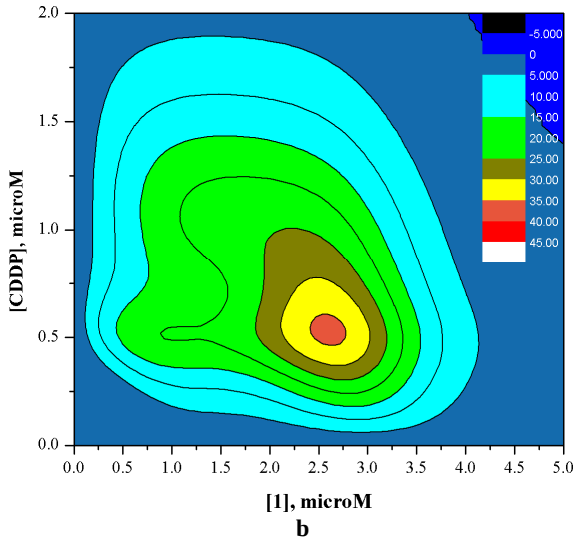

b

Fig. 2. Synergism surface (a) and contour plot of iso-values of % of synergism (b) as a function of the concentrations of the **1** and CDDP. As "% of synergism" is intended the difference between the experimental mortality and the additive effect, both expressed as %.

Since the maximum of synergistic effect occurs for almost integer ratios of copper complexes and CDDP concentrations, we wanted to verify the possible formation of mixed complexes between **1**, **2** and **C1** with CDDP by mass spectrometry.

We collected both Laser Desorption Ionization (LDI) and Matrix Assisted Laser Desorption Ionization (MALDI) mass spectra. Mass spectra of the mixtures of Cu(II) complexes and CDDP at 1:5 and 5:1 molar ratios were recorded, and no mixed copper-platinum complexes were detected.

In conclusion, we propose a new method to assess the synergism of mixture of drugs. Our approach is relatively easy, fast, and highly reproducible. The use of ANNs was found to be appropriate also for the evaluation of a small number of data. Moreover, the use of ED, to distribute the experiments on the working space, improves the quality of the results. The cytotoxicity values of the drugs can be predicted for all the possible mixtures in the studied concentration intervals, without any assumption about the mechanism of action.

Applying our method to the study of the combinations of **1**, **2** and **C1** with CDDP, a synergistic effect was revealed for all the systems. In particular the combinations with the maximum synergistic effect for the three systems, present a high

cytotoxic activity toward the tested cancer cells, with a required doses significantly lower than those needed for the drugs taken alone.

”Matteo Manca and Daniela Perra gratefully acknowledge Sardinia Regional Government for the financial support of their PhD scholarship (P.O.R. Sardegna F.S.E. Operational Programme of the Autonomous Region of Sardinia, European Social Fund 2007-2013 - Axis IV Human Resources, Objective l.3, Line of Activity l.3.1.)”.

Keywords: copper complexes · cisplatinum · cytotoxicity · synergistic effect · artificial neural network

[1] A. Estman, N. Schulte, *Biochem*. **1988**, *27*, 4730-4734.
[2] A.C.M. Plooy, M. van Dijk, P.H.M. Lohman, *Cancer Res*. **1984**, *44*. 2043-2051
[3] T. Faruta, T. Ueda, G. Aune, A Sarasin, K.H. Kraemer, Y. Pommier, *Cancer Res*. **2002**, *62*, 4899-4902.
[4] C.X. Zhang; S.J. Lippard, *Curr. Opin. Chem. Biol*. **2003**, *7(4*), 481-489.
[5] L.R. Kelland, *Drugs* **2000**, *59*, 1-8.
[6] K.J. Scanlon, M. Kashani-Sabet, H. Miyachi, L.C. Sowers, J. Rossi, *Anticancer Res.* **1989**, 9, 1301-1312.
[7] P.A. Andrews, S.B. Howell, *Cancer Cells* **1990**, *2*, 35-43.
[8] F. Kratz, P. Senter, H. Steinghagen, Drug delivery in oncology: from basic research to cancer therapy, 1th ed., WILEY-VCH Verlag GmbH & Co. KGaA **2012**.
[9] F. Carvallo-Chaigneau, C. Trejo-Solis, C. Gomez-Ruiz, E. Rodriguez-Aguilera, L. Macias-Rosales, E. Cortes-Barberena, C. Cedillo-Pelaez, I. Gracia-Mora, L. Ruiz-Azuara, V. Madrid-Marina, *Biometals* **2008**, *21*, 17-28.
[10] T. Pivetta, M.D. Cannas, F. Demartin, C.Castellano, S. Vascellari, G. Verani, F. Isaia, *J. Inorg. Biochem*. **2011**, *105*, 329-338.
[11] T. Pivetta, F. Isaia, G. Verani, C. Cannas, L. Serra, C. Castellano, F. Demartin, F. Pilla, M. Manca, A. Pani, *J. Inorg. Biochem*. **2012**, *114*, 28-37.
[12] EasyNN-plus 2011 v. 14.0, Neural Planner Software Ltd.
[13] Trajan Software, The Old Rectory, Low Toynton, Horncastle, Lincs., LN9 6JU, UK
[14] V.L. Damaraju, D.Y. Bouffard, C.K.W. Wong, M.L. Clarke, J.R. Mackey, L. Leblond, C.E. Cass, M. Grey, H. Gourdeau, *BMC Cancer* **2007,** *7*, 121-131.
[15] E. Frei, A. Elias, C. Wheeler, P. Richardson, W. Hryniuk, *Clin. Cancer Res*. **1998**, *4*, 2027-2037.
[16]W. Greco, G. Bravo, J.C. Parsons, *Pharmacol. Rev*. **1995**, 47, 331-385.
[17] M.C. Berenbaum, *Pharmacol. Rev*., **1989,** *41*, 93-141.
[18] T.C. Chou, *Mol. Pharmacol*. **1974**, *10*, 235-247.
[19] T.C. Chou, P. Talalay, *Eur. J. Biochem*. **1981**, 115, 207-216.
[20] S. Loewe, *Arzneim. Forsch*. **1953**, *3*, 285-290.
[21] T.C. Chou, *Pharmacol. Rev*. **2006**, *58*, 621-681.
[22] Webb, J. L. 1961. Effect of more than one inhibitor, p. 66 and 488. In Enzymes and metabolic inhibitors, vol. 1. Academic Press, New York, N.Y.
[23] C.I. Bliss, *Ann. Appl. Biol*. **1939**, *26*, 585-615.

Entry for the Table of Contents

Layout 2:

Tiziana PIVETTA*, Francesco ISAIA, Federica TRUDU, Alessandra PANI, Matteo MANCA, Daniela PERRA, Filippo AMATO, Josef HAVEL

Artificial Neural Networks and Experimental Design to assess the synergism of drugs: the case of copper(II) complexes with cisplatin

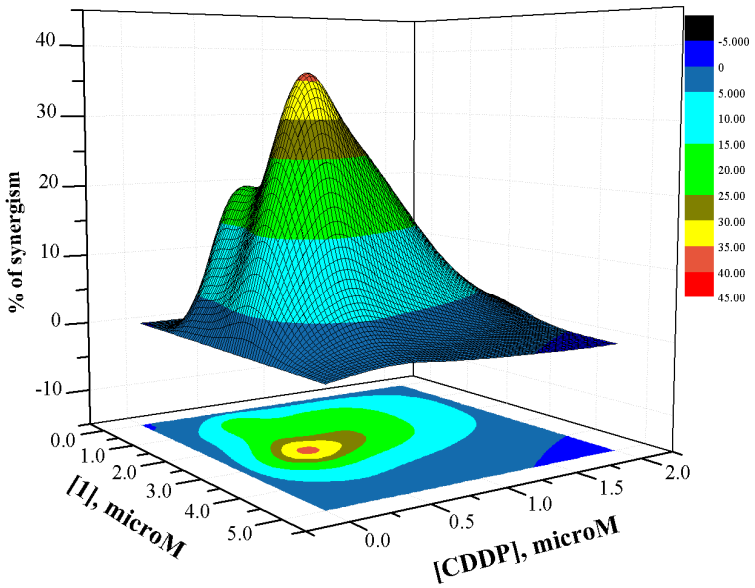

A new method to assess the synergism of drugs and choose their optimal combination in terms of activity and drug levels, by using Artificial Neural Networks and Experimental Design is proposed. The reliability of this method is evaluated for mixture of some copper(II) complexes and cisplatin. In figure, the surface of synergism for Cu(phen)(OH_2)($OClO_3$)$_2$ (**1**) and cisplatin (CDDP) is shown.

:

SUPPORTING INFORMATION:

1. Experimental part

1.1Reagents. $Cu_2(CO_3)(OH)_2$, 1,10-phenanthroline monohydrate, cisplatin, perchloric acid, ethanol, ethyl ether, DMSO, imidazolidine-2-thione, and acetonitrile were purchased from Sigma-Aldrich and used without any further purification. Red phosphorus was purchased from Riedel de Haën (Hannover, Germany). The 3-hydroxy picolinic acid was purchased from Sigma-Aldrich (Prague, Czech Republic). Water was double distilled from a quartz apparatus from Heraeus Quarzschmelze, (Hanau, Germany). CAUTION: Perchlorate complexes are potentially explosive, handle these compounds even in small amounts with care.

1.2Mass spectrometry. Mass spectra were recorded using AXIMA Resonance mass spectrometer from Kratos Analytical (Manchester, UK), equipped with a quadrupole ion trap (QIT) and a reflectron time-of-flight analyzer. The instrument for drying samples was from Kratos Analytical. Calibration was done using red phosphorus clusters as described in [1].

Laser desorption ionization (LDI) and matrix-assisted-laser-desorption-ionization (MALDI) were used. From several matrices examined, 3-hydroxo picolinic acid (HPA) was found to be the most suitable. It was found that all the species detected both in LDI and MALDI analysis were singly charged. The mixtures of **1**, **2**, and **C1** complexes with CDDP (5:1 molar ratio) were prepared in 50% acetonitrile/water. For LDI analysis 5 μL of the mixture was deposited on the metallic target of the instrument and after drying, the mass spectra were recorded. For MALDI analysis first 5 μL of saturated solution of matrix was deposited and, after drying, 5 μL of the mixture was deposited on the matrix layer and dried again. Mass spectra were recorded in both reflectron positive and negative ion mode after the pressure was below 10^{-4} Torr. Mass spectra recorded in negative ion mode were found to be not suitable. Positive ion mode mass spectra were used further as ionization is efficient even at lower laser energy.

1.3Synthesis. 1, **2** and **C1** were prepared as previously reported [2, 3]

1.4Studied combination for the systems 1-CDDP, 2-CDDP and C1-CDDP. 42 combinations of 1 and CDDP, 9 solutions of CDDP alone and 9 solutions of 1 alone were prepared following the Experimental Design reported in Fig. S2a. Among the 60 solutions, 25 were used as training set, 24 as validating set and 11 as test set (Table S1). 34 combination of 2 and CDDP, 6 solutions of CDDP alone and 4 solutions of 2 alone were prepared following the the Experimental Design reported in Fig. S2c. Among the 44 solutions, 18 were used as training set,16 as validating set and 10 as test set (Table S2). 33 combinations of C1 and CDDP, 7 solutions of CDDP alone and 5 solutions of C1 alone were prepared following the Experimental Design reported in Fig. S2d. Among the 46 solutions, 21 were used as training set,19 as validating set and 6 as test set (Table S3).

1.5Cell lines. The CCRF-CEM (acute T-lymphoblastic leukemia) human cell line was purchased from the American Type Culture Collection. The cell line was grown at 37°C in a 5% CO_2 atmosphere in its specific media and according to ATCC instructions in the presence of 10% fetal calf serum (FCS), 100 U/ml penicillin, and 100 μg/ml streptomycin. The cell line was maintained in exponential growth by periodically splitting high density suspension cultures (i.e. 106/ml). Cell culture was periodically tested for the absence of mycoplasma contamination.

1.6Cytotoxic assay. The cytotoxic effect of test compounds was evaluated in exponentially growing cell cultures. Stock solutions of test compounds were made at 1 mM in DMSO and stored at 4°C in the dark. For the evaluation of cytotoxicity, each compound was serially diluted in specific growth medium so that the concentration of DMSO was never higher than 0.1%. Cell growth in absence and in presence of test compounds was determined after 96 h of incubation, corresponding to three duplication rounds of untreated cells, by the 3-(4,5- dimethylthiazol-2-yl)-2,5-diphenyl-tetrazolium bromide (MTT) method [4]. Numbers of viable cells were also determined by the trypan blue dye exclusion method. Cell growth at each drug concentration was expressed as the percentage of untreated controls. Each compound was tested in least three independent assays. Statistical analysis was performed with Student's t-test, and significance was set at $p \leq 0.05$. The antitumor agent 6-mercaptopurine was used as a reference compound.

2. Theoretical basis

2.1 Artificial Neural Networks. The mathematical description of the processes occurring in a physico-chemical system is generally called "model" and it allows the estimation of the system's response for different experimental conditions. A model is called "hard" when it is derived from a rigorous physical theory. As a consequence, for systems with intricate behavior, "hard" models are often difficult to be found. An approach in which a set of conditions-response data is used to model the system without the use of a rigorous physical theory, is usually called "soft" modeling., Multiple regression techniques are generally employed, but such methods suffer of several disadvantages that restrict their use [5].

Artificial Neural Networks (ANNs) are a powerful mathematical tool by which the limitations of multiple regression methods can be avoided. An ANN is a formal object that emulates the structure of the brain and its "*learning*" ability. A series of logic units, called "*neurons*", is organized in layers, *input*, *hidden* and *output*. Generally, the ANN architecture is represented as (*i, j, k*) where *i, j, k* are the number of neurons in the input, hidden and output layers, respectively. An example of ANN architecture is given in Fig. S1.

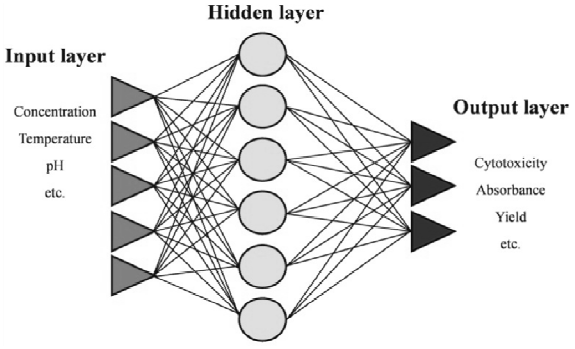

Fig. S1: A general ANN architecture with one hidden layer

The role of the neurons in the hidden layers is to perform simple mathematical operations on the incoming data from the input layers and to transfer the result to the neurons of the subsequent layers. At the end, the neurons in the output layer generate the network output. The links connecting each neuron of a layer to all the neurons in the subsequent layers are weighed. The role of the weights is to modulate the information flowing from the input layer toward the output one. As for a biological brain, an artificial neural network needs to be trained before its use for "*prediction*". This is done using a "*training set*" formed by known *conditions-response* data (e.g. concentrations of the drugs – cytotoxicity). The conditions and the corresponding response are called "*inputs"* and "*outputs"*, respectively. Inputs are iteratively processed by the network in order to estimate the actual outputs in the training set. The root mean square error (RMSE) is calculated according to Eq. (1).

$$RMSE = \sqrt{\frac{\sum_{p=1}^{N}\sum_{k=1}^{M}\left(o_{pk} - o_{pk}^{*}\right)}{N * M}}$$

where N, M, o_{pk}, o_{pk}^{*} are the number of *input-output* data used for training, the number of response variables, the estimated output value and the actual one, respectively. The "*learning*" is improved by using the actual value of the *RMSE* to alter the values of the weights after each iteration. This is done according to a suitable mathematical rule called "*training algorithm*". Several training algorithms are available [6] as for example, standard back-propagation [7], R-propagation [8] and quick-propagation [9]. During the training, the *RMSE* value decreases after each iteration and when it is acceptably low, the learning is stopped. The value of *RMSE* depends strongly upon the architecture of the network used and then, the optimal number of hidden layers and that of neurons therein is searched for using the criteria of the lowest *RMSE* value. In fact, as the number *q* of neurons in a hidden layer increases, the *RMSE* value decreases rapidly at first but, after an optimal value of *q*, the improvement becomes rather poor or the *RMSE* value starts to increase. Once the network is trained, its generalization ability is checked with the "*verification step*" by presenting another series of *input-output* data that were not previously used to train the network. If the estimation of the actual output values for the verification dataset is acceptable, this means that it is possible to use the network for the prediction of the system response for new conditions (e.g. new combinations of drugs) otherwise the network must be trained again. Once the network is trained and verified, it should be tested. This is done in the so called "*test step*". The network is tested by comparing the estimated and experimental response for selected combinations of the drugs.

2.2Experimental Design. Modeling techniques deal with the approximation of the response surface corresponding to a *"working space"* defined by the values of the input variables (*conditions*). The distribution of the experiments on the working space influences the quality of the model. The experiments are represented by points on the working space. A set of *n* experiments can be distributed in various ways on the working space. However, the distribution of the experiments, as well as their number, affect the quality of the approximation of the response surface. Experimental Design (ED) allows to distribute *n* experiments on the working space in a way suitable to get the highest content of information to build the model.

2.3 Considerations on the isobologram and combination index methods. The isobologram method (I.B.), introduced by Loewe [11], consists in the construction of a graph in which equally effective doses of two drugs (isoboles) are reported for a single effect level. Once a specific level is chosen, such as 50% of the maximum, the doses of two drugs A and B that give the same % of effect, are plotted as axial points in a cartesian plot. The straight line connecting A and B defines the combinations that produce a pure additive effect. The experimental points which fall below or above that line, have synergistic or antagonistic effect respectively. As the I.B. analysis, the combination index method (C.I.) [12] tries to provide a qualitative and quantitative measure of the extent of the drug interactions. It considers the existence of a relationship between the fraction affected and unaffected by a drug and the ratio $(D/D_m)^m$, where *D* is the dose of the drug and D_m is the dose that kills a defined number of cells. Once defined m and Dm a C.I. have to be calculated, in fact a C.I. lower than, equal to, and higher than 1 indicates synergism, additivity, and antagonism, respectively.

Following the C.I. and I.B. methods, the concentrations of the drugs alone and the combinations that provide the same cytotoxic effect have to be compared. For example, let consider the drugs **1** and CDDP with a concentration of 3.0 μM and 0.9 μM respectively; at these concentrations they both show a cytotoxicity of 50% while their combination presents a cytotoxic activity of 94.3 %; these two solutions should be compared with all the drugs combinations which show the same cytotoxic activity, for example the combination **1**-cddp with concentration of 1.88 and 0.6 μM, respectively. Applying the C.I. or B.I. methods this combination shows a strong antagonistic effect.

In our view, instead, the effects that the drugs alone provide for a given combination at the same concentration, should be compared with the final effect of the combination. In fact, if we compare the cytotoxic activity of **1** at the concentration of 1.88 μM, which is equal to 8.5%, and that of the CDDP at the concentration of 0.6 μM, which is equal to 17.7%, it appears evident that the cytotoxic activity of the combination (94.2%) is really higher than even a simple algebraic sum of the effects, then a strong synergistic effect is present.

Let now analyze some other results reported in the literature by T.C. Chou for the system CDDP-paclitaxel [13], the following data are shown: the cytotoxic activity of paclitaxel (pac) at 0.01 μM is 88.2% and that of CDDP at 1.0 μM is 82.1%, their combination has a cytotoxic activity of 96.8%. According to the method of C.I. this combination has a strong synergistic effect (C.I. = 0,602 << 1), but if we apply our method, we find that the purely additive effect of two drugs is equal to 97.9%. Comparing this value with the effect of the combination, which is 96.8 (difference is -1.1) it appear impossible to talk about synergy, but at most about additivity. Let compare another combination with pac at 0,002 μM and CDDP at 0.2 μM, with cytotoxic activity of the drugs alone of 42.9% and 30.1% respectively, this combination has cytotoxic activity equal to 70.1. %. According to Chou [13], this combination has a synergistic effect, but lower than the previous combination because C.I. (0.815) is closer to 1 than the other value (0.602). According to our calculation the purely additive effect of the drugs alone is 60.1% which is lower than the experimental value of 70.1 % (difference is 10), then there is a clear synergistic effect, unlike the previous case.

In our opinion the C.I. and I.B. methods fail because they try to explain the cytotoxic effect considering only the inhibition of enzymatic activity.

The first assumption of the C.I. method is that the relationship between the fraction affected (*fa*) and unaffected (*fu* = 1 - *fa*) depends on the ratio $(D/Dm)^m$, where *D* is the dose of the drug and *Dm* is the dose that kills a defined number of cells, for example 50%, according to Eq. 2.

$\frac{f_a}{(1-f_a)} = \left(\frac{D}{D_m}\right)^m$ (2)

The determination of the values *m* and *Dm*, is done by applying the logarithm to eq. 2, which gives *log (fa / fu) = m log (D) - m log (Dm)*. By plotting the function *y = log (fa / fu)* vs. *x = log (D)*, a straight line is obtained, whose slope is the variable *m* and whose intercept allows the calculation of *Dm* (10^(-intercept/slope)).

If a system does not respond according to the enzyme kinetics, then the application of the method C.I. is a force when it tries to linearize a pattern which is not *a priori* exponential. In fact the application of the mathematical operator logarithm to linearize a function is justified only when the trend of the function is exponential on its whole existence interval, the choice to consider only the points that lie on a portion of a straight line, i.e. those which lie around the inflection point on the original curve, is not mathematically rigorous and shows even more the inability of the method to generalize, leading only to the estimation of the *Dm* value.

As a second step of the method, according to the logic of the enzymatic kinetics, the value of *Dx* for each drugs, according to Eq. 3, and finally the Combination Index (Eq. 4), have to be calculated (the numbers 1 and 2 are the indices of the two drugs).

$D_x = D_m \left(\frac{f_a}{1-f_a}\right)^{\frac{1}{m}}$ (3)

$C.I. = \frac{D^1}{D_x^1} + \frac{D^2}{D_x^2}$ (4)

Then, the experimental values of the toxicity of the mixtures are interpreted with the same key previously applied, that was not able to accurately describe the behavior of the drugs alone.

The method introduced by Webb [14] and later reviewed by Bliss [15] has been widely criticized by Greek, Bravo, and J.C. Parsons [16] with extremely fragile points. In fact, let us consider two drugs A and B with equal cytotoxicity values, 5% at a concentration of 0.5 μM and 70 % at a concentration of 1 μM, and suppose also that a their combination (0.5 μM A and 0.5 μM B) presents a toxicity value equal to 60%. According to the method proposed by Bliss, the reference toxicity value, i.e. the pure additive effect, is equal to (5 + 5 - 5 * 5/100) or 9.75%, and since the measured activity, 60%, is greater than 9.75% then the combination has a synergistic effect.

In their review, Greek, Bravo, and J.C. Parsons [16] state that this method of calculation is surely wrong, for two reasons:

1) if we consider a drug alone, A or B, at the concentration of 1 μM, its toxicity value of 70% is already greater than the value of 60%.

2) If we imagine mixing two solutions which contains the same drug, without our knowledge, we would conclude absurdly that the drugs shows a synergistic effect, for the same reasons set out in the point 1.

These two assertions are not correct: the authors compare the cytotoxic activity of the mixture of A and B (both at 0.5 μM) with that of the two drugs alone at concentration of 1μM, as if the concentration of the mixture would be 1μM and this is chemically incorrect. Moreover, they suggest (see point 2), that mixing 0.5 μM of A with 0.5 μM of A, it leads to a new solution in which A is present at 1 μM of concentration. Of course, this conclusion is not real at all. In fact, in the final solution, A still has a concentration of 0.5 μM; as a consequence, no Bliss synergism could be observed, being the cytotoxic activity equal to 5%.

Table S1: Concentrations, experimental and calculated mortality values for the **1**-CDDP system

Sol. n°	[1] µM	[CDDP] µM	Experimental mortality %	Calculated mortality %	Sol. n°	[1] µM	[CDDP] µM	Experimental mortality %	Calculated mortality %
Training set					**31**	0.50	0.13	0	0.3
1	0.00	0.06	0.0	0.0	**32**	0.50	0.25	5.8	2.5
2	0.00	0.13	0.0	0.0	**33**	0.50	0.50	18.2	22.9
3	0.00	0.25	0.0	0.1	**34**	0.50	1.00	66.5	69.0
4	0.00	0.50	5.7	6.9	**35**	0.50	1.50	92.1	92.4
5	0.00	0.75	37.0	35.8	**36**	0.50	2.00	97.3	98.5
6	0.00	1.00	55.9	57.3	**37**	1.00	0.06	8.0	1.6
7	0.00	1.50	85.7	84.0	**38**	1.00	0.13	4.0	3.4
8	0.00	2.00	94.0	95.9	**39**	1.00	0.25	10.3	9.2
9	0.00	0.60	18.0	17.7	**40**	1.50	0.50	35.7	31.5
10	0.25	0.00	0.0	0.0	**41**	2.00	0.06	22.4	12.9
11	0.50	0.00	0.0	0.0	**42**	2.00	0.13	17.9	15.9
12	1.00	0.00	0.1	0.7	**43**	2.00	1.00	88.3	86.5
13	1.00	1.00	76.7	76.6	**44**	2.00	2.00	99.7	99.8
14	1.00	2.00	99.9	99.4	**45**	3.00	0.50	81.3	83.2
15	1.50	0.00	5.45	4.2	**46**	3.00	1.00	96.7	95.6
16	2.00	0.00	11.0	10.5	**47**	3.00	1.50	99.5	98.8
17	2.50	0.00	21.9	24.0	**48**	3.00	2.00	100.0	99.6
18	2.50	1.00	91.5	91.8	**49**	3.50	0.50	91.0	92.7
19	2.50	1.50	99.2	98.5	**Test set**				
20	3.00	0.00	50.6	49.1	**50**	0.25	0.25	1.6	0.5
21	3.50	0.00	73.0	75.0	**51**	0.50	0.06	0.0	0.0
22	3.50	1.00	98.2	97.6	**52**	1.00	0.50	29.5	27.7
23	5.00	0.00	98.0	97.5	**53**	1.50	1.00	80.0	81.5
24	5.00	2.00	100.0	99.6	**54**	2.00	0.25	25.9	23.0
25	5.00	1.00	100.0	99.3	**55**	2.00	0.50	46.8	43.8
Validating set					**56**	2.50	0.50	63.7	64.8
26	0.25	0.06	0.0	0.0	**57**	3.00	0.75	92.0	91.4
27	0.25	0.13	0.0	0.0	**58**	3.50	1.50	100.0	99.1
28	0.25	0.50	11.3	15.9	**59**	1.50	0.75	61.2	58.0
29	0.25	1.00	57.7	63.7	**60**	2.50	0.60	72.0	72.5
30	0.25	2.00	95.4	97.5					

Table S2: Concentrations, experimental and calculated mortality values for the **2**-CDDP system

Sol. n°	[2] µM	[CDDP] µM	Experimental mortality %	Calculated mortality %
Training set				
1	2.00	2.00	99.7	99.9
2	2.00	1.00	100.0	99.8
3	1.00	1.00	82.4	84.8
4	2.00	0.50	99.3	99.2
5	2.00	0.25	97.1	97.9
6	0.25	0.25	0.4	4.2
7	2.00	0.13	97.6	96.4
8	2.00	0.06	95.3	95.3
9	0.00	2.00	93.4	94.7
10	0.00	1.00	37.4	37.4
11	0.00	0.50	12.3	5.9
12	0.00	0.25	2.1	3.6
13	0.00	0.13	2.5	3.1
14	0.00	0.06	0.7	2.9
15	2.00	0.00	92.9	94.2
16	1.00	0.00	16.8	18.1
17	0.50	0.00	9.1	4.0
18	0.25	0.00	10.0	3.1
Validation set				
19	1.00	2.00	99.2	97.2
20	0.50	2.00	97.1	95.1
21	0.25	2.00	93.5	94.8
22	0.50	1.00	60.3	56.4
23	0.25	1.00	41.7	46.1
24	1.00	0.50	48.2	45.1
25	0.50	0.50	6.9	**7**.0
26	0.25	0.50	5.4	7.6
27	1.00	0.25	21.0	25.8
28	0.50	0.25	0.9	5.7
29	1.00	0.13	23.9	20.9
30	0.50	0.13	8.1	4.6
31	0.25	0.13	1.6	3.5
32	1.00	0.06	17.6	19.2
33	0.50	0.06	5.9	4.28
34	0.25	0.06	2.3	3.29
Test set				
35	1.50	1.50	99.2	99.9
36	1.00	1.50	96.2	94.3
37	0.50	1.50	90.2	87.4
38	1.50	1.00	96.9	98.9
39	1.25	0.75	87.1	91.4
40	1.00	0.75	70.2	70.0
41	1.50	0.50	89.9	95.4
42	0.50	0.50	13.6	11.2
43	0.75	0.75	51.5	43.9
44	0.25	0.25	3.6	4.2

Table S3: Concentrations, experimental and calculated mortality values for the **C1**-CDDP system

Progr. n°	[C1] µM	[CDDP] µM	Experimental mortality %	Calculated mortality %
Training set				
1	2.00	0.00	100.0	99.2
2	1.50	0.00	96.6	96.8
3	1.00	0.00	53.0	53.1
4	0.50	0.00	9.0	7.7
5	0.25	0.00	6.0	4.2
6	0.00	2.00	98.5	97.6
7	0.00	1.50	93.6	93.5
8	0.00	1.00	75.7	77.5
9	0.00	0.50	35.6	32.6
10	0.00	0.25	9.5	11.6
11	0.00	0.13	5.5	5.9
12	0.00	0.06	2.0	3.9
13	2.00	2.00	100.0	100.0
14	1.00	2.00	100.0	99.9
15	1.00	1.00	100.0	99.2
16	1.00	0.50	87.0	94.1
17	0.50	1.50	99.2	97.4
18	0.50	0.50	54.5	55.1
19	0.25	2.00	100.0	98.3
20	0.25	0.06	5.3	6.0
Validation set				
21	2.00	1.00	100.0	100.0
22	2.00	0.50	100.0	99.9
23	2.00	0.25	100.0	99.7
24	2.00	0.13	100.0	99.5
25	2.00	0.06	100.0	99.4
26	1.50	1.50	100.0	99.9
27	1.50	1.00	100.0	99.9
28	1.50	0.50	100.0	99.7
29	1.00	0.25	77.4	82.6
30	1.00	0.13	65.0	70.5
31	1.00	0.06	63.0	62.0
32	0.50	2.00	100.0	99.2
33	0.50	1.00	89.0	89.4
34	0.50	0.25	27.3	26.5
35	0.50	0.13	13.2	15.1
36	0.50	0.06	16.0	10.8
37	0.25	1.00	82.0	82.3
39	0.25	0.50	36.4	40.6
39	0.25	0.25	19.0	16.3
Test set				
40	0.75	1.25	94.5	100.0
41	1.25	0.75	94.3	100.0
42	0.75	0.75	86.6	89.9
43	0.75	0.5	56.2	67.8
44	1.25	0.25	84.6	90.0
45	0.75	0.25	31.3	37.8

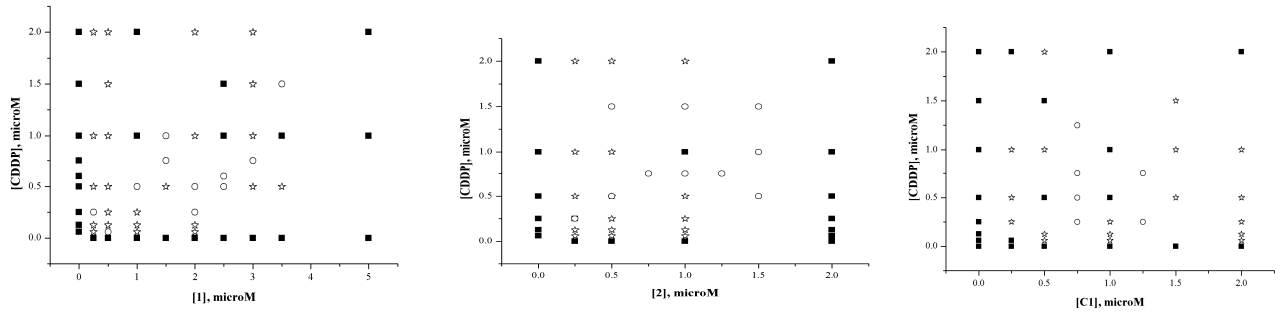

a **B** **c**

Figure S2: Experimental Design (■ training, ☆ validating,○ test set) for the systems a) **1**-CDDP, b) **2**-CDDP and c) **C1**-CDDP.

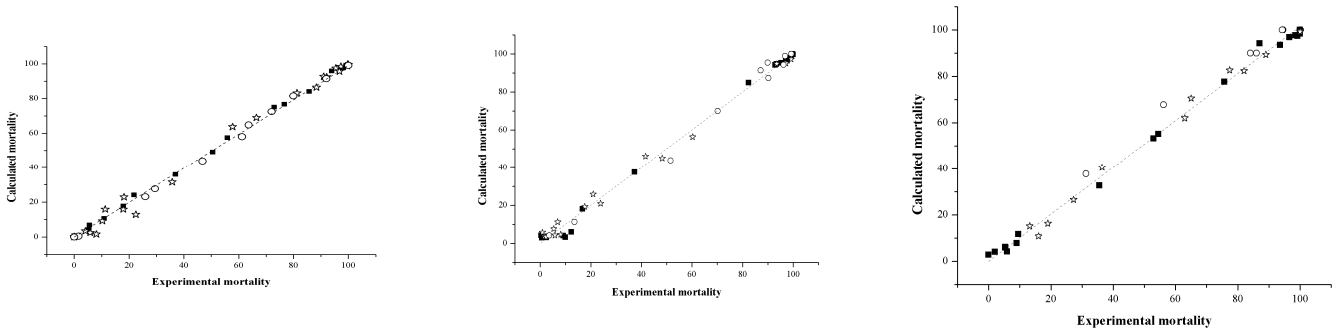

a **B** **c**

Figure S3: Comparison between experimental and calculated mortality values (■ training, ☆ validating,○ test set) for the systems a) **1**- CDDP, b) **2**-CDDP and c) **C1**–CDDP (linear fitting parameters for the equation y = mX are m = 0.999(3) with r = 0.9999 for training set, m = 1.00 (1) and r = 0.9986 for validation set, m = 0.990(1) and r = 0.9995 for test set, m = 1.00(1) and r = 0.9993 for all the data values for **1**-CDDP; m = 1.00(1) with r = 0.9991 for training set, m = 0.99(1) and r = 0.9978 for validation set, m = 1.00(1) and r = 0.9988 for test set, m = 1.00(1) and r = 0.9988 for all the data values for **2**-CDDP; m = 1.00(1) with r = 0.9991 for training set, m = 1.00(1) and r = 0.9995 for validation set, m = 1.08(2) and r = 0.9977 for test set, m = 1.02(1) and r = 0.9988 for all the data values for **C1**-CDDP).

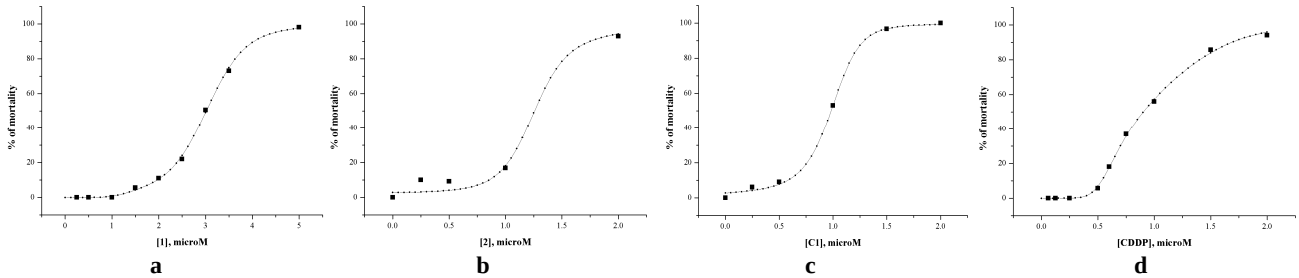

a **b** **c** **d**

Figure S4. Calculated (-•-) and experimental (■) dose-response data for a) **1**, b) **2**, c) **C1** and d) CDDP against CCRF-CEM cell line.

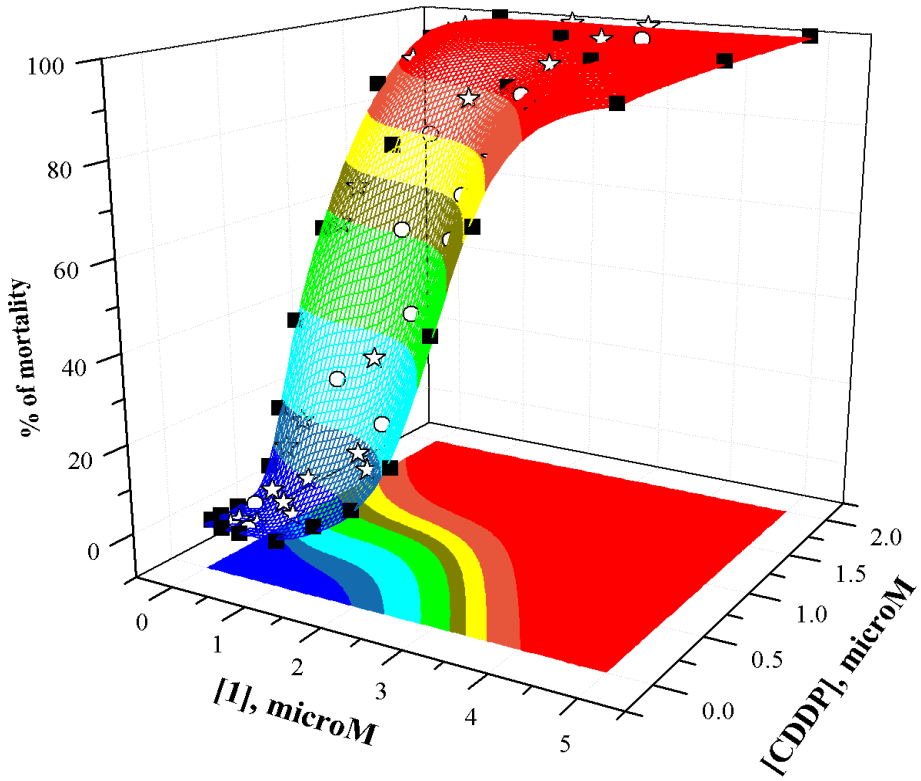

a

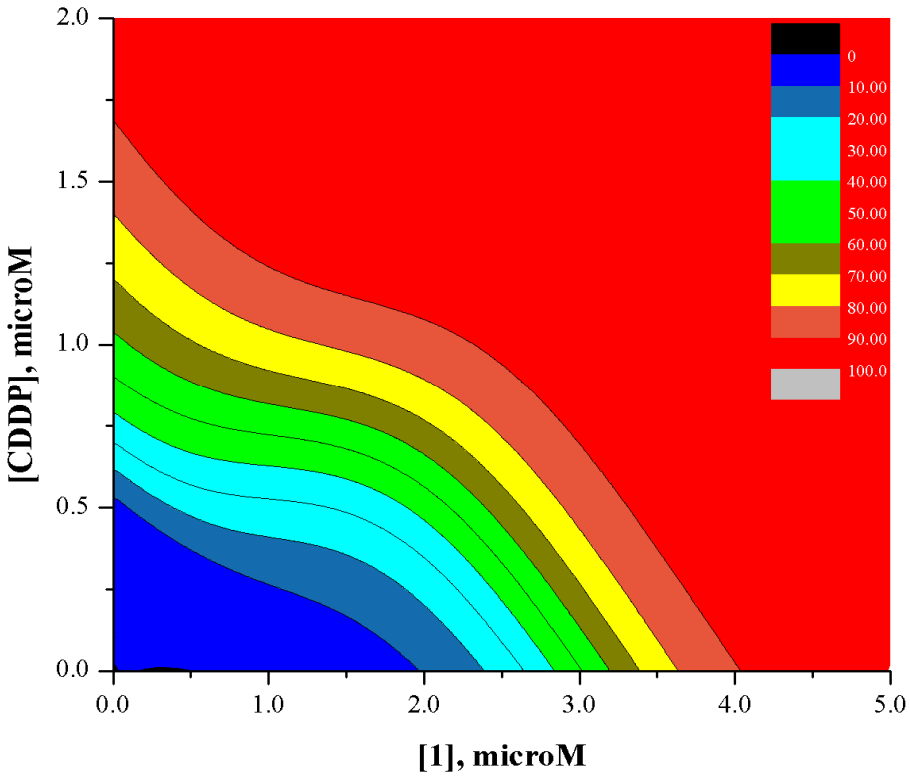

b

Figure S5. Response surface with experimental data (■ training set, ☆ validation set and ○ test set) (a) and contour plot of cytotoxicity isovalues (b) for the system **1**-CDDP.

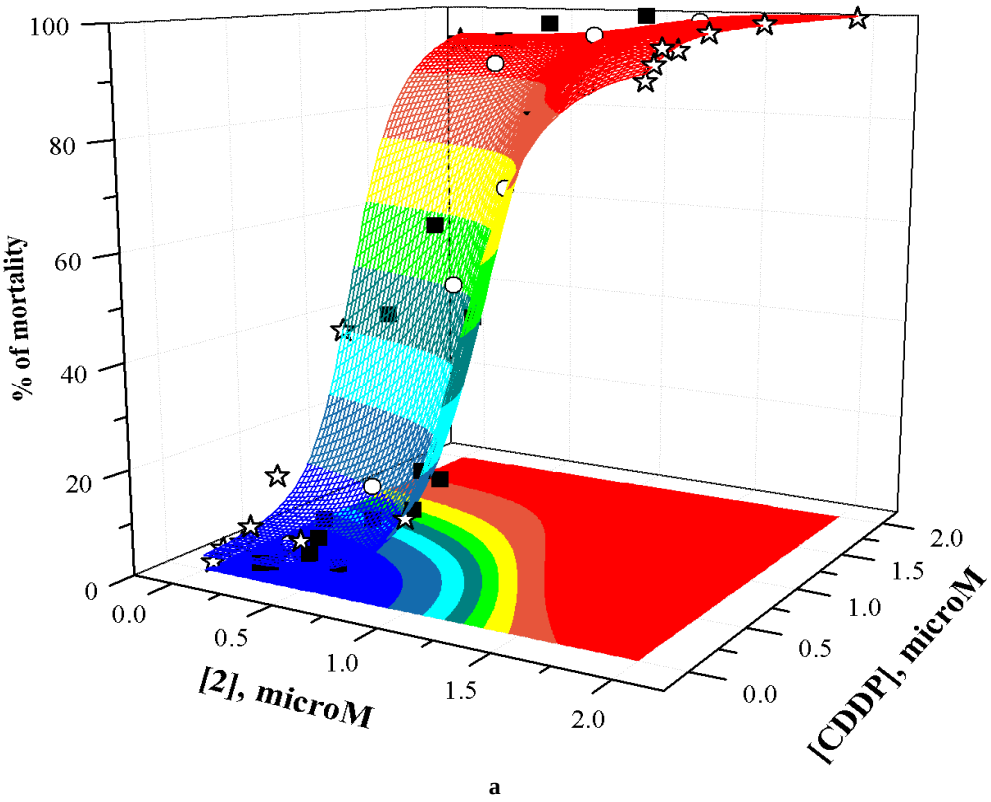

a

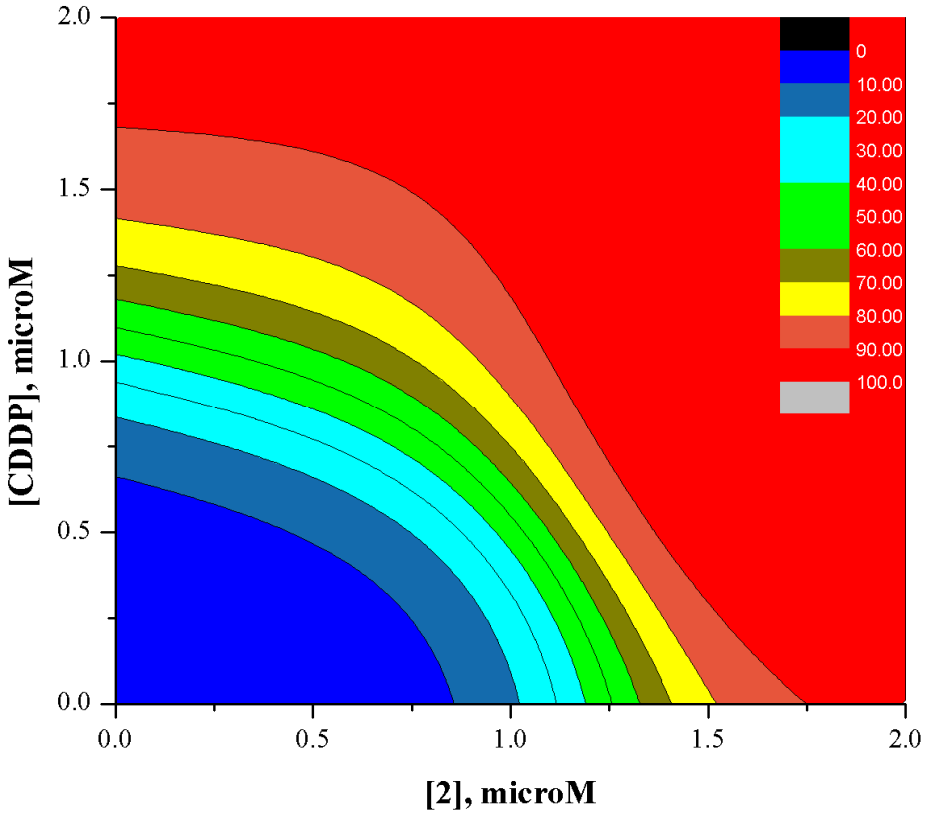

b

Figure S6. Response surface with experimental data (■ training set, ☆ validation set and ○ test set) (a) and contour plot of cytotoxicity isovalues (b) for the system **2**-CDDP.

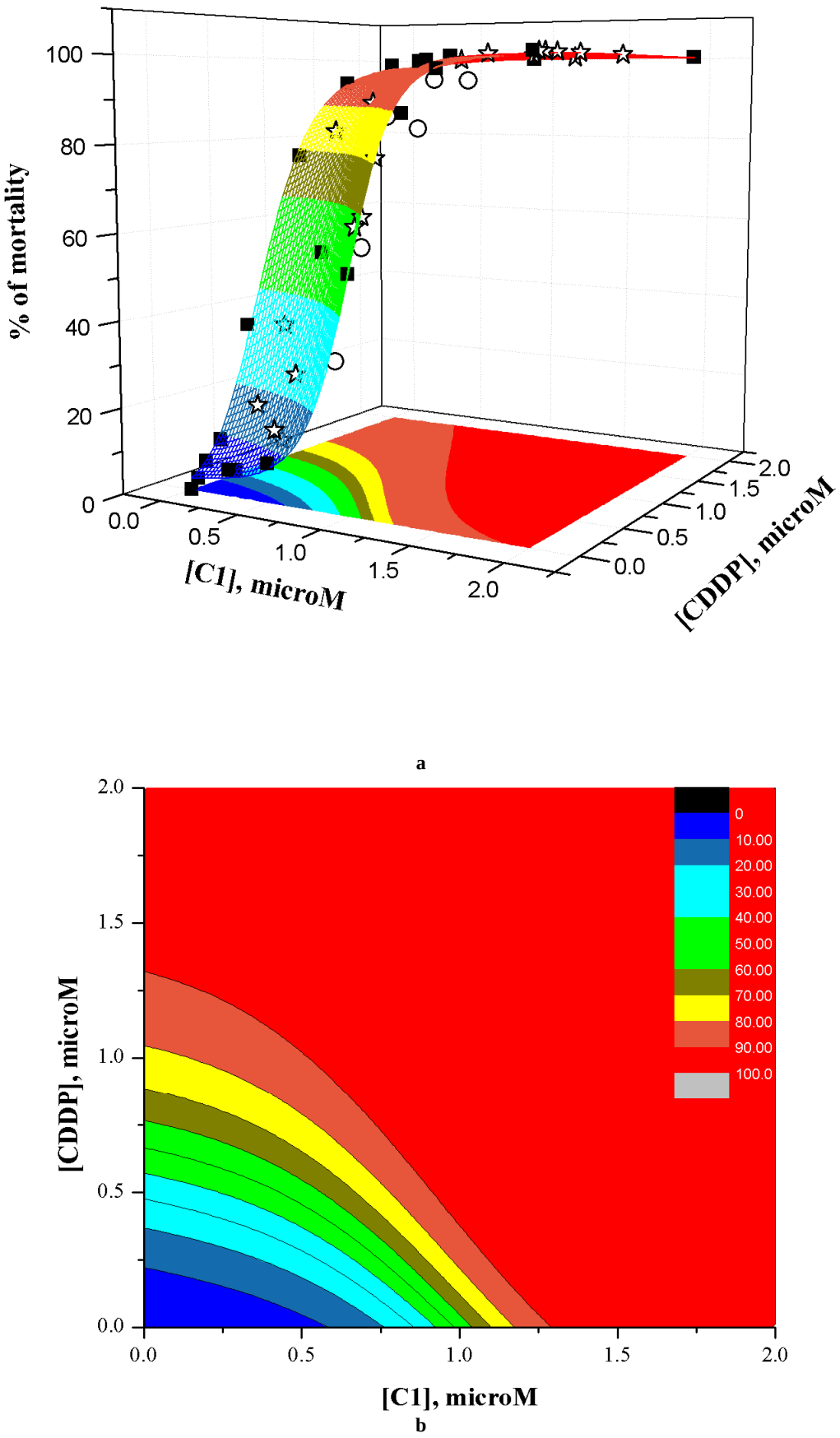

Figure S7. Response surface with experimental data (■ training set, ☆ validation set and ○ test set) (a) and contour plot of cytotoxicity isovalues (b) for the system **C1**-CDDP.

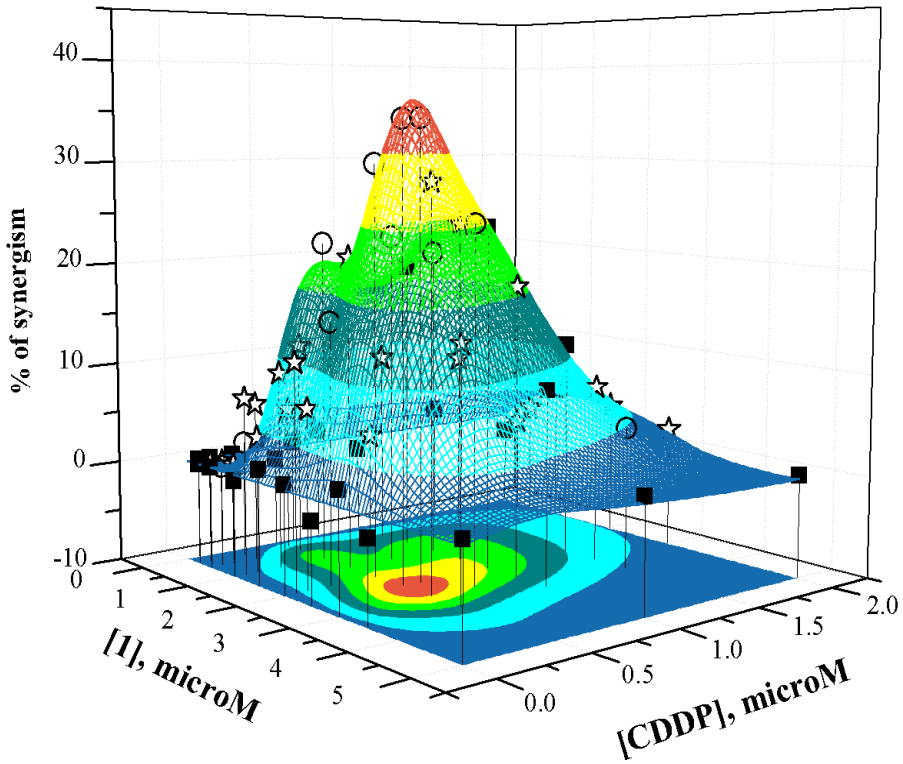

a

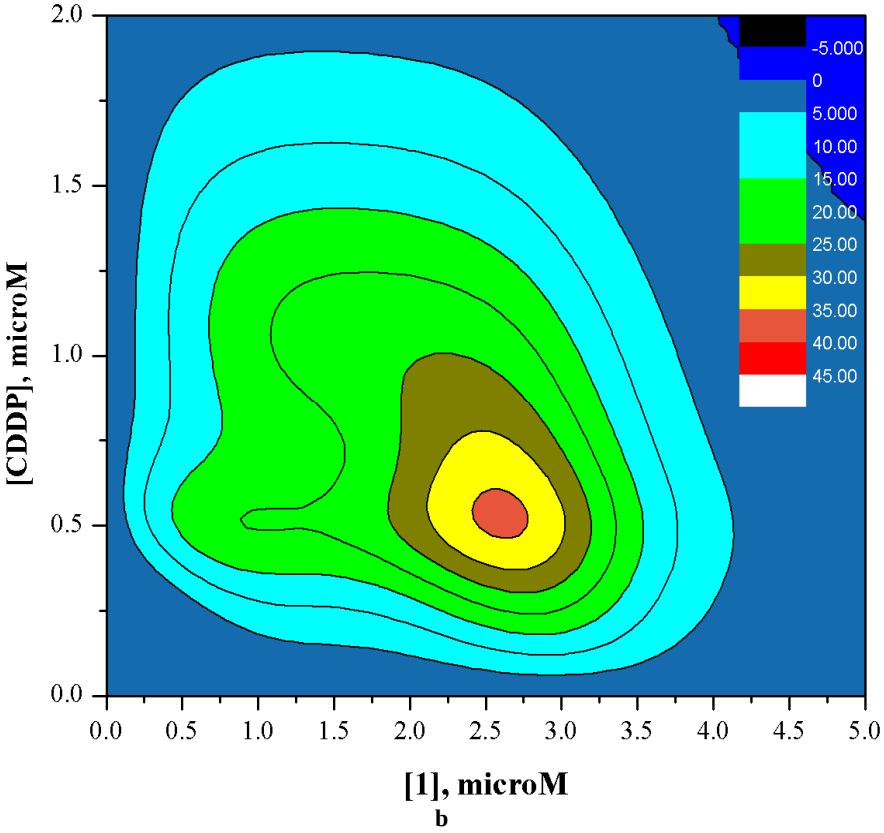

b

Figure S8. Synergism surface with the experimental data (■ training set, ☆ validation set and ○ test set) (a) and contour plot of synergism isovalues (b) for the systems 1-CDDP. As "% of synergism" is intended the difference between the experimental mortality and the additive effect, both expressed as %.

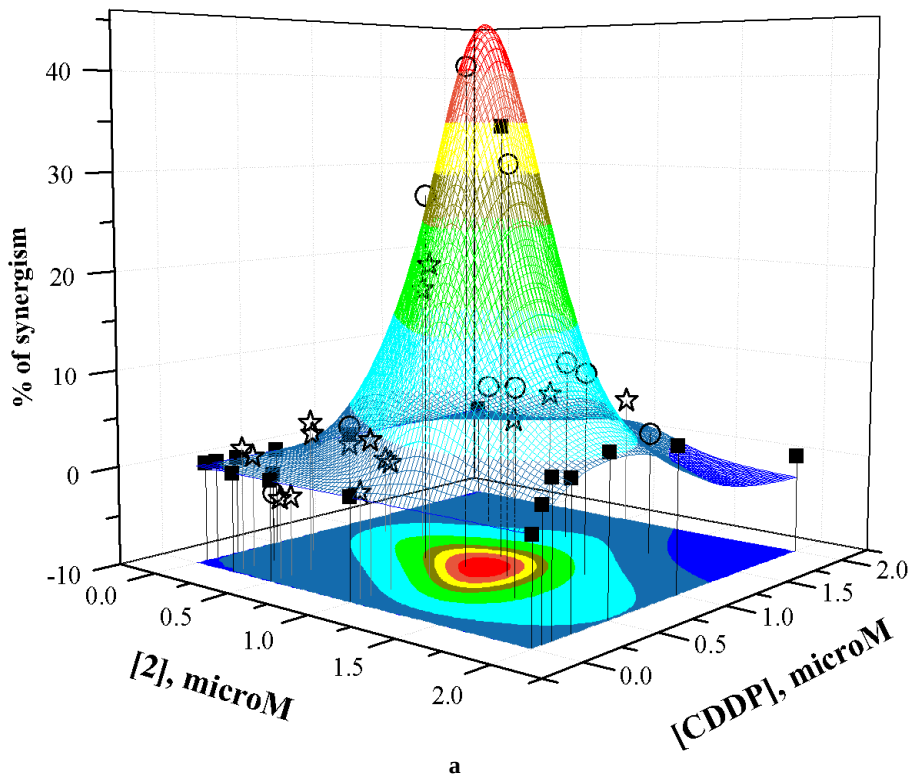

a

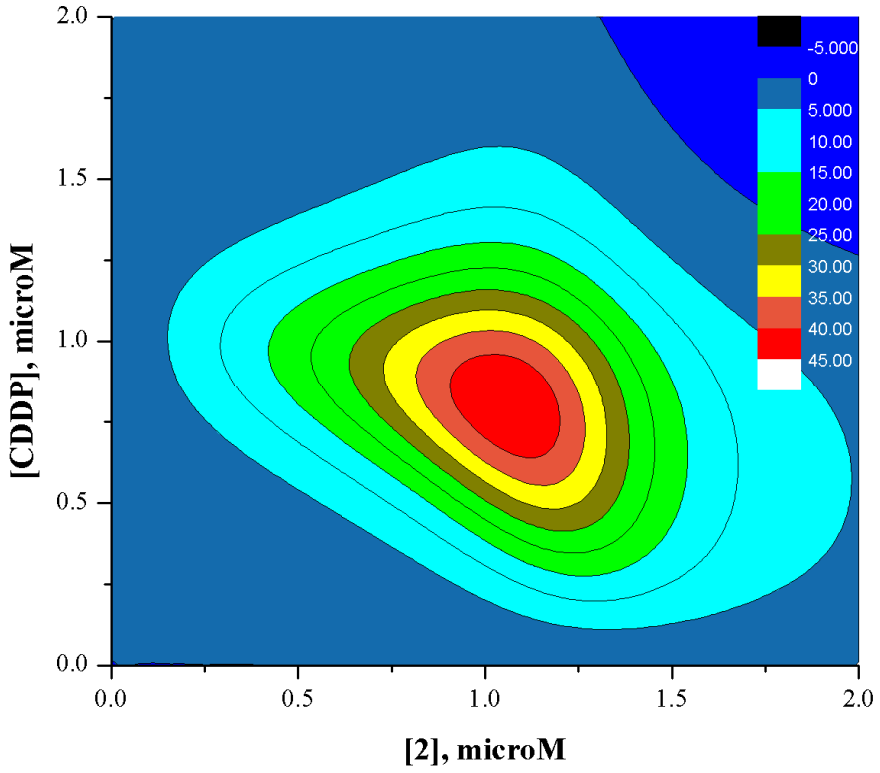

b

Figure S9. Synergism surface with the experimental data (■ training set, ☆ validation set and ○ test set) (a) and contour plot of synergism isovalues (b) for the systems **2**-CDDP. As "% of synergism" is intended the difference between the experimental mortality and the additive effect, both expressed as %.

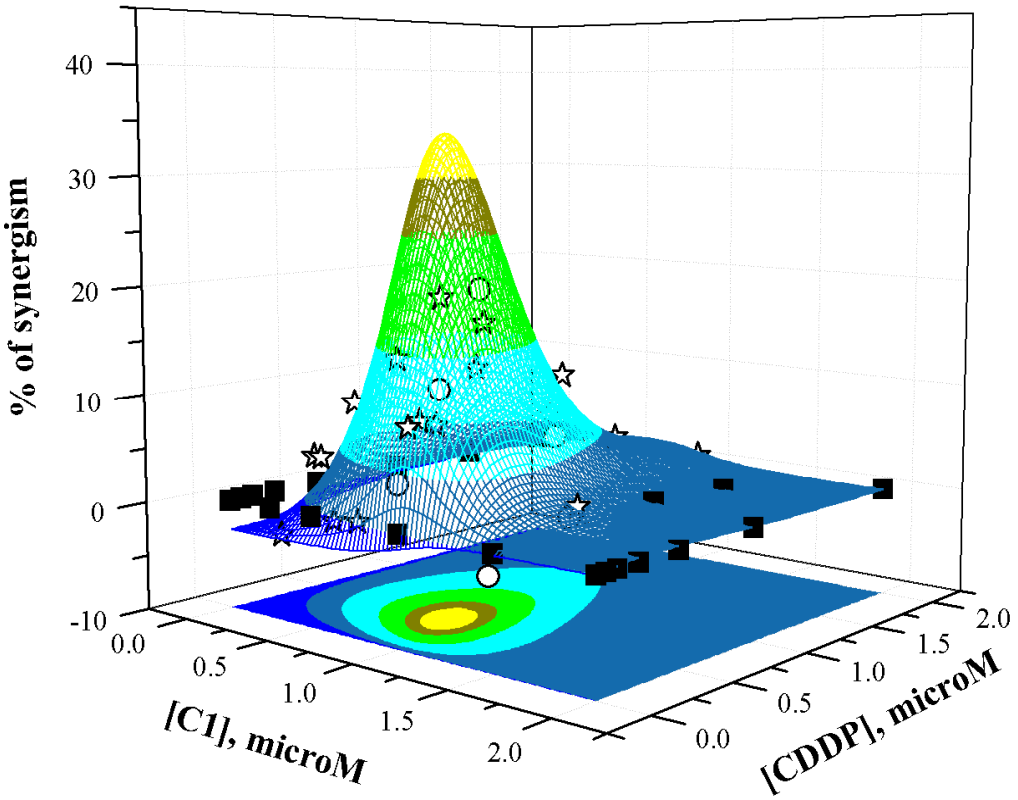

a

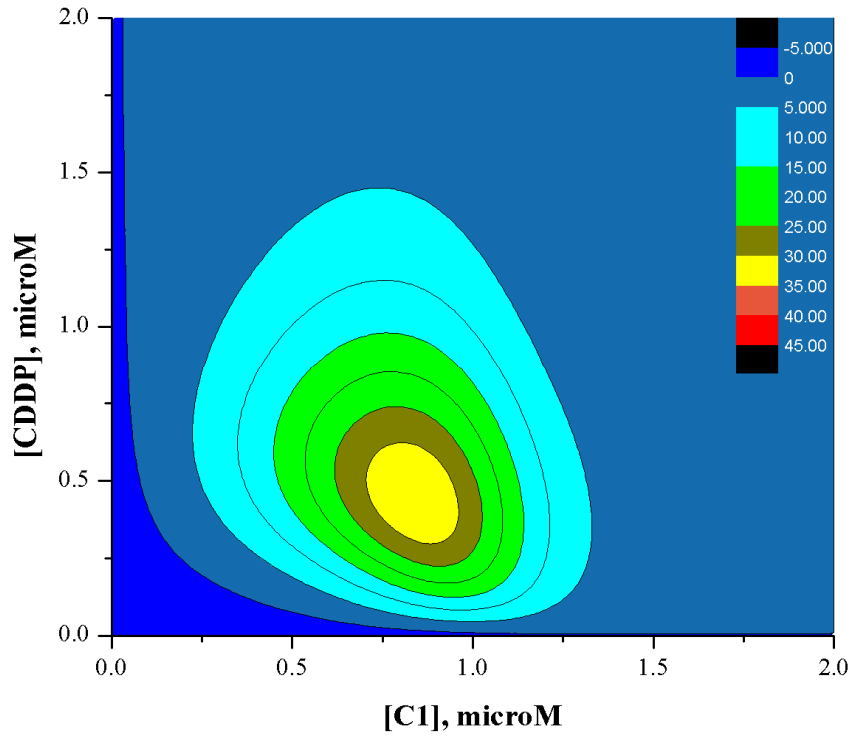

b

Figure S10. Synergism surface with the experimental data (■ training set, ☆ validation set and ○ test set) (a) and contour plot of synergism isovalues (b) for the systems **C1**-CDDP. As "% of synergism" is intended the difference between the experimental mortality and the additive effect, both expressed as %.

[1] Kateřina Sladkova, Jan Houška and Josef Havel, Laser desorption ionisation of red phosphorus clusters and their use for mass calibration in time-of -flight mass spectrometry, *Rapid Commun. Mass Spectrom.* **2009**, *23*, 3114-3118.
[2] T. Pivetta, M.D. Cannas, F. Demartin, C.Castellano, S. Vascellari, G. Verani, F. Isaia, *J. Inorg. Biochem*. **2011**, *105*, 329-338.
[3] T. Pivetta, F. Isaia, G. Verani, C. Cannas, L. Serra, C. Castellano, F. Demartin, F. Pilla, M. Manca, A. Pani, *J. Inorg. Biochem*. **2012**, *114*, 28-37.
[4] R. Pauwels, J. Balzarini, M. Baba, R. Snoeck, D. Schols, P. Herdewijn, J. Desmyster, E. De Clercq, *J. Virol. Methods* **1988**, *20*, 309-321.
[5] D. Bas, İ.H. BoyacI, *Journal of Food Engineering* **2007**, *78*, 836-845.
[6] I.A. Basheer, M. Hajmeer, *Journal of Microbiological Methods* **2000**, *43*, 3-31.
[7] Svozil, V. Kvasnička, J. Pospíchal, *Chemometrics and Intelligent Laboratory Systems* **1997**, *39*, 43-62.
[8] M. Riedmiller, H. Braun, in: IEEE *International Conference on Neural Networks Volume* 1, **1993**, pp. 586-591.
[9] S.S. Rao, *Optimisation: Theory and Applications* Ravi. Acharya for Wiley Eastern, New Delhi, 1978.
[10] D.L. Massart, B.G.M. Vandeginste, L.M.C. Buydens, S.D. Jong, P.J. Lewi, J. Smeyers-Verbeke, Handbook of Chemometrics and Qualimetrics, Elsevier Science, 1997.
[11] S. Loewe, *Arzneim. Forsch*. **1953**, *3*, 285-290.
[12] T.C. Chou, *Mol. Pharmacol*. **1974**, *10*, 235-247; T.C. Chou, P. Talalay, *Eur. J. Biochem*. **1981**, *115*, 207-216.
[13] T.C. Chou, *Pharmacol. Rev*. **2006**, *58*, 621-681.
[14] Webb, J. L. 1961. Effect of more than one inhibitor, p. 66 and 488. In Enzymes and metabolic inhibitors, vol. 1. Academic Press, New York, N.Y.
[15] C.I. Bliss, *Ann. Appl. Biol*. **1939**, *26*, 585-615.
[16] W. Greco, G. Bravo, J.C. Parsons, *Pharmacol. Rev*. **1995**, *47*, 331-385.

Chapter II - Copper-Platinum complexes as a mechanism to explain the synergism of combinations of CDDP with Cu(II)complexes

The ANN method was also used to assess if the CDDP-Cu(II)complexes associations proved to be synergic also in CDDP-resistant cells.

Human acute T-lymphoblastic leukemia (CCRF-CEM) and human ovarian carcinoma (A2780) cell lines, as well as their respective cisplatin-resistant sublines (CCRF-CEM-res; A2780-res) were used in the study. The CCRF-CEM-res subline was obtained by us, by serial passages of the wild type cells in the presence of increasing cisplatin concentrations, starting from a sub-inhibitory concentration (0.5 μM); A2780 and A2780-res cells were a generous gift from Dr. Fischer Eva (Tumor Biology Laboratory, The Ion Chiricuta Oncology Institute, Cluj-Napoca, Romania). The choice of A2780 cell lines in this study, lies in the fact that the CDDP represents in clinical therapy the drug of choice in the treatment of this type of neoplasm.

The combinations of drugs used have proved able to suppress the CDDP resistance in both cell lines. The synergistic effect shown by cisplatin in combination with complexes of copper could be due to the simultaneous involvement of the same or different targets (DNA, proteins, enzymes, biomolecules), or by the formation of adducts, containing copper and platinum. To verify the presence of these adducts, have been measured mass spectra of solutions containing CDDP and, one at a time, the complexes of Cu (II), using the atmospheric pressure Electrospray Ionisation at atmospheric pressure Mass Spectroscopy (ESI-MS). This method was more useful than others, because the processes of fragmentation are greatly reduced, allowing the detection of even weak complexes, which can not be put in evidence with the other systems of ionization stronger which detected only the signals of the individual complexes. The stoichiometry of the complex observed with this method was then evaluated based on the models and the results of isotopic fragmentation spectroscopy tandem MS-MS. In all cases, regardless of the copper complex used, it was detected the formation of a mixed complex in which the ions of copper and platinum are connected by a bridge of two chlorine atoms, with stoichiometry $[CuPt(1,10\text{-phenathroline})(NH_3)(H_2O)Cl]^+$. In reactions of Cu(II)-phen 2 or Cu(II)-phen C1 with CDDP it is also released a phenanthroline, that being itself cytotoxic, could explain the higher antiproliferative activity shown by the mixtures containing these two complexes, rather than the one containing the Cu(II)-phen 1.

In conclusion, our combinations showed a synergistic cytotoxic effect in both CDDP-resistant cell lines, CCRF-CEM-res and A2780-res, and have proved able to suppress the drug-resistance. The ED-ANN approach used to assess the interaction of the drugs has produced valid and reliable results since, in all cases, the data expected from the network have been confirmed experimentally. The spectrometry ESI-MS and tandem MS-MS results are instruments suitable to verify adduct formation in solution from the combinations which we used. Despite the process of transition from solution to the gas phase can influence the structure of the complexes (especially of large molecules), they may be obtained relevant information on the stability of the solution and the reactivity of complexes that are not easily isolable in the solid state. The formation of the mixed compound detected with this method, could be a possible mechanism at the basis of the synergistic effect observed with our combinations against the cell line tested. Since the synergistic effect was observed also against cisplatin-resistant cell lines, it could also be involved in one or more of the mechanisms that lead to resistance to cisplatin. The results of this study are described in the manuscript below reported, which is presently under review for publication in the Journal of Inorganic Biochemistry.

Formation of mixed copper-platinum complexes as a mechanism to explain the synergistic antiproliferative effect exhibited by binary mixtures of cisplatin and copper-1,10-phenanthroline complexes: an ESI-MS study

Tiziana Pivetta[*1], Viola Lallai[1], Elisa Valletta[1], Federica Trudu[1], Franco Isaia[1], Daniela Perra[2], Elisabetta Pinna[2], Alessandra Pani[2]
[1]Dipartimento di Scienze Chimiche e Geologiche, Dipartimento di Scienze Biomediche[2], University of Cagliari, Cittadella Universitaria, 09042 Monserrato – CA (ITALY).

Abstract

Cisplatin, *cis*-diammineplatinum(II) dichloride, is a metal complex widely used in clinical practice for the treatment of cancer. Despite its great efficacy it causes adverse reactions and the most of the patients develop resistance to cisplatin. To overcome these issues, a multidrug therapy was introduced as a modern approach to exploit the drug synergy. A synergistic effect has been found testing *in vitro* binary combinations of cisplatin and three copper complexes, namely Cu(1,10-phenanthroline)$(OH_2)_2(OClO_3)_2$**,** $[Cu(1,10\text{-phenanthroline})_2(OH_2)](ClO_4)_2$ and [Cu(1,10-phenanthroline)$_2$(imidazolidin-2-thione)]$(ClO_4)_2$, against the human acute T-lymphoblastic leukaemia cell line (CCRF-CEM). Binary combinations of cisplatin and $[Cu(1,10\text{-phenanthroline})_2(OH_2)](ClO_4)_2$ were tested also on the cisplatin-resistant sublines of human acute T-lymphoblastic leukaemia cell line (CCRF-CEM-res) and ovarian (A2780-res) cancer cell line. The tested combination showed on the resistant cells a synergistic effect. The possibility that this effect was due to the formation of new adducts was considered and mass spectra of solutions containing cisplatin and one at a time of the three copper complexes were measured by using the electrospray ionisation at atmospheric pressure mass spectroscopy. A mixed complex was detected and its stoichiometry was assessed on the basis of the isotopic pattern and the results of tandem MS-MS experiments. In the formed complex with stoichiometry $[CuPt(1,10\text{-phenathroline})(NH_3)(H_2O)Cl]^+$ the copper and platinum ions are linked by two bridging chlorines. The coordination spheres of copper is completed by one 1,10-phenathroline unit and by an hydroxide ion, that of platinum by an ammonia and a water molecules.

1. Introduction

Cisplatin, *cis*-diammineplatinum(II) dichloride, is a metal complex widely used in clinical practice for the treatment of cancer. Cisplatin is able to enter the cells *via* passive diffusion and with protein-mediated transport systems as human organic cation transporter hOCT2 and copper transporter Ctr1 [1–3]. Cisplatin exerts its biological activity by interaction with DNA. In fact, once inside the cell, the chloride ligands of the complex are displaced by water molecules in a two-steps mechanism to form with DNA a bi-functional adduct $[Pt(DNA)(NH_3)_2]^{2+}$[4–7]. Despite its great efficacy against very deadly kinds of tumour, such as breast, ovarian, prostate, testes, and non-small cell lung cancers[8–11], it causes adverse reactions with dose-dependent side effects. Furthermore, after the first treatments, the most of the patients develop resistance to cisplatin[12], and to reach the same therapeutic efficacy higher doses of the drug are required, with a higher incidence of the side effects related to the doses. The cisplatin resistance could be due to several mechanisms, such as a decreased influx inside the cell, an increased deactivation by the biomolecules present in the cytosol, an increased capacity of DNA repair and an increased efflux outside the cell [13,14]. To defeat the drug resistance and reduce the side effects, a multidrug therapy (MD) was introduced as a modern approach. Under MD regimen, two or more drugs are administered simultaneously to exploit their synergism[15] reaching several advantages. Synergism arises when the mixture of drugs shows a cytotoxic activity higher than the pure additive effect of the single drugs. In synergistic drug combinations, lower doses of each drug can be administered achieving equal or higher therapeutic effect while reducing side effects and the development of the resistance. As a matter of fact, cisplatin has often been proposed in combinatorial therapies with other drugs or with natural products [16–22]. In a previous work, we tested *in vitro* several binary combinations of cisplatin with three different copper complexes against the human acute T-lymphoblastic leukaemia cell line (CCRF-CEM) finding a synergistic effect [15]. Copper(II) complexes are supposed to act on cancer cells in different way with respect the cisplatin, but the real mechanisms are not completely clarified up to date [23]. Furthermore, as both copper(I) and copper(II) involved in several biological functions, it is not universally accepted if the cytotoxic properties of the copper complexes are related to a redox reaction of the metal ion. In the most of the studies, cell apoptosis and enzyme inhibitions (proteasome, topoisomerase I and II, tyrosin protein kinase) are involved [24,25] while the DNA appears the target of copper complexes containing nitrogen chelators as 1,10-phenanthroline (phen) [26]. The synergistic effect shown by cisplatin and our copper complexes containing one or two phen molecules, may then arise from several mechanisms, i.e. simultaneous involvement of same or different targets, such as DNA, proteins, enzymes, biomolecules, but also through formation of new adducts. This possibility is due to a some chemical affinity of the ions. In fact, platinum(II) and copper(I) are both of them soft ions, and copper(II) has an hard-soft intermediate character. The affinity of these ions for the same ligands provides the possible formation of polinuclear complexes containing both platinum and copper. Starting from the above considerations, we decided to verify the formation of mixed complexes measuring the mass spectra of solutions containing cisplatin and one at a time of the three copper complexes. Moreover, we extended the study of the cytotoxic activity of the most promising copper complex on cisplatin-resistant leukemic (CCRF-CEM-res) and ovarian (A2780-res) cancer cell lines. We measured the mass spectra of binary combinations of the chosen copper complexes and cisplatin by using the electrospray ionisation at atmospheric pressure mass spectroscopy (ESI-API-MS). This ionisation system limits the fragmentation processes allowing the detection also of weak complexes. Preliminary measurements made by using stronger ionisation systems, such as laser desorption ionisation (LDI) or matrix assisted laser desorption ionisation (MALDI), put in evidence signals of platinum ion and of copper-phen complexes only. By using ESI-API-MS, instead, polynuclear complexes containing copper and platinum were found and their stoichiometry was assessed on the basis of the isotopic patterns and on the fragmentation results of the tandem MS-MS spectroscopy. The copper complexes studied in combination with cisplatin were Cu(1,10-phenanthroline)$(OH_2)_2(OClO_3)_2$ (**1**)**,** $[Cu(1,10\text{-phenanthroline})_2(OH_2)](ClO_4)_2$ (**2**) and [Cu(1,10-phenanthroline)$_2$(imidazolidin-2-thione)]$(ClO_4)_2$ (**C1**). The molecules studied in this work are reported in Fig. 1.

2. Experimental section

2.1 Reagents and apparatus

Methanol (CH_3OH), dimethylsulfoxide (DMSO), imidazolidine-2-thione (H_2dit), 1,10-phenanthroline (phen) and trifluoro acetic acid (HTFA) were purchased from Sigma-Aldrich. *Cis*-diammineplatinum(II) dichloride (cisplatin) was purchased from Alfa-Aesar. The commercial reagents were used without any further purification. ultra-pure water obtained with MilliQ Millipore was used for all the experiments. Mass spectra in positive ion mode were obtained on a triple quadruple QqQ Varian 310-MS mass spectrometer, with atmospheric pressure electron spray ionization (ESI-API) technique. The sample solutions were infused directly into the ESI-API source using a programmable syringe pump, with a flow rate of 1.50 ml/h. A dwell time of 14 sec was used and the spectra were accumulated for at least 10 min in order to increase the signal to noise ratio. Tandem MS-MS was performed with Argon as collision gas (1.8 PSI) using needle voltage at 6000 volts, shield voltage 800 volts, housing temperature 60 °C, drying gas temperature 120 °C, nebuliser gas pressure 40 PSI, drying gas pressure 20 PSI, detector voltage 2000 volts. Collision energy was varied from 2 to 45 V. The isotopic patterns of the signals in the mass spectra were analyzed using mMass 5.5.0 software package[27–29].

2.2 Preparation

Synthesis of **1**, **2** and **C1** were previously reported [30,31]. However, in this work we report new synthesis with less-toxic solvents and/or with higher yield.

Cu(1,10-phenanthroline)$(OH_2)_2(OClO_3)_2$ (1): Basic carbonate of copper(II) $Cu_2(CO_3)(OH)_2$ (1.0 g, 4.54 mmoles) was suspended in isopropanol (50 ml) and the suspension was warmed till boiling point. Concentrated perchloric acid was slowly added to the suspension under stirring, until a clear blue solution is obtained. The solution was boiled for 10 min to remove all the formed carbon dioxide, then it was cooled to room temperature. An isopropanolic solution of phen (0.4 g, 2.22 mmoles) was slowly added drop by drop under stirring. In presence of opalescence, the addition of phen was interrupted and the solution was left under stirring until the precipitate disappeared, then the phen addition was resumed. The entire process required 3 hours. The resulting blue solution was filtered, concentrate under vacuum (10 ml) and let crystallize. Blue crystals were obtained after 12 hours. The percent yield was 95 % (calculated on the basis of the phen amount). Anal. Calcd. for $Cu(phen)(OH_2)_2(ClO_4)_2$: C 30.11, H 2.53, N 5.85, found: C 30.87, H 2.66, N 5.79.

[Cu(1,10-phenanthroline)$_2(OH_2)](ClO_4)_2$ (2): Basic carbonate of copper(II) $Cu_2(CO_3)(OH)_2$ (1.0 g, 2.22 mmoles) was suspended in isopropanol (50 ml) and the suspension was warmed till boiling point. Concentrated perchloric acid was slowly added to the suspension under stirring, until a clear blue solution is obtained. The solution was boiled for 10 min to remove all the formed carbon dioxide, then it was cooled to room temperature and a propanolic solution of phen (1.64 g, 4.44 mmoles) was slowly added. The resulting turquoise precipitate was filtered off under vacuum, washed with isopropanol and dried at room temperature. The percent yield was 88%. Anal. Calcd. for $Cu(phen)_2(OH_2)(ClO_4)_2$: C 44.98, H 2.84, N 8.74, found: C 44.30, H 2.96, N 8.91.

[Cu(1,10-phenanthroline)$_2$(imidazolidin-2-thione)]$(ClO_4)_2$ (C1): 0.30 g of **2** and 0.048 g of H_2dit (clourless) were suspended in 50 ml of distilled water. The suspension was stirred for 12 hours at room temperature, after this time a green powder was recovered by filtration under vacuum. The product was washed with water and dried at room temperature. Yield 80 %. Anal. Calcd. for $Cu(phen)_2(H_2dit)(ClO_4)_2$: C 44.73, H 3.06, N 11.59, found: C 45.01, H 2.98, N 11.30.

2.3 ESI-MS measurements

2.3.1. Copper complexes

Solutions of 1 was prepared dissolving the proper amount of compound in water containing 0.05 % of HTFA (v/v). Solutions of 2 and C1, insoluble in water, were prepared dissolving the proper amount of compound in 100 ul of DMSO and diluting to 50 ml with water containing 0.05 % of HTFA (v/v). All the sample solutions were mixed with methanol in 1:1 H_2O:CH_3OH volume ratio immediately before the mass measurements to improve the quality of the spectra. Mass spectra of **1**, **2** and **C1** were recorded in the 100-1000 m/z range, at a final concentration of 0.5 mM. The same experimental conditions were used for the three compounds (needle voltage 4500 volts, shield voltage 600 volts, housing temperature 60 °C, drying gas temperature 120 °C, nebuliser gas pressure 40 PSI, drying gas pressure 20 PSI, detector voltage 1450 volts).

2.3.2. Cisplatin

Solution of cisplatin was prepared dissolving the proper amount of compound in water containing 0.05 % of HTFA (v/v). The solution was mixed with methanol in 1:1 H_2O:CH_3OH volume ratio immediately before the mass measurements to improve the quality of the spectra. Mass spectrum of cisplatin was recorded in the 100-1000 m/z range, at a final concentration of 0.5 mM. The experimental conditions were: needle voltage 6000 volts, shield voltage 600 volts, housing temperature 60 °C, drying gas temperature 120 °C, nebuliser gas pressure 40 PSI, drying gas pressure 20 PSI, detector voltage 2000 volts.

2.3.3. Binary Combinations

Solutions containing copper complex and cisplatin in 10:1, 5:1 and 1:1 Pt/Cu molar ratios were prepared keeping constant the cisplatin concentration (1.0 mM). Sample solutions were mixed with methanol in 1:1 H_2O:CH_3OH volume ratio to improve the quality of the spectra. In order not to alter the complex formation equilibria, methanol was added immediately before the mass spectra measurements. Solutions containing cisplatin and the copper complex were analysed at 4500, 600 and 1500 volts as needle, shield and detector voltages, respectively, for studying masses in the range 100-450 m/z, and at 6000, 800 and 2000 volts as needle, shield and detector voltages for studying masses in the range 450-1000 m/z. The other parameters were kept constants during all the experiments (housing temperature 60 °C, drying gas temperature 120 °C, nebuliser gas pressure 40 PSI and drying gas pressure 20 PSI).

2.3.4. Biological assays

2.3.4.1 Cell lines

Human acute T-lymphoblastic leukemia (CCRF-CEM) and human ovarian carcinoma (A2780) cell lines, as well as their respective cisplatin-resistant sublines (CCRF-CEM-res; A2780-res) were used in the study. CCRF-CEM cells were purchased from the American Type Culture Collection (ATCC, USA) while the CCRF-CEM-res subline was obtained by us (see below); both the cell lines were maintained in culture between 1x105 cells/ml and 1x106 cells/ml of RPMI 10% FBS with 1% kanamycin (growth medium). A2780 and A2780-res cells were a generous gift from Dr. Fischer Eva (Tumor Biology Laboratory, The Ion Chiricuta Oncology Institute, Cluj-Napoca, Romania) and were grown in RPMI medium addicted with 2mM Glutamine and 10% FBS; A2780-res were cultured in the presence of 1 μM cisplatin after subculture of attached cells (necessary only 2-3 passages). Cell monolayers reached 70% confluency in 3-4 days and then they need a split 1:3 i.e a seeding at $1x10^6$ total cells in $75cm^2$ flaskes using 0.25% trypsin/EDTA.

2.3.4.2 Selection of the cisplatin-resistant CCRF-CEM subline

A CCRF-CEM sub-line able to grow at the same extent in the absence and in the presence of 5 μM cisplatin (CCRF-CEM-res) was obtained by serial passages of the wild type cells in the presence of increasing cisplatin concentrations, starting from a sub-inhibitory concentration (0.5 μM). At each cell passage (every 3-4 days), the number of viable cells of cisplatin treated-cultures was compared to that of duplicate untreated cultures. The cisplatin concentration was increased at each cell passage up to 1.50 μM; from then on, cisplatin-treated cultures grew much slower and poorly than their untreated counterparts, and were kept on (5 to 10 passages) at the same concentration until the cell population had regained original viability and growth timing. At intervals during the selection process, the level of cisplatin resistance was checked by the MTT method in cells grown for one passage without the drug; doxorubicin was used as reference compounds to evaluated the drug-resistance specificity. Given that cell cultures never survived at concentrations over 5μM, the cell population growing at 5μM cisplatin was stabilized by 15 further passages, then grown without drug for one passage, checked for resistance as described above, and finally stored in aliquots in liquid nitrogen.

2.3.4.3 Cytotoxic assays

Stock solutions of cisplatin, 1, 2 and C1 were made in DMSO at 50mM. Dilutions of stocks for biologic investigations were made in RPMI medium at 2x the final concentration for single drug evaluations, or at 4x the final concentration for evaluation of dual drug combinations. The concentration of DMSO on the cells was never higher than 0.1%. Effects of drugs and drug combinations were evaluated in exponentially growing cell cultures; for experiments in cisplatin-resistant cell cultures, both the CCRF-CEM-res and A2780-res cells were allowed to grow in the absence of drug for one passage. CCRF-CEM and CCRF-CEM-res were seeded at a density of 1×105 cells/ml of growth medium in a flat-bottom 96-well plate and simultaneously exposed to the 2x or 4x concentrations of drugs. A2780wt and A2780-res were seeded at $5x10^3$ cells/well in flat-bottom 96-well plate and allowed to adhere overnight before the addition of the 2x or 4x concentrations of drugs. Cell growth in the absence and in the presence of drugs and drug combinations was determined after 96 hours of incubation at 37°C and 5% CO2 (corresponding to three to four duplication rounds of untreated cells), by both cell counting with the trypan blue exclusion method and the MTT method (ref). Cell numbers and viability in drug-treated samples were expressed as percentage of those of their respective controls. Dose-response curves for each drug were determined and the IC50s of single drug and drug combinations were calculated with OriginPro8.

Results and discussion

3.1. Synthesis

The new synthesis of **1** led to a crystalline product with high purity level (≥ 95%) and with high yield. The obtained compound is hygroscopic and deliquescent and must be stored under vacuum. It is stable for months at room temperature in desiccator, but if warmed it converts eventually in **2**, more stable thermodynamically. In this case, a change in the colour, from blue to turquoise, is seen. In the synthesis of **C1**, the previously used solvent CH_3CN was changed with H_2O. The reagents are not water soluble, however a long stirring (≈ 12 h) gives the necessary energy to drive the reaction towards the formation of the product, also not water soluble. The yield (80%) could be slightly enhanced (85 %) extending the stirring time to 24 h.

3.2. Cytotoxicity measurements

The cytotoxic activities of **2** and cisplatin, alone and in dual drug combinations, were evaluated against cisplatin-resistant T-leukaemia (CCFR-CEM-res) and ovarian carcinoma (A2780-res) human cell lines. Dose-response curves for **2** and cisplatin were obtained, and the IC50 values (concentration required to inhibit cell proliferation by 50% with respect to untreated cells) were determined. Copper complex **2** showed IC50 values of 0.75 μM and 0.24 μM in CCFR-CEM-res and A2780-res cells, respectively. Cisplatin showed IC50 values of 6.98 μM and 5.3 μM for CCFR-CEM-res and A2780-res cells, respectively. Dose-response curves of **2** and cisplatin in cisplatin-resistant cell lines are shown in Fig. 2. The effects of single drugs and dual drug combinations on the tested cell lines are reported in Table 1 as % of untreated controls. In all cases, combinatorial treatments gave rise to a synergistic type of interaction of cisplatin with the studied copper complexes. In particular, it is worth mentioning the synergistic effect shown by combinatorial treatments against cisplatin-resistant cell lines for its evident potential in the clinic of cisplatin-resistant cancers.

3.2. ESI-MS results

3.2.1. Copper complexes

In the mass spectra of **1**, **2** and **C1**, only mono-charged species containing copper(II) or copper(I) were put in evidence. Reduction of Cu(II) to Cu(I) is commonly observed in ESI phase for solutions of Cu(II) salts[32]. Characteristic isotope peaks for copper- and copper-chlorine-containing ions were clearly seen and the isotopic patterns of these peaks confirmed the elemental composition of the observed ions. The most relevant peaks are assigned in the shown spectra (Fig. 3) while calculated and experimental isotopic patterns for selected peaks are reported in the Supporting Information (Fig. S1). In the spectrum of **1** (Fig. 3A) the signals with the highest intensity correspond to $[Cu^{(II)}(phen)(TFA)]^+$ (356 m/z), $[Cu^{(II)}(phen)Cl]^+$ (278 m/z), $[Cu^{(II)}(phen)F]^+$ (262 m/z), and $[Cu^{(I)}(phen)]^+$ (243 m/z) ions. A low signal of $[Cu^{(II)}(phen)_2(TFA)]^+$ is present at 536 m/z. In the spectrum of **2** (Fig. 3B) some species observed in the spectrum of **1** are present ($[Cu^{(II)}(phen)Cl]^+$, $[Cu^{(II)}(phen)(TFA)]^+$, $[Cu^{(II)}(phen)_2(TFA)]^+$) together with $[phen+H^+]^+$ (181 m/z), $[Cu^{(I)}(phen)_2]^+$ (423 m/z), $[Cu^{(II)}(phen)_2Cl]^+$ (458 m/z), $[Cu^{(II)}(phen)_2(ClO_4)]^+$ (522 m/z).
Also in the spectrum of **C1** (Fig. 3C) some species observed in the spectrum of **1** and **2** are present ($[phen+H^+]^+$, $[Cu^{(I)}(phen)]^+$, $[Cu^{(II)}(phen)Cl]^+$, $[Cu^{(II)}(phen)(TFA)]^+$, $[Cu^{(I)}(phen)_2]^+$, $[Cu^{(II)}(phen)_2Cl]^+$, $[Cu^{(II)}(phen)_2(ClO_4)]^+$, $[Cu^{(II)}(phen)_2(TFA)]^+$) together with species containing the thionic ligand H_2dit, i.e. $[Cu^{(II)}(phen)_2(Hdit)]^+$ (524 m/z), $[Cu^{(II)}(phen)(Hdit)]^+$ (344 m/z), $[H_2dit+H^+]$ (103 m/z). It is interesting to remark that, although the copper complexes have been measured at the same concentration, their mass spectra presented different intensity, from 4.5×10^9 (for **1**) to 1.75×10^9 a.u. (for **2**). The different intensity was related to the ionizability of the complexes, in the order **2** < **C1** < **1**.

3.2. Cisplatin

The ESI-MS spectrum of cisplatin is reported from 200 to 600 m/z in Fig. 4. The signal related to the protonated cisplatin, $[Pt(NH_3)_2Cl_2+H^+]^+$ appears at 300 m/z. Other signals related to $[Pt(NH_3)_2Cl_2]^+$, $[Pt(NH_3)Cl]^+$ and $[Pt(NH_2)]^+$ are present at 263, 246 and 210 m/z, respectively. A signal interpreted as due to a mixture of $[Pt(NH_3)_3(H_2O)_2Cl]^+$ (78%) and $[Pt(NH_3)_2(H_2O)_3Cl]^+$ (22%) is present at 319 m/z. At 547 and 564 m/z signals due to the polynuclear complexes $[Pt_2(NH_3)_3Cl_3]^+$ and $[Pt_2(NH_3)_4Cl_3]^+$ can be seen. Calculated and experimental isotopic patterns for selected peaks are reported in the Supporting Information (Fig. S2). In the species containing platinum and NH_2^-, a double bond between platinum and nitrogen ions is present, as also reported from other authors [33,34]. It is important to remark that the mass spectral profile of cisplatin solutions starts changing after 1 h from the preparation as the compound undergoes hydrolysis. In fact, the signals at 300, 263 and 246 m/z decrease in intensity and adducts with water and methanol are formed.

3.3. Binary Combinations

3.3.1. Cisplatin and copper complexes

The number and the aspect of the signals present in the spectra resulted strongly dependent on the chosen experimental conditions of needle, shield and detector voltage. Generally, rising the voltage of needle, shield and detector, the fragmentation processes increase. The fragmentations are helpful since they are characteristic of the molecule and provide structural information. However, as the fragments themselves can undergo to a further fragmentation, the resulting spectra could became difficult to understand. On the other hand, a too low voltage determines a fall in the overall ion current and then in a reduction of the ionization efficiency. These issues could determine non-reliable signals [35]. The mass spectra of the binary combinations were collected varying the voltage values in order to find the optimal conditions. In all the experiments, signals with isotopic pattern characteristic of species containing both copper and platinum were observed. However at needle, shield and detector voltage of 4500, 600 and 1500 volts, respectively, the signals with reliable intensity (10^9 magnitudo order) were characteristic of species containing only copper as metal ion. In particular were present signals of the species $[Cu^{(II)}(phen)(TFA)]^+$ (356 m/z), $[Cu^{(I)}(phen)(H_2O)]^+$ (261 m/z) and $[Cu^{(I)}(phen)]^+$ (243 m/z). To observe with sufficient intensity also the signals of the other ions, needle, shield and detector voltage of 6000, 800 and 2000 volts, respectively, were used. The binary combinations were tested also in excess of cisplatin (at 1:1, 5:1 and 10:1 platinum/copper molar ratios) being the signals originated by the copper complexes more intense than those originated by cisplatin at the same concentration, due to a greater ionizability of the copper complexes. The measured mass spectra of the solutions containing cisplatin and **2** at the three different molar ratios, are reported as an example in Fig. S3. The signals of the mixed complexes containing both copper and platinum appeared at any molar ratios for all the studied systems, however, at 1:1 platinum/copper molar ratio, the more intense signals (marked with "*" in Fig.S3) were due to mononuclear and polynuclear copper complexes. The stoichiometry of these complexes were identified from the m/z value and from the isotopic pattern as $[Cu^{(II)}{}_2(phen)_2(TFA)Cl_2]^+$ (671 m/z), $[Cu^{(I)}{}_3(phen)_2(TFA)(OH)(H_2O)_2]^+$ (717 m/z), $[Cu^{(II)}{}_2(phen)_2(TFA)_2Cl]^+$ (749 m/z), $[Cu^{(II)}{}_2(phen)_2(TFA)_2(ClO_4)]^+$ (811 m/z). At 10:1 platinum/copper molar ratio, together with signals of copper and mixed copper-platinum complexes, also signals of polynuclear complexes containing two or more platinum ions and a variable number of chlorine, ammonia and water molecules, were present in the range 800-1000 m/z. The lack of a good pattern resolution prevented the determination of the their exact stoichiometry. From these results, it followed that the combination at 5:1 platinum/copper molar ratio was the best one to study the mixed platinum-copper complexes. In Fig. 5 the mass spectra of solutions containing cisplatin and **1**, cisplatin and **2** and cisplatin and **C1** at 5:1 platinum/copper molar ratio are reported (signals due to the copper complexes are marked with "*"). As can be seen, the mass spectra of all the systems present a similar profile, even if with different intensity, indicating that the same mixed complexes were formed. In particular, the signals with the isotopic pattern typical of mixed platinum-copper complexes fall in the range 540-660 m/z. As for the copper complexes, the stoichiometry of these mixed complexes were identified from the m/z value and from their isotopic pattern. In many cases, convoluted signal were observed due to the simultaneous presence of complexes with similar masses. In this case the experimental pattern was due to a weighted combination of the isotopic pattern of the different molecules. The weights, i.e. the % in which each molecule was present, were obtained by multivariate regression analysis of the experimental data. An example of this treatment is reported in Fig. S4, where the experimental pattern can be compared to the theoretical one, calculated as a contribution of 4 molecules.

From the analysis of the spectra, we identified three principal complexes, all mono-charged, with stoichiometry: **I**) $[CuPt(phen)(H_2O)_2(OH)Cl_2]^+$(561 m/z), **II**) $[CuPt(phen)(H_2O)(NH_3)(OH)Cl_2]^+$ (560 m/z) and **III**) $[CuPt(phen)(H_2O)_2Cl_2]^+$ (544 m/z). Together with **I**-**III**, other 9 complexes were identified, but they resulted to be adducts with TFA or product of exchange reactions with the fluorine carried out by the TFA. These 9 complexes could be thought as byproducts (the complete list of these complexes is reported in the Supporting, Table S1).

3.3.1.1 Tandem MS-MS

The tandem mass spectrometry (MS-MS) was essential to confirm the proposed stoichiometry and to hypothesize the structure of the formed complexes. The MS-MS consists in multiple steps of mass spectrometry selection and between these steps several fragmentation processes occur. On a triple quadrupole $Q_1q_2Q_3$ it is possible to select an ion of a certain mass (parent ion) in the first quadrupole Q_1 and send it in the second quadrupole q_2 that represents a collision cell. Here the ion in presence of an inert gas such as Ar, He, or N_2, is fragmented. The resulting fragments are passed within the third quadrupole Q_3, therein scanned and detected. The correct stoichiometry and structure of the parent ion can be deduced from the fragmentation profile. Also the energy required to fragment the ion gives information on its stability. In fact, when the MS-MS is applied on a metal complex, as in our case, the collision-induced dissociation determines the loss of neutral ligands such as water or ammonia at low collision energy (CE) (~2-15 V), the breaking of bonds and also the macro-cycle destruction at medium CE (~15-30 V), and even the expulsion of the free metal ion at high CE (~30-50 V). The necessary CE is highly specific for each process and for each complex and it is strictly related to the strength of the bonds and to the stability of the complex. Once obtained the fragmentation profile, the structure of the parent ion may be reconstructed starting from the littlest fragments whose structure could be easily hypothesized, as the fragments were pieces of a puzzle. Of course the fragments may re-arrange in ESI phase, but this method generally leads to the most probable structure of the parent ion.
The fragmentation profile obtained for compounds **I-III** are reported in Fig.s 6-8. As can be seen in Fig. 7 for **I**, species with stoichiometry $[Cu(phen)]^+$ (243 m/z), $[Cu(phen)Cl]^+$ (278 m/z), $[CuPt(phen)Cl_2]^+$ (508 m/z), $[CuPt(phen)Cl_2(H_2O)_2]^+$ (544 m/z) were visible as fragments of the parent compound. The structures of these ions were easily proposed, as shown in the figure. To define the structure of the parent compound at 561 m/z, it was convenient to consider it as (544 m/z + 17 m/z). Ammonia or hydroxide ion have 17 m/s, then two possibilities were considered: hydroxide or ammonia linked to the copper. If OH^- was linked to the copper, the resulting complex should have had +1 as charge, while if it was present the ammonia, the charge of the complex should have been +2 (note that when copper is tetra-coordinated or penta-coordinated has +1 or +2 as oxidation number, respectively). Being the fragment mono-charged, only the OH- ion were considered. Then the structure of the parent ion were proposed as reported in the figure.
The study of the compound **II** appeared more complicated. As far **I**, the structures of the $[Cu(phen)]^+$, $[Cu(phen)Cl]^+$, and $[CuPt(phen)Cl_2]^+$ ions were easily proposed, as shown in the Fig. 8. As regards the fragment at 525, it was considered as (508 m/z + 17 m/z). Then four possibilities were considered: hydroxide linked to platinum (*i*) or to copper (*ii*), ammonia linked to platinum (*iii*) or to copper (*iv*). If OH^- or NH_3 were linked to platinum, the resulting complexes (cases *i* and *iii*) should have had 0 or +1 as charge, respectively. If OH^- or NH_3 were linked to copper, the resulting complexes (cases *ii* and *iv*) should have had +1 or +2 as charge, respectively. Being the fragment mono-charged, only the case *ii* and *iii* were considered. As regards the fragment at 542 m/z, as before, it was considered as (525 m/z + 17 m/z). Then 6 possibilities were taken into account starting from the previous cases (*ii*) and (*iii*): (*ii*) + OH^- or NH_3 linked to platinum (cases *v* and *vi*); (*iii*) + OH^- or NH_3 linked to copper (cases *vi* and *ix*); (*iii*) + OH^- or NH_3 linked to platinum (cases *vii* and *viii*); being the fragments mono-charged, the only possibilities that were considered were *vi* and *vii*. The last fragment was considered as (525 m/z + 18 m/z), then a water molecule was added to *vi* and *vii*, to obtain *x*, with +1 as charge, and *xi* with +2 as charge. Then, the most probable structure of the parent ion was that of *x*. The entire route is shown in Fig. S4. As far as the compound **III**, similar considerations were made to obtain as the most probable structure, that shown in the Fig. 8. All the reported fragmentations were obtained with a CE of 20 eV. To fragment also the complex $[Cu(phen)]^+$ a collision energy of 45 eV was necessary, but at this energy value, the other fragments were no longer observable.
Compound **III** can be considered as a fragment of **I**, that itself can be considered as a hydrolysis product of **II**. A precursor with formula $[CuPt(phen)(NH_3)_2(OH)Cl_2]^+$ can be hypothesized in solution, however, this species was not detected in our experiments. The proposed reaction between copper complexes and cisplatin is finally resumed in Scheme 1. As can be seen, the same complex is formed regardless which copper complex **1**, **2** or **C1** is involved. In the reaction of **2** or **C1** with cisplatin, one phen unit is released; in the case of **C2**, a dit unit is also released. In the formed complex, copper and platinum are linked by two bridging chlorines, the coordination spheres of copper is completed by a phen and by an hydroxide ion, that of platinum by an ammonia and a water molecules. From the mass spectral evidences, the mixed copper-platinum complex was formed in aqueous solution after few minutes from the mixing of the reagents and it was stable for at least one week. The same reaction carried out in water-acetonitrile required three weeks to be completed.

3. Conclusions

A mixed complex containing copper and platinum ions is formed by reaction of Cu(1,10-phenanthroline)$(OH_2)_2(OClO_3)_2$, $[Cu(1,10\text{-phenanthroline})_2(OH_2)](ClO_4)_2$ and $[Cu(1,10\text{-phenanthroline})_2(\text{imidazolidin-2-thione})](ClO_4)_2$ with cisplatin in aqueous solution. In the mixed complex, copper is coordinated by one phenanthrolinic unit and by an hydroxide ion, platinum is linked by bridging chlorines and is coordinated by one ammonia and one water molecule. In the reaction of $[Cu(1,10\text{-phenanthroline})_2(OH_2)](ClO_4)_2$ and $[Cu(1,10\text{-phenanthroline})_2(\text{imidazolidin-2-thione})](ClO_4)_2$ one phenanthrolinic unit is released. The 1,10-phenanthroline itself presents an IC50 values of approx. 2 μM towards the tested cell lines, then the higher cytotoxic activity shown by the mixtures containing cisplatin and **2** or **C1**, with respect to that shown by the mixture with **1**, may be due also to the freed 1,10-phenanthroline. Also an imidazolidine-2-thione molecule is released during the reaction of **C1** with cisplatin but it is devoid of any biological activity against the tested cells. The formation of the mixed copper-platinum compound that was experimentally established could be a possible mechanism to explain the synergistic effect that combinations of the studied copper complexes with cisplatin shown towards the tested cell line. Given that the synergistic effect was evident also against cisplatin-resistant cells, the formed copper-platinum complex could likely interfere with one or more of the mechanisms that lead to the cisplatin resistance. In this regards, as future perspective we intend extend these studies to other cisplatin resistant cell lines in order to obtain more useful insights

and possibly clarify the underlining molecular mechanism(s). From the reported results, the ESI-MS and the tandem MS-MS altogether appear as suitable tools for the study of the metal complexes formed in solution. Of course, in the transition process from solution to gas phase, the structure of the complexes may be affected, and this is particularly relevant for big molecules, such as metal complexes with biomolecules. Nevertheless, relevant information on the solution stability and reactivity of complexes not easily isolable in the solid state can be obtained, also in several experimental conditions such as different media, pH, or ionic buffer.

Acknowledgments

Federica Trudu, Daniela Perra, Elisabetta Pinna gratefully acknowledge the Sardinia Regional Government for the financial support of her PhD scholarship (P.O.R. Sardegna F.S.E. Operational Programme of the Autonomous Region of Sardinia, European Social Fund 2007-2013 - Axis IV Human Resources, Objective l.3, Line of Activity l.3.1.).

References

[1] S. Ishida, J. Lee, D.J. Thiele, I. Herskowitz, Uptake of the anticancer drug cisplatin mediated by the copper transporter Ctr1 in yeast and mammals., Proc. Natl. Acad. Sci. U. S. A. 99 (2002) 14298–302. doi:10.1073/pnas.162491399.
[2] I. Song, N. Savaraj, Z.H. Siddik, P. Liu, Y. Wei, C.J. Wu, et al., Role of human copper transporter Ctr1 in the transport of platinum-based antitumor agents in cisplatin-sensitive and cisplatin-resistant cells, Mol. Cancer Ther. 3 (2005) 1543–1549.
[3] H. Burger, a Zoumaro-Djayoon, a W.M. Boersma, J. Helleman, E.M.J.J. Berns, R.H.J. Mathijssen, et al., Differential transport of platinum compounds by the human organic cation transporter hOCT2 (hSLC22A2)., Br. J. Pharmacol. 159 (2010) 898–908. doi:10.1111/j.1476-5381.2009.00569.x.
[4] R.A. Alderden, M.D. Hall, T.W. Hambley, The Discovery and Development of Cisplatin, J. Chem. Educ. 83 (2006) 728–734.
[5] S. Trzaska, Cisplatin, Chem. Eng. News. 83 (2005).
[6] E.R. Jamieson, S.J. Lippard, Structure, Recognition, and Processing of Cisplatin-DNA Adducts., Chem. Rev. 99 (1999) 2467–98.
[7] R.C. Todd, S.J. Lippard, Inhibition of transcription by platinum antitumor compounds., Metallomics. 1 (2009) 280–91. doi:10.1039/b907567d.
[8] N. Eckstein, Platinum resistance in breast and ovarian cancer cell lines, J. Exp. Clin. Cancer Res. 30 (2011) 91–102. doi:10.1186/1756-9966-30-91.
[9] S. Dhar, F.X. Gu, R. Langer, O.C. Farokhzad, S.J. Lippard, Targeted delivery of cisplatin to prostate cancer cells by aptamer functionalized Pt(IV) prodrug-PLGA-PEG nanoparticles., Proc. Natl. Acad. Sci. U. S. A. 105 (2008) 17356–17361. doi:10.1073/pnas.0809154105.
[10] O. Rixe, W. Ortuzar, M. Alvarez, R. Parker, E. Reed, K. Paull, et al., Carboplatin : Spectrum of Activity in Drug-Resistant Cell Lines and in the Cell Lines of the National Cancer Institutès Anticancer Drug Screen Panel, Biochem. Pharmacol. 52 (1996) 1855–1865.
[11] J. Michels, I. Vitale, L. Galluzzi, J. Adam, K.A. Olaussen, O. Kepp, et al., Cisplatin Resistance Associated with PARP Hyperactivation, Cancer Res. . 73 (2013) 2271–2280.
[12] B. Desoize, Metals and metal compounds in cancer treatment., Anticancer Res. 24 (2004) 1529–44. http://www.ncbi.nlm.nih.gov/pubmed/15274320 (accessed February 27, 2014).
[13] P.A. Andrews, S.B. Howell, Cellular pharmacology of cisplatin: perspectives on mechanisms of acquired resistance, Cancer Cells. 2 (1990) 35–43.
[14] K.J. Scanlon, M. Kashani-Sabet, H. Miyachi, L.C. Sowers, J.J. Rossi, Molecular basis of cisplatin resistance in human carcinomas: Model systems and patients., Anticancer Res. 9 (1989) 1301–1312.
[15] T. Pivetta, F. Isaia, F. Trudu, A. Pani, M. Manca, D. Perra, et al., Development and validation of a general approach to predict and quantify the synergism of anti-cancer drugs using experimental design and artificial neural networks, Talanta. 115 (2013) 84–93. doi:10.1016/j.talanta.2013.04.031.
[16] L. Huang, L.-M. Liao, A.-W. Liu, J.-B. Wu, X.-L. Cheng, J.-X. Lin, et al., Analysis of the impact of platinum-based combination chemotherapy in small cell cervical carcinoma: a multicenter retrospective study in Chinese patients., BMC Cancer. 14 (2014) 140. doi:10.1186/1471-2407-14-140.
[17] J. Ma, M. Maliepaard, K. Nooter, a W. Boersma, J. Verweij, G. Stoter, et al., Synergistic cytotoxicity of cisplatin and topotecan or SN-38 in a panel of eight solid-tumor cell lines in vitro., Cancer Chemother. Pharmacol. 41 (1998) 307–16. http://www.ncbi.nlm.nih.gov/pubmed/9488600.
[18] B. Taylor-Harding, S. Orsulic, B.Y. Karlan, A.J. Li, Fluvastatin and cisplatin demonstrate synergistic cytotoxicity in epithelial ovarian cancer cells., Gynecol. Oncol. 119 (2010) 549–56. doi:10.1016/j.ygyno.2010.08.017.
[19] Y. Lin, M. Tsai, S. Weng, Y. Kuo, Y. Chiu, Synergistic effect of curcumin and cisplatin via downregulation of thymidine phosphorylase and ERCC1, Mol. Pharmacol. 80 (2011) 136–146. doi:10.1124/mol.111.071316.
[20] E.E. Vokes, K.E. Choi, R.L. Schilsky, W.J. Moran, C.M. Guarnieri, R.R. Weichselbaum, et al., Cisplatin, fluorouracil, and high-dose leucovorin for recurrent or metastatic head and neck cancer., J. Clin. Oncol. . 6 (1988) 618–626.
[21] C. Andreadis, K. Vahtsevanos, T. Sidiras, I. Thomaidis, K. Antoniadis, D. Mouratidou, 5-Fluorouracil and cisplatin in the treatment of advanced oral cancer, Oral Oncol. 39 (2003) 380–385. doi:10.1016/S1368-8375(02)00141-0.
[22] C. Faivre, P. Rougier, M. Ducreux, E. Mitry, A. Lusinchi, P. Lasser, et al., 5-fluorouracile and cisplatinum combination chemotherapy for metastatic squamous-cell anal cancer, Bull. Cancer. 86 (1999) 861–865.
[23] C. Santini, M. Pellei, V. Gandin, M. Porchia, F. Tisato, C. Marzano, Advances in copper complexes as anticancer agents., Chem. Rev. 114 (2014) 815–62. doi:10.1021/cr400135x.
[24] L. Tripathi, P. Kumar, A.K. Singhai, Role of chelates in treatment of cancer, Indian J. Cancer. 44 (2007) 62–71.
[25] M.M. Cox, D.L. Nelson, Lehninger Principles of Biochemistry, 5th ed., 2008.
[26] D.S. Sigman, D.R. Graham, V.D. Aurora, A.M. Stern, Oxygen-dependent Cleavage of DNA by the 1,10-Phenanthroline Cuprous Complex, J. Biol. Chem. 254 (1979) 12269–72.

[27] T.H.J. Niedermeyer, M. Strohalm, mMass as a software tool for the annotation of cyclic peptide tandem mass spectra., PLoS One. 7 (2012) e44913. doi:10.1371/journal.pone.0044913.
[28] M. Strohalm, D. Kavan, P. Nova, M. Volny, mMass 3 : A Cross-Platform Software Environment for Precise Analysis of Mass Spectrometric Data, Anal. Chem. 82 (2010) 4648–4651.
[29] M. Strohalm, M. Hassman, B. Kosata, M. Kodicek, RCM Letter to the Editor, Rapid Commun. Mass Spectrom. 22 (2008) 905–908. doi:10.1002/rcm.
[30] T. Pivetta, F. Isaia, G. Verani, C. Cannas, L. Serra, C. Castellano, et al., Mixed-1,10-phenanthroline-Cu(II) complexes: synthesis, cytotoxic activity versus hematological and solid tumor cells and complex formation equilibria with glutathione., J. Inorg. Biochem. 114 (2012) 28–37. doi:10.1016/j.jinorgbio.2012.04.017.
[31] T. Pivetta, M.D. Cannas, F. Demartin, C. Castellano, S. Vascellari, G. Verani, et al., Synthesis, structural characterization, formation constants and in vitro cytotoxicity of phenanthroline and imidazolidine-2-thione copper(II) complexes., J. Inorg. Biochem. 105 (2011) 329–38. doi:10.1016/j.jinorgbio.2010.11.017.
[32] C. Hao, R.E. March, Electrospray ionization tandem mass spectrometric study of salt cluster ions: part 2--salts of polyatomic acid groups and of multivalent metals., J. Mass Spectrom. 36 (2001) 509–21. doi:10.1002/jms.150.
[33] D. Esteban-Fernández, B. Cañas, I. Pizarro, M. a. Palacios, M.M. Gómez-Gómez, SEC-ICP-MS and ESI-MS as tools to study the interaction between cisplatin and cytosolic biomolecules, J. Anal. At. Spectrom. 22 (2007) 1113. doi:10.1039/b706251f.
[34] M. Cui, Z. Mester, Electrospray ionization mass spectrometry coupled to liquid chromatography for detection of cisplatin and its hydrated complexes., Rapid Commun. Mass Spectrom. 17 (2003) 1517–27. doi:10.1002/rcm.1030.
[35] W. Henderson, J.S. McIndoe, Mass Spectrometry of Inorganic, Coordination and Organometallic Compounds, John Wiley & Sons, Ltd, Chichester, UK, 2005. doi:10.1002/0470014318.
[36] T. Pivetta, F. Isaia, F. Trudu, A. Pani, M. Manca, Development and validation of a general approach to predict and quantify the synergism of anti-cancer drugs using experimental design and artificial neural networks, Talanta. 115 (2013) 84–93. http://www.sciencedirect.com/science/article/pii/S0039914013003469 (accessed February 24, 2014).

Captions

Fig. 1. Formulas and acronyms of the molecules studied in this work. **1** is Cu(1,10-phenanthroline)$(OH_2)_2(OClO_3)_2$, **2** is $[Cu(1,10\text{-phenanthroline})_2(OH_2)](ClO_4)_2$, **C1** is $[Cu(1,10\text{-phenanthroline})_2(\text{imidazolidin-2-thione})](ClO_4)_2$ and cisplatin is *cis*-diammineplatinum(II) dichloride.
Fig. 2. Dose-response curves for **2** (**A**) and cisplatin (**B**) on leukemic cisplatin-resistant cancer cells (CCRF-CEM-res, ●) and ovarian cisplatin-resistant cancer cells (A2780-res, ▲). Antiproliferative effect is expressed as % on untreated controls.
Fig. 3. ESI mass spectra (+) of **1** (**A**), **2** (**B**) and **C1** (**C**); 0.5 mM, 50:50 methanol and water with 0.05 % of trifluroacetic acid. Phen is 1,10-phenanthroline, H_2dit is the imidazolidine-2-thione, TFA is trifluroacetate ion.
Fig. 4. ESI-MS (+) spectrum of cisplatin; 0.5 mM, 50:50 methanol and water with 0.05 % of trifluroacetic acid, w is water.
Fig. 5. ESI mass (+) spectra of cisplatin and **1** (A), cisplatin and **2** (B), cisplatin and **C1** (C) (cisplatin 0.5 mM, copper complex 0.1 mM, 50:50 methanol : water with 0.05 % of trifluroacetic acid). In the spectra copper complexes are marked with "*****".
Fig. 6. Tandem MS-MS spectrum of the signals at 561 m/z. Due to the low intensity of the signals, the isotopic pattern is lost (collision energy 20 V, charges are omitted for clarity).
Fig. 7. Tandem MS-MS spectrum of the signals at 560 m/z. Due to the low intensity of the signals, the isotopic pattern is lost (collision energy 20 V, charges are omitted for clarity).
Fig. 8. Tandem MS-MS spectrum of the signals at 560 m/z. Due to the low intensity of the signals, the isotopic pattern is lost (collision energy 20 V, charges are omitted for clarity).
Table 1. Antiproliferative activity (%) against leukemic cancer cells (CCRF-CEM), cisplatin resistant leukemic cancer cells (CCRF-CEM-res), cisplatin resistant ovarian cancer cells (A2780-res) exhibited by the studied copper complexes, cisplatin and their binary combinations.
Scheme 1. Reaction mechanism between **1** and cisplatin (**A**) and **2** or **C1** and cisplatin (**B**).

FIGURES:

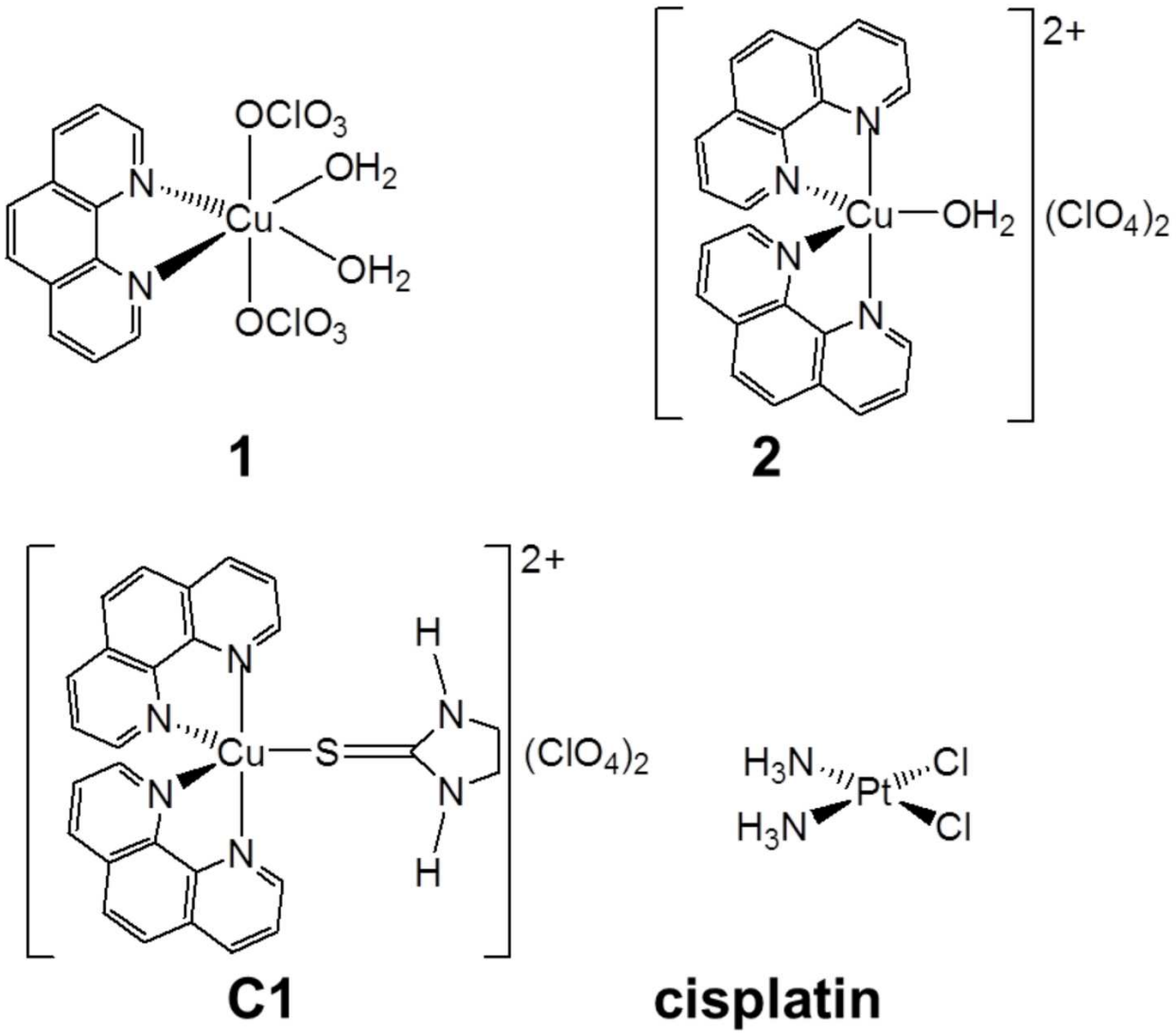

Fig. 1. Formulas and acronyms of the molecules studied in this work. **1** is Cu(1,10-phenanthroline)$(OH_2)_2(OClO_3)_2$, **2** is $[Cu(1,10\text{-phenanthroline})_2(OH_2)](ClO_4)_2$, **C1** is $[Cu(1,10\text{-phenanthroline})_2(\text{imidazolidin-2-thione})](ClO_4)_2$ and cisplatin is *cis*-diammineplatinum(II) dichloride.

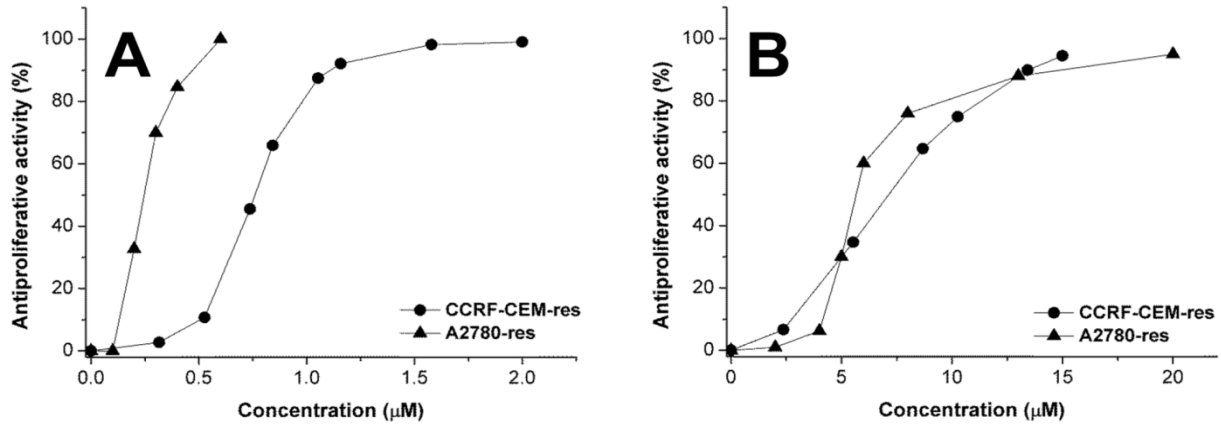

Fig. 2. Dose-response curves for **2** (**A**) and cisplatin (**B**) on leukemic cisplatin-resistant cancer cells (CCRF-CEM-res, ●) and ovarian cisplatin-resistant cancer cells (A2780-res, ▲). Antiproliferative effect is expressed as % on untreated controls.

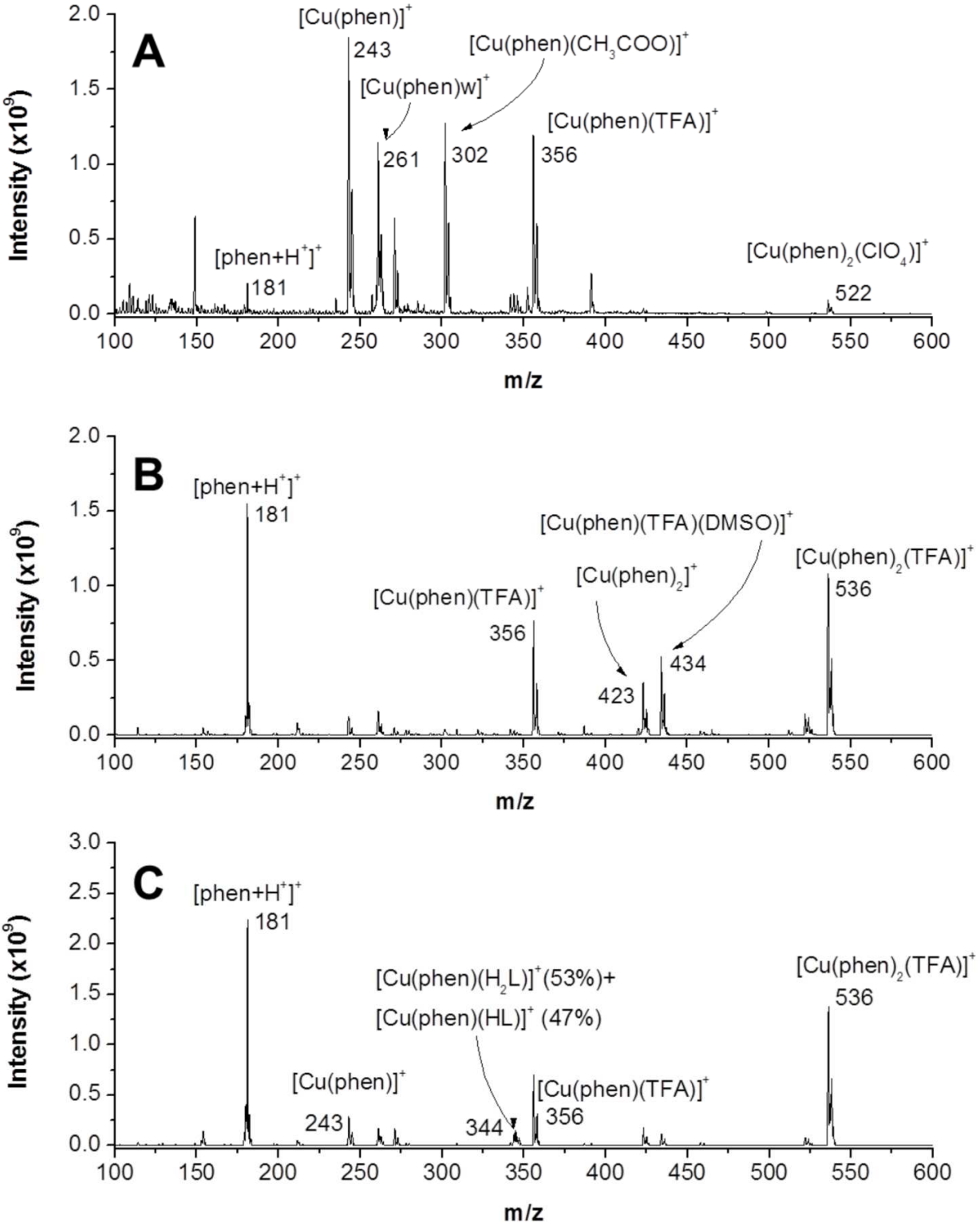

Fig. 3. ESI mass spectra (+) of **1** (**A**), **2** (**B**) and **C1** (**C**); 0.5 mM, 50:50 methanol and water with 0.05 % of trifluroacetic acid. Phen is 1,10-phenanthroline, H_2dit is the imidazolidine-2-thione, TFA is trifluroacetate ion.

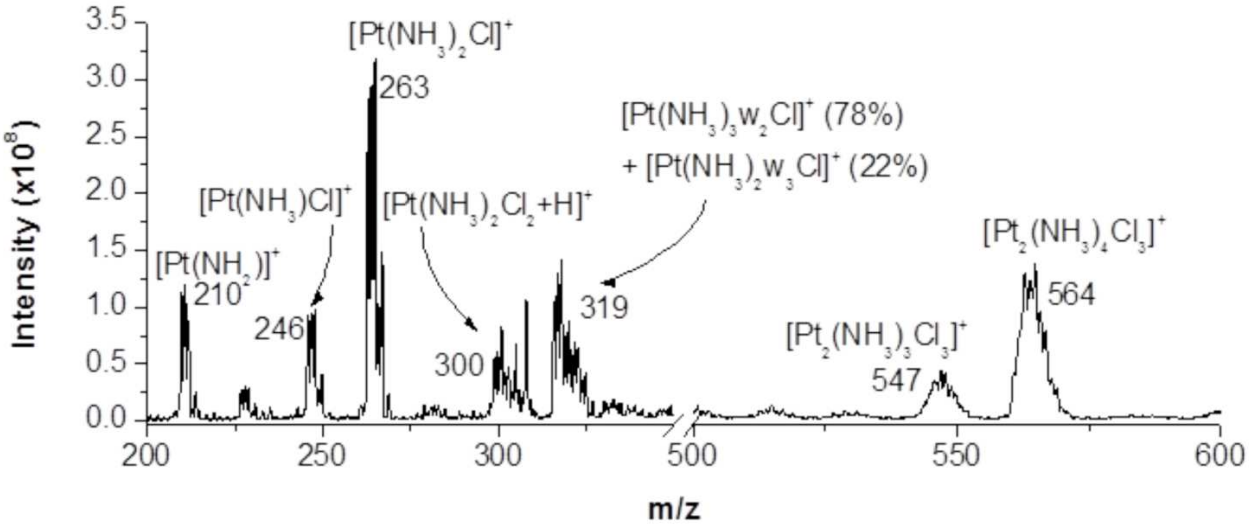

Fig. 4. ESI-MS (+) spectrum of cisplatin; 0.5 mM, 50:50 methanol and water with 0.05 % of trifluroacetic acid, w is water.

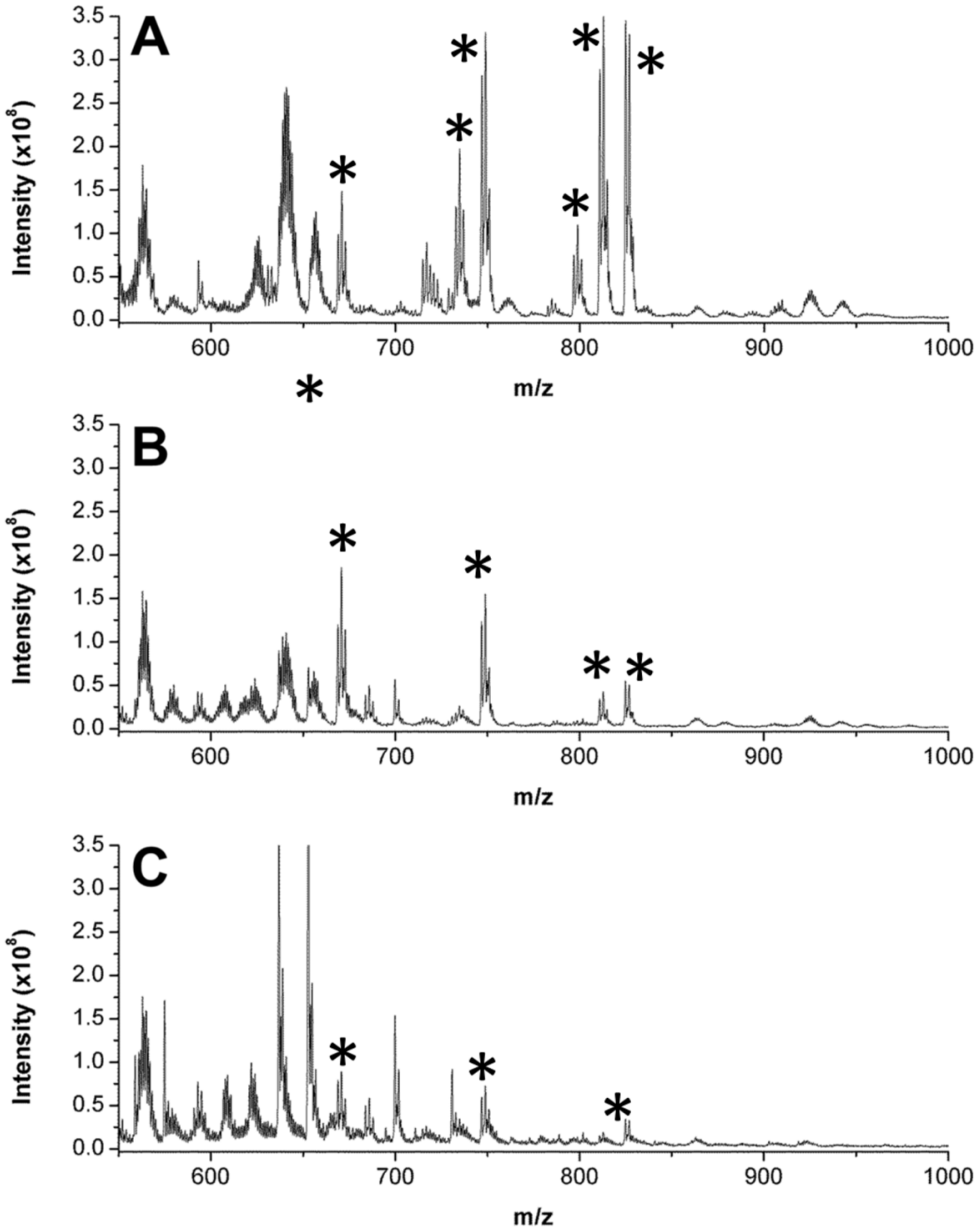

Fig. 5. ESI mass (+) spectra of cisplatin and **1** (A), cisplatin and **2** (B), cisplatin and **C1** (C) (cisplatin 0.5 mM, copper complex 0.1 mM, 50:50 methanol : water with 0.05 % of trifluroacetic acid). In the spectra copper complexes are marked with "*".

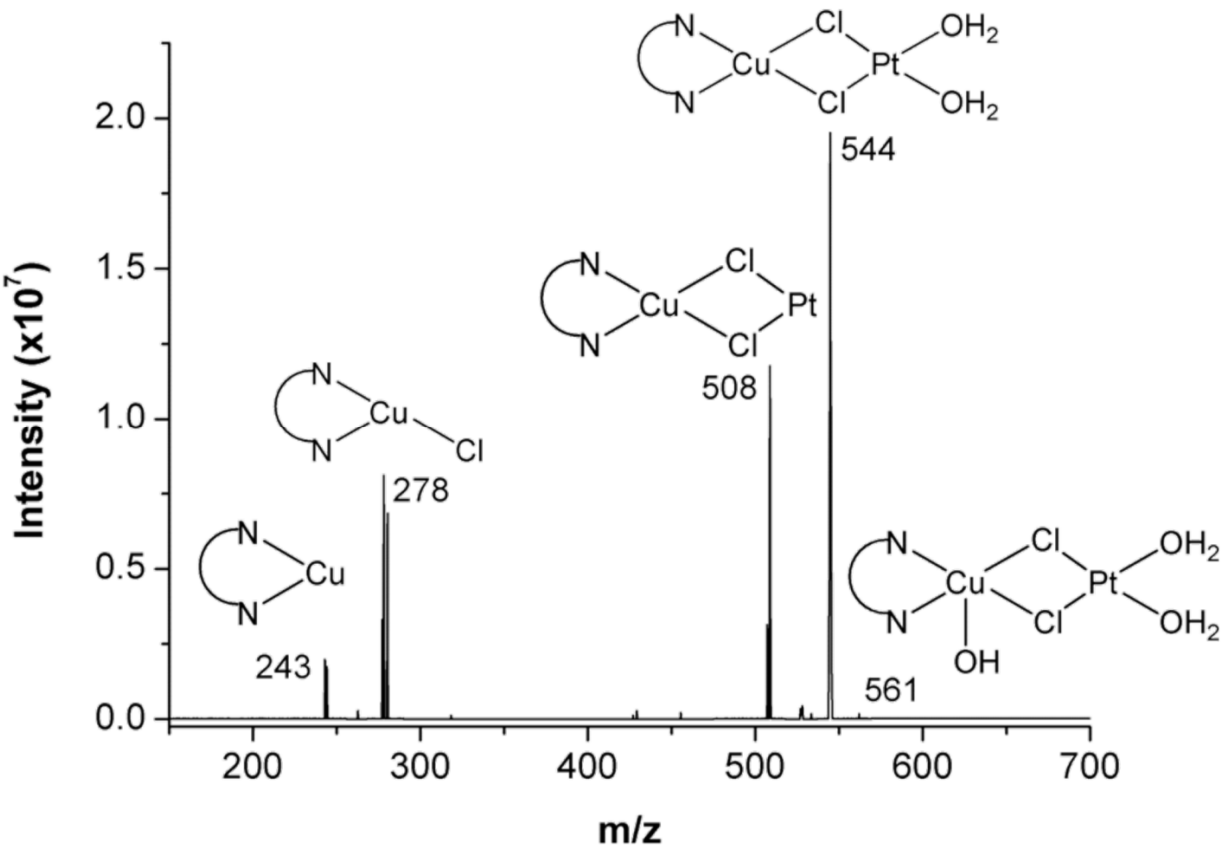

Fig. 6. Tandem MS-MS spectrum of the signals at 561 m/z. Due to the low intensity of the signals, the isotopic pattern is lost (collision energy 20 V, charges are omitted for clarity).

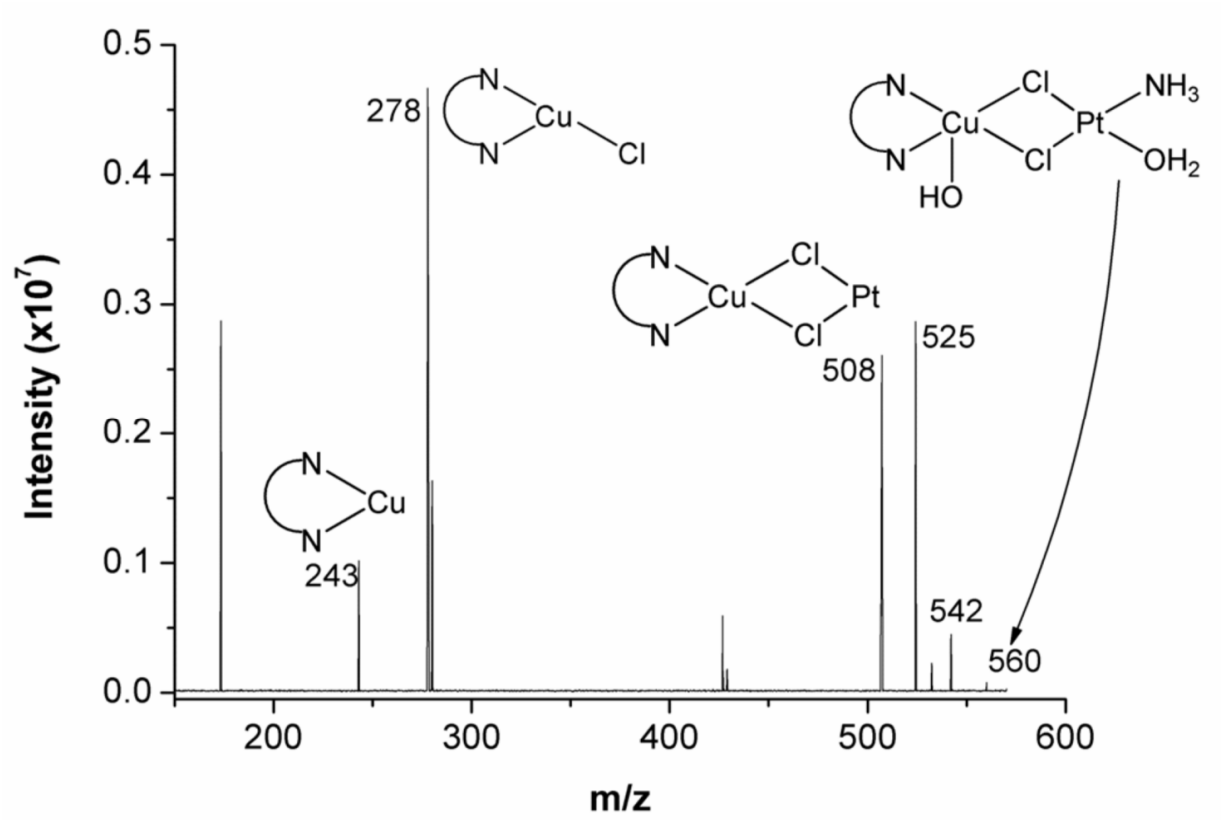

Fig. 7. Tandem MS-MS spectrum of the signals at 560 m/z. Due to the low intensity of the signals, the isotopic pattern is lost (collision energy 20 V, charges are omitted for clarity).

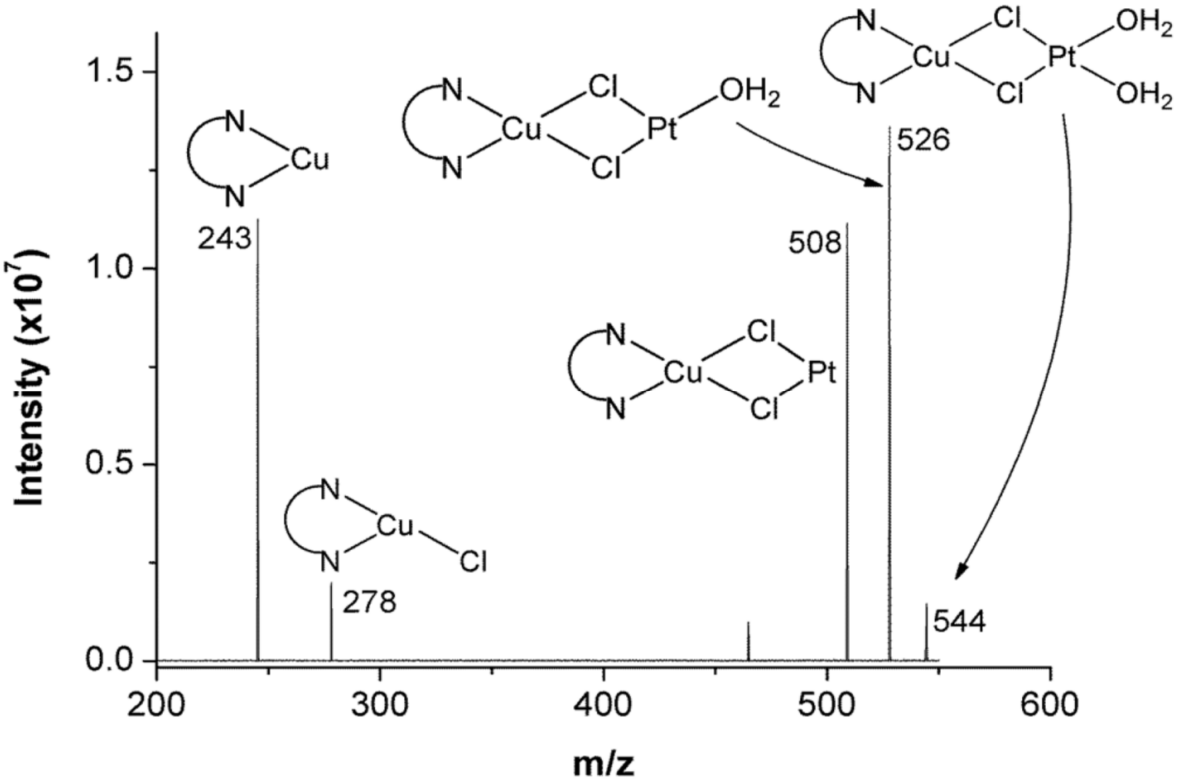

Fig. 8. Tandem MS-MS spectrum of the signals at 560 m/z. Due to the low intensity of the signals, the isotopic pattern is lost (collision energy 20 V, charges are omitted for clarity).

TABLE

Table 1. Antiproliferative activity (%) against leukemic cancer cells (CCRF-CEM), cisplatin resistant leukemic cancer cells (CCRF-CEM-res), cisplatin resistant ovarian cancer cells (A2780-res) exhibited by the studied copper complexes, cisplatin and their binary combinations.

1 (μM)	2 (μM)	C1 (μM)	Cisplatin (μM)	Antiproliferative activity (%)	Cell line	Effect	Index of synergy**
2.63			-	29.3	CCRF-CEM*		
			0.55	11.8			
2.63			0.55	73.6		synergism	36 %
	1.05		-	19.7			
	-		0.85	18.5			
	1.05		0.85	81.6		synergism	47 %
		0.87		32.9			
			0.45	27.5			
		0.87	0.45	82.8		synergism	31 %
	0.67			40.0	CCRF-CEM cisplatin resistant		
			5.0	28.2			
	0.67		5.0	88.0		synergism	31 %
	0.60			24.0			
			4.0	17.5			
	0.60		4.0	59.5		synergism	22 %
	0.20			32.7	A2780 cisplatin resistant		
			4.0	6.0			
	0.20		4.0	58.4		synergism	22 %
	0.10			6.0			
	0.10		4.0	20.0		synergism	8 %

* From ref. [36], ** calculated as in [36]

SCHEME

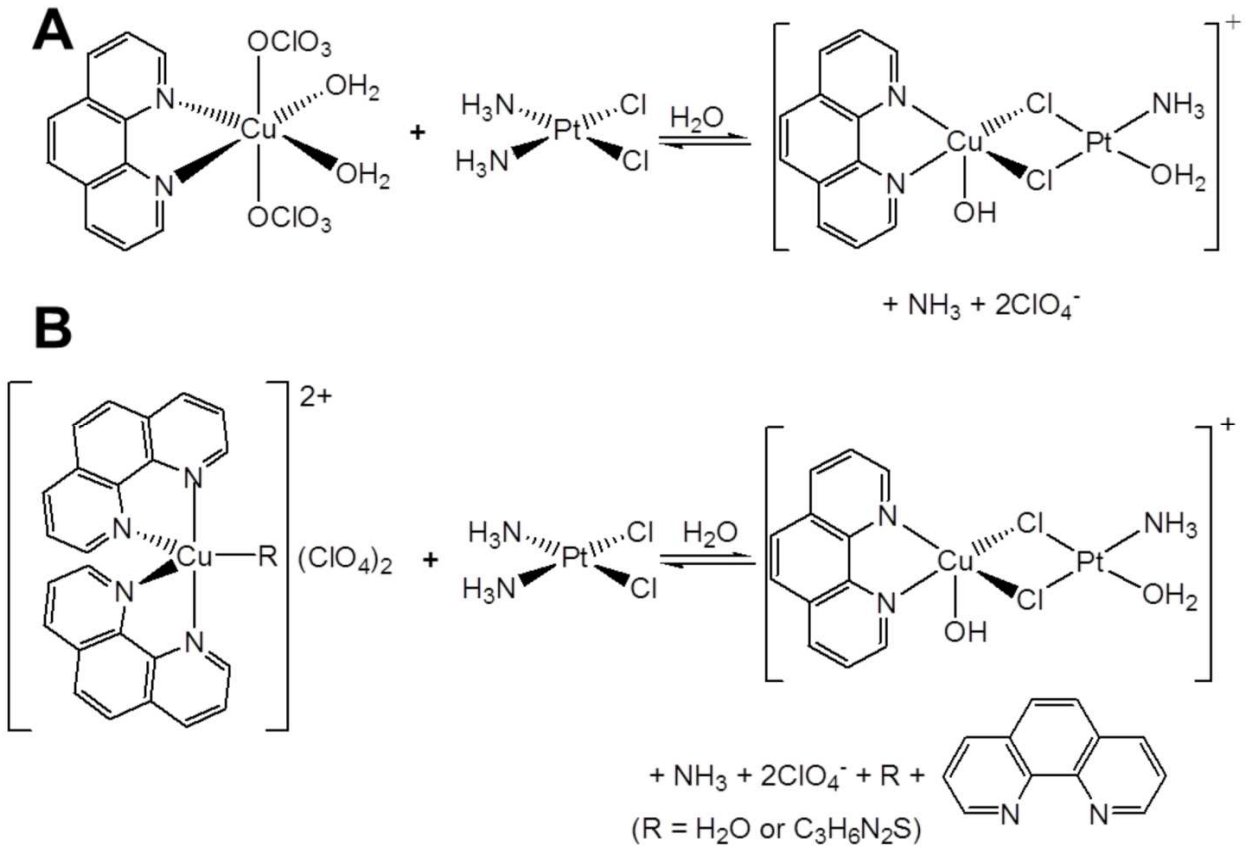

Scheme 1. Reaction mechanism between **1** and cisplatin (**A**) and **2** or **C1** and cisplatin (**B**).

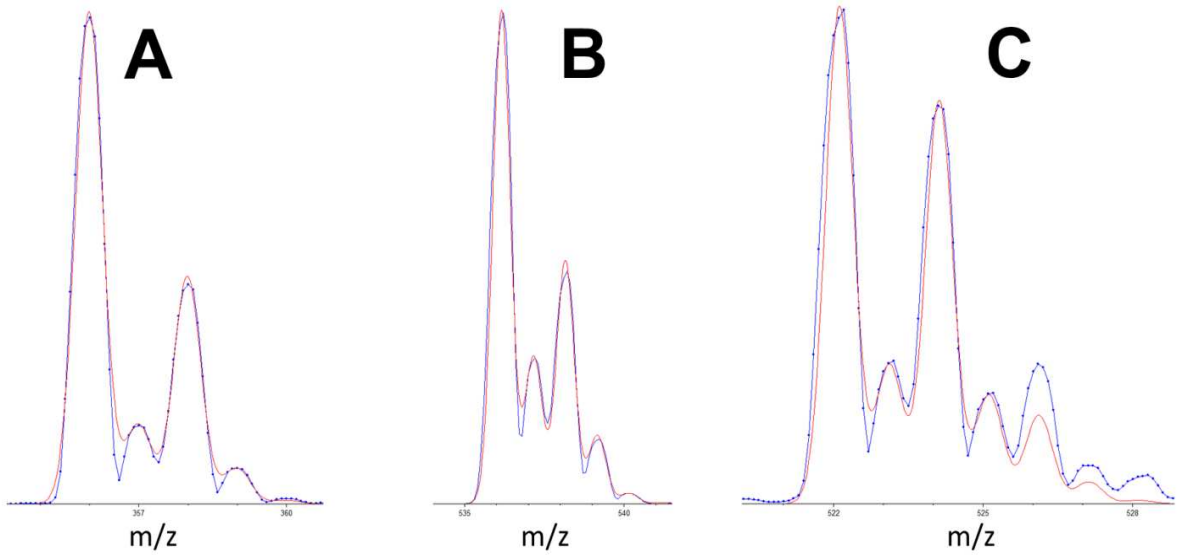

Fig. S1. Calculated (red line) and experimental (blue line) isotopic pattern for (**A**) $[Cu(phen)(TFA)]^+$ (356 m/z), (**B**) $[Cu(phen)_2(TFA)]^+$ (536 m/z), (**C**) $[Cu(phen)_2(ClO_4)]^+$ (522 m/z).

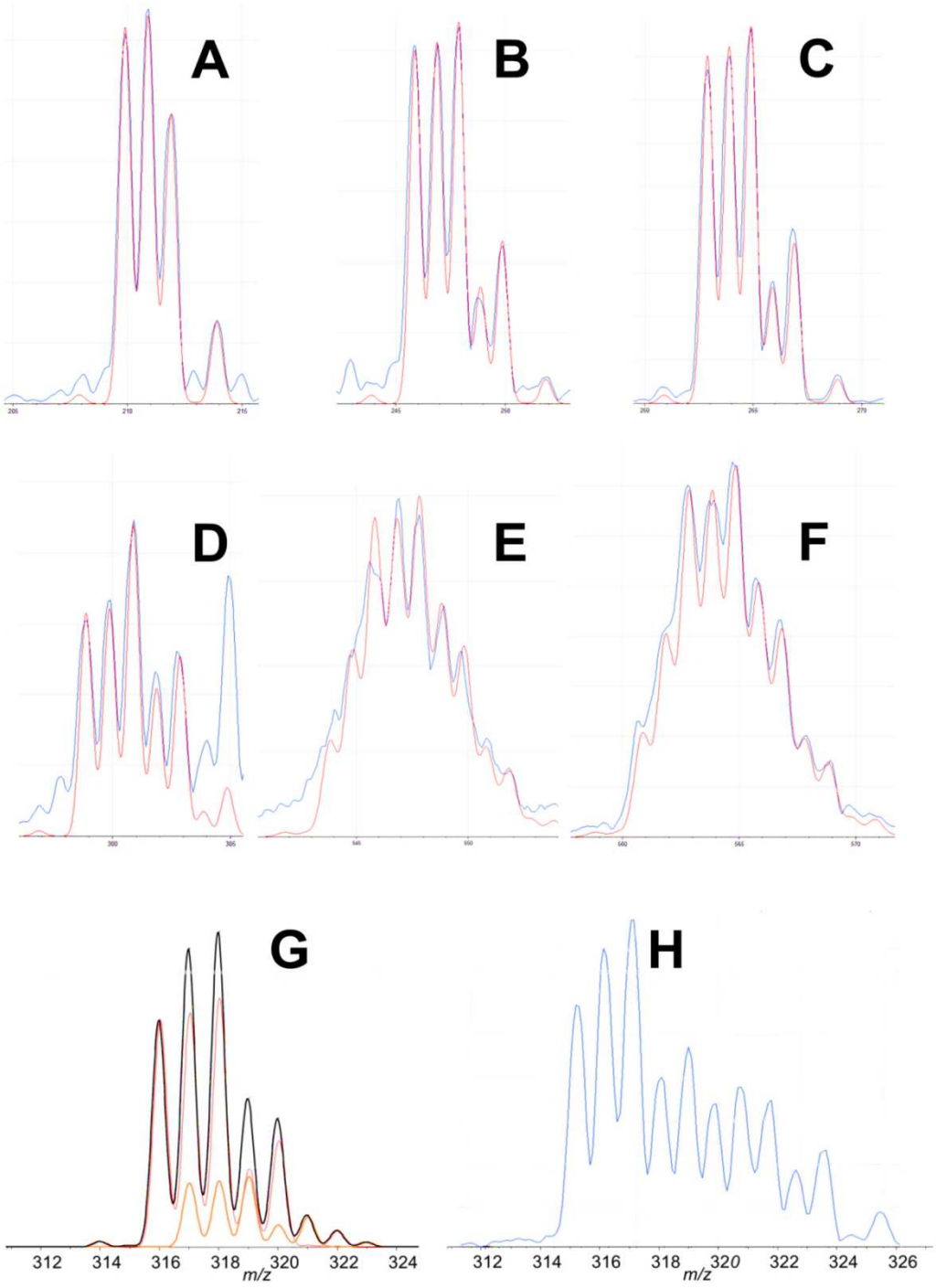

Fig. S2. Calculated (red line) and experimental (blue line) isotopic pattern for (**A**) $[Pt(NH_2)]^+$ (210 m/z), (**B**) $[Pt(NH_3)Cl]^+$ (246 m/z), (**C**) $[Pt(NH_3)_2Cl]^+$ (263 m/z), (**D**) $[Pt(NH_3)_2Cl_2+H^+]^+$ (300 m/z), (**E**) $[Pt_2(NH_3)_3Cl_3]^+$ (547 m/z), (**F**) $[Pt_2(NH_3)_4Cl_3]^+$ (547 m/z). Calculated pattern (**G**, black line) as a sum of $[Pt(NH_3)_3(H_2O)_2Cl]^+$ (78%, red line) and $[Pt(NH_3)_2(H_2O)_3Cl]^+$ (22%, orange line) and experimental data (**H**, blue line) in 314-320 m/z range.

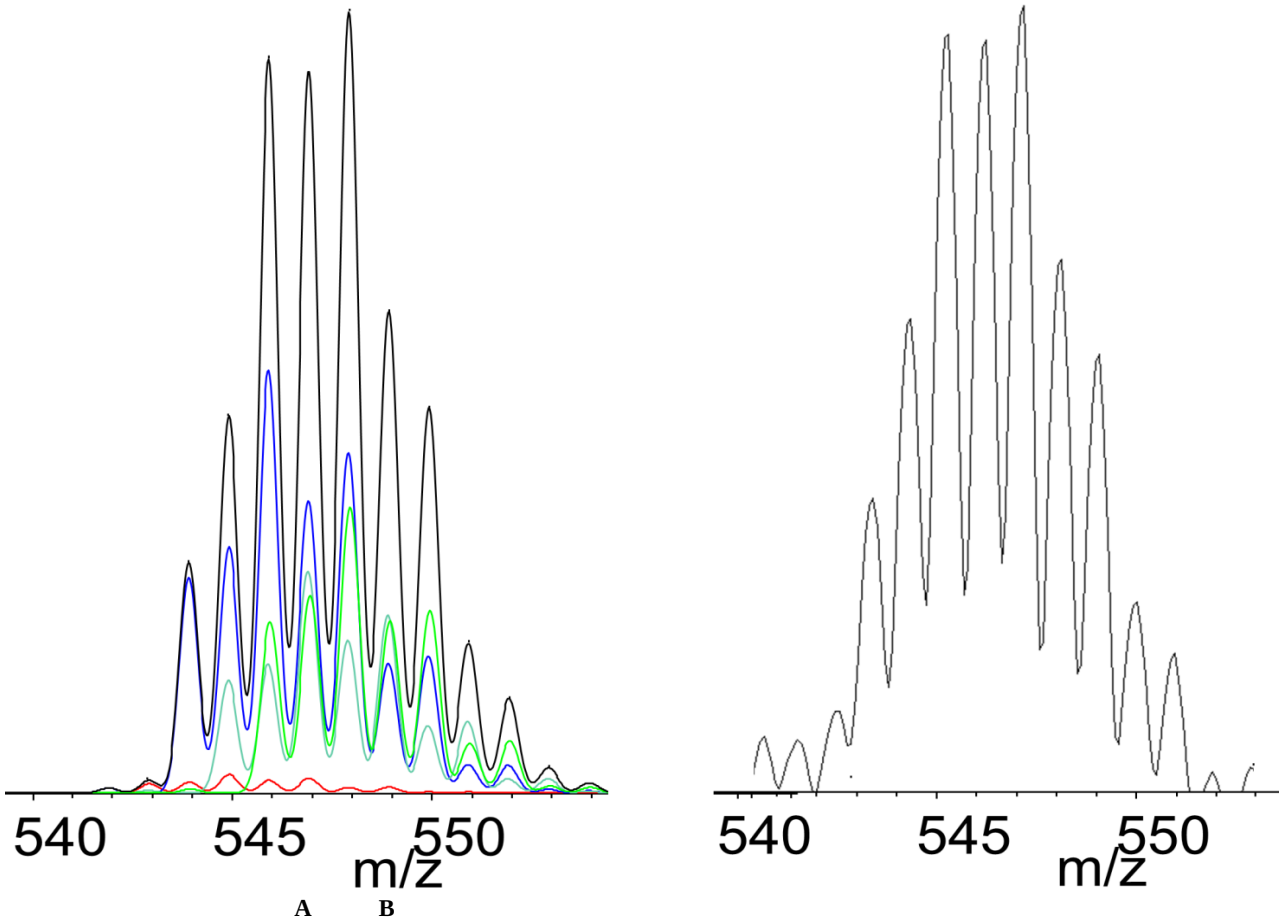

Fig. S3. Theoretical (**A**) and experimental (**B**) isotopic pattern for signal centered at 547 m/z. The signal is due to a mixture of $[Cu(phen)Cl_2Pt(H_2O)F]^+$ (46 %, blue line), $[Cu(phen)ClPt(H_2O)_2F_2]^+$ (28 %, green line), $[Cu(phen)Cl_2PtF_2]^{*+}$ (24 %, cyan line) and $[Cu(phen)Cl_2Pt(H_2O)_2]^+$ (2 %, red line).

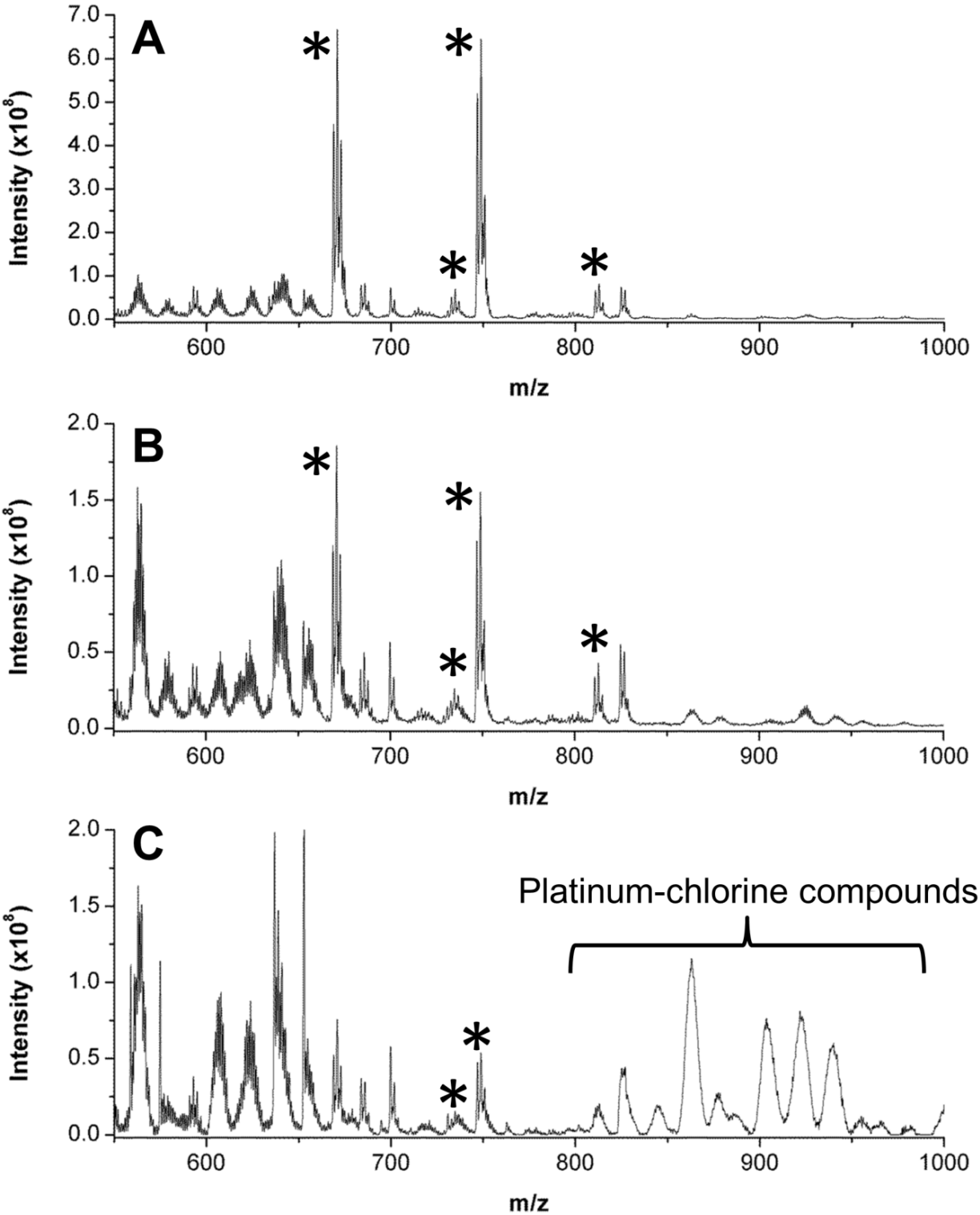

Fig. S4. ESI mass (+) spectra of cisplatin and **2** at 1:1 (**A**), 5:1 (**B**) and 10:1 (**C**) platinum/copper molar ratios (concentration of cisplatin is 0.5 mM, 50:50 methanol and water with 0.05 % of trifluroacetic acid). In the spectra copper complexes are marked with "*", polynuclear complexes containing two or more platinum ions and a variable number of chlorine, ammonia and water molecules are also pointed out.

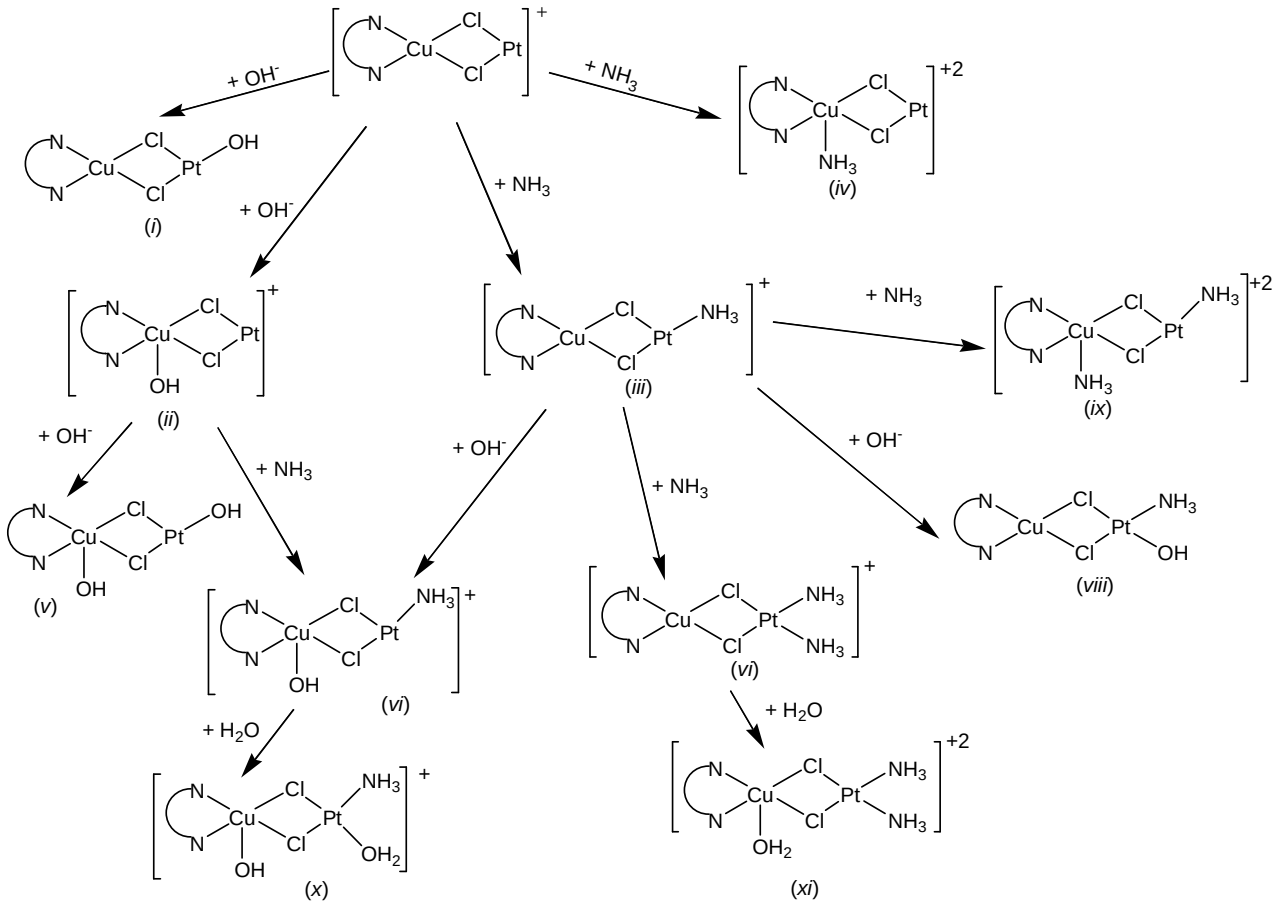

Fig. S5. A description of the possible structures as obtained from the tandem MS-MS experiments on the parent ion at 560 m/z.

Table S1. List of the species containing copper and platinum identified from the ESI-MS studies

N°	Stoichiometry	m/z
1	$[CuPt(phen)(H_2O)FCl_2]^+$	545
2	$[CuPt(phen)F_2Cl_2]^+$	546
3	$[CuPt(phen)(H_2O)_2F_2Cl]^+$	547
4	$[CuPt(phen)(TFA)(HO)_3(H_2O)]^+$	620
5	$[CuPt(phen)(TFA)(HO)_2(H_2O)_2]^+$	621
6	$[CuPt(phen)(TFA)(HO)F(H_2O)_2]^+$	623
7	$[CuPt(phen)(TFA)(H_2O)_2F_2]^+$	625
8	$[CuPt(phen)(TFA)(H_2O)_3Cl]^+$	640
9	$[CuPt(phen)(TFA)(H_2O)_2ClF]^+$	641

References

(Alphabetical order)

Chou TC, Talalay P, **Generalized equations for the analysis of inhibitions of Michaelis-Menten and higher-order kinetic systems with two or more mutually exclusive and nonexclusive inhibitors.** Eur J Biochem. (1981); 115:207-16.

Eckstein N, **Platinum resistance in breast and ovarian cancer cell lines.** J Exp Clin Cancer Res. (2011); 30:91.

Dhar S, Gu FX, Langer R, Farokhzad OC, Lippard SJ, **Targeted delivery of cisplatin to prostate cancer cells by aptamer functionalized Pt(IV) prodrug-PLGA-PEG nanopaticles.** Proc Natl Acad Sci U S A. (2008); 105:17356-61.

Michels J, Vitale I, Galluzzi L, Adam J, Olaussen KA, Kepp O, Senovilla L, Talhaoui I, Guegan J, Enot DP, Talbot M, Robin A, Girard P, Oréar C, Lissa D,Sukkurwala AQ, Garcia P, Behnam-Motlagh P, Kohno K, Wu GS, Brenner C, Dessen P, Saparbaev M, Soria JC, Castedo M, Kroemer G, **Cisplatin resistance associated with PARP hyperactivation.** Cancer Res. (2013);73:2271-80.

Pivetta T, Cannas MD, Demartin F, Castellano C, Vascellari S, Verani G, Isaia F, **Synthesis, structural characterization, formation constants and in vitro cytotoxicity of phenanthroline and imidazolidine-2-thione copper(II) complexes.** J Inorg Biochem. (2011); 105:329-38.

Pivetta T, Isaia F, Verani G, Cannas C, Serra L, Castellano C, Demartin F, Pilla F, Manca M, Pani A, **Mixed-1,10-phenanthroline-Cu(II) complexes: synthesis, cytotoxic activity versus hematological and solid tumor cells and complex formation equilibria with glutathione.** J Inorg Biochem. (2012); 114:28-37.

Rixe O, Ortuzar W, Alvarez M, Parker R, Reed E, Paull K, Fojo T, **Oxaliplatin, tetraplatin, cisplatin, and carboplatin: spectrum of activity in drug-resistant cell lines and in the cell lines of tha Natinal Cancer Institute's Anticancer Drug Screen panel.** Biochem Pharmacol. (1996); 52:1855-65.

Part II – Studies on the prion structure and pathogenesis of prion diseases

Introduction

Transmissible Spongiform Encephalopathies (TSEs) or prion diseases are fatal neurodegenerative disorders that include Creutzfeldt-Jakob disease (CJD, in human), bovine spongiform encephalopathy (BSE, in bovines), Scrapie (in sheep and goats) and Chronic Wasting Disease (CWD, in cervids).
The infectious agent, or Prion, of TSEs appears to be composed primarily of an abnormal, misfolded, oligomeric form of the prion protein (PrPSc). PrPSc is formed post-translationally from the normal cellular prion protein (PrPC; Borchelt et al., The Journal of Cell Biology 1990; Caughey et al., J Biol Chem. 1991), a raft-resident protein expressed in cells of many tissues, particularly in neuronal and immune cells (Johnson, Lancet Neurol. 2005; Ramasamy et al., Lancet Infect Dis. 2003). The normal function of PrPc is unclear, although there is increasing evidence to suggest it may be involved in the binding and transport of copper ions and cell survival in the face of oxidative stress (Deleault et al., Proc Natl Acad Sci U S A 2007).
TSEs, which together with Alzheimer's and Parkinson's diseases among many others, are classified as protein-based diseases, are chronic neurodegenerative disorders characterized by a long preclinical phase in which progressive neuropathological events follow one another before any clinical sign is evident. Consequently, relevant results in the clinic will be obtained only if therapy is given to pre-symptomatic, or mildly symptomatic, subjects. At present, the major limiting factor for the achievement of this goal is the lack of early peripheral biomarker(s) signaling the ongoing neurodegeneration (Pani et al., Curr Drug Targets. 2010) that would allow, on the one hand, the early in vitam diagnosis, and on the other, the development of effective drugs that target the aggregation/deposition of the pathogenic protein (Pani et al., Curr Drug Targets. 2010).

The primary structure of PrPC is not different in the pathogenic isoform (PrPSc); the differences between the two isoforms rely instead the their 3D structure. While the 3D structure is well known for many mammalian PrPCs, in the case of the pathogenic forms the conformational analysis and the resulting characterization are hampered due to the unavailability of PrPSc in the crystalline form. Moreover, PrPSc is insoluble and therefore cannot be analyzed by X-ray diffraction and NMR in solution.
Current studies are therefore aimed at: a) understanding the structural changes that the PrPC to PrPSc undergoes in his metamorphosis, essential to identify the mechanism that underlies the process of aggregation; b) the identification of which regions (aa sequences) of PrPC play a key role in enabling its conformational rearrangement into PrPSc; c) the identification of the metabolic/molecular changes that favor/arise as a result of the misfolding/aggregation process in the brain; d) the identification of peripheral biomarkers that would allow the early diagnosis of the disease; e) the design of drugs targeting the misfolding of PrPC and/or the aggregation process of PrPSc.

Chapter I - NMR analysis of metabolic changes in the brains of sheep naturally infected with Scrapie

Reasearch rational / Aims of the project

The interaction between PrPC and PrPSc occurs in specific regions of the plasma membrane rich in cholesterol and sphingolipids named raft domains, and is therefore affected by the cholesterol content. Lipid rafts act as organizing centers for various cellular processes, including membrane trafficking and membrane-protein functions.

During the first phase of Scrapie disease, sheep appear clinically healthy. Following a 2 year-long incubation time, the onset of clinical Scrapie is associated with diffuse PrPSc deposition, neuronal vacuolation, astrocytosis and microglia activation in the CNS (Prusiner, Proc Natl Acad Sci U S A. 1998).

All these changes may involve changes in the affected tissues, and in the level of brain metabolites and molecules. Determining the metabolite and molecule modifications in the asymptomatic and symptomatic phases of the disease might thus help to clarify some of the molecular mechanisms of the pathogenesis of prion diseases. Alterations of cellular metabolites have been studied by means of low resolution Magnetic Resonance Spectroscopy (MRS) in *in vivo* and *ex vivo* mouse brains and by High Resolution Proton Nuclear Magnetic Resonance (1H NMR) in brain extracts (Tsang et al., J Proteome Res. 2006; Holmes et al., NeuroRx. 2006; Broom et al., Neurobiol Dis. 2007).

Studies in brains of mice and in neuronal murine cell lines experimentally infected with scrapie, revealed the presence of major molecular and biochemical modifications in the cholesterol network (Bach et al., J Biol Chem. 2009; Bate et al., BMC Biol. 2008; Pani et al., Antimicrob Agents Chemother. 2007; Vascellari et al., Lipids Health Dis. 2011). On the other hand, no major differences were reported in the content/composition of fatty acids, polar lipids, neutral lipids, phospholipids, and plasmalogens in the brain of scrapie-infected mice and hamsters (Pamplona et al., Free Radic Biol Med. 2008; Guan et al., J Neurochem. 1996; Dees et al., J Gen Virol. 1985; Heitzman and Skipworth S, J Neurochem. 1969).

In a previous work from my lab, in an attempt to identify a lipid profile linked to prion ailments, brain extracts of three groups of Sarda breed sheep, i.e. uninfected (healthy), scrapie-affected (symptomatic, I/sympt), and scrapie-infected asymptomatic (I/asympt), all coming from the same farm hit by Scrapie, were analyzed for the lipid composition by gas chromatography(GC) and high performance liquid chromatography (HPLC) methods. GC fatty acid data were studied by means of multivariate statistical analysis (MVA), and the unsupervised Principal Component Analysis (PCA) was applied to picture the fatty acid profiles of healthy and infected sheep.

Although the results of the study failed to reveal severe alterations in brain lipids among the different groups, some interesting differences were observed in the I/sympt group vs. healthy and I/asympt groups; these latter two showing similar lipid characteristics. Interestingly, however, the analysis revealed abnormalities in the brain FA unsaturation of the I/sympt animals, indicating the loss of many crucial membrane-associated functions in the clinical stage of disease. An alteration of the FA unsaturation in cell membrane has also been reported by others in a variety of other pathological states, including neurological diseases (Ariyama et al., J Biol Chem. 2010).

The observed increase in the cerebral saturated fatty acids provides a rough indication of presumed alterations in lipid raft domains of nervous cells during scrapie, suggesting that they may exist in a notable viscous liquid-ordered state. Such physicochemical alteration would have a profound impact on the raft thermodynamic properties, its spatial organization, signal transduction, and raft-resident protein functions and trafficking, all potentially relevant for the generation of prion.

In an attempt to identify a metabolite profile linked to prion ailments, we then analyzed and compared by means of ^{1}H NMR spectroscopy coupled with different MVA, the pool of hydro-soluble low molecular weight compounds in the brain hydro-soluble extracts of the Sarda breed sheep, previously investigated in terms of lipids. The results we obtained show that clinically scrapie-affected sheep have a different brain metabolite profile compared to the healthy ones, while the asymptomatic scrapie-affected animals, although more similar to the healthy group, have also their own metabolite features. The results of this study are fully described in the manuscript attached below (accepted April 2015 in Molecular BioSystems. Doi: 10.1039/C5MB00138B.
http://pubs.rsc.org/en/content/articlepdf/2015/mb/c5mb00138b?page=search). Worth to mention is that, to our knowledge, this is the first metabonomic study performed in sheep naturally infected with scrapie.

^{1}H NMR brain metabonomics of scrapie exposed sheep

Paola Scano[1]*, Antonella Rosa[2], Alessandra Incani[2],Caterina Maestrale[3], Cinzia Santucciu[3], Daniela Perra[2],Sarah Vascellari[2],Alessandra Pani[2],Ciriaco Ligios[3]

[1]Department of Chemical and Geological Sciences, University of Cagliari, Monserrato, Italy
[2]Department of Biomedical Sciences, University of Cagliari, Monserrato, Italy
[3]Istituto Zooprofilattico Sperimentale della Sardegna, Sassari, Italy

Abstract

While neurochemical metabolite modifications, found by different techniques,have been diffusely reported in human and mice brains affected by Transmissible Spongiform Encephalopathies (TSEs), this aspect has been little studied in the natural animal host with the same pathological conditionso far.Herein, we investigated, by High Resolution ^{1}H NMR spectroscopy and Multivariate Statistical data Analysis,thebrain metabolite profile of sheep exposed to scrapie agent in a naturally affected flock.On the basis of clinical examinations andWestern Blotting analysis for pathological prion protein (PrP^{Sc}) in brain tissues,sheep were catalogued as not infected (H),infected with clinical signs (S), and infected without clinical signs (A).By discriminant analysis of spectral data,comparing S *vs* H, we found a different metabolite distribution, with inosine, cytosine, creatine, and lactate being higher in S than in H brains, while the branched chain amino acids (leucine, isoleucine, valine), phenylalanine, uracil, tyrosine, gamma-amino butyric acid, total aspartate (aspartate+N-acetylaspartate) being lower in S. By a soft independent modelling of class analogy approach, 1 out of 3 A samples wasassigned to H class. Furthermore, A brains were found to be higher in choline and choline-containing compounds. By means of Partial Least Squares regression, an excellent correlation was found between PrP^{Sc}amount and ^{1}H NMR metabolite profile of infected (S and A) sheep, the metabolite mostly correlated with PrP^{Sc} wasalanine. The overall results, obtained by different chemometric tools, were able to describe a brain metabolite profile of infected sheep with and without clinical sign, compared to healthy ones, and indicated alanine as a biomarker forPrP^{Sc}amountsin scrapie brains.

Introduction

Scrapie is a fatal neurodegenerative disease that affect sheep and goats. This disease belongs to the Transmissible Spongiform Encephalopathies (TSEs), or prion diseases,a group of pathologic conditions that includes bovine spongiformencephalopathy (BSE) of cattle, chronic wasting disease (CWD) ofdeer, Creutzfeldt-Jakob disease (CJD), and variant CJD (vCJD) in man[1]. TSEsconsist in the deposition, within the central nervous system (CNS) and in anumber of peripheral nervous and lymphoid tissue districts, of the pathologicalisoform (PrP^{Sc}) of a normal host protein ("*prion protein*", PrP^{c}) [1].Studies in rodent models and field observations in sheep suggested that the classical scrapie agent enters into the host's body through the mucosa of the ileal tract of the gut, with thefirst PrP^{Sc} deposition being observed in Peyer's patches (PPs) and then in other districts of the lymphoreticular system (LRS) [2].From theLRS, prions enter inside the CNS through the sympathetic and parasympathetic fibers of the autonomic nervous system, with the first appearance of PrP^{Sc} deposition at the level of the *nucleus parasympathicus nervi vagi* (NPNV) and the intermedio-lateral (IML) cell column of the thoracic spinal cord [3].During the lymphoid spreading of PrP^{Sc} and its early phase of neurodeposition, sheep appear clinically healthy. Following a 2 years-long incubation time, onset of clinical scrapie is associated with diffuse PrP^{Sc} deposition, neuronal vacuolation, astrocytosis and microglia activation in the CNS[1]. All these changes result in complex alterations of cellular metabolites that have been studied by means of low resolution Magnetic Resonance Spectroscopy (MRS) *in vivo* and *ex vivo* brains and tissues and by High Resolution Proton Nuclear Magnetic Resonance (^{1}H NMR) in brain extracts [4-6]. In our previous work, analyzingby different techniques lipid composition in brain extracts from healthy and naturally scrapie infected sheep it was observed a significant enrichment in symptomatic- sheep brain of saturated fatty acids, which may affect thermodynamic properties and phase behavior of neuronal membranes [7].

"Metabonomics" has been defined as the "understanding the metabolic responses of living systems to pathophysiological stimuli *via* multivariate statistical analysis (MVA) of biological NMR spectroscopic data"[8].MVA is apowerful tool that allows to extract qualitative andquantitative information from large data sets.Among MVA, qualitative techniques as cluster analysis,principal components analysis (PCA), soft independent modelling of class analogy(SIMCA)are aimed at find similarities and dissimilarities among samples. For sample classification and biomarker identification,discriminant analysis (DA) are more appropriate. Among regression techniques, Partial Least Squares (PLS)can be used to linearly correlate multivariate data with measured response. Multivariate statistical approaches, differentlyfrom univariate tests, takingintoaccount correlations among variables,highlightall the concomitant changes of metabolites, thus giving a more amplepicture of biomarker candidates and a more robust classification.

In this work, in the attempt to identify a metabolite profile linked to prion ailments, we studied,by means of ^{1}H NMR spectroscopy coupled with different MVA,the pool of hydro-soluble low molecular weight compounds in brain extractsfrom Sarda breed sheep exposed to scrapie agent in a historically affected flock. To accomplish this goal, brains were collected from healthy (H), scrapie-infected symptomatic (S), and infected asymptomatic (A) sheep.Modifications of brain metabolite profile were correlated with PrP^{Sc} deposition,as measured by WB analysis, in brains of the affected animals.

Material and Methods

Sheep selection, scrapie diagnosis and brain treatments

Ascrapie-affected Sarda sheep flock, located in Sardinia (Italy), was studied.The flock was randomly selected among those with high incidence of clinical scrapie. After notification of clinically suspect cases, inside the context ofpassive surveillance for scrapie,presence of the diseasein the flock was assessed by conventional protocols. In this flock, inside the framework of appropriate actions for

eradicating scrapie, all the susceptible animals, with or without clinical signs, were euthanized. Whole brains were removed by standard necropsy procedures as soon after death as possible. Collected brains were divided into two hemi-parts by a medial cutting before being frozen at −80◦C. One half underwent Western Blotting (WB) examination [9] and PrP^{Sc} relative quantification. Eighteen brains were selected, based on WB results they were classified as follows: n=7, PrP^{Sc} negative, as healthy (H-1 to H-7);among 11 PrP^{Sc} positive,when clinical signs were previously reported they were classified as symptomatic (n= 8, from S-1 to S-8), otherwise asymptomatic (n=3, from A-1 to A-3).The second half brain wasweighed and immediately homogenized in ice for 2 min in saline solution, 1:1 weight:volume, using an ultra Turrax blender. Aliquotsof homogenates werestored at −80◦C.

Extraction of the water-soluble low molecular weight components

For each brain threealiquots were submitted to extraction. The low molecular weight water-soluble components were extracted from homogenized brain samples using a solution of $CHCl_3$/MeOH/H_2O (2/1/1 v/v/v) according to the Folch method [10]. Briefly, 12 ml of $CHCl_3$/MeOH were added to brain homogenates (500 mg of wet brain/ml of saline solution). After 1 h, 3 ml H_2O were added in order to solubilize the hydrophilic components. After centrifugation at 900*g* for 1 h, the H_2O/MeOH mixture, containing the water soluble low molecular weight components, was separated from the $CHCl_3$ phase, that contains the lipid fraction. The water soluble phase (4 ml) was dried by rotor vacuum and redissolved in 600 µl of D_2O. From each brain, three samples were prepared for NMR analysis.

^{1}H NMR experiments

^{1}H NMR spectrawere recorded at 499.839 MHz, using a Varian UNITY INOVA 500 spectrometer (Agilent Technologies, CA, USA). Experiments were carried out at 300K,with an acquisition time of 3 s, 20 s relaxation delay,a 90° pulse, and 128 scans.For suppression of residual water resonance, the 1-D NOESY pulse sequence with a mixing time of 1 ms was applied. To the free induction decays (FID) a zero-filling to 128K and a line broadening of 0.3 Hz were applied.Chemical shifts were referred to theresonance of the standardsodium 3-trimethylsilyl-propionate-2,2,3,3,-d_4 (TSP) set at 0.00 ppm. Assignment of signals to metabolites was based ondata reported in the literature[11-14],and with the aid of 2D NMR experiments. FID processing, manual phasing, baseline correction and area integration were performed usingMestReNova program (Version 7.1.2. Mestrelab Research S.L.).

Data pre-treatment and multivariate statistical data analysis

Spectral data pre-treatmentswereperformedto make the samples comparable and the overall data suitable for statistical analysis. To overcome dilution problems, within each sample the integrated area of the spectral regions of interest was reported as percentage of the total integratedareas. The resulting data matrix **X**, in which the rows are samples and columns the spectral integral values (as mean over three spectra from as many as extracts for each brain) was imported into the SIMCA-P+ program (Version 13.0, Umetrics, Sweden), and mean centered and scaled to unit variance, column wise. When distribution of a variable presented Skewness, column wise, it was log-transformed.

The multivariate statistical approaches for data analysis here employed were: (i) the unsupervised PCA for sample distribution overview, where information regarding class membership are not given. PCA results were graphically reported in the score plots where samples are projected in the multivariate space; (ii) the supervised Partial Least Square - Discriminant Analysis (PLS-DA) and its Orthogonal variant (OPLS-DA)for classification and identification of the most discriminant variables that characterize classes. In the 2-classes OPLS-DA, the between classes variance is expressed in the first component, further orthogonal components are irrelevant to the discrimination, this is of particular interest when a high intra-class variability exist [15]. PLS-DA model quality was evaluated on the basisof the parameters R^2Y(goodness of fit) and Q^2Y(goodness of prediction, determined through cross validation), and tested for overfitting by permutation test (n=400), as implemented in the SIMCA program.Results of two OPLS-DA models can be depicted in theSUS-plot (Shared and Unique Structures–plot), this is a 2D scatter plot of the loading correlation vectors of the predictive components of the two separate models [16]; (iii) the supervised classification technique Soft Independent Modelling of Class Analogy (SIMCA) to classify samples as belonging to an already givenclass,forwhich they show the largest similarity. In contrast to other supervised pattern recognition techniques (PLS-DA for example), SIMCAis a more versatile approach (soft modeling) which allows the classification of a sample in one or moreclasses, or in none of them, while discriminant techniques (hard modelling) only allows to classify a sample in a singleclass.In SIMCA, for each class of samples a PCA is performed, where the appropriate number Principal Components (PCs) to be included isbased on the cross-validation procedure, in fact, although the variance explained by the PCA model (R^2X) increases with additionalPCs, the analogous in cross-validation, expressed by Q^2X,does not continuouslyincrease with incremental PCs, indicating, at a certain point, that the addition of more PCs into the model will only add noise. SIMCA results were plotted as Cooman's plot, it provides the orthogonal distance from samples to be classified to two selected PCA classes. The critical cut-off class membership limits are also reported,they define distance of samples from each PCA class model,if a sample belongs to a predefined class it should liewithin its boundaries. PLS regression is used to find linear relations between a set of independent variables (**X**) and ameasured variable (**y**). This technique uses measured properties, to constructmodels, often based on minimaldifferences between similar samples, that seek regularities in variable changes linked to the measured property under study. The orthogonal variation of PLS (OPLS) separates the systematic variation in X into two parts, one part that is correlated (predictive) to **y** and the other is uncorrelated (orthogonal) to **y**. [17].

PrP^{Sc} quantification in brain

To determine the relative amount of PrP^{Sc}/ µg inthe whole brain of asymptomatic and clinically scrapie sick sheep, we compared the intensity of the WB signals of each brain to a standard curve generated from WB signals of serial naturally-scrapie-infected brain dilutions.To this purpose we used a WB procedurein which the quantification of the total loaded brain proteins was performed with the BCA Protein Assay Kit (23-225 BCA™ Protein Assay Kit, Pierce) and the intensity of the WB signals of the typical PrP^{Sc} bands were captured and quantified by densiometric analysis using a Chemidoc Imager System (BioRad)[18].

Ethics statement

The protocol used for the slaughtering procedures involving the sheep investigated herein was officially approved by the Service for Animal Welfare of the Istituto Zooprofilattico Sperimentale della Sardegna according to the guidelines n. I 09 044, in tight agreement with the guidelines of Italian National Law n. 116/1992. Sheep were humanely euthanized with a barbituate solution, followed by injection of 4 ml of embutramide and mebenzonic-iodide (Hoechst Roussel Vet, Italy).

We declare that the study was carried out on private animals under the request of the owners and all sheep were institutionally examined in the framework of the scrapie surveillance plan, thereby no permission from an ethics committee was needed. The Istituto Zooprofilattico Sperimentale della Sardegna has been commissioned by Italian Health Ministry to carry out all the analysis related to the regional scrapie surveillance plan.

Results

^{1}H NMR experiments

The ^{1}H NMR technique was applied to study the brain metabolite profile of infected and healthy sheep. The ^{1}H NMR spectra of the aqueous phase of brain extracts are characterized by sharp peaks assigned to functional groups of low molecular weight metabolites found in a free state. A representative ^{1}H NMR spectrum of brain extract is shown in Fig.1, whereit has been divided intwomain spectral regions having different intensities. The first, Fig.1A, from 0.5 to 5.0ppm, contains signals from the aliphatic groups of free amino acids and derivatives, including the three branched chain amino acids (BCAA: valine, leucine, isoleucine), glutamine (Gln), alanine (Ala), aspartate (Asp), N-acetylaspartate (NAA),gamma-aminobutyric acid (GABA),taurine (Tau); signals of organic acids such as lactate (Lac) and acetate (Ace), the trimethylamine group of choline and choline-containing compounds: 3-glycero-phosphocholine/phosphocoline (Chol), *myo*-inositol (MI), and creatine (Crt).In the spectral portion between 5.5 and 9.0 ppm, Fig.1B, resonate less intense signals, attributed to the aromatic protons of amino acids such as tyrosine (Tyr), phenylalanine (Phe), and of nucleosides and nucleobases such as uracil (Ura), cytosine (Cyt), inosine (Ino), and hypoxanthine (Hyp);of nicotinammide adenin dinucleotide (NAD),formate (Form) and fumarate (Fum). Other detected NMR peaks were not unambiguously identified, also due to the possible loss of information, linked to ^{2}H exchange of labile protons [19]. Once the spectra were fully assigned,those areas representative of the most relevant metabolites were measured by means of spectral area integration.Being in the intrinsic nature of ^{1}H NMR spectroscopy to detect, in principle, all hydrogens in a molecule, excluding the fast changing ones, several metabolites, such as MI, exhibit resonances in different regions of the spectrum, taking into consideration this observation, areas to be integrated, diagnostic of a single metabolite, were carefully chosen among those being not overlapped and baseline well resolved. Results arereported in Table 1. Seldom, when the 3different extracts of the same brain were examined,quantitative differences ofNAA and its hydrolysis products:N-Ace (N-acetyl) and Asp were observed. Quantitative analysis of the 3 compounds indicated that, to a certain extent, hydrolysis of NAA has takenplace [20-21]during samplehandling.Considering the reported relevance of NAA in brain diseases [5,22] to do not lose these information and to, on the other hand, overcome this bias, these molecular componentswere considered as an unique variable, therefore NAA (2.67 – 2.65 ppm) and Asp (2.83 – 2.76ppm) normalized integrals were summed up and the new variable was named Asp-tot;analogously, Ace-tot was obtained by summingup N-Ace (singlet at 2.01 ppm) and Ace(singlet at 1.91 ppm) integrals.Following these proceduresfor each brain a total of 24 variables (reported as means over 3 extracts) ready for MVA were obtained.

Data set overview by PCA

At a glance, no spectral differences weredetectablebetween the ^{1}H NMR spectra of healthy and infected symptomatic as well as asymptomaticbrain extracts. To extractthe information, in terms of similarities and dissimilarities of samples based on metabolite characteristics, contained in the set of spectra,a PCA of the spectral data(20 samples and24 variables) was performed.The first twoPCs described 59% of the variance and no outliers were detected. From the analysis of the score plot PC1 *vs* PC2, shown in Fig.2, it can be seen that S samples lie, although scattered in two groups, in the left side of the plot, while H and A samples, that tend to cluster, are projected in the right side. The results of this unsupervised analysis showed that the healthy and infected brains had different metabolite profiles, and that A brain samples shared common features with the H ones.

Discriminant analysis for metabolite identification of H *vs*S samples

The results of the PCAshowedthat the H and Ssamples had different metabolite profiles and that the S samples presented a higher intra-class variability. To find thosemetabolitesthat discriminate the different classes of samplesan OPLS-DA was performed on 2 sample classes, H *vs*S. Thisproduced a 2 componentsvalidated model with $R^2Y = 0.94$ and $Q^2 = 0.89$, indicating a good fitting and a good classification power. Loading values along the predictive component were studied to attribute discriminant metabolites to each class. Results are reported in Table 2, whereonly the most important metabolites, i.e. those having the highest loading values that indicate a higher importance (weight) of the variable in discriminating sample class, are reported.The most discriminant variables were found to be Ino, Cyt, Crt, andLac, up regulated in S samples, while Asp-tot, GABA, Tyr, Ura, Phe, and BCAA were down-regulated.

Characterization of A samples

The PCA score plot of Fig. 2 showed that H and A samples clustered. To deeper investigate the characteristics of A samples, although numerically very limited, we performed further MVA.SIMCA was used for predicting class belonging of A samples with regard to H and S classes and results visualized in the Cooman's plot reported in Fig.3, where the multivariate spaces pertinent to H and Sclasses are shown.This showed that all the S and H samples were placed in their class membership zone. One (A10) out of the 3 infected

asymptomatic samples projected into this space, was classified as healthy, while the remaining 2, as not lying within the boundaries of any of the 2 (H and S) predefined classes, were classified to neither of the 2 classes.
With the aim of finding thosemetabolites that characterize the A class of sampleswe performed and cross-compared results of two pair wise OPLS-DA models: "H *vs*A", and "H *vs* S", that were satisfactorily validated ($R^2Y = 0.97$ and $Q^2Y = 0.62$; $R^2Y = 0.94$ and $Q^2Y = 0.89$, respectively). The results,in terms of loading values, are showed as SUS-plot (Fig.4). It is clearly visible that Chol was the variable that mostly characterized the A samples. It is worth reminding that Chol variable comprises metabolites predominantly involved in choline phospholipid metabolism (choline, phosphocholine and glycerol phosphocholine) [12]. The two classes of infected samples (S and A) shared the metabolite Ino. Metabolites up-regulated in A samples are reported in Table 2.

PrP^{sc}amounts and correlation with spectral data by PLS regression

The WB analysis, applied to the brain samples of infected symptomatic and asymptomatic sheep, revealed the same PrP^{Sc} molecular signature, thus suggesting that the same scrapie agent was involved in all the examined affected sheep. PrP^{Sc} deposition was demonstrated in all the examined brains of S and A sheep and data reported in Table 3 and(Fig. 5).The PrP^{Sc}amounts weregenerally higherin the Ssheep compared to those in A sheepalthough Student's *t* test indicated that means are not statistically different.To ascertain whether the metabolite profile of brains is linked to PrP^{sc} quantities, we performed anOPLS regression on NMR data with PrP^{sc}amount as response. Qualityof the OPLS regression model washigh satisfactory (1+2 components, $R^2Y=0.997$ and $Q^2Y=0.87$), thus indicating that there were modifications in the metabolite profile strongly linearly linked to PrP^{sc}amounts. In Table 4 we report the metabolites having the strongest (either positive or negative) correlation with PrP^{sc}levels. Result of *t*-test on Ala data of infected and healthy samples reject the null hypothesis at $p>0.05$.

Discussion and Conclusions

Our results indicated that clinically scrapie affected sheep have differentbrain metabolite profile compared to healthy ones, while the asymptomatic affected animals, although more similar to the healthy group, have also their own metabolite features.To our knowledge, this is the first metabonomic study performed in naturally infected sheep with scrapie.
In this study, although the number the sheep considered is relatively small, assessing the metabolite profile in the whole brain using ^1H NMR and different MVA,we found different metabolite profiles in H, S, and A sheep.As results of the OPLS-DA "S *vs* H" and, as shown in the SUS-plot, Ino is the metabolite having relative higher level in the infected sheep (S and A) when compared with the healthy ones.Cyt, Crt, Lac are discriminant of S samples, and as we can see in the SUS-plot, choline and choline containing compounds(phosphocholine and glycerol phosphocholine) characterized the A samples.Healthy brains were characterized by higher relative levels of BCAA, Phe, Ura, Tyr, GABA, and Asp-tot. It is interesting to note that, correlating the metabolite profiles to the PrP^{Sc}amounts, Ala was the most important metabolite, having the strongest positive correlation with PrP^{Sc}amount. GABA, Ura, and Asp-tot werethose metabolites that both were inversely correlated with PrP^{Sc} levelsand discriminated H samples.
We found a higher levelof Lac in the extracts of Sbrains when compared to the H ones. It, generally,indicates a more intense anaerobic metabolism which can be observed under hypoxic/anoxic stress situations affecting the brains or other organs and can indicate ischemic processes and apoptosis. Being not significantlycorrelated with PrP^{sc}amounts, it can be hypothesizethat increase of Lacis a sign of general sickness althoughnot specifically linked toPrP^{sc}generation. Ino was found to be in relatively higher quantity in S and A brains, it is the breakdown product of ATP, it is formed by deamination of adenosine, mainly at high intracellular concentrations, which are associated with hypoxia, ischemia and other forms of cellular stress [22]. Crt is higher in S brains and also correlated with PrP^{sc}. Crt is thought to have a multifaceted role in the brain. Besides being involved in brain osmoregulation, it has recently been implicated in energy homeostasis and direct antioxidant effects [24,25]. Furthermore, Crt plays an integral role in cellular energy metabolism, and thus an increase in concentration of this compound may be a result of metabolic stress. Dysregulation of Crt may implicate an energetic shift in the brain, suggesting an increased metabolic activity and/or a depletion of energy storage capacity [22, 24].Crt has several potential neuroprotective effects [25], including buffering intracellular mitochondrial energy reserves, stabilizing intracellular calcium, and inhibiting activation of the mitochondrial permeability transition pore, which have all been linked to apoptotic and oxidative cell death [27]. Asymptomatic samples are characterized by choline, phosphocholine and glycerol phosphocholine. Choline is an essential nutrient with a complex role in the body. It is required for synthesis of the neurotransmitter acetylcholine and of phosphatydilcholine the major constituent of membranes [11]. It is also involved in cell-membrane signaling (phospholipids), lipid transport (lipoproteins), and methyl group metabolism (homocysteine reduction)[28]. In MRS, choline is a marker of cellular membrane turnover, and is therefore elevated in neoplasms, demyelination and gliosis. Phosphocholine, that contributes to the choline resonance, may act as a biomarker for membrane phospholipid metabolism/turn over [29].Choline is also a constituent of sphingolipids that participate to the formation of the lipid rafts where the GPI protein is anchored. Naslavsky [30]reported that in neuroblastoma cells infected with prions, sphingolipid depletion increases formation of the PrP^{Sc}. Deregulation of sphingolipids metabolism in Alzheimer's disease has also been reported [31]. Choline biomarker in A brains could be an early sign of brain cellular membrane damage due to lipid raft formation and protein anchorage.Amino acids play important function as neurotransmitters providing both excitatory and inhibitory stimuli. Here, we found that the amino acid levels of Asp-tot, Tyr, Phe, BCAA are lower in the brains ofS sheep. This may be the consequence of the neurodegenerative phenomena affecting pre- and post-synaptic processes, a commune pattern observed in distinct brain regions when exposed to prion [32] or to beta-amyloid olygomers in Alzheimer's disease. The loss of a selective subpopulation GABAergic neurons has been demonstrated in experimentally prion infected mouse [33]by detecting immunohistochemically the glutamic acid decarboxylase, the GABA synthesizing enzyme. This correlates well with our observation of lower level of GABA in the S brains when compared to H. Moreover, the lower GABA levelseems to be relegated to the clinical stage of scrapie, as being not observed as discriminant in the asymptomatic sheep. In this respect, a decrease of the GABA activity has been observed at the clinical stage in scrapie infected hamster [34].Asp-tot (comprising NAA and Asp) level is lower in S and A sheep. Decrease of NAAis a finding already described also at earlier stages of disease in murine model after experimental prion infection [6]. NAA is an abundant metabolite which is present only in neurones in the adult brain, and although its role in the cell is little know, it is widely considered to be a marker of functional neurons. [6].A lower level of Urahas been observed in brains of symptomatic sheep when compared to the healthy ones. Although little is known on the neuronal functions of Ura,it has been suggested that it modulates many neurotransmitters or

neuromodulators, especially in the mature central nervous system [35]and its glycosylated form, Uridine, has been proposed as neuroprotectiveagent in neurodegenerative disorders [36].Ala was the metabolite more strongly linked to PrP^{sc} amount in scrapie sheep brains. Ala has been indicated as a biomarker of apoptosis and/or cellular stress processes in brain, which are both normally observed in scrapie neuropathology [37]. In addition, increase of Ala has been observed also in meningioma and following ischemia [38], as well as concentration of plasma Ala was significantly increased ($P < 0.05$) in infected BSE dairy cattle [39].
Among the biases that could affect the reliability of our results, the potential presence of different scrapie agent strains implicated in our cases should be taken into account. In general, neuropathological changes, including PrP^{Sc} molecular signature and its regional distribution in the brain, are strictly related to the TSE agent strain involved and to the PrP genotype of the host, thus these differences related to the host might influence the ^{1}HMRS neuro-metabolic profile [40]. Our study has the advantage that all cases belong to the same flock, and only one identical molecular signature was found among the different examined cases. In addition, it is worth to recall that only one identical scrapie agent strain has been found in Italy so far [41].

The approach here described was able to identify different metaboliteprofilespertaining to healthy and infected sheep brains, physiopathological roles of metabolitesmainly involved may explain their different expression in these two extreme situations. Determining the metabolite modifications in the asymptomatic and symptomatic phases of the disease might clarify some of the molecular mechanisms of the prion disease and disease progression. As in previous studies, our findings confirm the close relationship between scrapie and other neurodegenerative diseases, although to compare ruminant brain metabolites to human's can be, to some extent, hazardous.This study concerns*in vitro* analysis of the whole brain, whereas the pathology onsete widespread has specific neuroanatomical locations,in this respect, future investigations will be dedicated to the study of metabolite fingerprint in different affected areas.

Acknowledgement

We thank Prof. E. d'Aloja for helpful discussion and Dr. M.G. Cancedda for sheep brains recruitments.
D. Perra gratefully acknowledges Sardinia Regional Government for the financial support of her PhD scholarship (P.O.R. Sardegna F.S.E. Operational Programme of the Autonomous Region of Sardinia, European Social Fund 2007-2013 - Axis IV Human Resources Objective l.3, Line of Activity I.3.1).

Funding

This study was supported by grants from the Regione Autonomadella Sardegna (L.R. n◦7/2007, call 2008) .

References

1. Prusiner SB (1998) Prions. Proc Natl Acad Sci USA 95: 13363-13383.
2. Andréoletti O, Berthon P, Marc D, Sarradin P, Grosclaude J, van Keulen L, Schelcher F, Elsen JM, Lantier F (2000) Early accumulation of PrPSc in gut-associated lymphoid and nervous tissues of susceptible sheep from a Romanov flock with natural scrapie. J Gen Virol. 81:3115–3126.
3. van Keulen LJ, Schreuder BE, Vromans ME, Langeveld JP, Smits MA (2000) Pathogenesis of natural scrapie in sheep. Arch Virol Suppl. 16:57-71.
4. Tsang TM, Woodman B, McLoughlin GA, Griffin JL, Tabrizi SJ, Bates GP, Holmes E (2006) Metabolic characterization of the R6/2 transgenic mouse model of Huntington's disease by high-resolution MAS ^{1}H NMRspectroscopy.J Proteome Res. 5:483-92.
5. Holmes E, Tsang T M, Tabrizi SJ (2006) The application of NMR-based metabonomics in neurological disorders. *NeuroRx, 3:* 358-372.
6. Broom KA, Anthony DC, Lowe JP, Griffin JL, Scott H, Blamire AM, Styles P, Perry VH, Sibson NR (2007) MRI and MRS alterations in the preclinical phase of murine prion disease: association with neuropathological and behavioural changes.Neurobiol Dis. 26:707-17.
7. Rosa A, Scano P, Incani A, Pilla F, Maestrale C, Manca M, Ligios C, Pani A (2013) Lipid profiles in brains from sheep with natural scrapie. *Chemistry and physics of lipids*, 175, 33-40.
8. Nicholson JK, Lindon JC, Holmes E. (1999) 'Metabonomics': understanding the metabolic responses of living systems to pathophysiological stimuli via multivariate statistical analysis of biological NMR spectroscopic data. Xenobiotica 29:1181-9.
9. Ligios C, Cancedda MG, Madau L, Santucciu C, Maestrale C, Agrimi U, Ru G, DiGuardo G (2006). $PrP^{(Sc)}$ deposition in nervous tissues without lymphoid tissueinvolvement is frequently found in ARQ/ARQ Sarda breed sheep preclinicallyaffected with natural scrapie. Arch. Virol. 151: 2007–2020.
10.Folch J, Lees M, Sloane-Stanley GH (1957) A simple method for the isolation and purification of total lipid from animals tissues. J. Biol. Chem. 226,497–509.
11.Govindaraju V, Young K, Maudsley AA (2000) Proton NMR chemical shifts and coupling constants for brain metabolites. NMR Biomed. 13: 129–153.
12.Viola A, Saywell V, Villard L, Cozzone PJ, & Lutz NW (2007) Metabolic fingerprints of altered brain growth, osmoregulation and neurotransmission in a Rett syndrome model. PLoS One, 2(1), e157.
13.Wishart DS, Knox C, Guo AC, Eisner R, Young N, Gautam B, Hau DD, Psychogios N, Dong E, Bouatra S, Mandal R, Sinelnikov I, Xia J, Jia L, Cruz JA, Lim E, Sobsey CA, Shrivastava S, Huang P, Liu P, Fang L, Peng J, Fradette R, Cheng D, Tzur D, Clements M, Lewis A, De Souza A, Zuniga A, Dawe M, Xiong Y, Clive D, Greiner R, Nazyrova A, Shaykhutdinov R, Li L, Vogel HJ, Forsythe I (2009) HMDB: a knowledgebase for the human metabolome. Nucleic Acids Res. 37:603-10.
14.Scano P, Rosa A, Locci E, Manzo G, Dessì MA (2012) Modifications of the ^{1}H NMR metabolite profile of processed mullet (*Mugil cephalus*) roes under different storage conditions. Magnetic Resonance in Chemistry, 50; 436-442.
15.Bylesjö M, Rantalainen M, Cloarec O, Nicholson JK, Holmes E, Trygg J (2006) OPLS discriminant analysis: combining the strengths of PLS-DA and SIMCA classification. Journal of Chemometrics, 20:341-351.

16.Wiklund S, Johansson E, Sjöström L, Mellerowicz EJ, Edlund U, Shockcor JP, Gottfries J, Moritz T, and Trygg J(2008) Visualization of GC/TOF-MS-Based Metabolomics Data for Identification of Biochemically Interesting Compounds Using OPLS Class Models. Anal. Chem. 80:115-122.
17.Eriksson L, Johansson E, Kettaneh-Wold N, Trygg J, Wikstrom C, Wold S (2013) Multi-and Megavariate Data Analysis, 3rd edition; Umetrics Academy, Sweden.
18.Ligios C, Cancedda GM, Margalith I, Santucciu C, Madau L, Maestrale C, Basagni M, Saba M, Heikenwalder M. (2007) Intraepithelial and interstitial deposition of pathological prion protein in kidneys of scrapie-affected sheep.PLoS One12;2(9):e859.
19.Commodari F, Arnold DL, SanctuaryBC, Shoubridge EA (1991) ^{1}H NMR characterization of normal human cerebrospinal fluid and the detection of methylmalonic acid in a vitamin B12 deficient patient. NMR in biomedicine,4:192-200.
20.Ratai, E. M., Pilkenton, S., Lentz, M. R., Greco, J. B., Fuller, R. A., Kim, J. P., He, J., Cheng, L. L. and González, R. G. (2005), Comparisons of brain metabolites observed by HRMAS ^{1}H NMR of intact tissue and solution ^{1}H NMR of tissue extracts in SIV-infected macaques. NMR Biomed., 18: 242–251. doi: 10.1002/nbm.953.
21.Moffett JR, Arun P, Ariyannur PS, & Namboodiri AM (2013) N-Acetylaspartate reductions in brain injury: impact on post-injury neuroenergetics, lipid synthesis, and protein acetylation. *Frontiers in neuroenergetics*, *5*.
22.Baslow MH (2003) N-acetylaspartate in the vertebrate brain: metabolism and function. Neurochemical research, 28: 941-953.
23.Haskó G, Sitkovsky MV, Szabo C (2004) Immunomodulatory and neuroprotective effects of inosine. *Trends in pharmacological sciences*, *25:* 152-157.
24.Pears MR, Cooper JD, Mitchison HM, Mortishire-Smith RJ, Pearce DA, & Griffin JL (2005) High resolution ^{1}H NMR-based metabolomics indicates a neurotransmitter cycling deficit in cerebral tissue from a mouse model of Batten disease. Journal of Biological Chemistry, 280: 42508-42514.
25.Zhang W, Narayanan M and Friedlander RM (2003) Additive neuroprotective effects of minocycline with creatine in a mouse model of ALS. Ann Neurol., 53: 267–270. doi: 10.1002/ana.10476.
26.Lan MJ, McLoughlin GA, Griffin JL, Tsang TM, Huang JTJ, Yuan P, & Bahn S (2008) Metabonomic analysis identifies molecular changes associated with the pathophysiology and drug treatment of bipolar disorder. Molecular psychiatry, 14*:* 269-279.
27.Tabrizi SJ, Blamire AM, Manners DN, Rajagopalan B, Styles P, Schapira AH, Warner TT (2003) Creatine therapy for Huntington's disease: clinical and MRS findings in a 1-year pilot study. Neurology, 61(1):141-2.
28.Zeisel SH, Da Costa KA (2009) Choline: an essential nutrient for public health. Nutrition reviews, 67(11), 615-623.
29.Senaratne R, Milne AM, MacQueen GM, & Hall GB (2009) Increased choline-containing compounds in the orbitofrontal cortex and hippocampus in euthymic patients with bipolar disorder: a proton magnetic resonance spectroscopy study. Psychiatry Research: Neuroimaging, 172: 205-209.
30.Naslavsky N, Shmeeda H, Friedlander G, Yanai A, Futerman AH, Barenholz Y, Taraboulos A (1999) Sphingolipid depletion increases formation of the scrapie prion protein in neuroblastoma cells infected with prions. *Journal of Biological Chemistry*, *274*(30), 20763-20771.
31.He X, Huang Y, Li B, Gong CX, & Schuchman EH (2010) Deregulation of sphingolipid metabolism in Alzheimer's disease. Neurobiology of aging, 31: 398-408.
32.Siskova Z, Reynolds RA, O'Connor V, Perry VH (2013)Brain region specific pre-synaptic and post-synaptic degeneration are early components of neuropathology in prion disease. PLoS ONE 8(1): e55004. doi:10.1371/journal.pone.0055004.
33.Guentchev M, Groschup MH, Kordek R, Liberski PP, Budka H (1998) Severe, early and selective loss of a subpopulation of GABAergic inhibitory neurons in experimental transmissible spongiform encephalopathies. Brain Pathol. 8:615-23.
34.Durand-Gorde JM, Bert J, Nieoullon A (1984) Early changes in tyrosine hydroxylase, glutamic acid decarboxylase and choline acetyltransferase golden hamster striatum after intracerebral inculation of the nigrostriatal system with scrapie agent (263K). Neurosc. Lett. 51: 37-42.
35.Lecca D, Ceruti S (2008) Uracil nucleotides: From metabolic intermediates to neuroprotection and neuroinflammation. Biochemical Pharmacology, 75: 1869-1881, ISSN 0006-2952, doi:10.1016/j.bcp.2007.12.009.
36.Dobolyi A, Juhasz G, Kovacs Z, Kardos J (2011) Uridine function in the central nervous system. Current topics in medicinal chemistry, 11:1058-1067.
37.Schätzl HM, Laszlo L, Holtzman DM, Tatzelt J, DeArmond SJ, Weiner RI, Mobley WC, Prusiner SB (1997) A hypothalamic neuronal cell line persistently infected with scrapie prions exhibits apoptosis. J Virol. 71: 8821-31.
38.Reinke SN, Walsh BH, Boylan GB, Sykes BD, Kenny LC et al. (2013) ^{1}H NMR derived metabolomic profile of neonatal asphyxia in umbilical cord serum: implications for hypoxic ischemic encephalopathy. Journal of Proteome Research 12: 4230-4239.
39.Allison GG, Horton RA, Rees Stevens P, Jackman R, Moorby JM (2008) Changes in plasma metabolites and muscle glycogen are correlated to bovine spongiform encephalopathy in infected dairy cattle. Research in Veterinary Science, 80:40-46. j.rvsc.2006.11.008.
40.Lodi R, Parchi P, Tonon C, Manners D, Capellari S, Strammiello R, Rinaldi R, Testa C, Malucelli E, Mostacci B, Rizzo G, Pierangeli G, Cortelli P, Montagna P and Barbiroli B (2009) Magnetic resonance diagnostic markers in clinically sporadic prion disease: a combined brain magnetic resonance imaging and spectroscopy study. Brain: 132: 2669–2679.
41.Nonno R, Esposito E, Vaccari G, Conte M, Marcon S, Di Bari M, Ligios C, Di Guardo G, Agrimi U (2003) Molecular analysis of cases of Italian sheep scrapie and comparison with cases of bovine spongiform encephalopathy (BSE) and experimental BSE in sheep. J Clin Microbiol 41: 4127–4133.

Metabolites (abbreviations)	Functional group[a]	multiplicity[b]	range (ppm)[c]
BCAA[d]	$-CH_3$	M	1.06 - 0.89
Alanine (Ala)	$-CH_3$	S	1.49 - 1.46
Acetate (Ace)	$-CH_3$	S	1.91
N-Acetyl groups (N-Ace)	$-CH_3$	S	2.01
GABA	$-\beta CH_3$		2.32 - 2.27
Glutamate (Glu)	$-\gamma CH_2$	M	2.37 - 2.32
Glutamine (Gln)	$-\gamma CH_2$	M	2.48 - 2.42
N-acetyl aspartate (NAA)	$-\beta CH_2$	Dd	2.67 – 2.65
Aspartate (Asp)	$-\beta CH_2$	Dd	2.83 – 2.76
Choline[e] (Chol)	$-N(CH_3)_3$	S	3.25 - 3.19
***Scyllo*-inositol (SI)**	-CH	S	3.37 - 3.33
Taurine (Tau)	$S-CH_2$	T	3.46 - 3.41
Creatine (Crt)	$N-CH_2$	S	3.95 - 3.92
***Myo*-inositol (MI)**	-C2H	T	4.09 - 4.04
Lactate (Lac)	-CH	Q	4.15 - 4.08
Uracil (Ura)	-C5H	D	5.83 - 5.79
Nucleosides (Nucl)	-C3H, -C5H	D	5.94 - 5.90
Cytosine (Cyt)	-C5H	D	6.12 - 6.09
Fumarate (Fum)	$-(CH)_2$	S	6.51
Tyrosine (Tyr)	-C3H, -C5H	D	6.92 - 6.88
Phenylalanine (Phe)	-C3H, -C4H, -C5H, -C6H	M	7.45 - 7.31
Xanthine (Xan)	-CH	S	7.94
Hypoxanthine (Hyp)	-CH	S	8.28 - 8.17
Inosine (Ino)	-CH	S	8.36
ATP/ADP/AMP (AP)	-CH	S	8.45
NAD	-C6H	D	8.75 - 8.68
NAD	-C8H	S	8.96 - 8.90

Table 1. Selected spectral regions and assigned metabolites used for this study.
a) The molecule numbering system follows IUPAC rules; b) s= singlet, d= doublet, t = triplet, m= multiplet; c) ppm with respect to TSP; d) branched chain amino acids; e) choline and choline-containing compounds.

	Classes	
Metabolites	**S**	**A**
Ino[a]	↑[b]	↑
Chol	--	↑
Asp-tot	↓	↓
GABA	↓	↑
Lactate	↑	↑
BCAA	↓	↓
Cyt	↑	--
Phe	↓	--
Tyr	↓	--
Crt	↑	--
Uracil	↓	--
Ala	↑	↑
Fum	--	↓

Table 2. OPLS-DA most discriminant metabolites of S and Aclassescompared to H class.

a) Inosine (Ino), choline/phosphocholine/3-glycero-phosphocholine (Chol),aspartate + N-acetylaspartate (Asp-tot), gamma-aminobutyric acid (GABA), lactate (Lac), BCAA (branched chain aminoacids: isoleucine, leucine, and valine), cytosine (Cyt), phenylalanine (Phe), tyrosine (Tyr), creatine (Crt), uracil (Ura), alanine (Ala), fumarate (Fum).b) ↑up-regulated**,** ↓down-regulated, and-- stable, with respect to the H class**.**

Sample	Density OD/mm^2
Infected symptomatic S-1	181.89
S-2	130.02
S-3	223.09
S-4	198.06
S-5	187.92
S-6	176.35
S-7	204.60
S-8	167.03
Mean	183.62
SD	27.85
Infected asymptomatic	
A-9	104.26
A-10	171.93
A-11	124.01
Mean	133.40
SD	34.79

Table 3.PrP^{Sc}amounts[a], as calculated by WB analysis in brains of infected sheep.
a) means are not statistically different.

Metabolites	**r[a]**	**R[2b]**	**loadings[c]**	**loadings cv[d]**
Directly correlated ↑				
Ala	0.861	0.742	0.327	0.099
Cyt	0.803	0.645	0.300	0.103
Crt	0.639	0.408	0.248	0.119
Inversely correlated ↓				
Asp-tot	-0.780	0.608	-0.302	0.162
Ura	-0.609	0.370	-0.237	0.183
GABA	-0.602	0.363	-0.218	0.102

Table 4. OPLS metabolites having the strongest (positive or negative) correlation with PrP^{sc} amounts in brain homogenates.
a) coefficient of correlation and b) coefficient of determination of metabolite *vs*PrP^{sc} amounts; c) loading weights along the predictive component;d) Jack-knife standard error of loading weights computed from all rounds of cross validation. Alanine (Ala), cytosine (Cyt), creatine (Crt), aspartate + N-acetylaspartate (Asp-tot), uracil (Ura), gamma-aminobutyric acid (GABA).

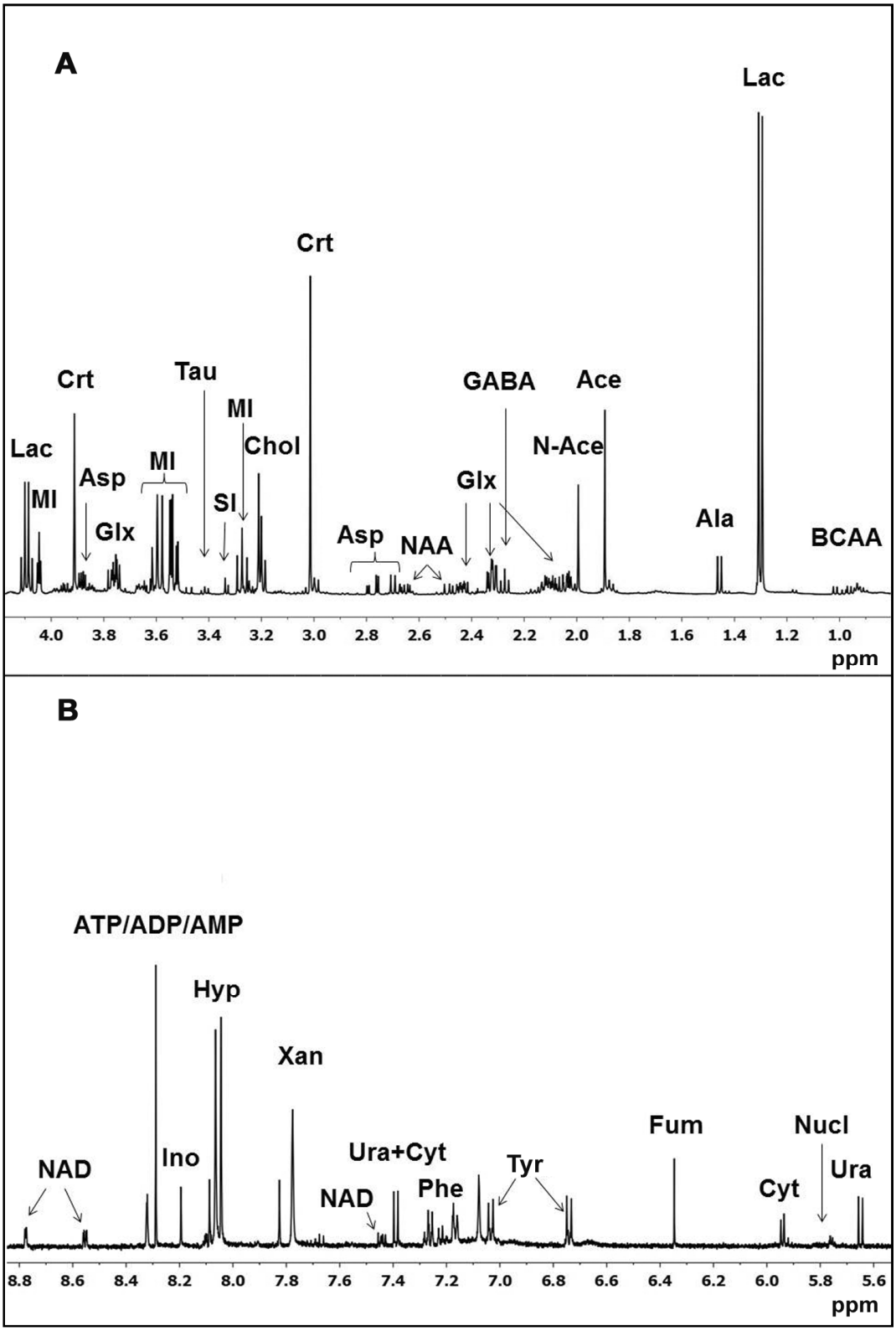
A
Lac
Crt
Crt
Tau
MI
Chol
GABA
Ace
Lac
MI
Asp
MI
SI
Glx
N-Ace
Glx
Asp
NAA
Ala
BCAA
4.0 3.8 3.6 3.4 3.2 3.0 2.8 2.6 2.4 2.2 2.0 1.8 1.6 1.4 1.2 1.0
ppm
B
ATP/ADP/AMP
Hyp
Xan
Fum
Nucl
NAD
Ino
Ura+Cyt
Tyr
Ura
NAD
Phe
Cyt
8.8 8.6 8.4 8.2 8.0 7.8 7.6 7.4 7.2 7.0 6.8 6.6 6.4 6.2 6.0 5.8 5.6
ppm

Fig. 1

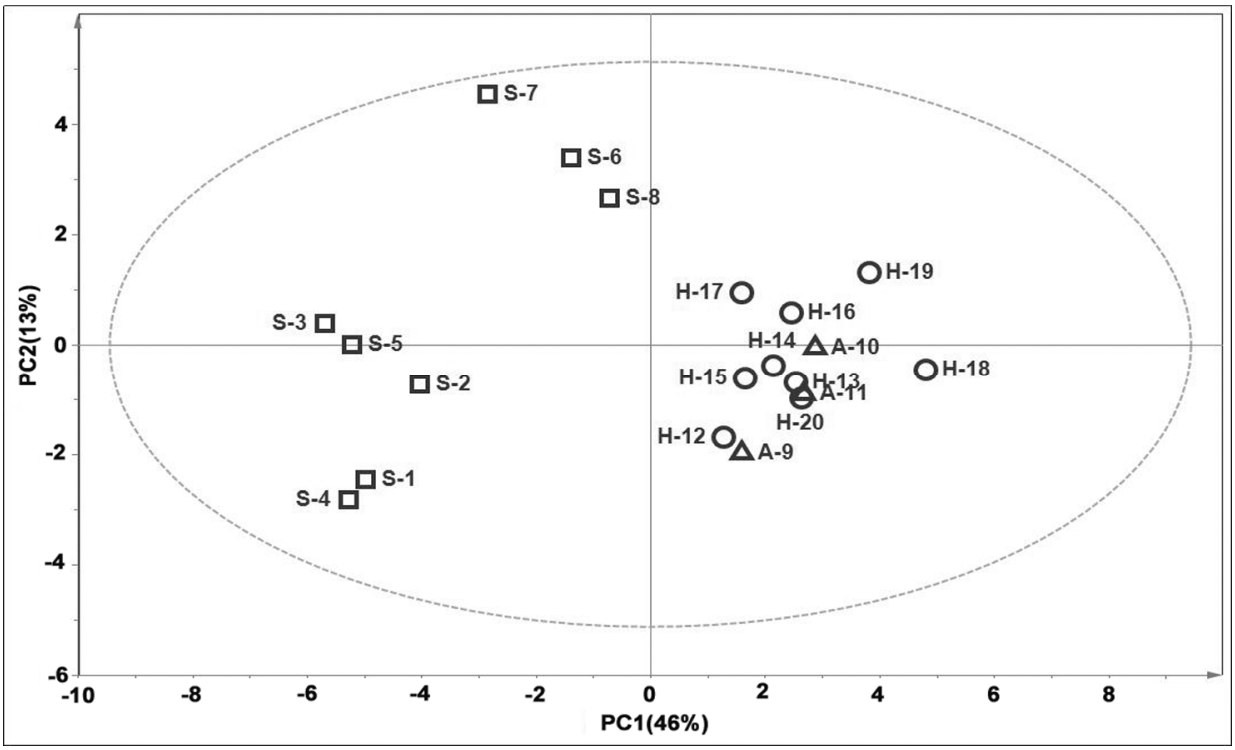
S-7
S-6
S-8
H-19
H-17
H-16
S-3
S-5
H-14
A-10
H-15
H-13
H-18
S-2
A-11
H-20
H-12
A-9
S-1
S-4
PC2(13%)
PC1(46%)
4
2
0
-2
-4
-6
-10
-8
-6
-4
-2
0
2
4
6
8

Fig. 2

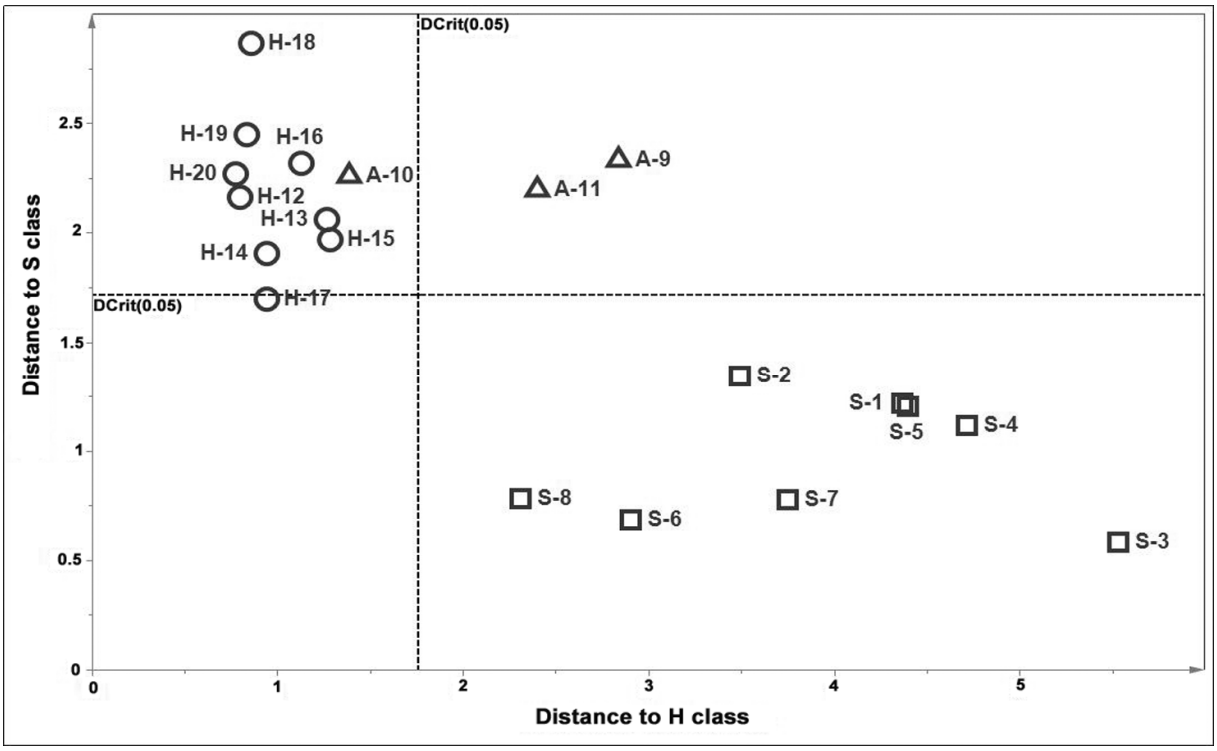
H-18
DCrit(0.05)
H-19
H-16
A-9
H-20
A-10
A-11
H-12
H-13
H-15
H-14
H-17
DCrit(0.05)
S-2
S-1
S-5
S-4
S-8
S-7
S-6
S-3
Distance to S class
Distance to H class
2.5
2
1.5
1
0.5
0
0
1
2
3
4
5

Fig. 3

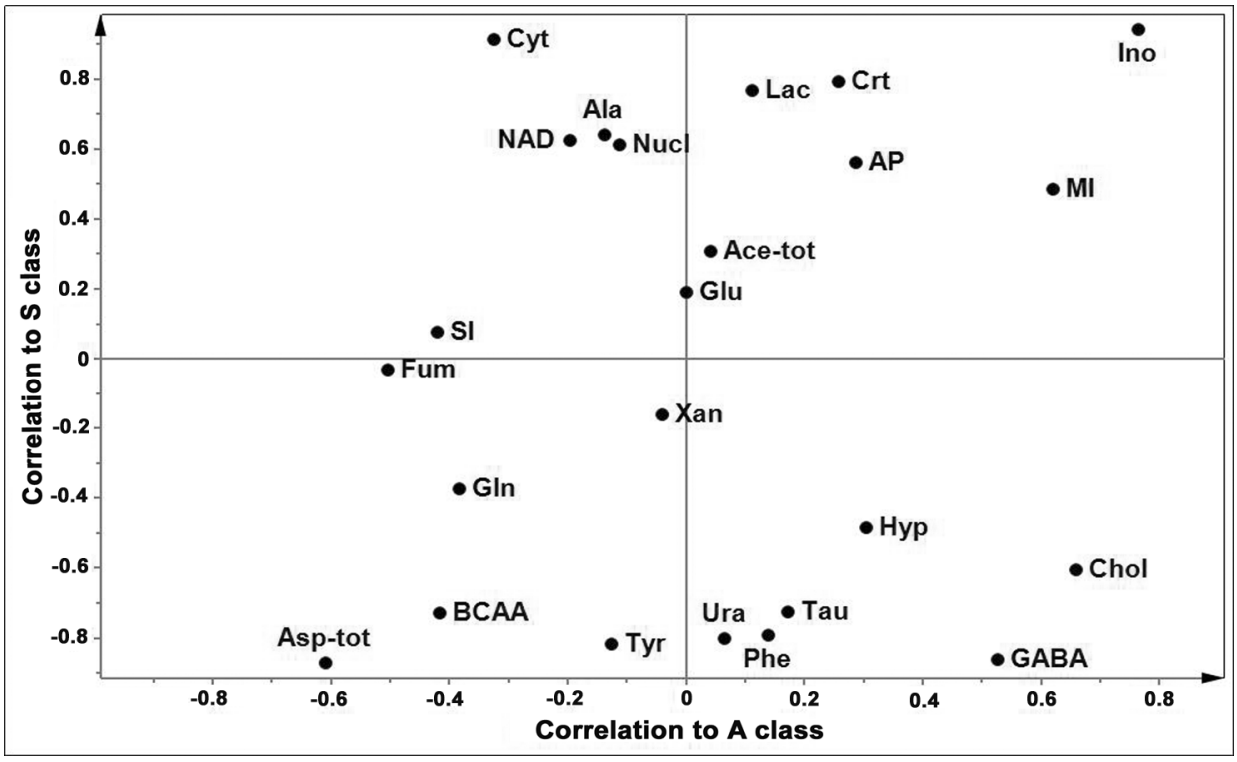
Cyt
Ino
Lac
Crt
Ala
NAD
Nucl
AP
MI
Ace-tot
Glu
SI
Fum
Xan
Gln
Hyp
Chol
BCAA
Ura
Tau
Asp-tot
Tyr
Phe
GABA
Correlation to S class
Correlation to A class
0.8
0.6
0.4
0.2
0
-0.2
-0.4
-0.6
-0.8
-0.8
-0.6
-0.4
-0.2
0
0.2
0.4
0.6
0.8

Fig. 4

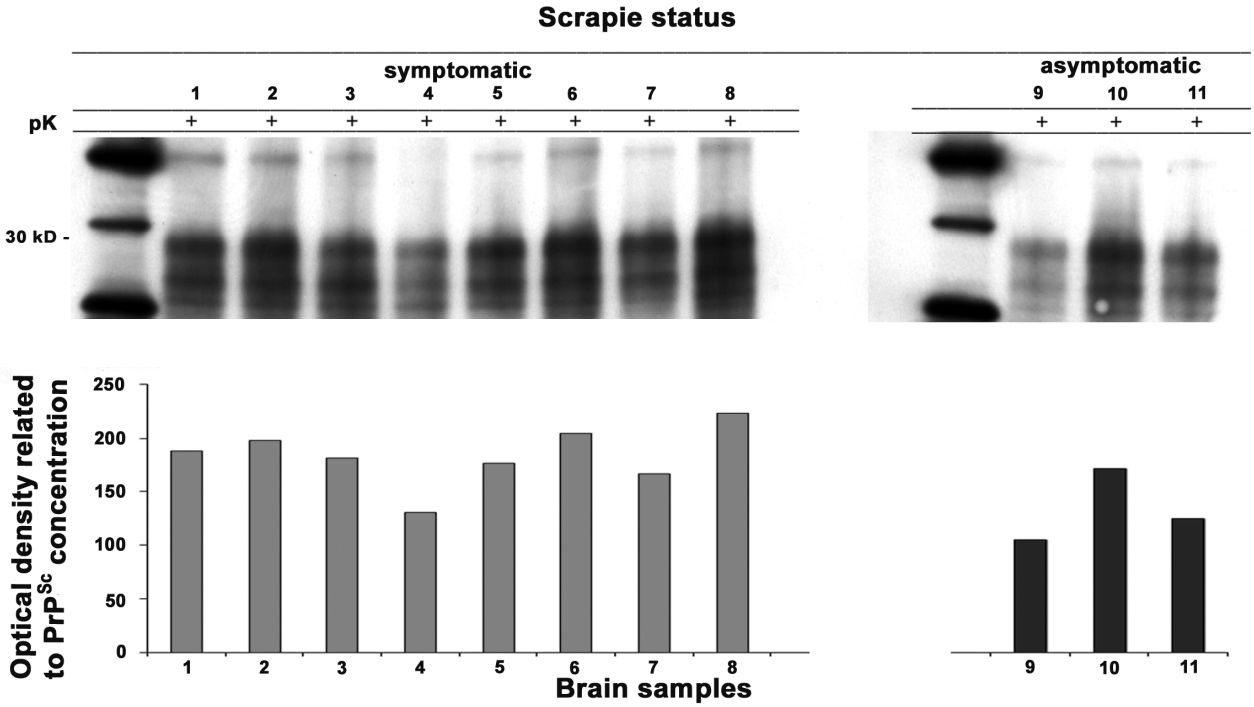
Scrapie status
symptomatic
asymptomatic
1
2
3
4
5
6
7
8
9
10
11
pK
+
30 kD -
Optical density related to PrP^Sc concentration
250
200
150
100
50
0
Brain samples

Fig. 5

Figure captions

Fig. 1. A representative ^{1}H NMR spectrum of brain extract. (A) spectral region from 0.5 to 5.0 ppm and (B) spectral region from 5.5 to 9.0 ppm (magnified). Major assignments are reported. Branched chain aminoacids: isoleucine, leucine, and valine (BCAA), lactate (Lac), alanine (Ala), acetate (Ace), N-acetyl groups (N-Ace), gamma-aminobutyric acid (GABA), glutamate/glutamine (Glx), N-Acetylaspartate (NAA), aspartate (Asp), creatine (Crt), choline/phosphocholine/3-glycero-phosphocholine (Chol), taurine (Tau), *myo*-inositol (MI), *scyllo*-inositol (SI), Cytosine (Cyt), Nucleosides (Nucl), Uracil (Ura),Fumarate (Fum), Tyrosine (Tyr), Phenylalanine (Phe), Xanthine (Xan), Hypoxanthine (Hyp), Inosine (Ino), ATP/ADP/AMP (AP), NAD.

Fig. 2. **PCA of brain extracts spectral data.** PCA of ^{1}H NMR spectral data of brain extracts, PC1 *vs* PC2 score plot of S (boxes), H (circles), and A (triangles) samples. The explained variance is reported in brackets. Ellipse encloses the 95% Hotelling T^2confidence region.

Fig. 3. **Cooman's plot of brain extracts spectral data.** SIMCA Cooman's plot. In the x-axis PCA of H samples: 47% of total variance expressed, 2 components; in the y-axis PCA of S samples: 65% of total variance expressed, 2 components for S. The plot is divided into four regions by the intersection of 95% confidence limit lines for each class. These regions identify the class membership: the NW region defining H only, the SE region defining S only, the SW region containing both H and S, and the NE region containing neither H nor S membership.

Fig. 4. **SUS plot of brain extracts spectral data.** Loading SUS-plot of OPLS-DA models of ^{1}H NMR data of brain extracts. In the x-axis the loading correlation values of "H *vs* A" model and in the y-axis the loading correlation values of "H *vs* S" model. Variables in the lower left corner are unique for H samples, variables in the higher right corner are shared in infected (S and A) samples. Variables higher in S and A samples exhibit high correlation values in the y- and x-axes, respectively. Branched chain aminoacids: isoleucine, leucine, and valine (BCAA), lactate (Lac), alanine (Ala), acetate + N-acetyl groups (Ace-tot), gamma-aminobutyric acid (GABA), glutamate (Glu), glutamine (Gln), aspartate + N-acetylaspartate (Asp-tot),creatine (Crt), choline/phosphocholine (Chol), taurine (Tau), myo-inositol (MI), scyllo-inositol (SI), Cytosine (Cyt), Nucleosides (Nucl), Uracil (Ura),Fumarate (Fum), Tyrosine (Tyr), Phenylalanine (Phe), Xanthine (Xan), Hypoxanthine (Hyp), Inosine (Ino), ATP/ADP/AMP (AP), NAD.

Fig. 5. Quantification of PrP^{Sc} in brain homogenates of naturally scrapie-affected sheep. (A) Western blot (WB) analysis of whole-brain homogenate after proteinase K (PK) digestion from independent symptomatic (lines 2 to 9) and asymptomatic (lines 10 to 13) scrapie affected sheep. A molecular weight marker is loaded in lane 1. (B) Quantification of the WB signal of the PrP^{Sc} present in the brain homogenates is represented as PrP optical density (OD) signals. Our results indicate that the higher average amount of PrP^{Sc} was detected in the symptomatic scrapie affected sheep. The brain homogenate samples were normalized in relation to the total protein amount.

Chapter II – Biochemical studies of PrPSc

Research rational / Aims of the project

As stated above, several aspects of prion disorders remain unclear, and among these also the molecular mechanism through which prions replicate it is not fully understood yet (Atarashi R et al., Prion. 2011). In this context, understanding the PrP structure seems critical to get more insight on the molecular processes leading to neurodegeneration during prion infections. Moreover, the knowledge of the prion structure can help to understand the molecular basis supporting the persistence of different prion strains, each of which exhibits distinct disease phenotypes as defined by incubation times, features of clinical disease, neuropathological targeting, and physicochemical properties, all of which remain stable over serial transmission (Telling, Genome Biol. 2004; Solforosi et al., J Biol Chem. 2007).
The N-terminal domain (aa residues 23-124) of PrPC is more flexible and less structured than the C-terminus (aa residues 125-231, sequence of hamster) which is characterized (see Figure 1) by the presence of three α-helices (H1: residues 145-153 , H2: 172-194, and H3: 200-226), and by a short β-sheet (B1: B2 and residues 129-133: 160-163).

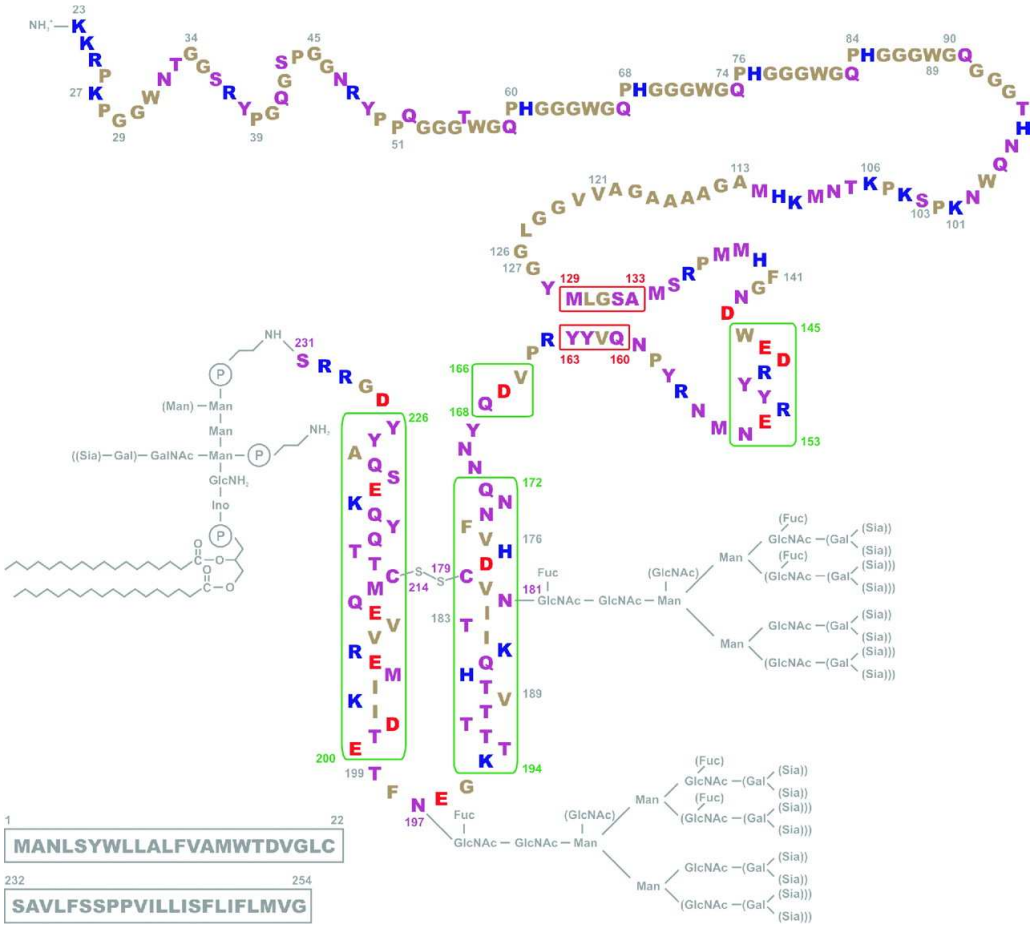

Figure 1. Amino acid sequence and post-translational modifications of hamster PrP. 1–22, ER signal peptide (cleaved); 23–231, major prion protein; 34–39 and 45–50, 2 hexarepeats; 51–91, 5 octarepeats; 113–128, conserved hydrophobic region; 121–231, NMR structure of rec SHa PrP; 129-133, β-strand 1; 145–153, α-helix 1; 160–163, β-strand 2; 166–194, α-helix 2; 179/214, disulphide bridge; 181, N-glycosylation 1; 197, N-glycosylation 2; 200–226, α-helix 3; 231, GPI-anchor; 232–254, GPI signal peptide (cleaved). Riesner D, Biochemistry and structure of PrP(C) and PrP(Sc). Br Med Bull. (2003); 66:21-33. ©2003 by Oxford University Press.

The prevalent structural model implies that PrPSc retains most of the native α-helices of the normal, non-infectious prion protein, PrPC, but evidence is now accumulating that these helices

are absent in the PrPSc amyloid fibrils. Moreover, recombinant PrPC can form fibrils *in vitro* that have parallel in-register intermolecular β-sheet architectures in the domains originally occupied by helices 2 and 3.
In the last decade, a number of cell-free assays depicting the metamorphosis of PrPC into PrPSc were developed; among them, the amplification technique QuIC (Quaking-Induced Conversion; Atarashi et al., Nat Methods. 2008) emerged as one of the most practical, fast and reliable method. The Real-Time Quaking Induced Conversion (RT-QuIC) is a variant of the QuIC method that exploits the capacity of the pathogenic prion protein (PrPSc) to convert the normal prion protein (Wilham et al., PLoS Pathog. 2010; Atarashi et al., Prion. 2011). This test allows the detection of PrPSc using ultrasensitive amplification reactions of the prion protein, which acts as a seed causing the conversion process, with consequent formation of amyloid fibrils. It uses a recombinant prion protein (rPrP), purified from a bacterial expression system, as a substrate allowing the conversion to occur using a minimum quantity of seed, and so far it has been adapted to different types of TSEs. Biological tissues that have proved compatible with these methods are brains, cerebrospinal fluids and nasal washes.
Studies conducted by the Caughey's group have shown that the RT-QuIC method is more efficient in converting the substrate (rPrPC) of the reaction into its proteinase-K (PK) resistant isoform (rPrPres) than the QuIC method originally described by Atarashi and colleagues (Atarashi et al., Nat Methods. 2008). The formation of the amplification product in the RT-QuIC is displayed in real time through the presence of Thioflavin T (ThT), a dye that fluoresces when it is associated with amyloid fibrils. A further advantage of this method is the ability to analyze numerous samples or variables simultaneously.
Approximately 50-60% of the substrate is used during the reaction to amplify PrPSc (initial seed) compared to about 10% in the standard QuIC (Atarashi et al., Nat Methods. 2008). These data suggest that the RT-QuIC is an efficient and easily reproducible method. Currently, the sensitivity of the method is 85 to 89% and the specificity is 100%. Because this technique is easily reproducible, highly sensitive, ensures maximum specificity, is more efficient in the conversion of the substrate than the other techniques, and it also offers the ability to analyze multiple samples or variables simultaneously, I have chosen to use it for the studies I have been involved in during my 14-month residency at the National Institutes of Health (NIAID/NIH, MT-USA).

Firstly, I focused my attention on the ability of the N-terminal portion of rPrPC (here indicated as rPrP 23-106) to inhibit the prion misfolding/aggregation process by RT-QuIC. In a previous study, in fact, the N-terminal portion of the prion protein showed a potent inhibitory effect on the aggregation of the amyloidogenic peptide Aβ1-42 of Alzheimer (Nieznanski et al., J Biol Chem. 2012). It was therefore considered that this portion of the protein could have inhibitory activity also in the process of conversion of the prion protein. Unfortunately, the results obtained, although showed some inhibitory activity on the formation of PrPSc fibrils, showed high variation in the inhibitory concentration of the rPrP 23-106 fragment (i.e. 5 μM - 25 μM). At the time, the continuation of these studies, aimed at finding application of the rPrP 23-106 fragment in the clinic of human TSEs, seemed problematic. The N-terminal region 23-106 might, in fact, be a portion too big to be effective in therapy, thus before to carry on further in vitro experiments, studies of the pharmacodynamic and pharmacokinetic properties of the peptide are necessary.

My attention was then moved to another aspect of the aggregation process and PrPSc fibrils structure. The main aim of the project was to verify if the portion indicated as the central hairpin (~aa 127-161), was able to form fibrils with parallel in-register intermolecular β-sheet structures, as recently proposed by the Caughey's group (Groveman et al., J Biol Chem. 2014). This study lead to some interesting results which are fully described below.

1. PrPSc fibril structure: evaluation of the capacity of Syrian Hamster rPrP 23-106 fragment to inhibit the infectivity/aggregation of the pathogenic prion protein

Newly synthesized PrPC polypeptide is composed of ~250 amino acids, and it undergoes a series ofprocessing before it reaches residency on the plasma membrane: it is removed a 22-amino acid N-terminal signal peptide, and a 23 C-terminal aa sequence upon the addition of the glycosylphosphatidylinositol (GPI)-anchor to Ser-231 (Donne et al., Proc Natl Acad Sci U S A. 1997).
The N-terminal domain of PrPC (aa residues 23–121) contains a number of unusual sequence features including four or more octapeptide repeats (eg. PHGGGWGQ) , whose high degree of conservation suggests an essential contribution to the function of PrPC, whatever that may be (Yao et al., J Neurochem. 2003; Wopfner et al., J Mol Biol. 1999).
The three-dimensional structure is characterized by a globular domain, consisting of residues 125–231 (depending on the Prnp genotype) that contains three α-helices, loops, and a short antiparallel, two-stranded β-sheet. The PrPC amino-proximal half (aa residues 23–124) is intrinsically disordered and highly dynamic (Taubner et al., J Mol Biol. 2010). This plastic region could feature in the conversion of PrPC to PrPSc by template-assisted formation of β-structure (Donne et al., Proc Natl Acad Sci U S A. 1997).
Circular dicroism (CD) and Fourier transform infrared (FT-IR) studies suggested conversion of α-helices into β-sheets features in the formation of PrPSc (Pan et al., Proc Natl Acad Sci U S A. 1993). It is therefore important to study the role of these portions in the PrPC to PrPSc conversion process.
Recently, it has been demonstrated that the soluble portion of the prion protein (i.e. glycophosphatidylinositol anchor-free) and its N-terminal fragment have a strong effect on the aggregation pathway of Aβ1-42 by inhibiting its assembly into amyloid fibrils, a step considered critical in the pathogenesis of Alzheimer's disease (Nieznanski et al., J Biol Chem. 2012).
During my residency at the National Institutes of Health (NIH, USA), I have undertaken a project to analyze the capacity of the N-terminal portion of rPrP (aa residues 23-106) to inhibit the infectivity of pathogenic prion protein. To this end, I used two different approaches:

- investigating the role of the N-terminal segment of PrP in the conversion process using the RT-QuIC assay.
- evaluating the effect of the N-terminal segment of PrP on the PrPSc propagation in scrapie-infected neuroblastoma mouse cells.

1.1 Results and Discussion

1.1.1 Bacteria screening

A consistent part of the work was aimed at purifying the Syrian Hamster rPrP 23-106 fragment. We started by identifying a bacterial clone that was a high expresser of this fragment. We analyzed protein levels of 4 bacteria clones, before and after centrifugation, by running the samples on a denaturing SDS-PAGE gel and stained the gel for total protein content (Coomassie blue).

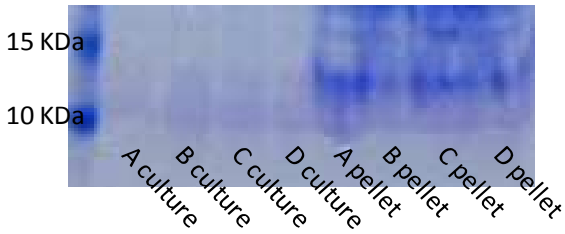

Figure 2. SDS-PAGE gel: Total protein staining of Rosetta DE3 bacteria. The gel was stained with a total protein stain (Coomasie Blue) to detect the Syrian Hamster rPrP 23-106 fragment. The stain show bands at about 10 KDa probably due to a different speed of migration of the attempted fragment.

Figure 2 shows, from left to right , the marker, the 4 different samples loaded before centrifugation (designated as A-D, cell suspensions) and 4 different samples loaded after centrifugation (designated as A -D pellet, cell pellets).
Because the 23-106 fragment has a molecular weight of 8.2 KDa , in the figure are shown only the bands at which the marker has a weight of 10 - 15kDa .
A band at about 10KDa is present in all samples. The molecular weight of the protein of interest is 8.2Kda, but it is not uncommon to see a several KDa shift with this type of sample on this type of gel. The bands observed with the lowest molecular weight are probably our protein of interest, which following binding with SDS, may be subject to a slowdown in the migration.
Electrophoresis showed the presence of several bands at different molecular weights which are likely due to impurities present in the sample.
Clone A seems to show a strong band only after centrifugation, while for the B clone the opposite situation is observed. For the C and D clones we observe a strong band that seem more intense for the C clone.
For this reason we concluded that clone C was our highest rPrP 23-106 expressor and thus grew a stock of these cells for purification.

1.1.2 Purification of Syrian Hamster rPrP 23-106 fragment

rPrP 23-106 was purified using Immobilized metal ion affinity chromatography (IMAC), which is an affinity chromatography that selects the protein through interactions between the resin with which the column is packed and chemical groups present in the protein of interest, such as N, O, S. Isolated inclusion bodies were incubated in the presence of Denaturing Buffer to solubilize them and to allow denaturation of PrP. Next, the denatured protein was incubated with Ni-NTA Superflow (Qiagen) to allow binding of the protein to the beads. Beads were then loaded onto a column and washed once using AKTA Explorer (Ge Healthcare) with denaturing buffer to eliminate excess unbound protein.
Figure 3 shows the UV absorbance following an 80minute wash.

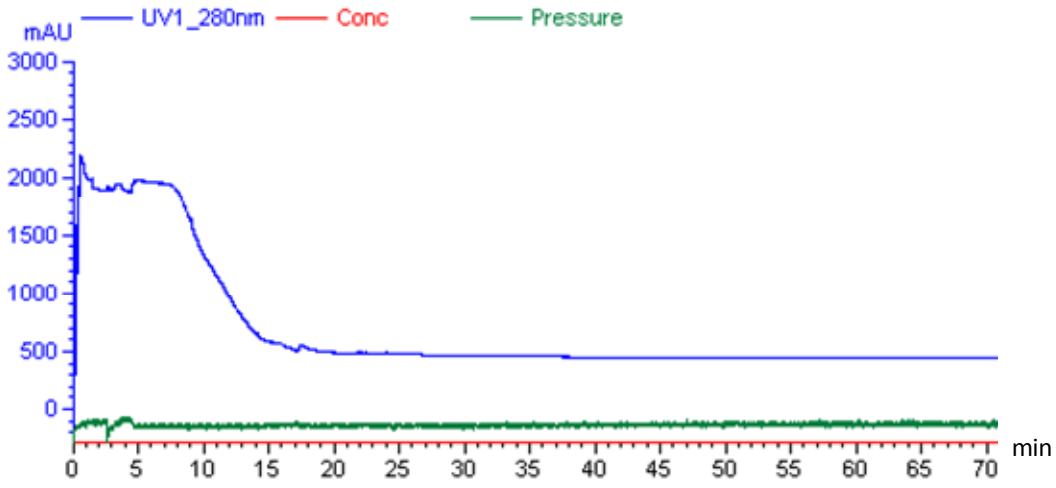

Figura 3. Wash UV absorbance with denaturing buffer in AKTA Explorer.

We initially observed a UV peak most likely due to loss of unbound protein followed by a plateau.
We performed a second wash of the column with refolding buffer, which showed no protein loss (Figure 4).

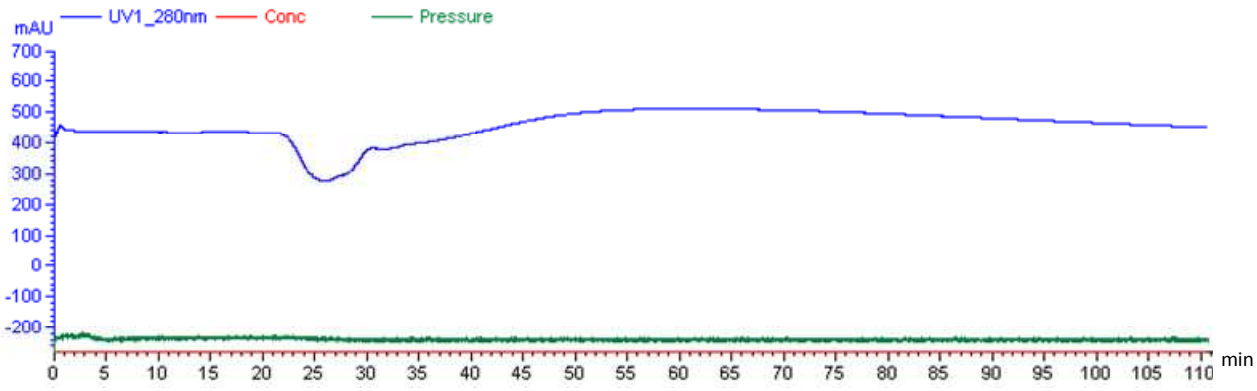

Figura 4. Wash UV absorbance with refolding buffer in AKTA Explorer.

This second wash gave no UV absorbance peak indicating that all unbound proteins were eliminated with the first wash.
Next, we moved onto the protein recovery step (or elution step) using Elution Buffer.

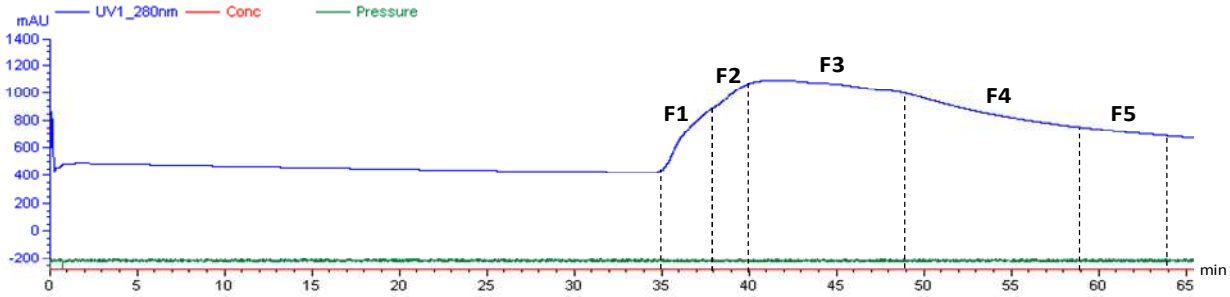

Figura 5. Elution UV curve of Syrian Hamster PrP 23-106 fragment using Immobilized metal ion affinity chromatography (IMAC).

Figure 5 shows an absorbance peak that corresponds to the moment in which the protein is eluting from the column. From minute 35 different fractions were collected (designated as F1-F5) to chose the fractions more concentrated. All fractions collected were considered suitable to proceed to the next step and were combined into a single pool.
To further purify the eluate, we performed an Ion-exchange chromatography. Different proteins bind the column with different affinity. Using the method of elution with gradients, the salt concentration of the solution that passes through the column is continuously increased and the different proteins are eluted sequentially depending on their affinity for the column
The protein was loaded directly into the SP Sepharose FF 1ml column (GE Healthcare) and the impurities washed away with a solution which has the same reagent (NaAc) of Elution Buffer but without salt (Solution A), using AKTA Explorer.

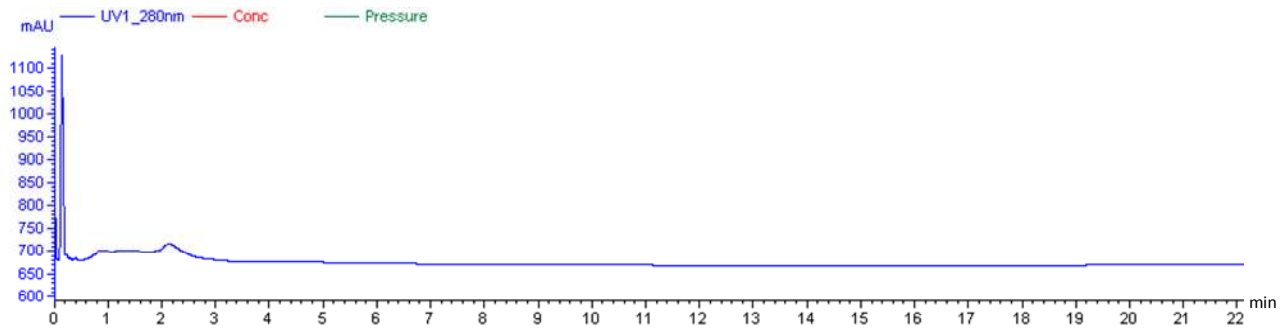

Figura 6. Wash UV absorbance with a solution non-saline (Solution A).

Figure 6 shows initially a UV peak, most likely due to loss of unbound protein, followed by a plateau. The elution was performed by increasing gradually the NaCl concentration from 0% to 100%, for which gradually the solution B replace the solution A in the column.

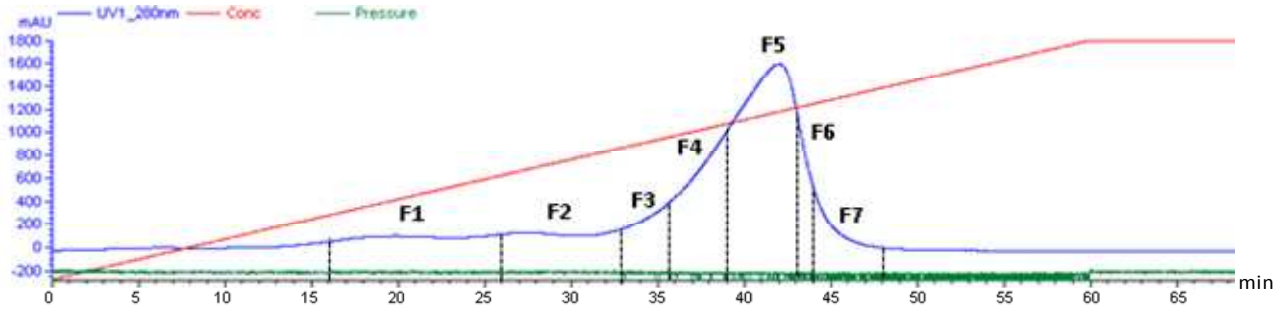

Figura 7. Elution UV curve of Syrian Hamster rPrP 23-106 fragment using an Ion-exchange chromatography.

Figure 7 shows an increase in UV absorbance from 33 minute, for which the protein is been collected from this moment. The maximum absorbance is observed at around 43 minutes, in correspondence with the fraction A.

Fractions were subsequently analyzed by Coomassie Blue method to analyze the proteic profile regarding to each aliquot (Figure 8).

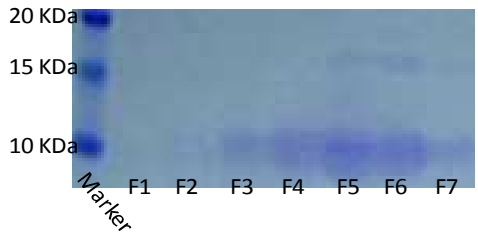

Figure 8. SDS-PAGE gel: Total protein staining of eluate after purification processes. The gel was stained with a total protein stain (Coomasie Blue) to detect Syrian Hamster rPrP 23-106 fragment. The stain show bands at about 10 KDa probably due to a different speed of migration of the attempted fragment.

A total of 7 aliquots were analyzed using an SDS-PAGE gel. Following staining, we found that fractions F4, F5 and F6 were the ones with a high concentration of the protein of interest. These fractions are collected to submit them to the dialysis process.
These three fractions were combined and transferred into dialysis tubing with a 3KDa cutoff and left for 24h within dialysis buffer, which is changed approximately every 6 hours.
At the end of the dialysis the protein was filtered and its concentration measured spectrophotometrically. The value of absorbance is measured 3 times with the spectrophotometer NanoDrop 2000 (Thermo Scientific) and the average is 0.485. The molar extinction coefficient for this fragment is 41480. By applying the Beer-Lambert law, the concentration calculated is 11.7 µM. We concentrated the protein using tubes Amicon ultra-4-Centrifugal filter ultracel-3K (Millipore) because we need high concentrations for RT-QuIC experiments. After centrifuging the protein in these tubes, the absorbance was 1.85, and the calculated protein concentration was 44.6µM.

1.1.3 RT-QuIC analysis with Syrian Hamster rPrP 23-106 fragment

RT-QuIC was used to determine if the Syrian Hamster rPrP 23-106 fragment inhibits the normal prion protein conversion into PrPSc using either hamster or human scrapie-infected brain homogenates as seeds. Full Length (FL, aa23-231) and truncated (rPrP 90-231, aa90-231) rPrP

were used as substrates. We started to analyze uninfected (HaNBH) vs. infected (263KBH) Hamster brain homogenates to test the inhibition by Hamster 23-106. The brain homogenate dilution used was 10-7 (corresponding to the concentration of 2fg/µl) and the substrate used was the FL.

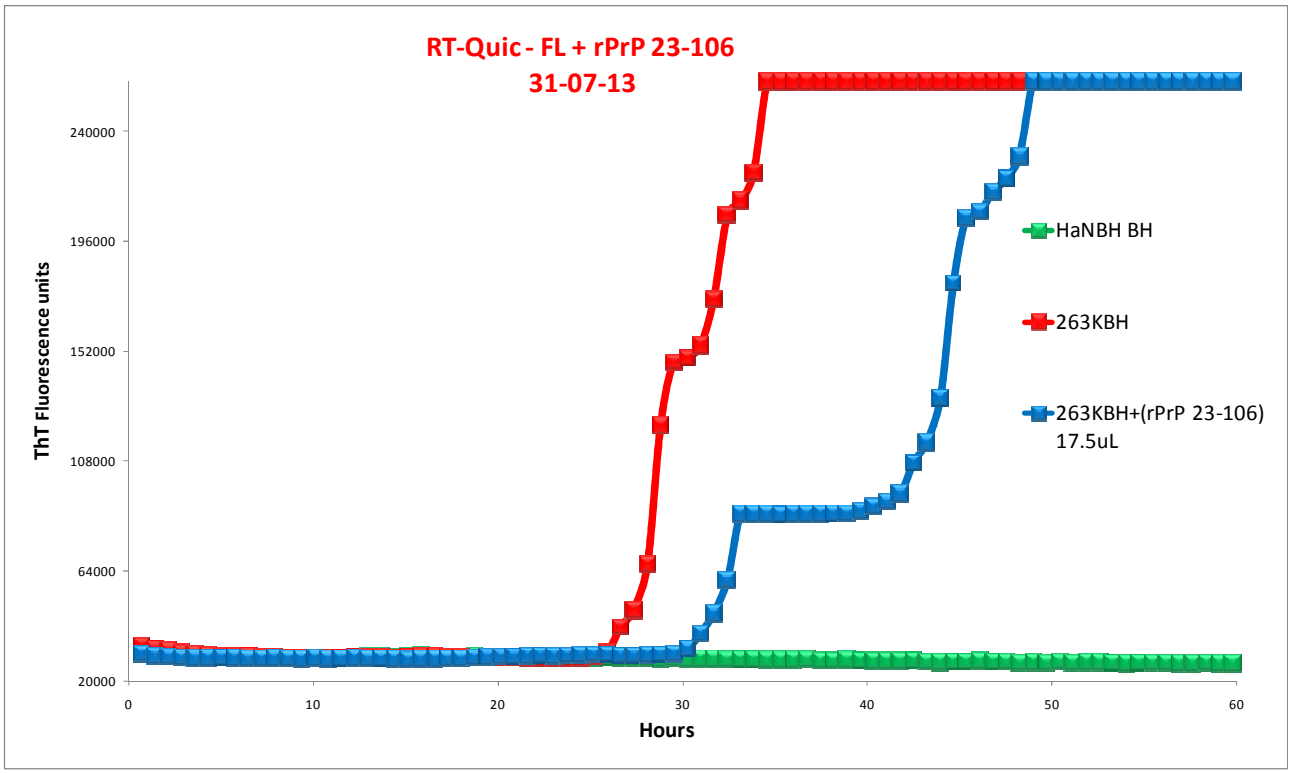

Figura 9. Analysis of the inhibitory capacity of the Syrian Hamster 23-106 (rPrP 23-106) in [2fg/µl] Hamster brain homogenate using Full Length (FL, aa23-231) as substrate.

Figure 9 shows that the amplification reaction starts approximately at 30 hours for the positive control non-treated with the rPrP 23-106 (263KBH, red), and for the brain homogenate treated with a final concentration of 8.25µM of this fragment (blue). The reaction seems to proceed more slowly in the latter case. For the negative control (green) there isn't, as expected, amplification reaction. Since the reaction started with a certain delay, we decided to repeat the experiment using an higher dilution of seed (10-8, concentration of 0.2fg/µl) and 23.5uM final concentration for our fragment.

Figure 10 shows that the amplification reaction starts around 20 hours for the untreated 263KBH (red), while for 236KBH (blue) treated with our fragment and for HaNBH (green) it is not observed any amplification reaction.
We then decided to repeat the experiments using brain homogenates of human patients suffering from sporadic Creutzfeldt–Jakob disease (sCDJ, with both substrates to analyze if the rPrP 23-106 shows the same activity in different conditions. The substrate concentration is the same as previous experiment (23.5µM).

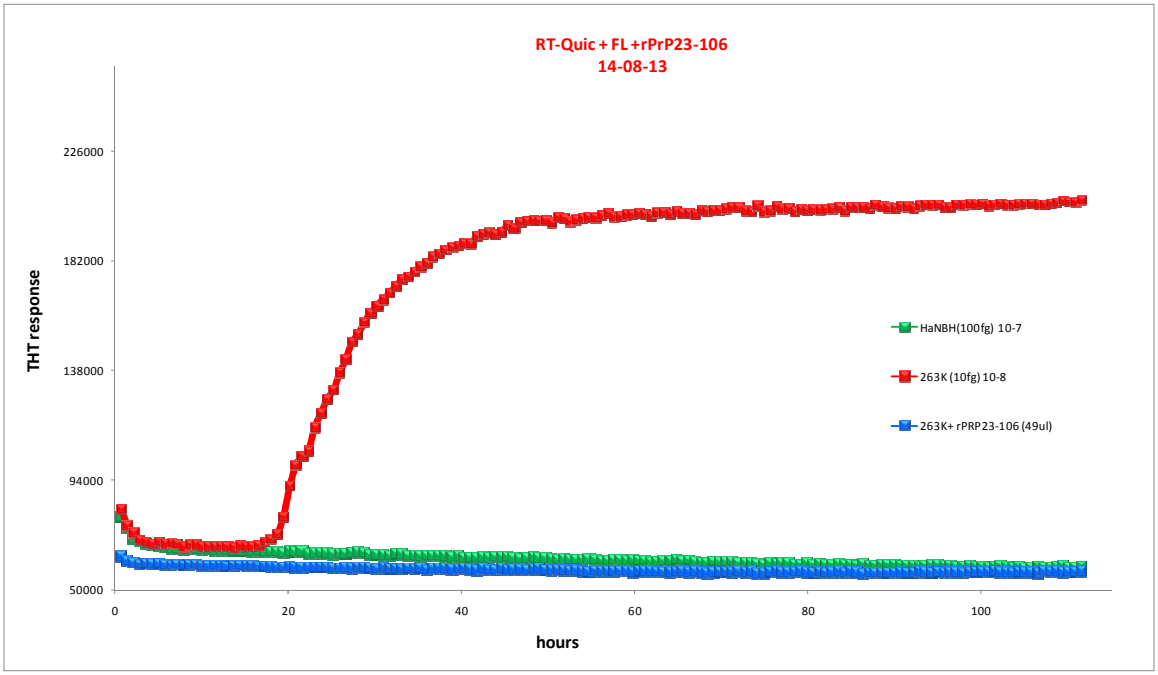

Figura 10. Analysis of the inhibitory capacity of rPrP 23-106 in [0.2fg/µl] Hamster brain homogenate using Full Length (FL, aa23-231) as substrate.

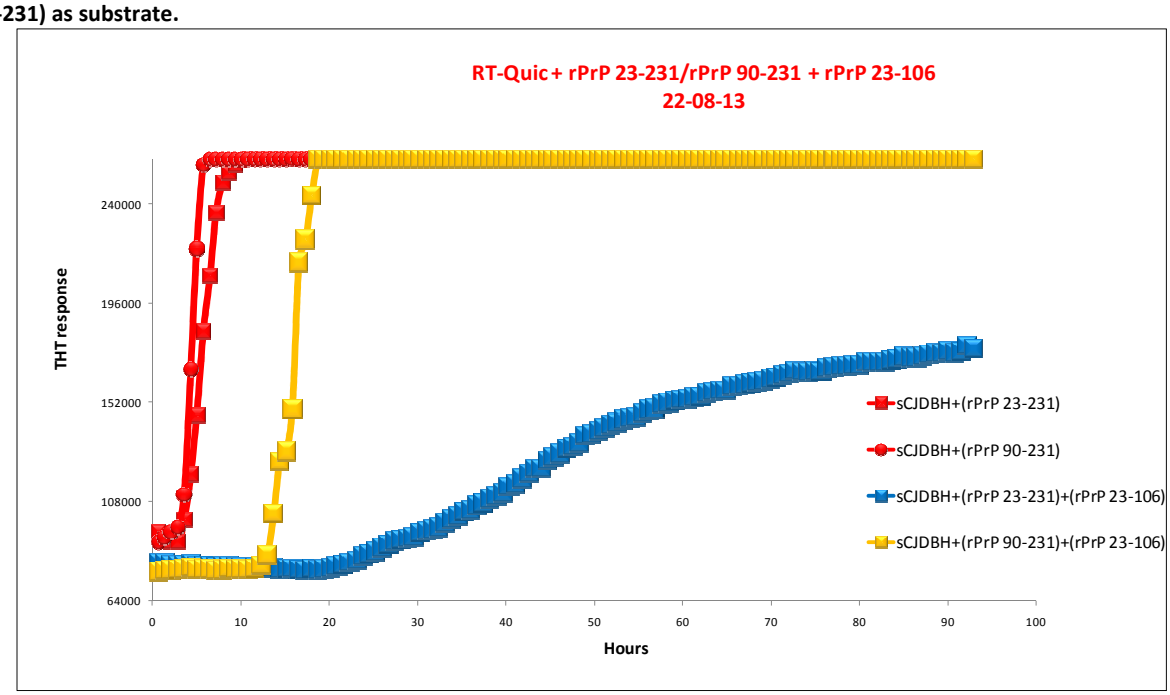

Figura 11. Analysis of the inhibitory capacity of rPrP 23-106 using brain homogenate of human patients suffering from sporadic Creutzfeldt–Jakob disease (sCDJ) and Full Length (FL, aa23-231) and truncated (rPrP 90-231) as substrate.

Figure 11 shows immediate amplification reactions for both positive untreated (sCJDBH+ rPrP 23-231 and sCJDBH+rPrP 90-231) controls, and the infected brain treated with the rPrP 23-106 fragment when the substrate was rPrP 90-231. Using FL as substrate the conversion reaction is retarded.

To analyze the activity of the fragment at different concentrations we performed a RT-QuIC titration, starting from a concentration higher than that used previously (25µm), two intermediate concentrations (10 and 5µM) and a concentration lower than that used previously (2.5µM). To validate and amplify my earlier experiments, I used the hamster brain homogenate as seed and FL as substrate.

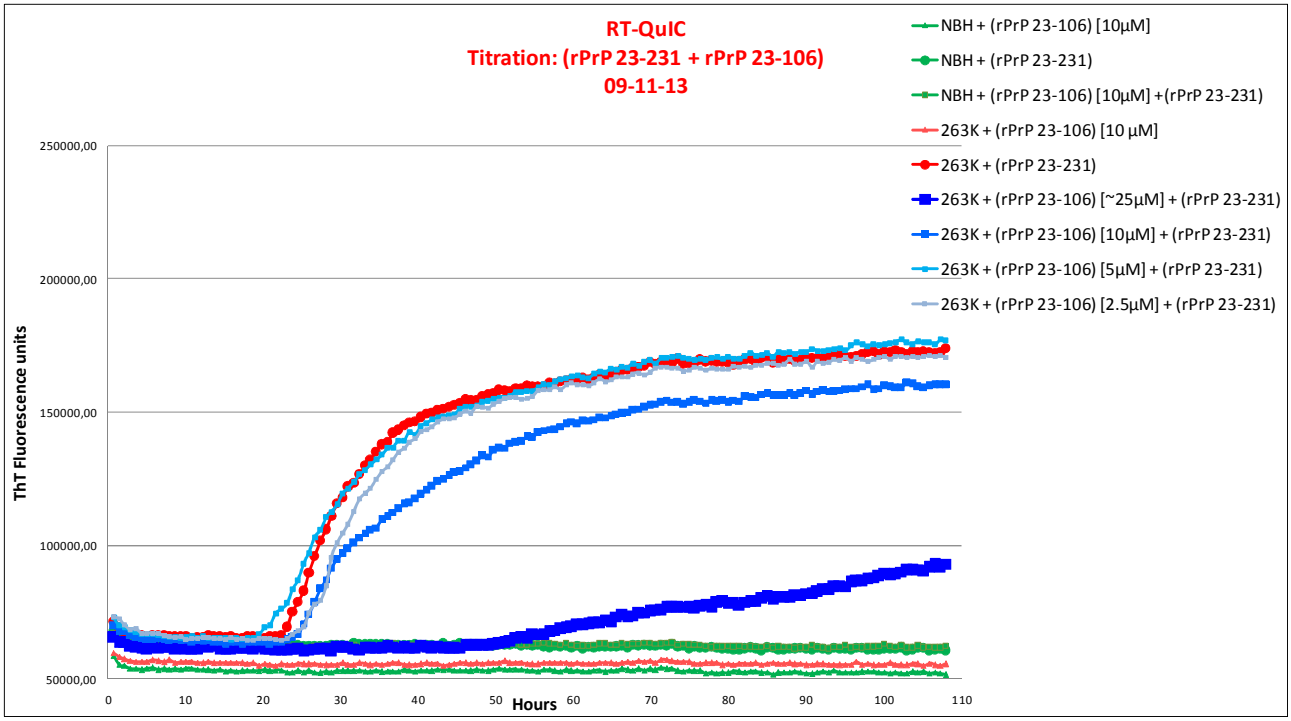

Figura 12. RTQuiC titration in [0.2fg/µL] Hamster brain homogenate using four different concentration (25, 10, 5, 2.5 µM) of rPrP 23-106 and FL as substrate.

Figure 12 shows that for the untreated 263KBH (red) and 263KBH treated with concentrations of 2.5, 5 and 10µM the conversion reaction starts at the same time and shows the same type of trend. For 263KBH treated with a concentration of 25µM the conversion reaction is retarded. The reaction, however, does not get to 260000 of fluorescence in any case.
The samples were also analyzed (Figure 13) in the presence of the Dialysis Buffer (sodium acetate, NaAc, in the fig), to exclude the possibility that the inhibition was due to reagents). In this case, the untreated 263KBH and the brain homogenate treated with NaAc (red) show the same trend. For the 263KBH treated with the rPrP 23-106 at a final concentration of 5, 10 ,25 µM (purple), we observe a retarded conversion reaction.

Then, I have simultaneously pre-incubated the brain homogenates, uninfected and scrapie-infected, for 30 minutes with the rPrP 23-106 in order to see if the fragment exerts its inhibitory activity by binding to the seed or to the substrate; in this latter case, a curve similar to that of Figure 14 should be obtained. However, given that all infected samples (Figure 13), untreated and pre-treated with NaAc or the rPrP 23-106, show the same kinetics, the inhibition appears not to be due to the binding of rPrP 23-106 to the seed.

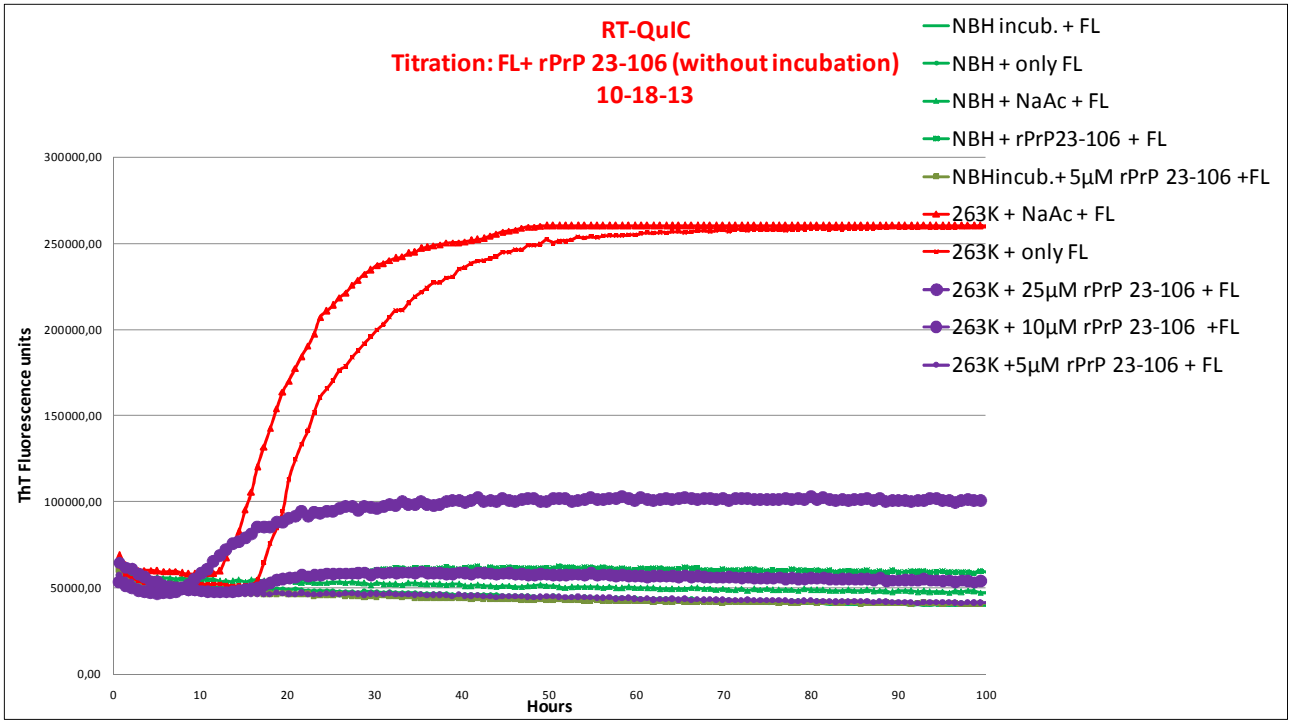

Figura 13. RTQuIC titration in [0.2fg/µL] Hamster brain homogenate using three different concentration (25, 10, 5 µM) of rPrP 23-106 and FL as substrate.

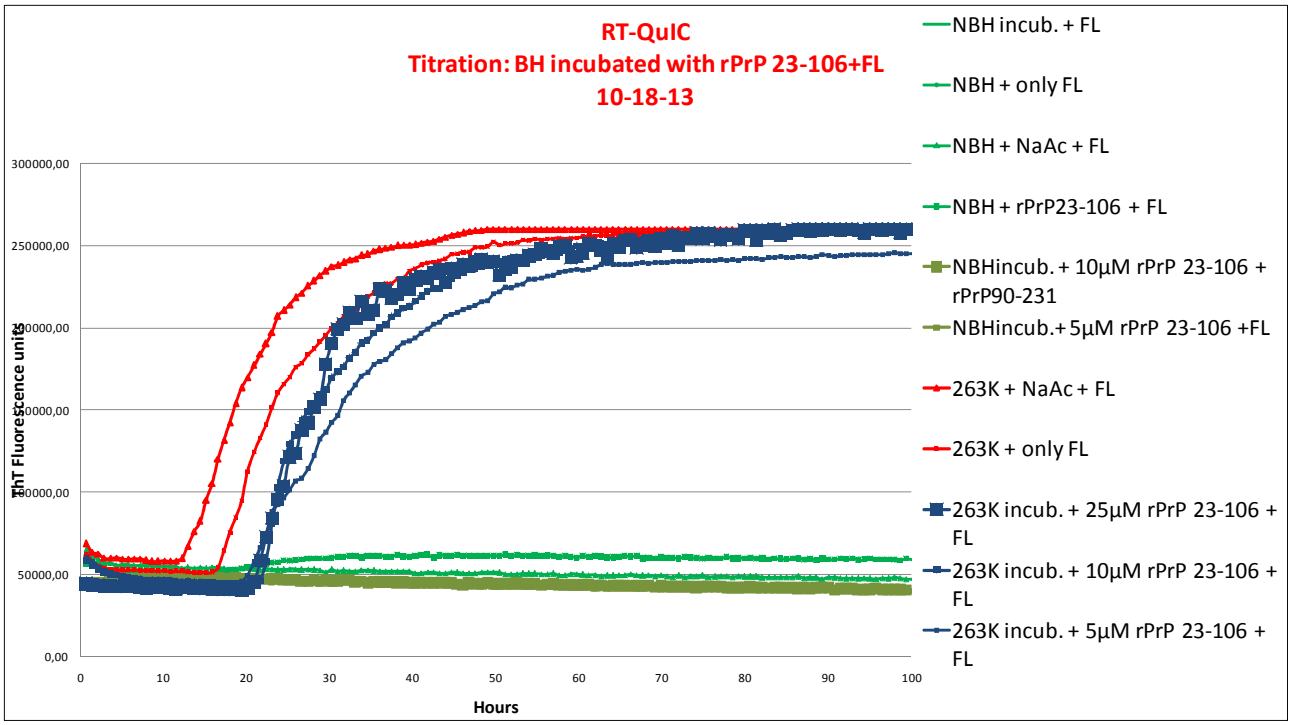

Figura 14. Analysis of the inhibitory capacity of rPrP 23-106 after incubation of [0.2fg/µL] Hamster brain homogenate with three different concentration (25, 10, 5 µM) of this fragment, using FL as substrate.

Therefore, we can conclude that the inhibitory activity of rPrP 23-106 is likely due to its interaction with the substrate (rPrP 23-231).

These results were confirmed in similar experiments using rPrP 90-231 (truncated rPrP) as a substrate in the RT-QuIC reaction (Figures 15 and 16).

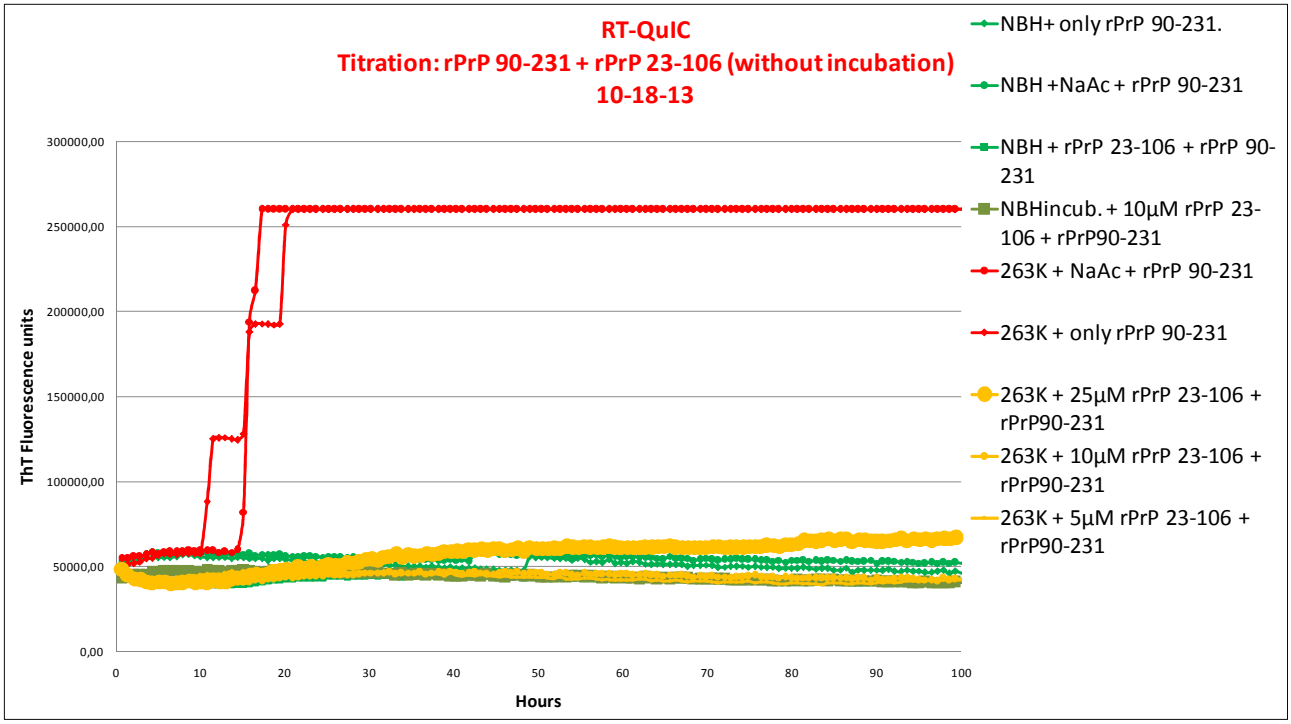

Figura 15. RT-QuIC titration in [0.2fg/µL] Hamster brain homogenate using three different concentration (25, 10, 5 µM) of rPrP 23-106 and the rPrP 90-231 (Truncated, aa 90-231) as substrate.

Figure 15 shows that the 263KBH, untreated and NaAc treated (red), have the same trend. A strong inhibitory activity of the rPrP 23-106 (yellow) was confirmed at all concentrations (5, 10 ,25 µM) with the substrate rPrP 90-231 .

Again, no differences in the kinetics of the reaction were observed using rPrP 90-231 substrate in the conversion reaction of 263KBH pre-incubated (30 minutes) or not with the rPrP 23-106 (Figure 16).

Then I performed two more titration experiments using the rPrP23-231 as substrate: the fragment has proved able to totally inhibit the aggregation reaction at a concentration of 10µM (Figures 17 and 18).

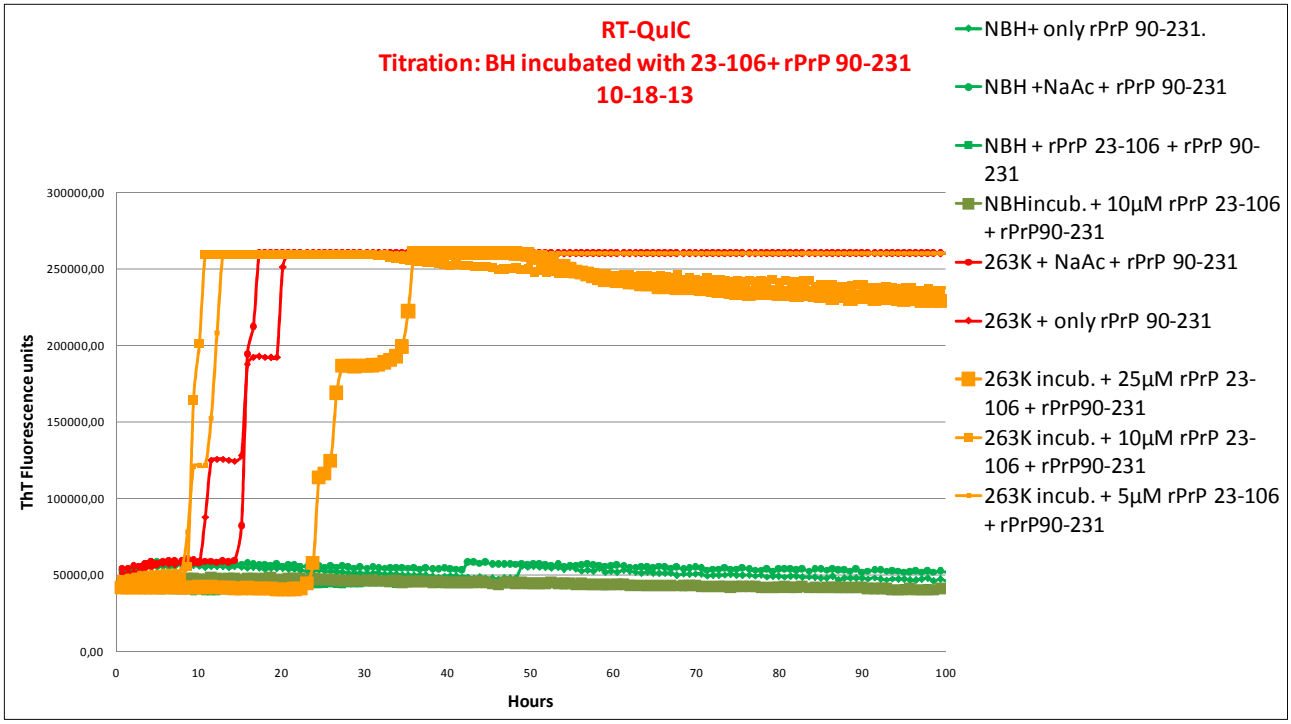

Figura 16. Analysis of the inhibitory activity of the rPrP 23-106 after preincubation (25, 10, 5 µM) with Hamster brain homogenates [0.2fg/µL], using rPrP 90-231 (Truncated, aa 90-231) as RT-QuIC substrate.

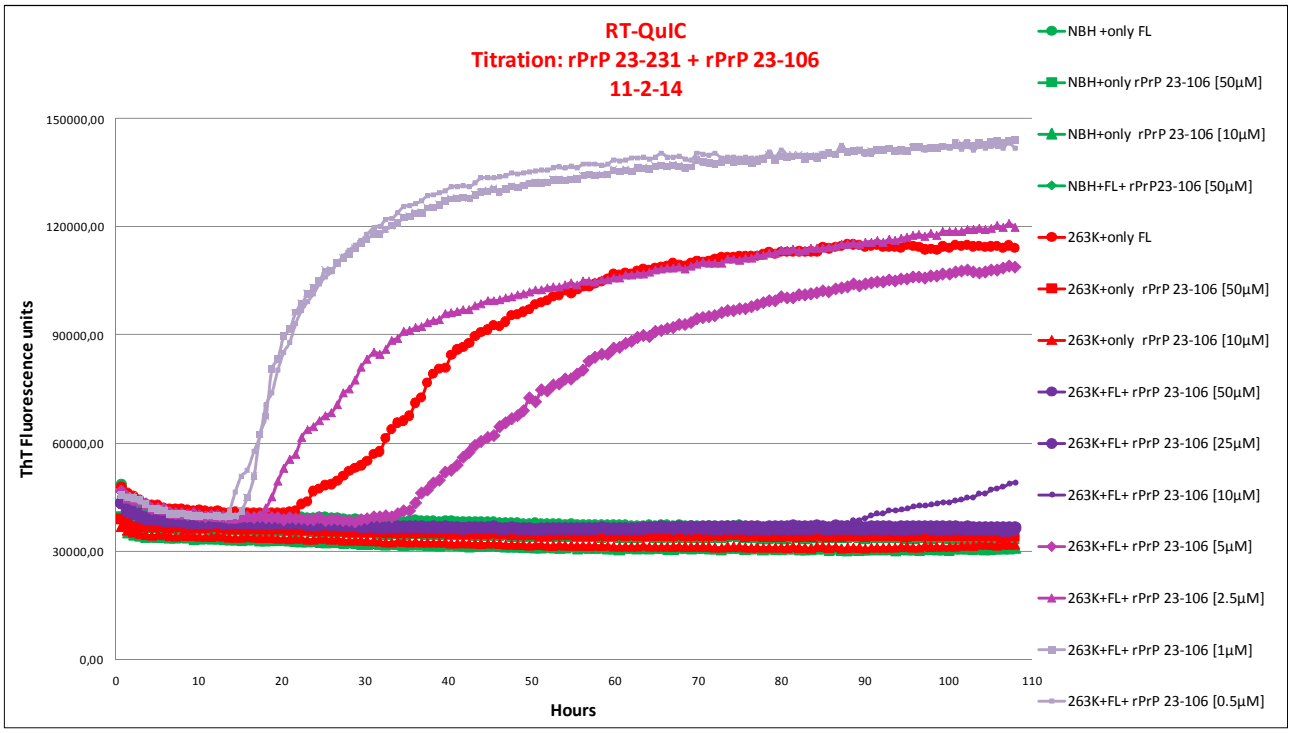

Figure 17. RT-QuIC titration in [0.2fg/µL] Hamster brain homogenate using seven different concentrations (50, 25, 10, 5, 2.5, 1, 0.5 µM) of rPrP23-106 and the Full Length rPrP (FL, aa 23-231) as substrate.

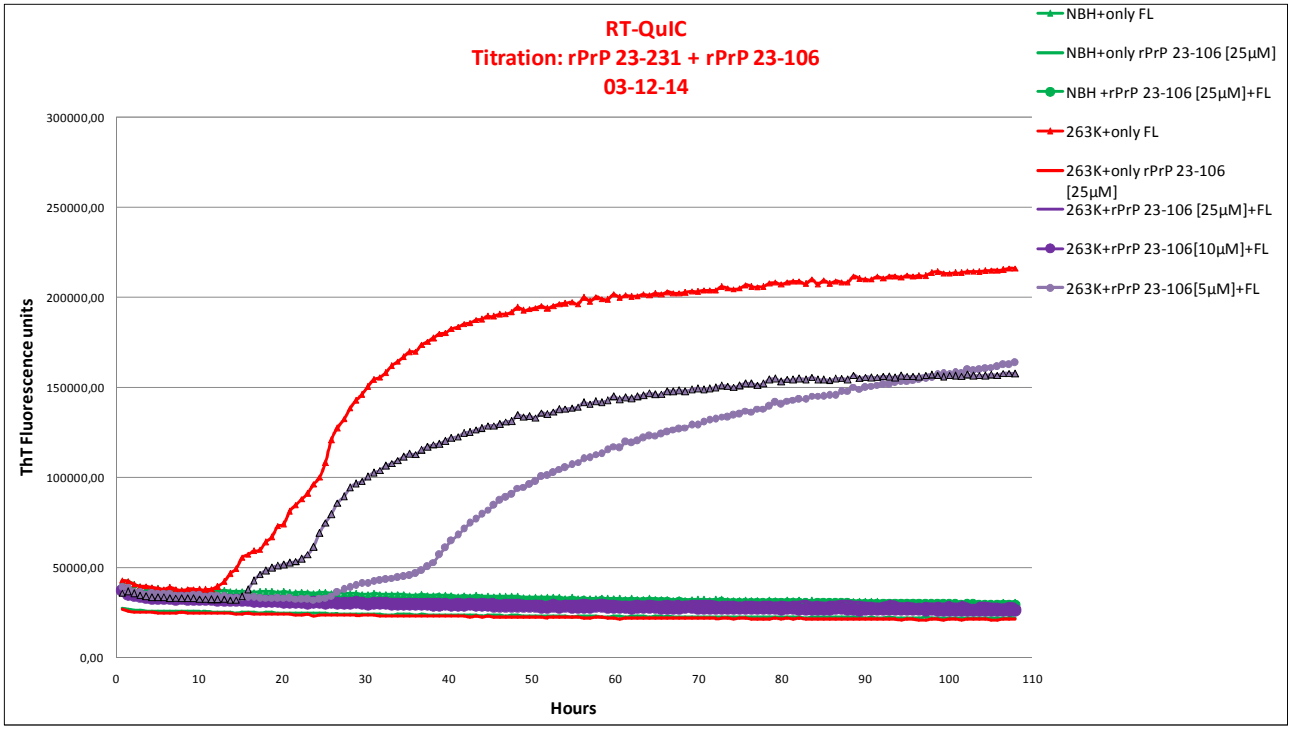

Figure 18. RT-QuIC titration in [0.2fg/µL] Hamster brain homogenate using four different concentrations (25, 10, 5, 2.5 µM) of rPrP23-106 fragment and the Full Length rPrP (FL, aa 23-231) as substrate.

Instead, two further titration experiments, conducted using rPrP90-231 as a substrate, have shown that in this case the compound is less active, leading to a slowing of the reaction at a concentration of 10µM in the first experiment (Figure 19), and of 25µM in the second experiment (Figure 20).

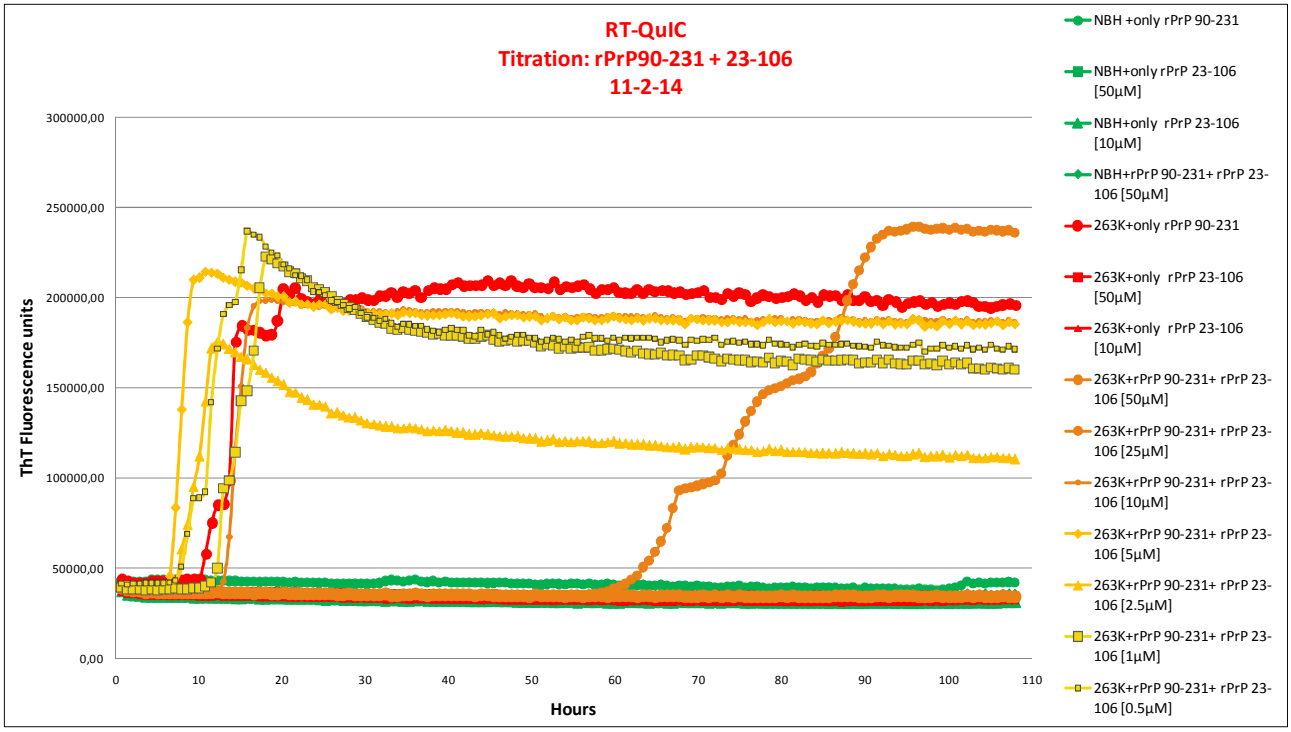

Figure 19. RT-QuIC titration in [0.2fg/µL] Hamster brain homogenate using seven different concentrations (50, 25, 10, 5, 2.5, 1, 0.5 µM) of rPrP23-106 fragment and the rPrP 90-231 (Truncated, aa 90-231) as substrate.

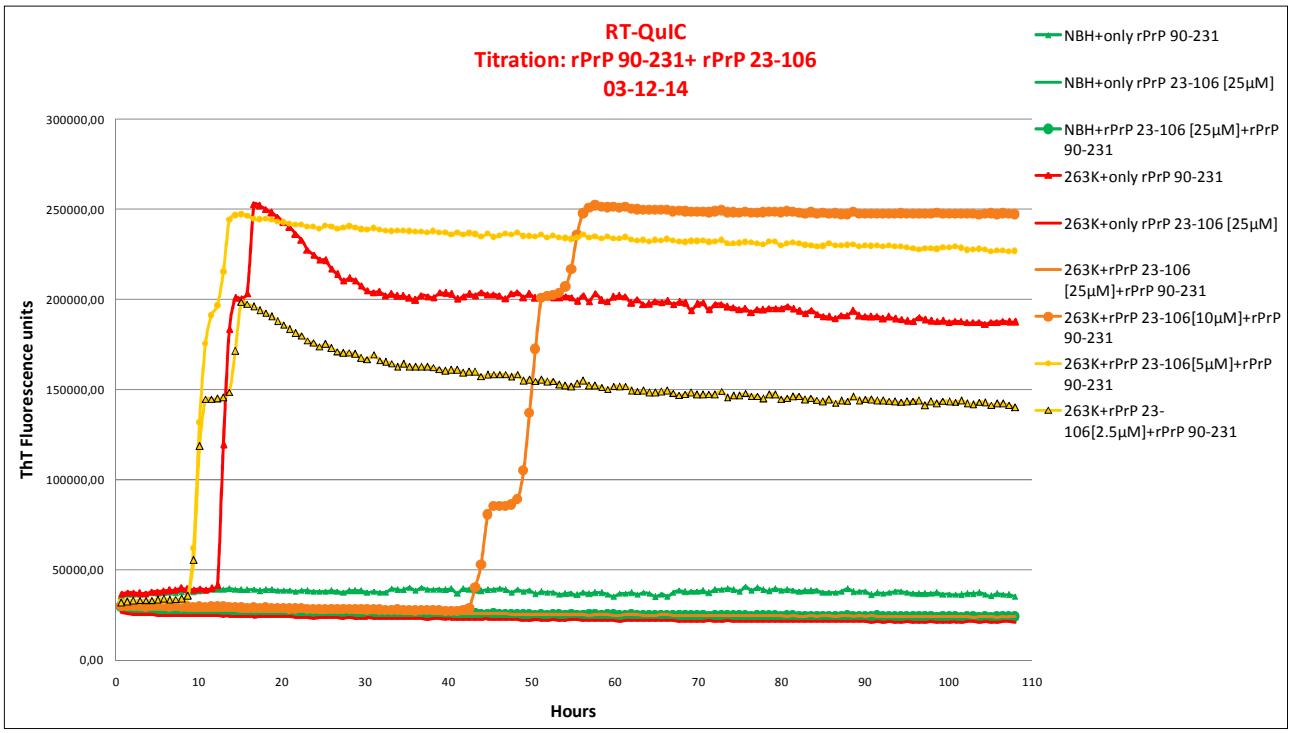

igure 20. RT-QuIC titration in [0.2fg/µL] Hamster brain homogenate using four different concentrations (25, 10, 5, 2.5 µM) of rPrP23-106 and the rPrP 90-231 (Truncated, aa 90-231) as substrate.

1.1.4 Inhibitory effect by Syrian Hamster rPrP 23-106 fragment on prion propagation in mouse neuroblastoma cells persistently infected with hamster-adapted scrapie

Cell-prion in vitro systems, such as mouse neuroblastoma N2a cell lines (N2aSC-) persistently infected with the 22L strains of scrapie (N2aSC+), have been widely used as a model for studying TSEs and for testing potential prion inhibitors. Therefore, I used this prion model in vitro to evaluate if cells grown up to five consecutive passages (P0-P4) in the constant presence of fragment 23-106, gave rise to reduced amounts of PrPSc, up to total loss of the signal of the prion protein. When cell monolayers reached about 90-95% of confluency, were lysed and analyzed with the Western blot method for the presence of PK-resistant bands.

It has been decided to examine two positive controls (N2aSc+ cells not treated with the fragment) treated with PK (SC cells + PK, P0/P4) corresponding to the first (P0), and the last (P4) treatment process carried out (Figure 19; lanes 1 and 2, respectively). The non-glycosylated, monoglycosylated and diglycosylated forms are displayed by the three characteristic bands of the pathogenic prion protein.

Line 3 shows the negative control (N2aSC- cells not treated with the fragment) treated with PK (Sc- cells +PK) corresponding to the P4 treatment process; the absence of bands has confirmed that the cells were not infected for the duration of the experiment.

Lines 4-8 are N2aSc+ cells treated with the fragment and the PK (P0-P4Sc+, +PK) in the five P0-P4 steps ; it was not possible to observe any type of band.

Lines 9-10 show N2aSc+ cells treated with the fragment, but not subjected to digestion with PK during treatment processes P0 and P4, respectively (P0/P4Sc+, -PK); curiously, only the sample (P4Sc +, -PK), showed a strong signal indicative of the presence of protein in the lysate. Instead, the sample (P0Sc+, -PK) is devoid of protein signals, probably due to a non-specific lysis, which could be due to the treatment with the trypsin used to resuspend the cells.

Lines 11-12 show N2aSc- cells treated with the fragment and subjected to digestion with PK during treatment processes P0 and P4, respectively (P0/P4Sc-, +PK); the absence of the bands confirms the absence in the cells of infected proteins.

Lines 13-14 show N2aSc- cells treated with the fragment but not subjected to digestion with PK during treatment processes P0 and P4, respectively (P0/P4Sc-, -PK); also in this case, only the sample (P4Sc-, -PK), showed the proper signal of non-infected cells, albeit weak, indicative of the presence of cellular proteins in the lysate. Instead, the sample (P0Sc-, -PK), devoid of signal, confirmed that the process of lysis on the sample corresponding to the passage of P0 treatment, has probably undergone a non-specific digestion of proteins.

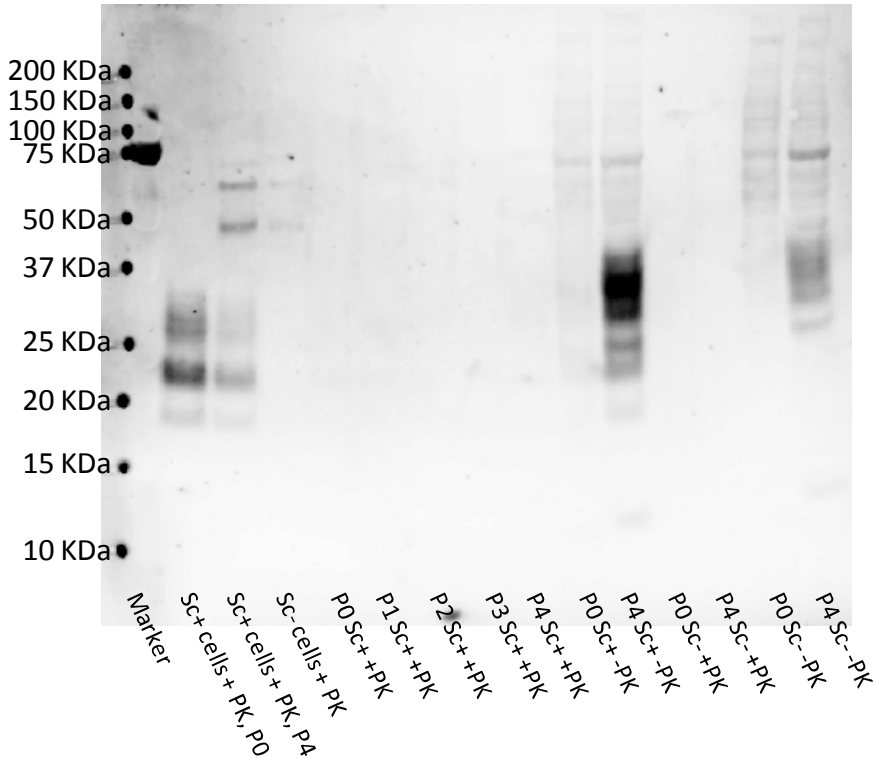

Figura 19. Proteic pattern of N2aSc- and N2aSc+ cells after treatment with the Syrian Hamster 23-106 fragment. The primary antibody used is 6D11 antibody, which recognizes the region into aa 93-109 of the prion protein.

1.2 Conclusions

The Syrian Hamster rPrP 23-106 fragment was used to evaluate its ability to inhibit the amyloid aggregation process and reduce the amount of PrPSc in scrapie-infected cell cultures.

RT-QuIC experiments have shown variable results. The fragment seemed to inhibit the process of aggregation at concentrations between 5µM and 25µM, both when using the Full Lenght (FL: rPP23-231), and when using the Truncated (rPrP90-231) as substrate. Moreover, it would seem that, when positive controls containing rPrP23-231 as substrate show a slowed trend, higher concentrations of the fragment are required in order to perform its activities. This could either be caused by an abnormality in the substrate used in the experiment or to other reaction components.

In the analysis carried out using as a seed the brain homogenate of human patients suffering from the disease of Sporadic Creutzfeldt-Jakob (sCDJ), it was observed that, even if the peptide was seeded at a concentration of 23.5µM, the reaction was not entirely inhibited, as in previous cases, but only slowed. This could indicate that the fragment probably exerts greater activity only when incubated in the presence of specific recombinant proteins, probably of the same species from which the fragment was derived.

Experiments performed with the fragment at three different concentrations (5, 10, 25 µM), have shown inhibitory activity at all concentrations. In parallel, experiments were conducted in which the fragment 23-106, instead of being used as a substrate during RT-QuIC assay, it was pre-incubated with the seed (hamster brain homogenate) and then added to normal RT-QuIC mixtures (rPrP23-231 and rPrP90-231 as substrate, without rPrP 23-106): in this case, all fragment concentrations (5, 10, 25 µM), contrarily showed positive reactions to the ThT, similarly to the positive control (ie seed not preincubated with the fragment). This suggests that the inhibition

appears not to be due to the binding of rPrP23-106 fragment to the seed, but to its interaction with the substrate.

The observation that 1) the inhibition appears to be due to the fragment interaction with the substrate; 2) reactions are almost completely inhibited at a concentration of 25µM in the hamster, while in humans almost at the same concentration (23.5µM), are slowed only; and 3) higher concentrations of the fragment were necessary when the control reaction was slowed down, altogether suggesting that the inhibitory role strongly depends on the conformation of the substrate. In this regard, one might think that the fragment can bind the rPrP in regions that serve as the attachment point for other proteins during the aggregation process. Slight modifications of the recombinant protein, may for example facilitate, or conversely make it difficult, the bond with the fragment. The model PIRIBIS (parallel in-register intermolecular β-sheet) proposed by Byron Caughey et al (Groveman et al., J Biol Chem. 2014), in which the proteins are superimposed one on the other, could be consistent with this theory.

Since inhibition was observed in the experiments RT-QuIC, we decided to analyze mouse neuroblastoma cells (N2aSc- and N2aSc+) to assess whether the same trend is observed in a system closer to *in vivo* systems. The Western blot analysis of cell lysates treated for five passages (P0-P4) with the fragment, seems to suggest that the fragment leads to a loss of PrPSc. In fact, the negative (N2aSc-) and positive (N2aSc+) samples were confirmed as such, for the absence and presence of bands following treatment with PK, respectively. Interestingly, P1-P4 lysates of cells N2aSc+ treated with the fragment, were similar to the negative control, because showed no bands after PK digestion. In conclusion, these preliminary findings suggest a possible inhibitory role of the fragment 23-106 in the process of conversion / aggregation of the prion protein, probably due to an interference of that fragment in the process of overlapping of PrPSc protein monomers, one above the other.

Unfortunately, despite the maximum accuracy payed to each step of the protocol in repeated experiments, the results were quite variable (inhibitory activity varied between 5 and 25um in RT-QuIC experiments); thus, further experiments are needed to understand the reasons of data variability and obtain totally reproducible results. Moreover, the size of N-terminal fragment of PrP may be too large to find a clinical application in the human TSEs; consequently, before proceeding in this direction, positive data of the pharmacodynamic and pharmacokinetic properties of the N-terminal region are required.

2. PrPSc structure: the central hairpin

The PIRIBS (Parallel In-Register Intermolecular Beta Sheet) structure, which has recently been proposed for PrPSc amyloid fibers (Groveman et al., J Biol Chem. 2014) is characterized by the parallel overlapping in-register of PrPRes molecules; each molecule is perpendicular to the fibril, by occupying the entire cross section, and is connected to the one below and above by intermolecular beta-sheet structures.

Several studies has indicated that most of the secondary helical structure of rPrPC (in particular the domains originally occupied by helices 2 and 3 and also the N-terminal residues 113-125 and 130-140; see Fig 1) can fold into parallel in-register intermolecular beta sheet structures, both spontaneously in vitro and in native conditions-like (Adrover et al., J Biol Chem. 2010).

The use of Fourier Transform Infrared Spectroscopy (FTIR) and mass spectrometry of H / D exchange for comparing the fibrils of rPrP generated spontaneously in vitro with the fibrils derived from the infected brain, would seem to confirm that, even in the latter case, there is a greater helical folding of the domains in both the N-terminal and C-terminal portion.

Parallel intermolecular β-sheet structures were also observed in some of yeast prions and in the case of Aß amyloid peptide (Toyama and Weissman, Annu Rev Biochem. 2011).

The studies conducted on the PIRIBS structure, have involved experiments on oligomer constructs of rPrP 90-231, which were subjected to energy minimization and molecular dynamics simulations. The results confirmed the biochemical and biophysical data that were obtained on the amyloid fibrils of prion-seeded rPrP 90-231: residues ~ 124-227 have maintained a more ordered and tightly packed structure than residues ~ 90-120; in particular, the C-terminal region 160-231, has preserved most of the β-sheet originally present.

These constructs were analyzed in the presence or in the absence of disulfide bridges on the pairs of residues: 127-161, 135-153, 140-145, 179-214 and 190-195. Artificial disulfide crosslinks within PrPC, compatible with PrPC secondary structures as well as with PrPRes formation in RML scrapie-infected cells, were described by Hafner-Bratkovic et al., J Biol Chem. (2011). These authors have interpreted their results to mean that the native PrPC secondary structure domains containing these residues, including the α-helices, are retained in PrPSc. However, these bridges may be also compatible with the formation of two different kind of hairpin in a parallel in-register β-sheet intermolecular configuration: an hairpin indicated as native disolfure (ND), since contains the disulfide bridge present in the physiological PrPC, and the hairpin comprising residues 127-161, here indicated as the central hairpin.

In this case, the term "β-hairpin" thus refers to a structure in which the bond occurs along the axis of the fibrils, between intermolecular hairpins, and not the classical β-hairpin in which the link occurs within of the same molecule.

Furthermore, studies on PIRIBS model suggest that variations in the relative orientations of β-sheets, hairpins and loops, may lead to different conformers, or to distinct prion strains.

Other groups have shown by ssNMR analysis that polymorphisms within the amyloid could lead to the displacement of β-sheets, while maintaining the architecture and global features (Jones et al., J Biol Chem. 2011; Wickner et al., FEMS Yeast Res. 2010). These structures could propagate faithfully via a nucleated polymerization mechanism in which the incoming PrP molecules would align along the template established by the polypeptide backbone of the preceding molecule at the end of the fibril (Wickner et al., FEMS Yeast Res. 2010). Indeed, nucleated polymerization in highly α-helical models seems more difficult as much smaller portions of incoming PrP molecules could contact the fibril template.

Analysis with Electron micrograph (EM) of amyloid fibers scrapie-associated, show axial elements within which the dye is often accumulated; most authors consider such structures as parallel

protofilaments, each containing one or more molecules PrP (Govaerts et al., Proc Natl Acad Sci U S A. 2004; DeMarco and Daggett, Proc Natl Acad Sci U S A. 2004).
However, such structures may actually be a single filament composed by a variety of overlapping molecules, characterized by the presence of one or more hairpins interconnected by flexible portions, indicated as "hinges", creating a type of conformation "stalk celery "or" half pipe ", inside which the dye could accumulate. In particular, the region between the central hairpin and the native hairpin, housing the binding sites of glycans, could represent a hinge, whose width varies according to the presence or not of them.
Fibrillar sub-structures have been observed with EM and are interpreted by most authors as individual protofilaments. Instead, according to the PIRIBS architecture, similar structures might result from proteolytic cleavage in the hinge regions that determine a complete separation of central and native hairpins.

With the aim of get better insight on the prion fibril structures I used the central hairpin region (aa127-161) of PrP to investigate if: i) only this portion of the protein was capable to aggregate spontaneously into fibrils; ii) the fibrils were generated in a beta sheet conformation, confirming the PIRIBS model;and thus iii) the EM images would show only fibrillar sub-structures (i.e. devoid of accumulated dye), further supporting the hypothesis implying proteolytic cleavages in the hinge, between central and native hairpins.
For the study of this region, peptide fragments, with and without the disulfide bridge between the Cysteine amino acids in the extremities (referred to hereinafter 127CC and 127notCC, respectively), comprising the entire amino acid sequence 127-161 have been analyzed. Since the position of the disulfide bonds is based on studies conducted in mice, we thought that in the hamster could involve amino acids of different positions, due to the lack in the mouse of an amino acid in position 55 which determines a shift of the amino acid sequence; consequently, were analyzed two additional peptide fragments containing a greater number of amino acids in the C-terminal portion: the amino acid sequence 128-164, with and without the disulfide bridge (referred to hereinafter 128CC and 128notCC).

2.1 Results and Discussion

2.1.1 RT-QuIC analysis of peptides from central hairpin

The fragments 127 CC, 127not CC, 128CC and 128notCC were used in the RT-QuIC mix as substrates of the reaction:

The negative and positive control of the reaction are represented by incubation of the full-length protein rPrP23-231 (one of the classic substrates in the reactions of RT-QuIC) with hamster brain homogenate, uninfected (NBH) and infected (263K), respectively (Figure 17). Both samples have confirmed the reaction as expected: the negative control showed no positive signal to the ThT for the duration of the experiment (110 hrs); the positive control showed positive signal to the ThT, but with a slowed down trend compared to the classical one. The choice of a high concentration of brain homogenate (20pg/µl 263K), in order to promote contact of PrPSc with the peptides (ie a template-driven propagation), may have caused the "choking" of the reaction due to an excess of the reagent, causing a slowdown in the curve of the positive control.

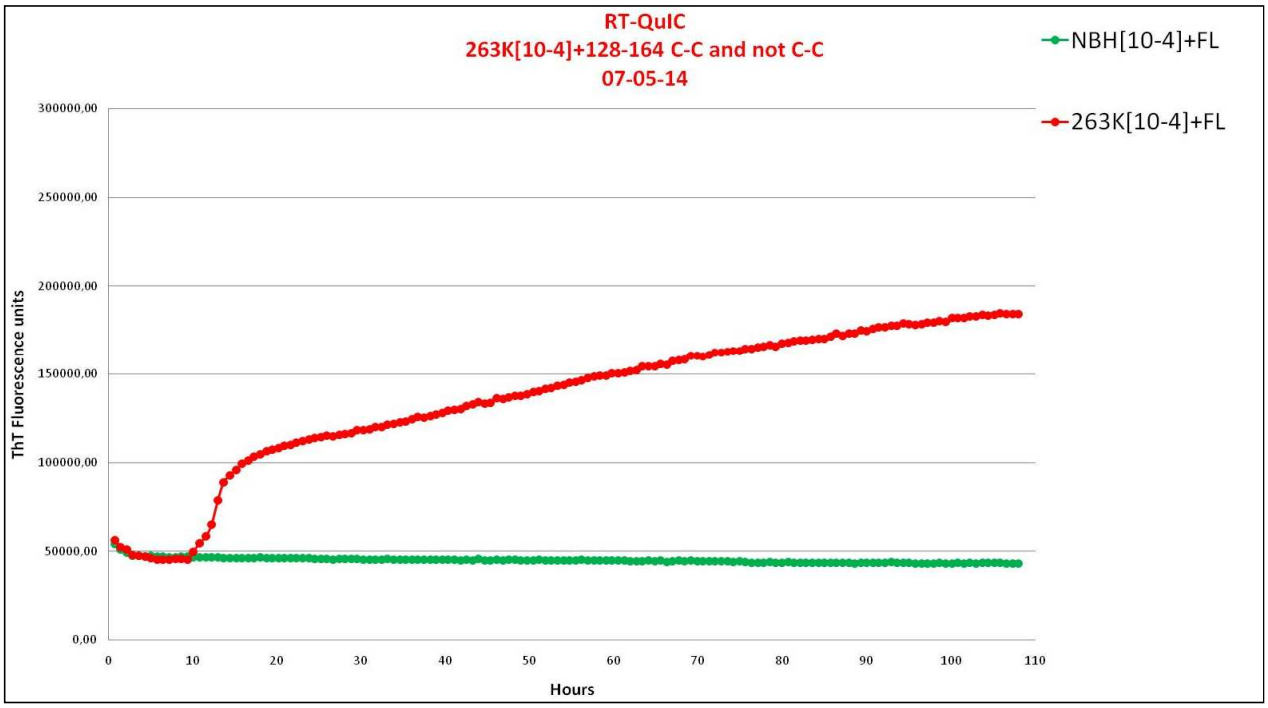

Figure 17. RT-QuIC analysis of control reactions. Along the abscissa axis is reported the time within which the reaction was monitored; in the axis of ordinates are represented the fluorescence values of ThT for the four wells in replicated. Over a period of 110 hrs, the negative control (rPrP23-231 incubated with the NBH, in green) showed a rectilinear trend non-increasing, confirming the specificity of the reaction. The positive control (rPrP23-231 incubated with 263K, in red), confirmed the infectivity of the brain, showing an increasing trend, although slowed down due to the excessive concentration of seed.

The peptides 128notCC (Figure 18) and 128CC (Figure 19) showed a similar trend, both in the incubation with the NBH and with 263K. The concentration of 0.1mg/ml was found to be the optimal one in this type of reaction, because the positive signal to the ThT, and then the probable formation of fibrils, is displayed after a short latency period, less than five hours. The differences observed between the two peptides are not statistically significant as they fall within the range of variability of the reaction, usually including in ten hours.

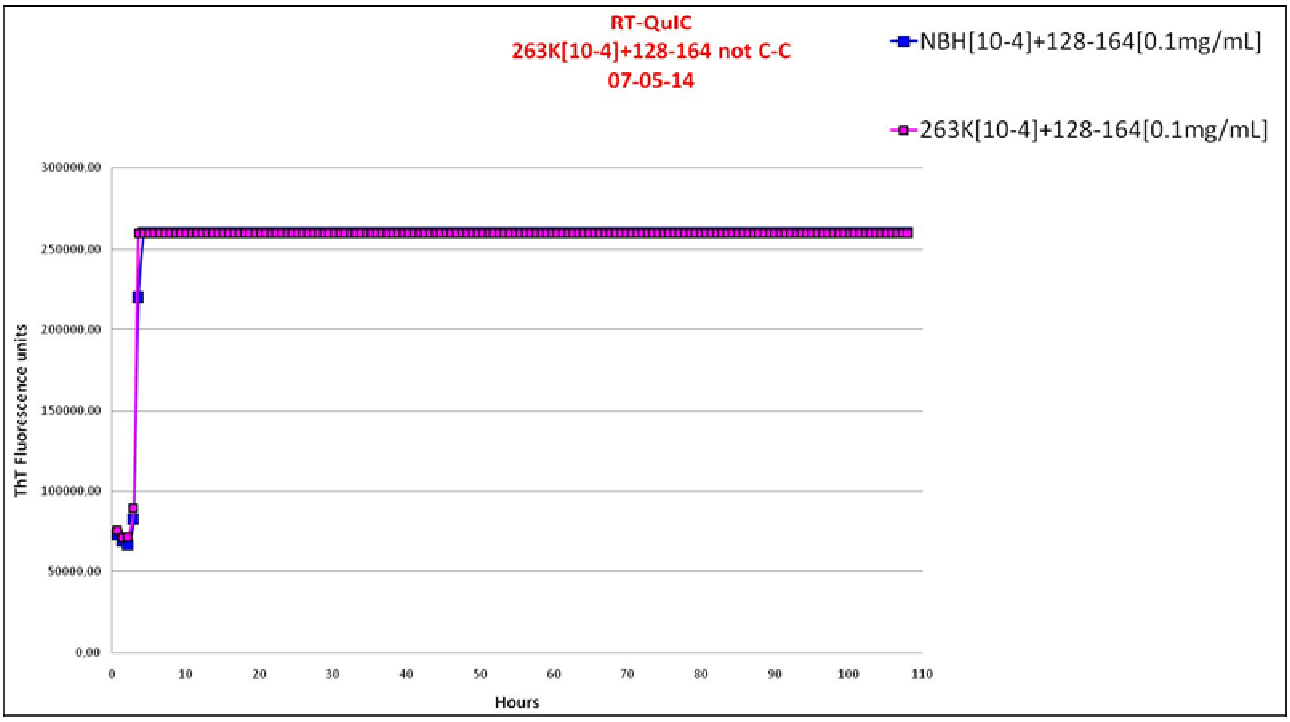

Figure 18. Peptide 128notCC incubated in the presence of NBH (in blue) or 263K (in pink) and analyzed by RT-QuIC. The reaction showed the formation of fibrils after an incubation period of less than five hours.

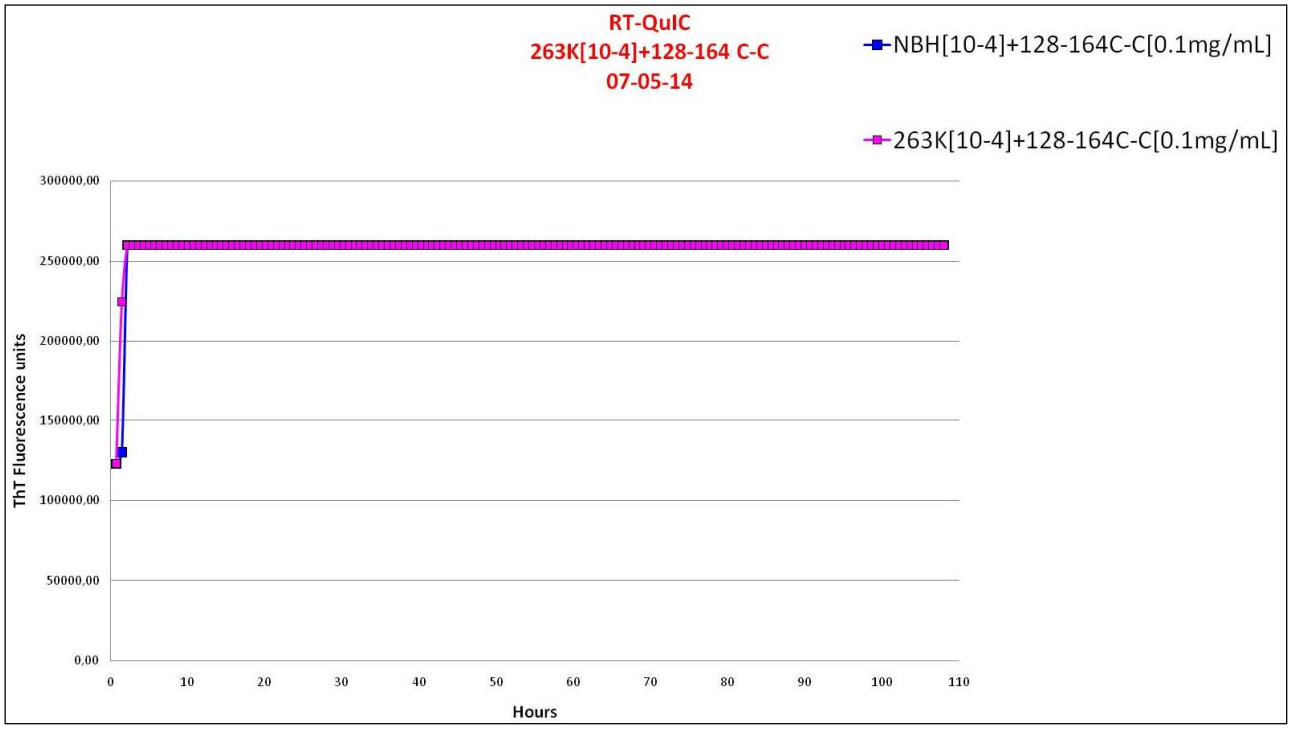

Figure 19. Peptide 128CC incubated in the presence of NBH (in blue) or 263K (in pink) and analyzed by RT-QuIC. The reaction showed the formation of fibrils after an incubation period of less than five hours.

Peptides 127notCC (Figure 20) and 127CC (Figure 21) showed a completely different trend. At a concentration of 0.1 mg/ml, the positive reaction to the ThT has been observed only in the case of the fragment devoid of disulfide bridge, and took place after a short latency period, before ten hours; instead, in the case of the fragment with the disulfide bridge, it was not observed any positive reaction within 110 hrs.

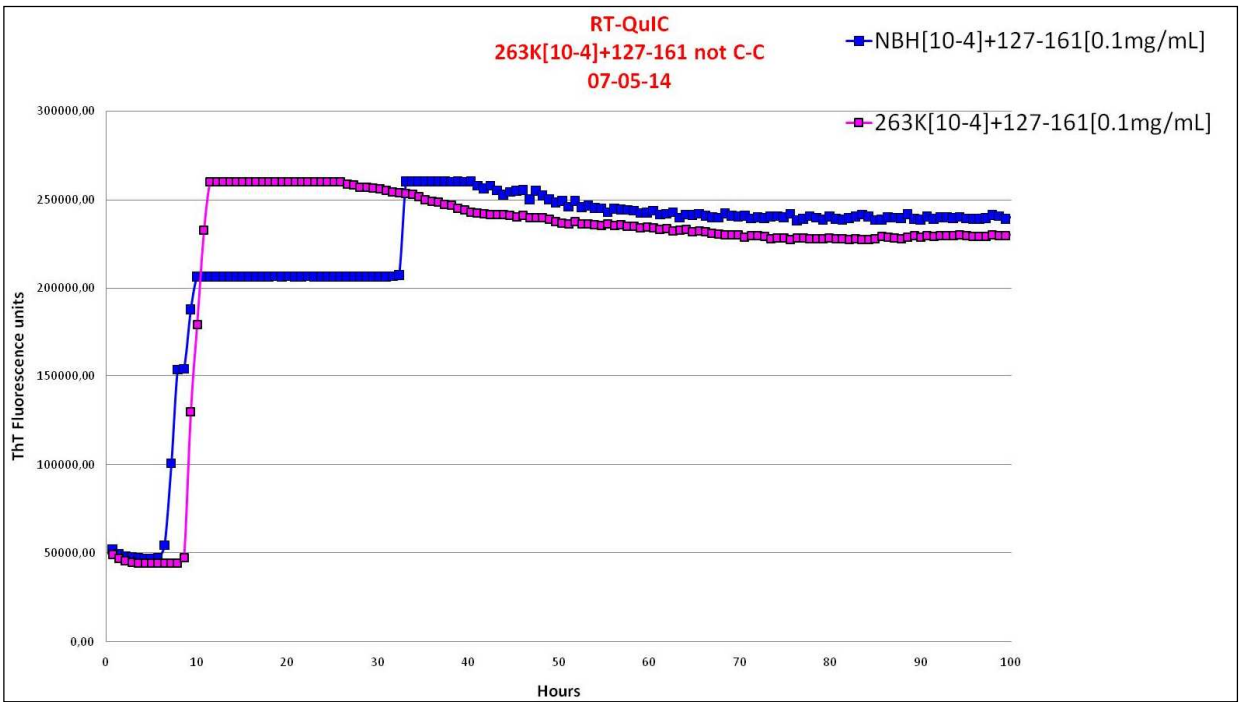

Figure 21. Peptide 127notCC incubated in the presence of NBH (in blue) or 263K (in pink) and analyzed by RT-QuIC. The reaction showed the formation of fibrils after an incubation period of less than ten hrs.

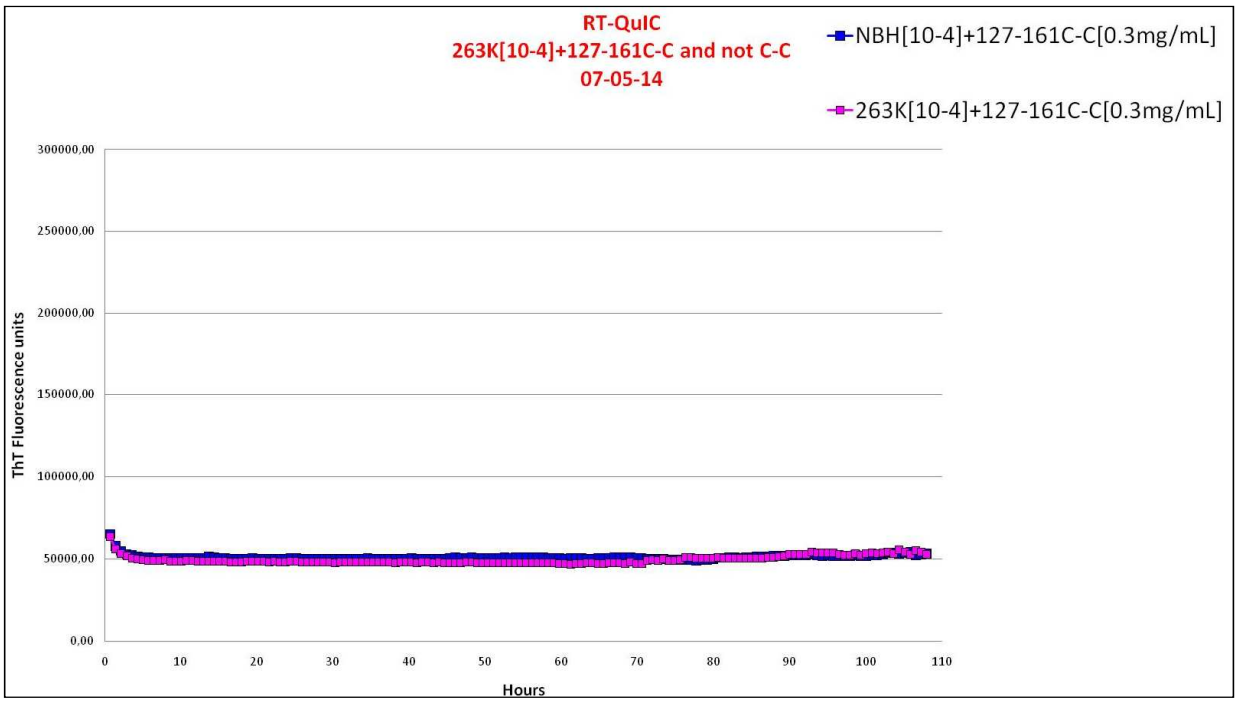

Figure 21. Peptide 127notCC incubated in the presence of NBH (in blue) or 263K (in pink) and analyzed by RT-QuIC. The reaction has not showed any formation of fibrils.

Peptides 128CC and 128notCC were able to form fibrils much more quickly than the 127notCC peptide. At the concentration of 0.05mg/ml, the peptide 128CC shows a positive reaction in a time span of about 5 hours (blue and pink lines), while the peptide 127notCC shows a weak positive reaction, but only after 30 hours of incubation with 263K (only 1/4 positive wells at 110 hours, green line) or after 55 hours of incubation with the NBH (only 2/4 positive wells at 110 hours, yellow line).

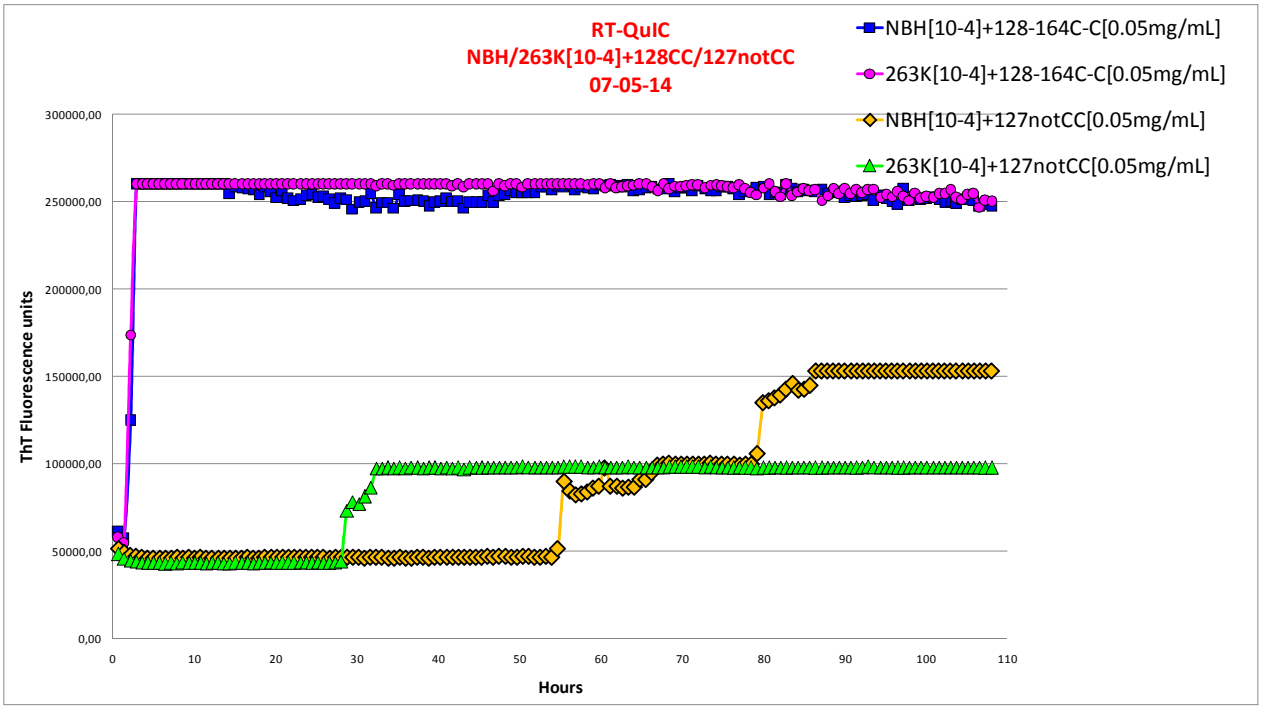

Figure 22. Comparative analysis by RT-QuIC of the peptide 128CC (incubated with the NBH, in blue, or with 263K, in pink) and the peptide 127notCC (incubated with the NBH, in yellow, or with 263K, in green) at 0.05 mg/ml. The reaction takes place immediately for the peptide 128CC, while occurs with difficulty with the peptide 127notCC.

2.1.2 Western blot analysis of peptides from central hairpin

The Western Blot analysis of all RT-QuIC products with the peptide 128notCC (ie incubated with NBH and 263K) at a concentration of 0.1 mg/ml, were completely digested by PK (Figure 23, b). At a concentration of 0.2 mg/ml, the control (ie peptide not subjected to RT-QuIC) showed a band slightly above to 3.5 kDa in the absence PK treatment (Figure 23 a), and no bands after treatment with PK; the peptide at the same concentration incubated with the 263K in RT-QuIC experiments showed a faintly visible band at 3.5KDa also following treatment with PK (Figure 23, b). At a concentration of 0.3mg/ml, in the absence of treatment with PK, the band was observed just above the 3.5KDa in all three cases (peptide and RT-QuIC products incubated with NBH and 263K, Figure 23 c); following treatment with PK, the band was lost in the case of 3mg / ml, whereas both RT-QuIC products are visible exactly in correspondence of 3.5KDa (Figure 23 d).

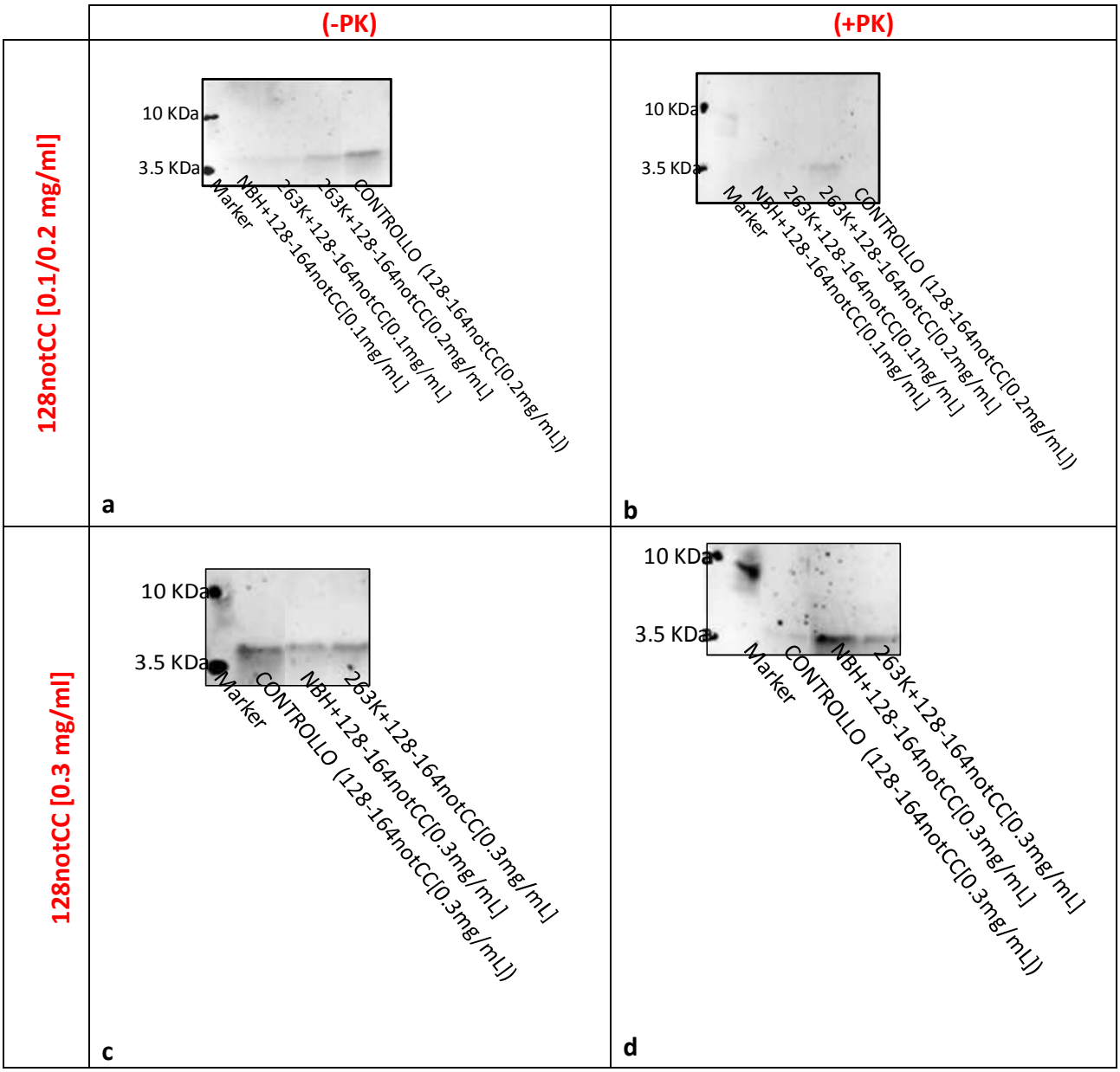

Figura 23. Western blot analysis of 128notCC peptide incubated with NBH and 263K. In the left column, were reported samples that have not been subjected to digestion with PK; on the right, are shown the corresponding samples treated with PK. In the first row (Figures a, b), were placed the samples to the concentration 0.1 mg / ml and 0.2 mg / ml; in the second line (Figures c, d) samples at a concentration of 0.3mg/ml.

The peptide 128CC confirms the results obtained with the peptide 128notCC: at a concentration of 0.3mg/ml, in the absence of treatment with PK, the band was in all cases (peptide stock and samples incubated with the NBH or 263K) observable at 3.5KDa (Figure 24, a); following treatment with PK, the band was lost in the case of the peptide stock at 3mg/ml, while RT-QuIC products were visible in correspondence of 3.5KDa (Figure 24, b). The peptide 128notCC was analyzed in the same experiment (data not shown), but did not reveal any band. It is known that PrPSc is characterized by the tendency to adhere to the tube, then 128notCC may have such properties; alternatively, the 128CC signal may be too strong and to cover 128notCC.

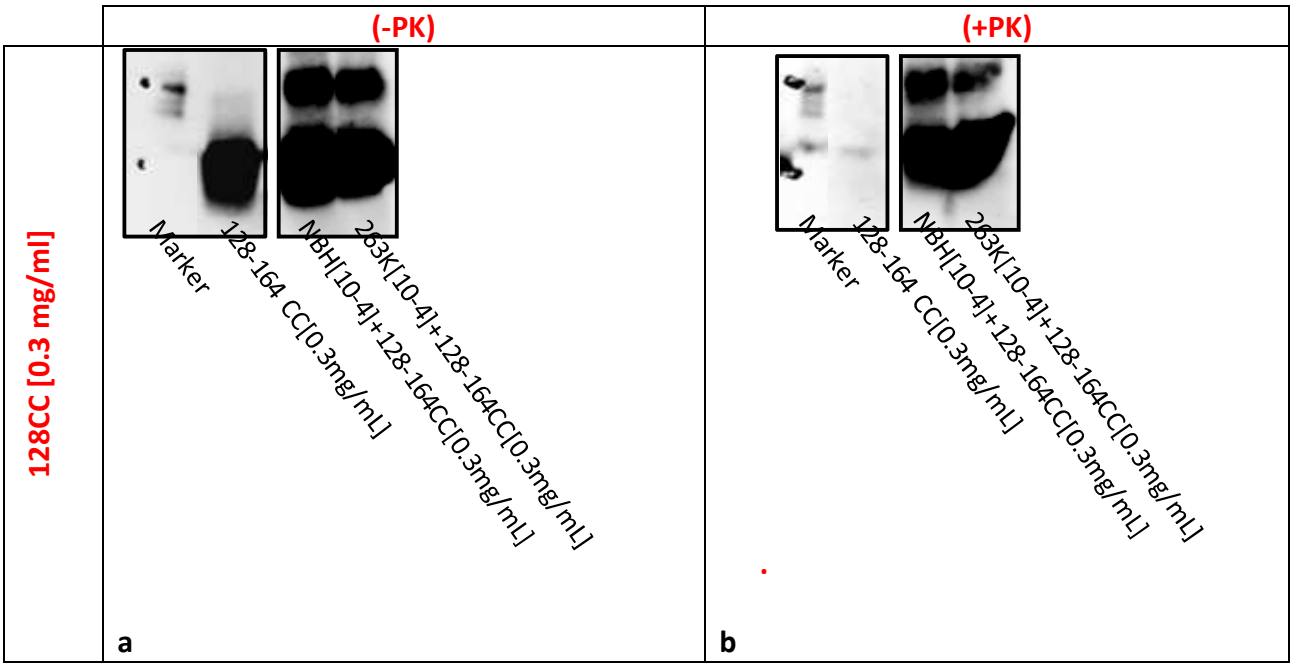

Figura 24. Western blot analysis of 128CC peptide incubated with NBH and 263K. In the left column, were reported samples that have not been subjected to digestion with PK; on the right, are shown the corresponding samples treated with PK. The analysis was performed on the sample at a concentration of 0.3mg / ml.

The 127notCC peptide showed no bands; having been analyzed with the peptide 127C, as for the case of the peptide 128notCC, the explanations may be the same.

The 127CC peptide at a concentration of 0.3mg / ml showed the expected band in all three cases, both in the absence and in the presence of the PK treatment (Figure 25, b). In this case the differences observed between 127CC peptide and 128notCC and 128CC peptides appeared less pronounced and more difficult to interpret because bands appear to be different even before the PK treatment, reason for which it is difficult to perform any type of comparison.

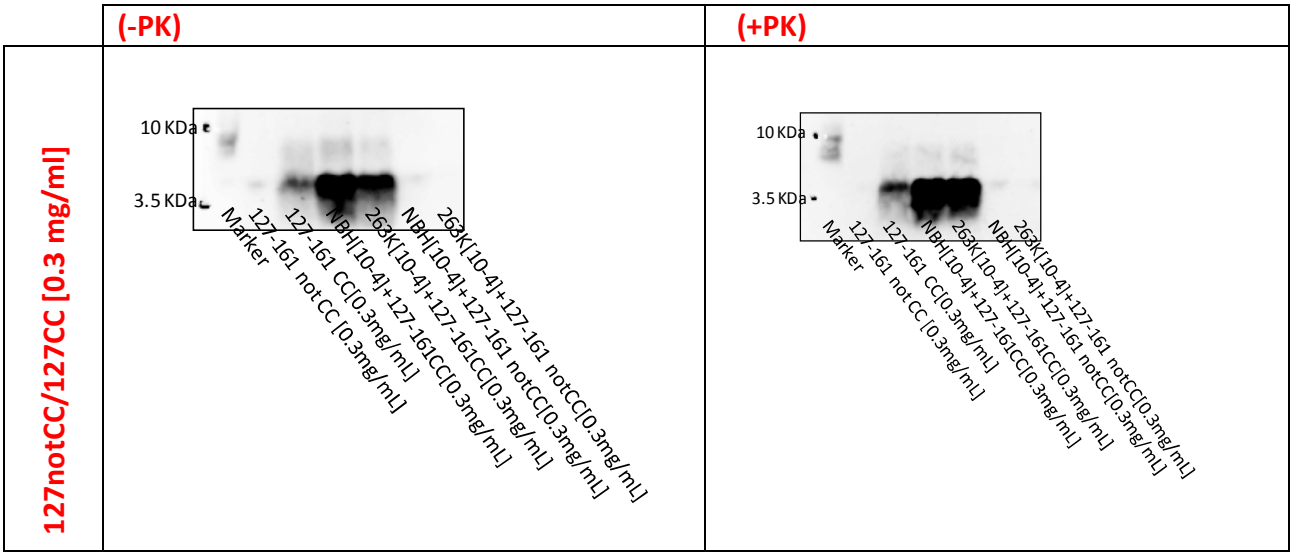

Figura 25. Western blot analysis of 127notCC and 127CC peptides incubated with NBH and 263K. In the left column, were reported samples that have not been subjected to digestion with PK; on the right, are shown the corresponding samples treated with PK. The analysis was performed on the sample at a concentration of 0.3mg/ml.

2.1.3 EM analysis of central hairpin peptides

The EM analysis of the RT-QuIC products with 0.1mg/ml of 128notCC peptide showed fibrils very weakly defined when incubated with the NBH (Figure 26, a); instead, the samples incubated with the 263K showed fibrillar EM structures better defined. In the latter case it was possible to measure the thickness of a fibril, presumably single, corresponding to 19nm (Figure 26, b);

New RT-QuIC mixtures were created in order to improve the capacity of isolation of the individual fibrils: 128notCC was incubated with a higher concentration of control and 263K brain homogenate with the aim to promote the process of template-driven propagation, ie the formation of amyloid fibrils as a result of contact of the peptide with the protein of the infected BH. In order to avoid that the fibrils would be fragmented, the new mixtures have not been subjected to agitation, and the incubation temperature was lowered from 42°C to 37°C so as to make the conversion process slower and avoid the formation of clusters that make difficult the EM observation. The peptide has been brought to the maximum possible concentration for the reaction (0.42mg/ml), in order to facilitate the process of fibril formation. Compared to the previous analysis, the fibrils were better defined, although they were more aggregated but less ordered in the samples incubated with the NBH than in those incubated with 263K (Figure 26, c, d). Incubations with 263K resulted in a large number of isolated fibrils, their thickness varying between 3.8 and 11.5nm, and some of which characterized by the classic twist.

To obtain a good compromise between formation of isolated fibrils and relatively short incubation times, it was decided to incubate the samples at 37 ° C but at a speed of 300rpm. The mixture led to the formation of fibrils in a few days in the case of the samples incubated with 263K, while it was not possible to observe fibrils in the same period of time in the samples incubated with NBH. The thickness of 128notCC fibrils in this case ranged from 4.52nm to 11.2nm (Figure 26e).

	RT-QuIC mix+NBH	RT-QuIC mix+263K
128notCC [0.1 mg/ml]	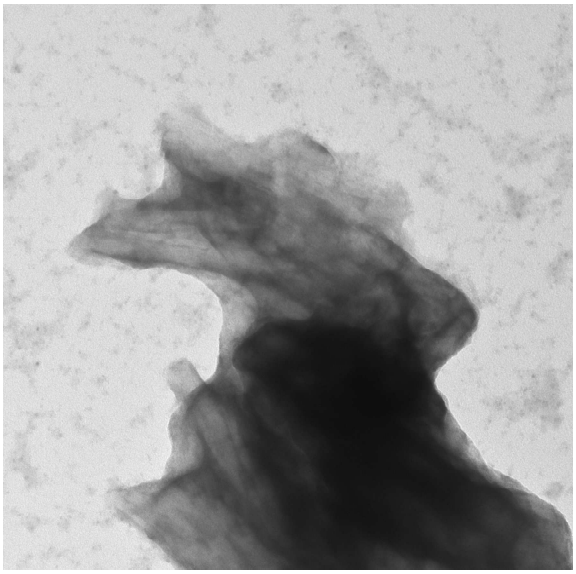 a	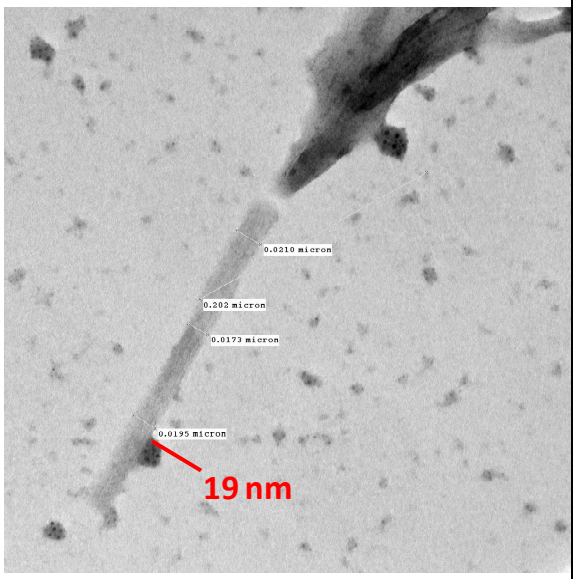 b

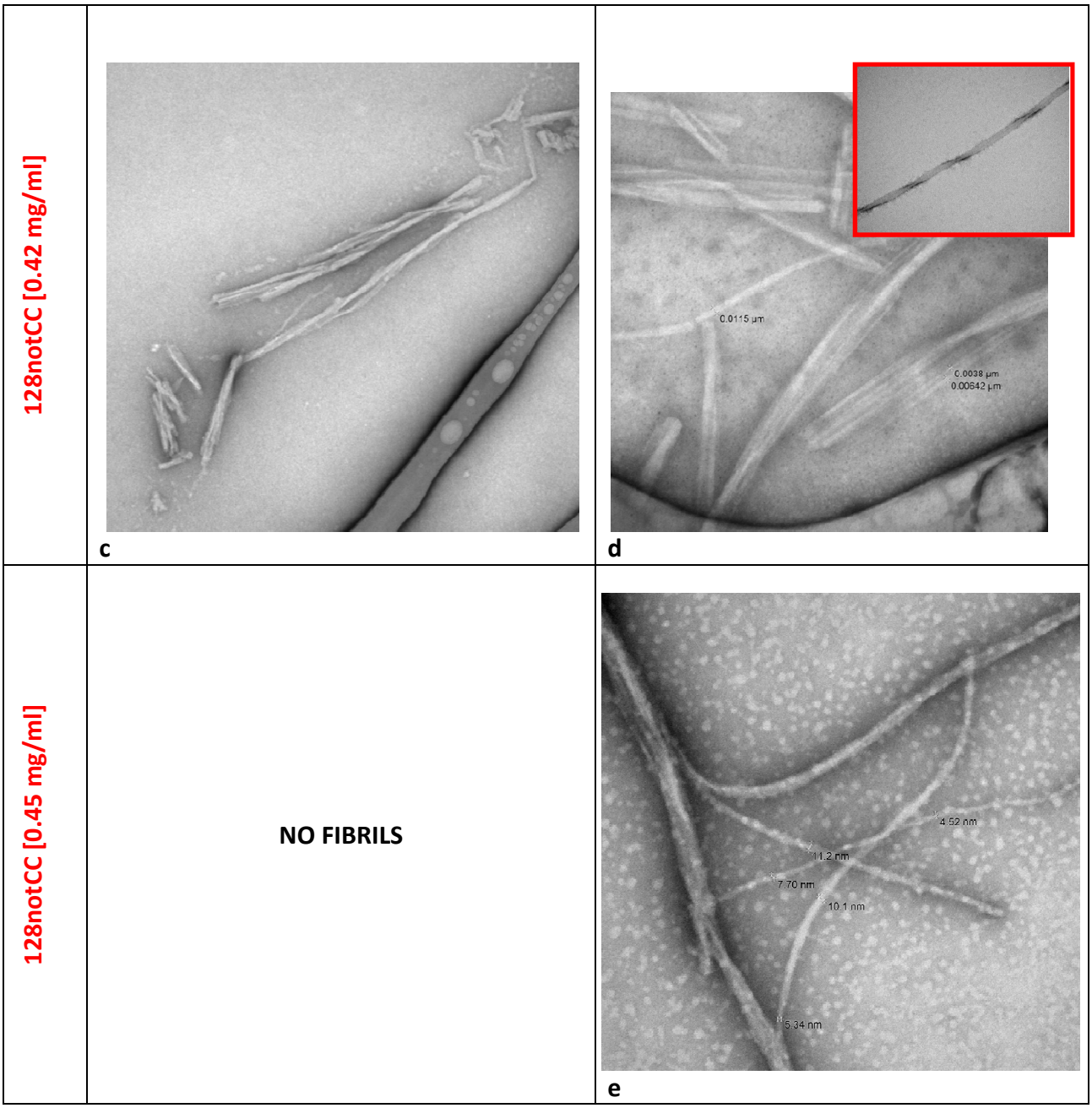

Figure 26. Peptide 128notCC analyzed by EM at the concentrations 0.1 mg/ml, 0.42 mg/ml, 0.45 mg/ml. The left column shows the samples incubated with NBH, recovered from experiments RT-QuIC (a, c); on the right are shown the corresponding samples incubated with the 263K (b, d, e). In the first row (a, b) have been reported samples at a concentration of 0.1 mg / ml; in the second line (c, d) those at 0.42 mg / ml and in the third (e) those at 0.45 mg/ml. In Figure d is reported the characteristic twist of parallel in-register β-sheet structures.

The EM analysis of RT-QuIC products with 128CC peptide showed a higher number of fibrils compared to 128notCC. Fibrils were also observed in the incubation with NBH at 37°C and 300rpm, unlike the peptide 128notCC, although much less numerous and less defined with respect to the incubation with the 263K (Figure 27, b). The thickness of the fibrils observed in the latter case ranged from 8.19nm to 10.7nm.

The 127notCC peptide incubated at 0.45mg / ml, 37°C and 300rpm, gave numerous fibrils rather ordered even in the incubation with the NBH (Figure 28, a). However, also in this case both the structure and fibril measures (ranging from 9.2nm to 18.7nm) suggest an aggregation of the fibrils in the bundles and thus a less ordered structure than that observed in the incubation of the

peptide with the 263K. Fibrils made with the 263K showed thickness ranging from 5:54 to 11.5nm; within the same fibril was possible to observe a twist, ie the thickness reached 13.1nm in the point of maximum width, and 8.03nm in the twist point (Figure 28, b).

The 127CC peptide incubated at 37C and 300rpm with both brain homogenates gave no rise to fibrils up to the maximum time of incubation.

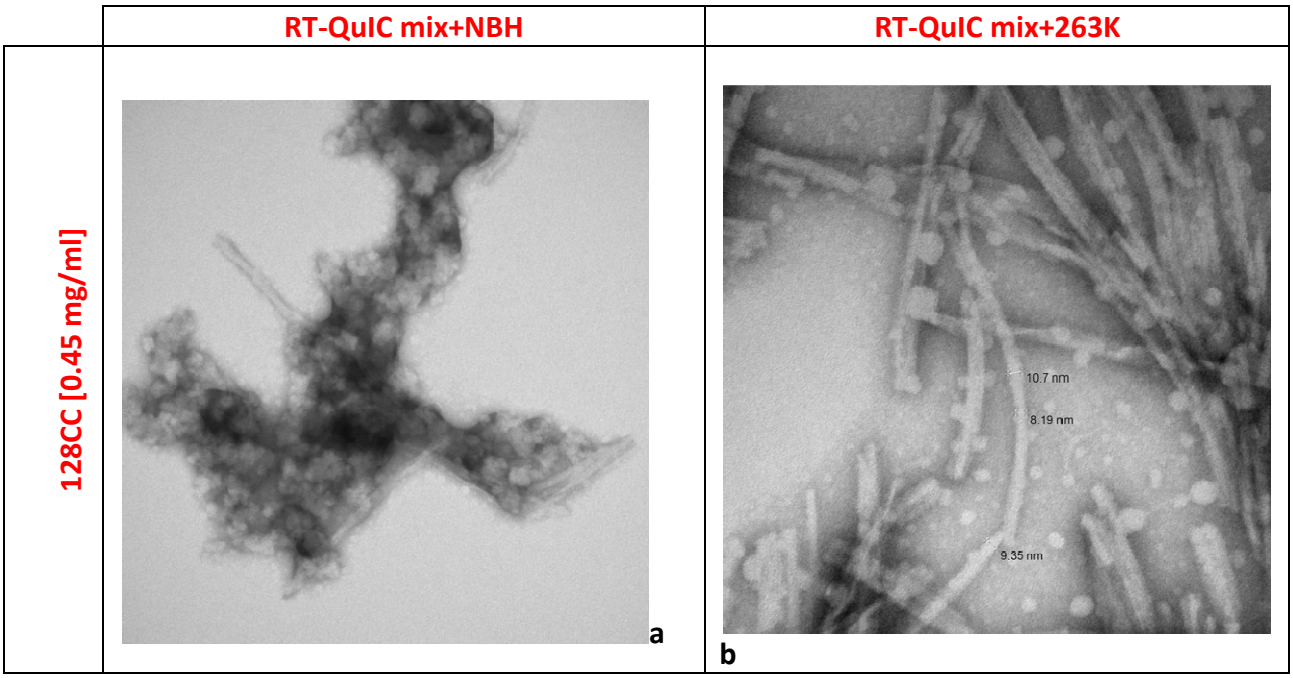

Figura 27. Peptide 128tCC analyzed by EM at the concentration 0.45 mg/ml. The left column (a) shows the sample incubated with NBH, recovered from experiments RT-QuIC; on the right are shown the corresponding samples incubated with the 263K (b).

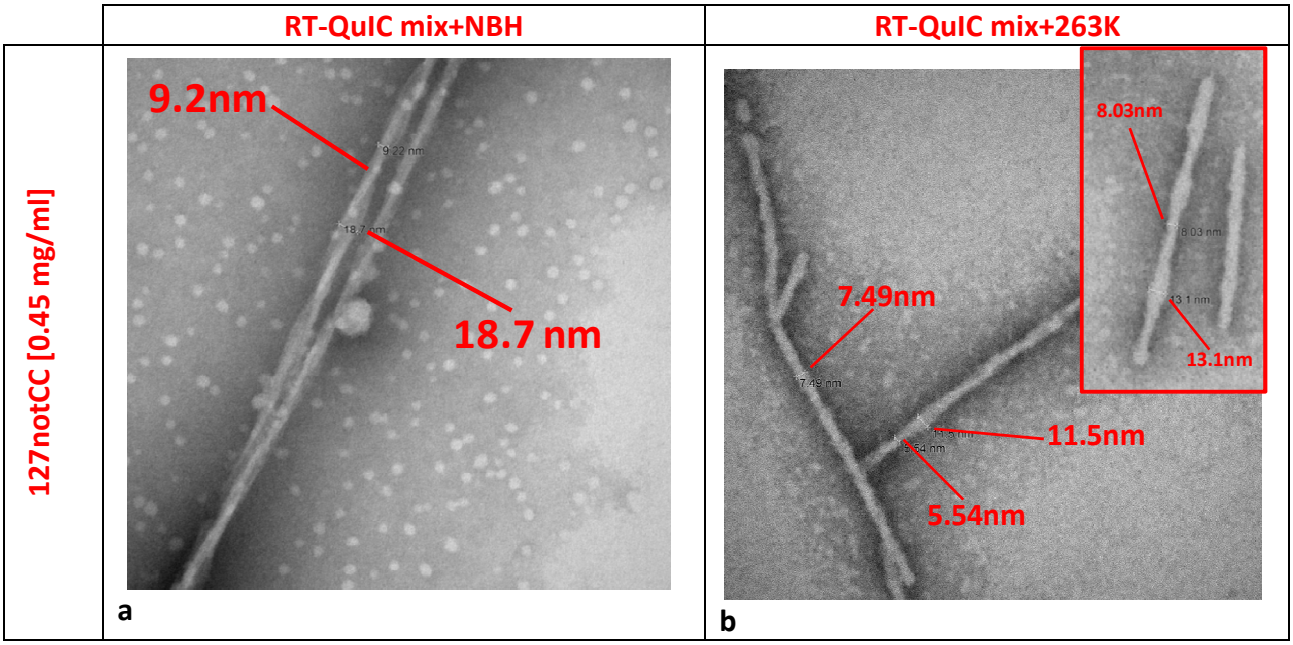

Figura 28. 127notCC peptide analyzed by EM at the concentration 0.45 mg/ml. The left column shows the sample incubated with NBH, recovered from experiments RT-QuIC (a); on the right are shown the corresponding samples incubated with the 263K (b). In b the characteristic twist of parallel in-register β-sheet structures is reported.

2.1.4 Fourier Transform Infrared Spectroscopy (FTIR) of central hairpin peptides

To test if the RT-QuIC products of ThT-positive reactions were in parallel beta-sheet conformations, they were performed analysis of the secondary structure of proteins by Fourier transform infrared spectroscopy (FT-IR).

Considering altogether the data obtained in RT-QuIC assays, and western blot and EM analysis, the 128-164, but not the 127-161, portion of the PrP seems actually involved in the formation of a hairpin in hamster. Furthermore, structural analysis of peptides lacking the disulfide bond would suggest how they fold in the absence of artificial links, as the disolfude bridge, which are actually present neither in the PrPC nor in PrPSc. Finally, for obtaining IR spectra of high quality, relatively high concentrations of fibrils are necessary; so far, however, RT-QuIC with the 127CC and 127notCC peptide did not produced enough fibrils to allow IR analysis. For these reasons, I decided to focus my further studies only on peptide 128notCC.

The 128notCC peptide incubated with the RT-QuIC mixture at the concentration of 0.42mg / ml, in the presence of NBH or 263K, at 37°C and in the absence of agitation, has revealed the presence of peaks in the two regions of the spectrum, known as Amide I and Amide II.

The Amide I band is due to carbonyl stretching vibrations, while the Amide II is due primarily to N-H bending vibrations. Because C = O and N-H bonds are involved in hydrogen bond established between the different elements of the secondary structure, their positions in the spectra give us information on the secondary structure of a protein.

The Amide II band is not a good predictor for the quantification and characterization of the secondary structure of proteins; its frequency band ranges between 1510 and 1580 cm^{-1}, and its spectrum is more complex than Amide I band. Amide I is the most intense absorption band in proteins, its frequency ranging between 1600 and 1700 cm^{-1}.

A large number of synthetic polypeptides having a known structure, have been used for the IR characterization. Therefore, this technic is based on theoretical and experimental work, which provided insights into the variability of wavelenght frequencies for particular conformations of the secondary structure of proteins. The location of the peaks are more easily obtained from the second derivative of the spectrum. The RT-QuIC products with 128notCC peptide had an FTIR absorbance maximum at: 1) ~1515 cm^{-1}, in the Amide II region, revealing the presence of protein in the sample; and 2) at 1611 and 1625 cm^{-1}, in the Amide I region, which is indicative of a high beta sheet paralleli content, confirming that aggregates from RT-QuIC assays actually contain parallel beta sheet structures.

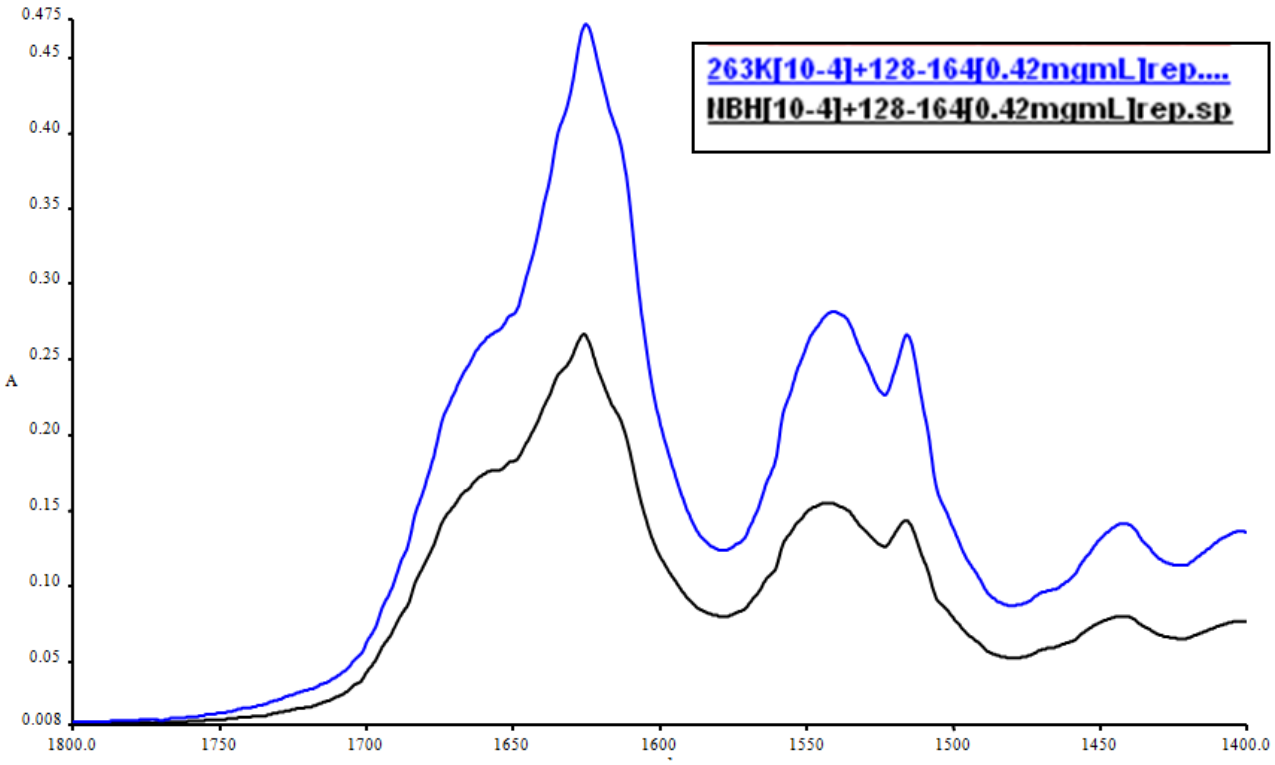

A

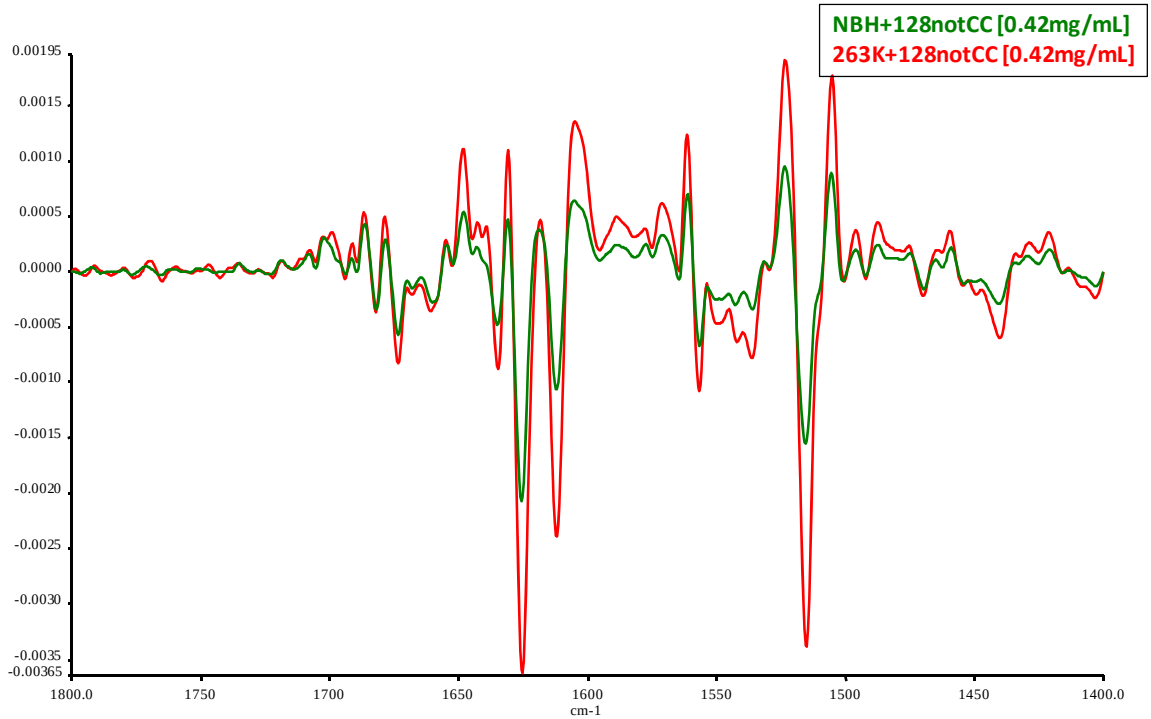

b

Figure 29. Original spectra (a) and second derivative amide I and amide II FTIR spectra (b) of 128notCC peptide at a concentration of 0.42mg/ml, incubated at 37°C, in the absence of agitation.

2.2 Conclusions

Peptides 127CC, 127notCC, 128CC and 128notCC were included in reaction mixtures of RT-QuIC assays instead of the normal substrates of the reaction (rPrP23-231 and rPrP90-231) to verify their ability to act as a substrate for the aggregation process or for ability to aggregate spontaneously.
The 127CC peptide did not show a reaction of conversion and amplification to the same concentration of the substrates classical (0.1 mg/ml); only at a concentration three times higher (0.3 mg/ml, data not shown) it was possible to observe a positive reaction, although after sixty hrs. The same peptide analyzed in the absence of the disulfide bridge (127notCC), and at the same concentrations, showed a positive reaction suggesting that the bond between the two amino acids and the relative position of these play an important role in the aggregation process. The peptides 128CC and 128notCC were faster in the formation of fibrils with respect to the peptide 127notCC: at the concentration of 0.05mg/ml the first ones have a positive signal over a few hours, while for the peptide 127notCC the reaction is much more slower, not observable before 55 hours.
Our hypothesis is that the disulfide bridge, designed by Hafner-Bratkovic et al., J Biol Chem. 2011, in the mouse, involves different amino acids in the hamsters ; this could be due to differences in amino acid sequence between the proteins of the two animals and to the shift of amino acids caused by the lack of an amino acid at position 55 in the mouse (hamster prion sequence: http://www.ncbi.nlm.nih.gov/protein/P04273.1, mouse prion sequence: http://www.ncbi.nlm.nih.gov/protein/NP_001265185.1). The presence of the disulfide bridge in a wrong position in the sequence of the hamster may prevent the normal process of assembly into fibrils with PIRIBS structure. Another important difference between the different peptides, regards the region B2, ie the region involved in the formation of intramolecular antiparallel beta sheet in the protein constituent; fragments 128notCC and 128CC possess the entire amino acid sequence of this structure, while the sequence 127-161 is devoid of two of its four amino acids. This secondary structure could provide a certain degree of stiffness/stability to the peptide, and consequently to the hairpin, by promoting the process of packaging in PIRIBS structures. Because peptides 128CC, 128notCC and 127notCC have showed similar behavior both with NBH (uninfected) and 263K (infected) brain homogenates, we have hypothesized that the aggregation process is not determined by the contact with the pathogenic form of the prion protein (template-driven propagation), but by a process of self-assembly. The conformation adopted seems to be in agreement with the PIRIBS structure, in which the proteins are stacked one above the other with a parallel in-register intermolecular beta-sheet structure. Each single protein should possess a conformation characterized by at least two important areas of folding, or hairpins, one comprising the loop C-terminal disulfide-linked formed by helices 2 and 3 in PrPC (called native hairpin) and the other comprising the hairpin central, formed from the amino acid sequences here analyzed.
Western blot analysis of RT-QuIC products with 127CC peptide showed that there were not significant differences compared to the control (ie, the peptidic stock) either before or after treatment with PK. The 128CC and 128notCC peptides showed bands mostly identical in the absence of treatment with PK, while after PK-treatment the bands were present only in RT-QUIC samples, but not for the peptidic stocks. This might indicate that the RT-QUIC products are located in complex structures, such as that PIRIBS, that do not allow easy access to the PK, by preventing it from degrading the structure.
Then, EM analysis have been carried out to verify the actual presence of fibrillar structures which were hypothesized based on the results of the previous experiments. In general, all the peptides incubated with the NBH were devoid of fibrils, or these appeared in disordered clusters, difficult to be isolated, surrounded by electrondense material. We think that these could be the components

of RT-QuIC mixture accumulated around sites genesis of the fibrils, with the task of facilitating their formation. If our model was correct, each fibril should have a thickness of about 10.8nm (value obtained by multiplying the measure of a single amino acid, 0.3nm, by the number of peptides, ~36). Given that the fibril obtained from a RT-QuIC experiment with 0.1mg/ml 128notCC peptide and 263K showed a thickness of 19nm, we think that the image observed could actually be that of two closely spaced fibrils.
Further investigation with the aim to obtain a greater number of individual fibers, have shown that the RT-QuIC products of peptides incubated with the 263K were: i) rich in fibrils with a thickness comprised between 3.8 nm and 11.5 nm, for the 128notCC peptide ; ii) between 10.7nm and 8.19nm for the 128CC peptide ; iii) between 5.54 and 11.5nm for the 127notCC peptide; while iiii) for the 127CC peptide, again, no fibrils were observed. We hypothesized that these differences in the thickness could be due to different positions of the fibrils in the grids of analysis. In the case of 128CC peptide, the fibrils were much more numerous, suggesting the possibility that these are formed more quickly than the corresponding peptide lacking the disulfide bond 128notCC. In addition, it was possible to observe the presence of a twist along a discrete number of fibrils of all three types of peptides (128notCC, 128CC and 127notCC), in particular those of the 128CC peptide. This structural feature is typical for parallel in-register beta sheet conformation, and corroborate our hypothesis. Moreover, the observation of FT-IR spectra of the RT-QuIC products with 128notCC peptide, has showed the position of peaks in the sprectrum at wavelengths indicative of high content of parallel beta sheet structures in the fibrils analyzed.

In conclusion, the results so far obtained seem to indicate that the 127notCC, 128notCC and 128CC peptides are able to form fibrils spontaneously, with a structural organization that is in agreement with the presence of the PIRIBS structures previously hypothesized. The thickness of most of the EM fibrils observed was about 11nm, in accordance with the aforementioned theory; the variability observed could be explained as: a) the ability to form hairpins with extremities more or less close together and/or as a different arrangement of the fibrils in the grids of analysis, b) the parallel association of more fibrils, in the cases where they reach higher dimensions to 11nm.
The EM observations have not detected zones of accumulation of dye between the fibrils; as already reported above, similar structures have been observed in EM images of scrapie-associated fibrils (Govaerts et al., Proc Natl Acad Sci U S A. 2004; DeMarco and Daggett, Proc Natl Acad Sci U S A. 2004). This seems to confirm the existence of proteolytic cleaveges which determine a complete separation of the central and native hairpins, with consequent visualization of individual protofilaments in EM images. The ability of prion rPrPC seeded to form amyloid fibrils in vitro with parallel-in register beta-sheet architectures in the C terminal region, between the helices 2 and 3 (linked by disulfide bond) had been established previously by the Byron's group (Groveman et al., J Biol Chem. 2014); here is provided an evidence that these structures are formed also by the central portion of the peptide, usually considered less stable in PrP.

3. Materials and methods

3.1 Purification of 23-106 PrP fragment

3.1.1 Buffers

- DENATURING BUFFER (inclusion body SOLUBILIZATION BUFFER):
  Guanidine HCl solution [6M] and Sodium Acetate [20mM], pH=8
- REFOLDING BUFFER:
  Sodium Acetate solution [20mM], pH=8.0
- ELUTION BUFFER:
  Sodium Acetate solution [20mM], pH=3.5
- SOLUTION A:
  Sodium Acetate solution [10mM] and Ethylenediaminetetraacetic acid (EDTA) [1mM], pH=5.0
- SOLUTION B:
  Sodium Acetate solution [10mM] and Ethylenediaminetetraacetic acid (EDTA) [1mM], and NaCl [1M]
- DIALYSIS BUFFER:
  Sodium Acetate solution [20mM], pH=5.0

3.1.2 Biological samples

We used a recombinant expression system to synthesize the rPrP 23-106 fragment of Syrian Hamster. The Escherichia Coli Rosetta2(DE3) strain is transformed with the plasmid pET-41a which is modified to contain this PrP sequence.
This strain, which is used to express the recombinant proteins, has been engineered to be able to control the expression of the gene of interest. The recombinant protein expression starts only at the appropriate time, so the toxicity that the foreign protein may cause is reduced.
This strain contains the T7 phage RNA polymerase gene which is under the control of the lac operon. This operon is present in bacterial DNA but is constitutively repressed by the product of the gene lac I and the T7 polymerase is not transcribed in significant amounts until the lac operon is activated. It is inducible with lactose or with its analogues such as isopropyl b-thiogalactopyranoside (IPTG). This molecule must be added from the outside because it isn't a bacterial product.
The gene of interest is placed under the control of the T7 promoter, so the messenger and the corresponding protein are synthesized only when the T7 RNA polymerase is synthesized. This occurs only after the addition of the IPTG to the culture medium, which induces the detachment of the lac repressor I from the T7 promoter RNA polymerase.

3.1.3 Bacterial cultures screening and stock bacterial preparation

The Escherichia Coli Rosetta2(DE3) stock was provided by the Caughey laboratory (NIH, Hamilton (USA)).
The bacteria stock, was stored at -80^{o}C in the presence of glycerol. This was a mixture of bacteria clones which may express the rPrP 23-106 differently.
We stored four different cultures at +4^{o}C in LB-agar starting from this stock and we analyzed the amount of protein produced in each clone with Coomassie Blue method. To do this we thawed the stock and incubated an aliquot for about 8 hours at 37^{o}C, 200 rpm in LB medium supplemented with the Kanamycin and Chloramphenicol antibiotics. We streaked each culture in LB-agar medium and incubated overnight at 37^{o}C, 5% CO_2. We chose 4 colonies from this plate and we incubated them in four tubes containing 10 ml fresh medium and then we stored them at 4^{o}C on LB-agar.

The 4 liquid cultures were also induced in the production of the Syrian hamster rPrP 23-106 fragment using the reagent IPTG and leaving them to incubate for about 2 hours.
I analyzed these total cultures and also their pellet with Coomassie Blue method solubilizing them in SaBu (Sample Buffer) 1:1.
Once we established which colony produce more protein of interest, we created several stocks: the bacteria were grown in traditional medium, supplemented with 20% glycerol and stored at-80C .

3.1.4 Inclusion bodies preparation

The bacteria were grown for 8 hours in LB medium supplemented with appropriate antibiotics and then induced using the kit Overnight ExpressTM Autoinduction Systems, Novagen. After 24 hours, the bacterial culture was centrifuged and the bacterial pellet was stored at-20C.
We solubilized the pellet in Bug Buster Master Mix which is a reagents mixture containing nuclease, lysozyme and a reagent for the protein extraction. We broke the bacteria membranes to release the inclusion bodies using OMNI International TH (Tissue Homogenizer).
After a series of washes- homogenization and centrifugations to remove impurities, the pellet was weighed and stored at-20C.

3.1.5 Immobilized metal ion affinity chromatography (IMAC)

The rPrP 23-106fragment can be purified by IMAC (Immobilized metal ion affinity chromatography). The proteins are able to form complexes with certain metal ions due to the presence of polarizable chemical groups (such N, O, S) present in the amino acid residues. This feature is exploited in IMAC chromatography (Porath et al., 1975; Hochuli, 1990).
The column is packed with a resin derivatized with chemical groups capable of chelating the metals. To increase the resolving power of this technique and to facilitate the chromatographic separation of the protein one generally introduces six contiguous histidines (6xHis-tag) into the sequence of the protein (at the N or C-terminal) through the use of an appropriate plasmid. This step isn't required to purify the rPrP because this fragment itself contains in the N terminal portion five non-continuous histidines that strongly binds the IMAC resin through the formation of coordinated bonds between the 6 rings of imidazole and the metal of the stationary phase. Other proteins that don't bind the column so strongly will be eluted during the washing steps.
The inclusion bodies are resuspended in denaturing buffer and then homogenized and centrifuged at 9000 rpm. The supernatant obtained is incubated with **"**Ni-NTA Superflow**"** (Qiagen) for 40 minutes, to allow the proteins to bind to the beads. This resin contains Ni2+ fixed to Sepharose beads through the chelating nitrilotriacetate (NTA).
We packed the chromatographic column with the inclusion bodies bound to the resin and we have eliminated the impurities (as proteins which bind the column with low affinity) by washing the column with denaturing and refolding buffer using AKTA Explorer (Ge Healthcare).
The fragment of interest was recovered using elution buffer. The pH change in the buffer allows the detachment of proteins. The fractions were collected by monitoring the absorption signal at 280 nm.
To further eliminate non-specific proteins, we did an additional step of purification using cation-exchange chromatography with SP Sepharose FF 1ml column, GE Healthcare.
Ion-exchange chromatography (or ion chromatography) is a process that allows the separation of ions and polar molecules based on their charge. It can be used for almost any kind of charged molecule including large proteins, small nucleotides and amino acids.

Proteins have numerous functional groups that can have both positive and negative charges. Ion exchange chromatography separates proteins according to their net charge, which is dependent on the composition of the mobile phase. By adjusting the pH or the ionic concentration of the mobile phase, various protein molecules can be separated (Wikipedia).
The protein was loaded directly into this column and the impurities washed away with a solution without salt (Solution A) using AKTA. The rPrP 23-106 fragment was elute using a gradient elution, that needs an ionic strength increase, using two different buffers, one without salts (Solution A) and one with high ionic concentration (1M NaCl, Solution B). The ionic strength increases gradually from 0% to 100%.
Each portion of the peak was collected by monitoring the absorption signal at 280 nm and analyzed with SDS-PAGE electrophoresis.
The more concentrated aliquots have been subjected to the process of dialysis, where the small molecules move from the dialysis tubing with a 3KDa cutoff to the Dialysis buffer following a concentration gradient which allows us to remove the components that could alter the protein properties or that could interfere with future studies .
After about 6 hours the external solution was replaced with fresh solution, to facilitate further removal of small molecules from the bag. The use of a large excess of the external solution, as well as the repeated exchange of this solution allowed us to eliminate or completely replace the small molecules of the protein solution.

3.2 Real-Time QuIC

3.2.1 RTQ buffer

The solution for the RT-QuIC (RTQ Buffer) had the following ingredients: 10 mM phosphate buffer (pH 7.4), 300 mM NaCl, 0.1 mg / ml of substrate (rPrP 23-231 or rPrP 90-231, Full Length and Truncated, respectively), 10 µM Thioflavin T (ThT), and 10 µM ethylenediaminetetraacetic acid tetrasodium salt (EDTA). The RTQB (98 µl / well) was loaded into the wells of a 96 multi-well plate with the transparent bottom (Nunc) and the reactions had as seed 2µL of sample for a final volume of 100 µL per reaction. The multi-well was sealed with a transparent film (Nalgene Nunc International sealer) and incubated in a BMG Fluostar plate reader at 42-46°C for about 100 hours with cycles of 1 minute of agitation (700 rpm double orbital) and 1 minute of rest throughout the incubation period of the reaction. The measurements of fluorescence (ThT, 450 +/- 10 nm excitation and 480 +/- 10 nm emission; reading from the bottom) was performed automatically by the instrument every 45 minutes.

3.2.2 Biological samples

We used hamster non-infected (NBH) and infected (263KBH, 263K prion strain) brain homogenates, human non-infected (HNBH) and infected (sCJD, from sporadic CJD patients) human brain homogenate as seed in RT-QuIC reactions.

3.2.3 Substrate

We used Truncated (rPrP90-231) and Full Length (rPrP23-231) hamster recombinant prion protein (rPrPC) as a substrate in the RT-QuIC control reactions (NBH/263K incubated with rPrP90-231/rPrP23-231 in RT-QuIC buffer, without the addition of other peptides or fragments) . The recombinant prion protein was purified as described by Wilham et al., PLoS Pathog. 2010.

RT-QuIC has been used to: 1) detect the ability of the N-terminal fragment 23-106 (rPrP 23-106) to inhibit the conversion reaction; 2) observe whether portions of the prion protein were able to

form fibrillar aggregates. To this end, the RT-QuIC mixture was modified by adding the rPrP23-106 fragment as a substrate, in the first case, and, in the second case, by replacing the substrate with one of the peptides to be analyzed (127CC, 127notCC, 128CC, 128notCC).
The rPrP 23-106, the N-terminal fragment, was purified as described above.
The 127CC, 127notCC, 128CC, 128notCC peptides were synthesized according to our requests by the company Peptide 2.0.
The 127notCC peptide was synthesized in order to contain the aa127-161 sequence of hamster PrP: vvgglggymlgsamsrpmmhfgndwedryyrenmnrypnqv.
The 128notCC peptide was synthesized in order to contain the aa128-164 sequence of hamster PrP: glggymlgsamsrpmmhfgndwedryyrenmnrypnqvyyr.
The corresponding peptides with the disulfide bridge, had the amino acids at the extremities substituted by Cysteine linked with a disolfure bridge.
5 mg of each peptide, in lyophilized form, were diluted in 5ml of solution (4.6/4.9ml of water + 400/100µl of Acetic acid) to obtain a final concentration of approximately 1mg/mL. The use of Acetic acid was required to facilitate the dilution.

3.3 N2aSc- and N2aSc+22L cells treatment

3.3.1 Biological Samples

For our cell culture testing of rPrP 23-106 we used a mouse neuroblastoma cell line, non-infected (N2aSc-) and prion-infected (N2aSc+22L). Cells were grown using Opti-Mem growth medium (Gibco) enriched with 10% FBS (Fetal Bovine Serum), 1 mM glutamine, 1% antibiotic penicillin/streptomycin (10,000 U/ml, Gibco).

3.3.2 Cell lysis

For biochemical analysis cells were washed with 2 ml of Trypsin to remove the excess medium (which inhibits trypsin's enzymatic activity); next they were incubated in the presence of 2 ml of trypsin for about 2 minutes. Part of the cells were passaged and maintained for future experiments and an aliquot was centrifuged at 2000 rpm for 5 minutes to recover the cell pellet for western blot analysis. Cells were lysed with Lysis Buffer (0.5% Triton-100, 0.5% DOC in PBS) to recover intracellular prion protein; spun at 3000 rpm for 5 minutes to eliminate cell debris, and PrP containing supernatant was recovered and stored at-20°C.

3.4 Polyacrylamide Gel Electrophoresis (SDS-PAGE)

SDS-PAGE (Sodium Dodecyl Sulphate - Polyacrylamide Gel Electrophoresis, electrophoresis on polyacrylamide gel in the presence of sodium dodecyl sulfate) is an analytical technique which allows the analysis of protein extracts. The principle underlying this technique is the electrophoretic activity of proteins which have been denatured by the SDS. The protein separation happens for the difference between the molecular weights because the correlation mass-charge to denatured protein with SDS remains constant. Cell lysates or inclusion bodies were diluted 1:1 in 2X sample buffer supplimented with urea that allows the denaturation and reduction of protein disulfide bonds), boiled for 10 minutes to complete denaturing reaction and loaded onto a NuPAGE 10%-12% Bis-Tris Gel, Novex®. We used a "Precision Plus Protein™ Dual Color Standards" or "Precision Plus Protein™ All Blue Standards" as a molecular weight marker to determine the molecular weight of the bands. Electophoresis was done at 200 mA for 30-60 min. Using MOPS SDS Running Buffer, Novex®. The gel was either Commassie blue stained for total protein content or proteins were transferred onto a PVDF membrane for western blot analysis. Coomassie Blue total protein staining was done as follows: gel was incubated for about 45 minutes in Coomassie

Brilliant Blue R-250 solution with Methanol-Acetic Acid-R-250 (50%:10%:0.1mg). Next the gel was destained using a solution of Ethanol an Acetic Acid (50%:10%). Results were visualized using a scanner connected to a personal computer.

3.5 Western Blotting

The Western Blotting protocol requires an initial separation of proteins by SDS-PAGE and then the transfer of the proteins from the gel to a PVDF membrane, previously treated with methanol and then washed in water and balanced in transfer buffer (33L H2O, 57.6g Glycine, 12.1g Tris/HCl, 800ml MeOH, 2ml 10%SDS). Constant electric field was applied to the gel to transfer the proteins out of the gel and onto the membrane; at the end of the transfer the membrane was submitted to saturation for one night with a 0.5% milk solution in TBS-T, to block all the free sites of hydrophobic interaction present on the PVDF sheet. Then, the blot was placed in contact for 1 hour with the primary antibody 6D11, 1:7500) that which recognizes a epitope of prion protein between amino acids 93-109. We did three fast washes and then 3 washes of 5 minutes each to wash away the antibody with a solution of TBS-T (TBS+tween20 Sigma-Aldrich). I proceeded with an incubation for 1 hour with the anti-mouse secondary antibody conjugated with the enzyme alkaline phosphatase (Sigma) diluted 1:5000 in milk. We repeated the wash with TBS-T to wash away the secondary antibody, then the membrane was treated for a maximum of 5 minutes with the reagent AttoPhos (Promega). This step is necessary for the development of the membrane, because it provides a substrate for alkaline phosphatase which produces a fluorescent signal which can be visualized. The membrane is dried for a minimum of 20 minutes and subsequently analyzed with the instrument **"**Molecular Dynamics (GE Healthcare) Typhoon 9410 Variable Mode Imager".

3.6 Fourier transform infrared spectroscopy (FTIR)

FTIR spectroscopy is an experimental technique established to study the composition of the secondary structure and the structural dynamics of proteins. Fourier Transform Infrared Spectroscopy (FTIR) is a method that exploits a mathematical tool known as Fourier transform (FT, Fourier Transform) in combination with the infrared spectroscopy. Infrared (IR) spectroscopy exploits the capacity of the different functional groups to absorb at specific frequencies, according to their structure. When an organic molecule is hit by an IR radiation the energy transferred by the radiation itself is converted into vibrational energy; the fundamental ways in which the molecule can vibrate are two: i) stretching, due to rhythmic stretching along the axis of binding, and ii) bending, due to variation of the angle of bond. When these vibrations result in a variation of the dipole moment of the molecule, then you have a vibration IR active. When it has such a variation, in fact, the molecule, vibrating, produces an oscillating electric field: this makes possible the exchange of energy with electromagnetic waves. The IR spectrum, obtained by plotting the intensity of the absorption as a function of the wavelength of the absorbed radiation, although it is reported to the molecule in its entirety, it is characterized by the peaks attributable to specific functional groups, forming part of its structure. It is thanks to the reproducibility of these peaks, and especially of the characteristic values of absorption, that we are able to be traced back to the structure of the molecule under examination.
FTIR allows to obtain infrared spectra by first collecting an interferogram of a sample signal using an interferometer, and then performing a Fourier Transform (FT) on the interferogram to obtain the spectrum. Most of the peak positions were easily found in the second derivative spectra.
They were established correlations between IR spectra and secondary structures of proteins. A large number of synthetic polypeptides was used for the characterization of infrared spectra for proteins with a defined secondary structure content. The work (theoretical and experimental) on a

large number of synthetic polypeptides provided useful information about the variability of frequencies for particular secondary structure conformations. The peptide group, a repeat unit of structural proteins, gives up to 9-band characteristics referred to as amide A, B, I, II ... VII. Of these, the Amide I and II bands are the two most important IR vibrational bands of the protein (Susi and Byler, Methods Enzymol. (1986).

In the Amide I region (1700−1600 cm^{-1}), each type of secondary structure gives rise to a somewhat different C=O stretching frequency due to unique molecular geometry and hydrogen bonding pattern. The Amide II band, in contrast, is mainly associated with in-plane N-H bending and with C-N stretching vibration. Amide II is more complex and shows much less protein conformational sensitivity than the Amide I region ancounterpart (Kong and , Acta Biochim Biophys Sin (Shanghai). 2007). High sensitivity to small variations in molecular geometry and hydrogen bonding patterns makes the Amide I band uniquely useful for the analysis of protein secondary structural composition and conformational changes. The nature of hydrogen bonding involving the C=O and NH moieties, determines the exact frequency of the vibration band. In turn, this is determined by the secondary structure adopted by the polypeptide chain, reflecting the backbone conformation and hydrogen-bonding pattern. In brief, the bands observed in Amide I region, consist of overlapping component bands, representing α-helices, β-sheets, turns and random structures.

It is very important to recognize that there is no simple correlation between IR spectra and the elements of protein secondary structure. FTIR spectra are complicated by the fact that each single spectrum has its own characteristics due to several micro-situations. Estimations of the side chain absorption in a protein spectra analysis is important because someone peptide may change the Amide I spectral band parameters (Venyaminov and Kalnin, Biopolymers. 1990). This must be kept in mind in analyzing spectra of proteins, in particular when the content of certain residues is high. To obtain IR spectra of high quality, it is necessary relatively high concentrations of protein (eg> 10 mg / ml). Sometimes the FTIR spectrum is complex: bands of the secondary structure elements can overlap, and the procedure for background subtraction could lead some experimental error.

In my experiments, FTIR was performed using a PerkinElmer Spectrum 100 FT-IR spectrometer equipped with a diamond attenuated total reflectance sample unit and an MCT detector. For analysis of the 128notCC peptide, 1 ml of a freshly thawed 0.42 mg/ml solution prepared as described above for use in RTQuIC was applied to the diamond. RT-QuIC products with 128notCC peptide, seeded and not seeded (ie, incubated with 263K and NBH respectively) were pelleted by centrifugation at 20,800 x *g* at 4 °C for 20 min, the supernatant was removed, and the pellet was resuspended with ultrapure water and centrifuged two times. The pellet was resuspended in nanopure water to a 50% (w/v) slurry and applied to the diamond. Then, the samples were dried under a stream of nitrogen while collecting serial background-subtracted spectra, each comprised of 32 accumulations (4 cm^{-1} resolution; 1 cm/s OPD velocity; strong apodization). Second derivative spectra were calculated with nine data points using Spectrum software (PerkinElmer Life Sciences).

3.7 Transmission Electron Microscopy

For negative stains of the fibrils, Formvar and carbon-coated grids (Ted Pella, Inc., Redding, CA) were subjected to glow discharge, quickly placed onto 10µl droplets of RT-QuIC products with the peptides (127CC, 127notCC, 128CC, 128notCC), and incubated for 30 min at room temperature. The grids were washed for 5 min each onto one/two droplets of deionized water, stained negatively with methylamine tungstate diluted 1:1 with water (Nanoprobes, Inc., Yaphank, NY) for 15 s, the excess liquid from the grids was removed and then air-dried. Negatively stained grids were examined at 80 kV on a model H-7500 transmission electron

microscope (Hitachi High Technologies, Dallas, TX) equipped with a model HR-100 digital camera system (Advanced Microscopy Techniques, Woburn, MA).

4. References

(Alphabetical order)

Adrover M, Pauwels K, Prigent S, de Chiara C, Xu Z, Chapuis C, Pastore A, Rezaei H, **Prion fibrillization is mediated by a native structural element that comprises helices H2 and H3.** J Biol Chem. (2010); 285:21004-12.

Ariyama H, Kono N, Matsuda S, Inoue T, Arai H, **Decrease in membrane phospholipid unsaturation induces unfolded protein response.** J Biol Chem. (2010); 285:22027-35.

Atarashi R, Wilham JM, Christensen L, Hughson AG, Moore RA, Johnson LM, Onwubiko HA, Priola SA, Caughey B, **Simplified ultrasensitive prion detection by recombinant PrP conversion with shaking.** Nat Methods. (2008); 5:211-2.

Atarashi R, Sano K, Satoh K, Nishida N, **Real-time quaking-induced conversion: a highly sensitive assay for prion detection.** Prion. (2011); 5:150-3.

Bach C, Gilch S, Rost R, Greenwood AD, Horsch M, Hajj GN, Brodesser S, Facius A, Schädler S, Sandhoff K, Beckers J, Leib-Mösch C, Schätzl HM, Vorberg I, **Prion-induced activation of cholesterogenic gene expression by Srebp2 in neuronal cells.** J Biol Chem. (2009); 284:31260-9.

Bate C, Tayebi M, Williams A, **Sequestration of free cholesterol in cell membranes by prions correlates with cytoplasmic phospholipase A2 activation.** BMC Biol. (2008); 6:8.

Borchelt DR, Scott M, Taraboulos A, Stahl N, Prusiner SB, **Scrapie and cellular prion proteins differ in their kinetics of synthesis and topology in cultured cells.** J Cell Biol. (1990); 110:743-52.

Broom KA, Anthony DC, Lowe JP, Griffin JL, Scott H, Blamire AM, Styles P, Perry VH, Sibson NR, **MRI and MRS alterations in the preclinical phase of murine prion disease: association with neuropathological and behavioural changes.** Neurobiol Dis. (2007); 26:707-17.

Caughey B, Raymond GJ, **The scrapie-associated form of PrP is made from a cell surface precursor that is both protease- and phospholipase-sensitive.** J Biol Chem. (1991); 266:18217-23.

Deleault NR, Harris BT, Rees JR, Supattapone S, **Formation of native prions from minimal components in vitro.** Proc Natl Acad Sci U S A. (2007); 104:9741-6.

Dees C, German TL, Wade WF, Marsh RF, **Characterization of lipids in membrane vesicles from scrapie-infected hamster brain.** J Gen Virol. (1985); 66:861-70.

DeMarco ML, Daggett V, From **conversion to aggregation: protofibril formation of the prion protein.** Proc Natl Acad Sci U S A. (2004); 101:2293-8.

Donne DG, Viles JH, Groth D, Mehlhorn I, James TL, Cohen FE, Prusiner SB, Wright PE, Dyson HJ, **Structure of the recombinant full-length hamster prion protein PrP(29-231): the N terminus is highly flexible.** Proc Natl Acad Sci U S A. (1997); 94:13452-7.

Govaerts C, Wille H, Prusiner SB, Cohen FE, **Evidence for assembly of prions with left-handed beta-helices into trimers.** Proc Natl Acad Sci U S A. (2004); 101:8342-7.

Groveman BR, Dolan MA, Taubner LM, Kraus A, Wickner RB, Caughey B, **Parallel in-register intermolecular β-sheet architectures for prion-seeded prion protein (PrP) amyloids.** J Biol Chem. (2014); 289:24129-42.

Guan Z, Söderberg M, Sindelar P, Prusiner SB, Kristensson K, Dallner G, **Lipid composition in scrapie-infected mouse brain: prion infection increases the levels of dolichyl phosphate and ubiquinone.** J Neurochem. (1996); 66:277-85.

Hafner-Bratkovic I, Bester R, Pristovsek P, Gaedtke L, Veranic P, Gaspersic J, Mancek-Keber M, Avbelj M, Polymenidou M, Julius C, Aguzzi A, Vorberg I, Jerala R, **Globular domain of the prion protein needs to be unlocked by domain swapping to support prion protein conversion.** J Biol Chem. (2011); 286:12149-56.

Heitzman RJ, Skipworth S, **The fatty composition of brain and myelin of normal and scrapie-affected mice.** J Neurochem. (1969); 16:121-2.

Holmes E, Tsang TM, Tabrizi SJ, The **application of NMR-based metabonomics in neurological disorders.** NeuroRx. (2006); 3:358-72.

Johnson RT, Prion diseases. **Lancet Neurol. (2005); 4:635-42.**

Kong J, Yu S, Fourier **transform infrared spectroscopic analysis of protein secondary structures. Acta Biochim Biophys Sin (Shanghai). (2007);** 39:549-59.

Nieznanski K, Choi JK, Chen S, Surewicz K, Surewicz WK, **Soluble prion protein inhibits amyloid-β (Aβ) fibrillization and toxicity.** J Biol Chem. (2012); 287:33104-8.

Pamplona R, Naudí A, Gavín R, Pastrana MA, Sajnani G, Ilieva EV, Del Río JA, Portero-Otín M, Ferrer I, Requena JR, **Increased oxidation, glycoxidation, and lipoxidation of brain proteins in prion disease.** Free Radic Biol Med. (2008); 45:1159-66.

Pani A, Norfo C, Abete C, Mulas C, Putzolu M, Laconi S, Orrù CD, Cannas MD, Vascellari S, La Colla P, Dessì S, **Antiprion activity of cholesterol esterification modulators: a comparative study using ex vivo sheep fibroblasts and lymphocytes and mouse neuroblastoma cell lines.** Antimicrob Agents Chemother. (2007); 51:4141-7.

Pani A, Mandas A, Dessì S, **Cholesterol, Alzheimer's disease, prion disorders: a ménage à trois?** Curr Drug Targets. (2010); 11:1018-31.

Pan KM, Baldwin M, Nguyen J, Gasset M, Serban A, Groth D, Mehlhorn I, Huang Z, Fletterick RJ, Cohen FE, et al., **Conversion of alpha-helices into beta-sheets features in the formation of the scrapie prion proteins.** Proc Natl Acad Sci U S A. (1993); 90:10962-6.

Prusiner SB, **Prions.** Proc Natl Acad Sci U S A. (1998); 95:13363-83.

Solforosi L, Bellon A, Schaller M, Cruite JT, Abalos GC, Williamson RA, **Toward molecular dissection of PrPC-PrPSc interactions.** J Biol Chem. (2007); 282:7465-71.

Susi H, Byler DM, **Resolution-enhanced Fourier transform infrared spectroscopy of enzymes.** Methods Enzymol. (1986); 130:290-311.

Taubner LM, Bienkiewicz EA, Copié V, Caughey B, **Structure of the flexible amino-terminal domain of prion protein bound to a sulfated glycan.** J Mol Biol. (2010); 395:475-90.

Telling GC, **The mechanism of prion strain propagation.** Genome Biol. (2004); 5:222.

Toyama BH, Weissman JS, Amyloid **structure: conformational diversity and consequences.** Annu Rev Biochem. (2011); 80:557-85.

Tsang TM, Woodman B, McLoughlin GA, Griffin JL, Tabrizi SJ, Bates GP, Holmes E, **Metabolic characterization of the R6/2 transgenic mouse model of Huntington's disease by high-resolution MAS 1H NMR spectroscopy.** J Proteome Res. (2006); 5:483-92.

Vascellari S, Banni S, Vacca C, Vetrugno V, Cardone F, Di Bari MA, La Colla P, Pani A, **Accumulation and aberrant composition of cholesteryl esters in Scrapie-infected N2a cells and C57BL/6 mouse brains.** Lipids Health Dis. (2011); 10:132.

Venyaminov SYu, Kalnin NN, **Quantitative IR spectrophotometry of peptide compounds in water**
(H2O) solutions. I. Spectral parameters of amino acid residue absorption bands. Biopolymers. (1990); 30:1243-57.

Wilham JM, Orrú CD, Bessen RA, Atarashi R, Sano K, Race B, Meade-White KD, Taubner LM, Timmes A, Caughey B, **Rapid end-point quantitation of prion seeding activity with sensitivity comparable to bioassays.** PLoS Pathog. (2010); 6:e1001217

Wopfner F, Weidenhöfer G, Schneider R, von Brunn A, Gilch S, Schwarz TF, Werner T, Schätzl HM, **Analysis of 27 mammalian and 9 avian PrPs reveals high conservation of flexible regions of the prion protein.** J Mol Biol. (1999); 289:1163-78.

Yao Y, Ren J, Jones IM, **Amino terminal interaction in the prion protein identified using fusion to green fluorescent protein.** J Neurochem. (2003); 87:1057-65.

Ramasamy I, Law M, Collins S, Brooke F, **Organ distribution of prion proteins in variant Creutzfeldt-Jakob disease.** Lancet Infect Dis. (2003); 3:214-22.

Jones EM, Wu B, Surewicz K, Nadaud PS, Helmus JJ, Chen S, Jaroniec CP, Surewicz WK, **Structural polymorphism in amyloids: new insights from studies with Y145Stop prion protein fibrils.** J Biol Chem. (2011); 286:42777-84.

Wickner RB, Shewmaker F, Edskes H, Kryndushkin D, Nemecek J, McGlinchey R, Bateman D, Winchester CL, **Prion amyloid structure explains templating: how proteins can be genes.** FEMS Yeast Res. (2010); 10:980-91.